Self-Assembled, Peptide-Based Scaffolds for Wound-Healing and Bone Regeneration

A Thesis Submitted

In the Partial Fulfillment of the Requirements for the Degree of

DOCTOR OF PHILOSOPHY

by

Vatan Chawla

Entry No. 2019CYZ0016

DEPARTMENT OF CHEMISTRY

INDIAN INSTITUTE OF TECHNOLOGY ROPAR

Rupnagar

December, 2024

Vatan Chawla: *Self-Assembled, Peptide-Based Scaffolds for Wound-Healing and Bone Regeneration*

"The important thing is not to stop questioning. Curiosity has its own reason for existing."

-Albert Einstein

Dedicated to my family

Declaration of Originality

I hereby declare that the work, which is being presented in the thesis, entitled **"Self-Assembled, Peptide-Based Scaffolds for Wound-Healing and Bone Regeneration"** has been solely authored by me. It presents the result of my own independent investigation/research conducted during the time period from July, 2019 to August, 2024 under the supervision of Dr. Yashveer Singh, Associate Professor, Department of Chemistry, IIT Ropar, Rupnagar. To the best of my knowledge, it is an original work, both in terms of research content and narrative, and has not been submitted or accepted elsewhere, in part or in full, for the award of any degree, diploma, fellowship, associateship, or similar title of any university or institution. Further, due credit has been attributed to the relevant state-of-the-art and collaborations with appropriate citations and acknowledgments, in line with the established ethical norms and practices. I also declare that any idea/data/fact/source stated in my thesis has not been fabricated/ falsified/ misrepresented. All the principles of academic honesty and integrity have been followed. I fully understand that if the thesis is found to be unoriginal, fabricated, or plagiarized, the Institute reserves the right to withdraw the thesis from its archive and revoke the associated Degree conferred. Additionally, the Institute also reserves the right to appraise all concerned sections of society of the matter for their information and necessary action. If accepted, I hereby consent for my thesis to be available online in the Institute's Open Access repository, inter-library loan, and the title & abstract to be made available to outside organizations.

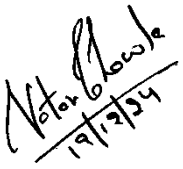

Signature:

Name: Vatan Chawla
Entry Number: 2019CYZ0016
Program: PhD
Department: Chemistry
Indian Institute of Technology Ropar
Rupnagar, Punjab 140001

Date: 19th December 2024

Acknowledgments

Undertaking this PhD has been a life changing experience for me, and it would not have been possible without the support and guidance I received from many people. First and foremost, I would like to express my deepest gratitude to God, whose blessings and guidance have been my source of strength throughout this journey. His grace has given me the perseverance and resilience to overcome challenges and achieve my goals.

The path to completing this work has been fraught with professional and personal challenges. However, I am profoundly grateful to my supervisor, **Dr. Yashveer Singh**, for his unwavering support, guidance, and encouragement throughout my PhD journey. His expertise, insightful feedback, and continuous motivation have been instrumental in shaping this work. I am truly thankful for the opportunity to learn under his mentorship and for the countless hours he dedicated to reviewing my work, reports, presentations, and providing constructive feedback along with invaluable advice. His commitment to ethics, both in work and life, has always been a source of inspiration for me. I am incredibly grateful for the lessons he has imparted, which extend far beyond the lab. Also, I would like to acknowledge my Doctoral Committee members, **Prof. Rajendra Srivastava, Dr. Anupam Bandyopadhyay, Dr. Durba Pal, and** the Chairperson, **Dr. T. J. Dhilip Kumar**, for timely monitoring my research and providing valuable suggestions. I am deeply grateful for the generosity, time, and expertise of all the Doctoral Committee members. I am extremely thankful to **Prof. Rajendra Srivastava** and **Dr. Durba Pal** for providing access to their lab facilities and playing a crucial role in the progress of my work. Dr. Anupam Bandyopadhyay always gave deep insights and feedback that were instrumental to my research. Additionally, I would like to acknowledge the administrative and technical staff of the Department of Chemistry, IIT Ropar, for their assistance and support. Their efforts in ensuring the smooth functioning of the research facilities and providing administrative support have been invaluable.

I am indebted to my colleagues and lab mates for their collaboration, discussions, and support. Their unwavering support has been instrumental throughout my journey. I am genuinely grateful to my seniors, Dr. Neelam Chauhan, Dr. Moumita Halder, and Dr. Nahid Rasool, for their constant encouragement and attentive ear whenever I have encountered challenges. Their insightful discussions, support, and patience have been invaluable. I want to extend my most profound appreciation to my lab mates Deepa, Pruthviraj, Gurpreet, Saurav, and Yashika, and friends, including Anmol, Sandeep, Soumyajit, Ankit, Saurav, Dr. Siddhant, Dr. Amanpreet, Palla Ramprasad, Pulak, and Shubham for their scientific and personal support. A heartfelt thanks to Dimpy, Neeraj, Mohit, Anwesha, Deepika, Taruna, Afreen, Apoorv, Nakshatra, Dr. Sheetanshu, Atul, and Dr. Rajesh. I want to acknowledge my master's interns, Subhajit Das, Sakshi Sharma, and John Raju, for their hard work and dedication. I also thank the other master's students, Yatin, Shubham, Gunjan, Meghna, Mukul, Ananya, Ankur, Srijani, Tumpa, and Gayathri, for their assistance and generosity.

Lastly, my heartfelt thanks go to my family for their unconditional love, support, and understanding.

To my parents, thank you for your constant encouragement, prayers, and for believing in me even when I doubted myself. Your sacrifices and support have been the backbone of my academic endeavours. To my sister, thank you for your love and for always being there to cheer me on. To my wife, Geetika, thank you for your unwavering love, patience, and support throughout this journey. Your understanding and encouragement have been my source of strength during the challenging times.

I am deeply grateful to everyone who has supported and believed in me throughout this PhD journey. This thesis is a testament to their encouragement, guidance, and unwavering support. Thank you all for being a part of this journey and making it possible.

I gratefully acknowledge the Ministry of Education (MoE), India for providing me with a Prime Minister Research Fellowship (PMRF, ID: 2900675, Application No. PMRF-192002-167)) and financial assistance for conducting my research. I also acknowledge the financial assistance from the Department of Biotechnology, India (DBT, (grant # BT/PR40669/MED/32/761/2020)) to the PhD mentor.

Certificate

This is to certify that the thesis, entitled **"Self-Assembled, Peptide-Based Scaffolds for Wound-Healing and Bone Regeneration"**, submitted by **Vatan Chawla (Entry # 2019CYZ0016)** for the award of the degree of **Doctor of Philosophy** of the Indian Institute of Technology Ropar, Rupnagar, is a record of original research work carried out under my guidance and supervision at the Department of Chemistry, IIT Ropar, Rupnagar. All other sources of information, material, and mentorship have been acknowledged at appropriate places in the thesis. To the best of my knowledge and belief, the work presented in this thesis is original and has not been submitted, either in part or full, for the award of any other degree, diploma, fellowship, associateship or similar title of any university or institution.

In my opinion, the thesis meets the requirements of the regulations relating to the award of PhD degree.

Signature of the Supervisor

Dr. Yashveer Singh

Department: Chemistry

Indian Institute of Technology Ropar

Rupnagar, Punjab 140001

Date: 19th December 2024

Lay Summary

Peptides are widely acknowledged as highly versatile building blocks for the fabrication of bioactive materials due to their relative ease of synthesis and scalability. Comprised of amino acids, which are naturally abundant in the body, peptides demonstrate inherent biocompatibility. Under the influence of external stimuli, such as pH, temperature, solvent, and counter ions, peptides undergo self-assembly and give rise to a diverse array of architectures in nano dimension, which includes vesicles, micelles, fibres, tubes, tapes, and ribbons. By modifying the amino acid composition or functionalization, these self-assembled peptides can be designed for various biomedical applications. In addition, their design can be further optimized to induce specific responses from cells by integrating bioactive epitopes, such as cell adhesion motifs, growth factors, or enzyme-mimicking sequences. Over the past two decades, there has been extensive research into the use of self-assembled, peptide-based scaffolds for tissue regeneration. This thesis outlines the utilization of self-assembled peptide-based nano assemblies to manage difficult to heal wounds (chronic wounds) and bone defects (bone regeneration). Chapter 1 provides an overview of peptide self-assembly, factors influencing it, and a review of its diverse biomedical applications. In addition, this chapter also provides the summary of challenges in the field and outlines the objectives of the thesis to address those challenges. Chapter 2 presents a multifunctional wound healing peptide gel with antibacterial, anti-inflammatory, and angiogenesis promoting properties. Chapter 3 discusses the development of cyclic hexapeptide nanotubes for promoting growth of damaged blood vessels in difficult to treat diabetic wounds. The fabrication and assessment of alkaline phosphatase (ALP)-mimicking cyclic peptide nanotubes for bone regeneration to treat bone defects is detailed in Chapter 4. Chapter 5 present the major conclusions of the thesis with a summary of the work done and its contribution to the field. It also discusses the future perspectives for the peptide-based gels and nanotubes developed in this thesis.

Abstract

Molecular self-assembly is a process of bottom-up development in which molecular building blocks interact at the nanoscale level upwards via non-covalent interactions to allow ordering into highly organized supramolecular materials with desired functionalities. The non-covalent interactions involved are hydrogen bonding, van der Waal's forces, electrostatic, and hydrophobic interactions. At the molecular level, biomolecules like DNA, RNA, phospholipids, polysaccharides, proteins, and peptides can spontaneously form self-assembling structures. However, self-assembling peptide-based systems have emerged as the most prevalent due to the significant advantages over the other polymeric biomaterials. They are easy to synthesize with tailored functional groups, scalable, and mimic the natural nanofibrous morphology of *in vivo* extracellular matrix (ECM). While the polymeric biomaterials generate an immunogenic response, the biodegradation products of peptides, amino acids, are in general, non-toxic to the surrounding cells and tissues. As the structural and functional domains of naturally occurring proteins, peptides have been widely used to fabricate biomaterials to promote wound healing and bone regeneration. By introducing different amino acids, peptides can be self-assembled into nanostructures like vesicles, micelles, rods, ribbons, tapes, tubes, and nanofibers under the given physicochemical conditions, which can further be utilized for different biomedical applications. The majority of existing peptide-based biomaterials either involve the utilization of growth factors or drugs for their therapeutic responses. However, the erratic release of the drugs, stability of growth factors, and immunogenic responses limit their clinical translation. In this thesis, we have addressed these challenges by developing growth factor and drug-free peptide-based nanoarchitectures adorned with bioactive functional groups to promote chronic wound healing and bone regeneration. These scaffolds address the existing knowledge gaps in the field and provide a novel approach to promote tissue regeneration. The thesis has been organized into five chapters.

Chapter 1 introduces the self-assembled peptide scaffolds, with emphasis on their significance in wound healing and bone regeneration. An overview is provided on the peptide self-assembly, interaction involved, factors affecting the process of self-assembly, nanostructure formation along with their biomedical applications in wound healing and bone regeneration. The role of extracellular matrix (ECM) and the need for biomaterials mimicking native extracellular matrices is also explained. The chapter also presents comprehensive literature survey, knowledge gap/problem definition, thesis objectives and scope, and organization of thesis.

Chronic wounds are a major healthcare burden worldwide, seriously affecting the life quality of patients. The pathophysiological mechanisms of chronic wounds are complex and, therefore, multipronged approaches that address several different biological mechanisms are desirable. Conventional bandages, gauzes, and hydrogels merely provides a physical barrier and absorb the wound exudates keeping the

moist environment. However, they overlook the underlying complex cellular mechanisms in chronic wounds. Therefore, in **chapter 2,** we have developed a multifunctional, nanofibrous lauric acid-peptide conjugate gel incorporating bioactive Y_2O_3 nanoparticles targeting various aspects of chronic wound. The gel exhibited potent ROS scavenging and bactericidal properties against *E. coli* and *S. aureus*, the prevalent strains at the wound site. The material was cytocompatible and provided a matrix for cell migration and proliferation, thus, resulting in efficient wound healing. The Y_2O_3-loaded gel also exhibited the angiogenic properties by activating hypoxia-induced cellular pathways. The peptide gel provides a drug-free, multifunctional approach for wound healing with proangiogenic, ROS scavenging, and antibacterial properties.

Diabetes mellitus is a chronic disease characterized by hyperglycemia due to defects in insulin secretion or function. Elevated proteases and dysfunctional cellular pathways in diabetes compromises the angiogenesis. The strategies of exogenously delivering growth factors, angiogenic drugs, and gene therapies have major challenges of immunological reactions, degradation, and batch-to-batch variability in efficacy. Therefore, **chapter 3** involves the development of growth factor-free proangiogenic cyclic hexapeptide ($PWLSEK_s$) nanotubes. Nanotubes have heparin-mimicking functional groups to endogenously effect the angiogenic cellular pathways to promote diabetic wound healing. The nanotubes exhibited excellent cytocompatibility and induced no immunogenic response. The proangiogenic studies on hyperglycemic human umbilical vein endothelial cells (HG-HUVECs) showed an upregulated expression of proangiogenic marker proteins and genes. The nanotubes elevated the endothelial tube formation with a significant increase in tube length, number of nodes, junctions, and master segments. The *in vitro* wound healing studies on HG-HUVECs showed an increase in 2D and 3D-cell migration and invasion, thus, resulting in efficient wound healing in diabetic conditions. Proangiogenic cyclic peptide nanotubes, therefore, offer a promising approach for accelerating diabetic wound healing without the need for exogenous growth factors, drugs, and glycosaminoglycans, like heparin.

The Bone Health and Osteoporosis Foundation estimates the total cost of care associated with osteoporotic and non-union fractures will reach $95 billion in 2040. The use of gold standard, allografts, are impeded by potential infection, limited availability, a high non-union rate, and risk of consequent surgeries. Thus, there is requirement of bio-interactive materials inducing the osteogenesis and bone mineralization. The use of natural enzymes in regenerative scaffolds are hampered by their vulnerability to denaturation, time, cost, and effort required for their purification and processing. Therefore, the development of synthetic biomaterials mimicking enzymes is critical for tissue regeneration. **In chapter 4,** we focused on developing alkaline phosphatase (ALP)-mimicking cyclic peptide nanotubes to induce osteogenesis and bone mineralization. The nanotubes consist of histidine residues with imidazole rings in close proximation, which is a critical group in the functional domain of ALP. Nanotubes demonstrated

compatibility with murine pre-osteoblast MC3T3-E1 cells along with a notable ROS scavenging and anti-inflammatory properties. The enhanced phosphatase activity and formation of bone-like nodules showed osteogenic differentiation and bone mineralization. Subsequently, the biomaterial was found to upregulate the expression of genes marking osteogenic differentiation, namely osteopontin, osteocalcin, alkaline phosphatase, and runt-related transcription factor-2, following incubation periods of 7 and 14 days. Furthermore, the nanotubes were shown to inhibit osteoclastogenesis by reducing the expression of critical cytokines involved in this process, RANKL and TRAP. The developed biomaterial promoted the differentiation of preosteoblast cells into osteoblasts, which is a significant challenge for the currently available bone grafts. These biocompatible enzyme-like, peptide scaffolds can be exploited to develop novel multifunctional biomaterials for bone regeneration.

Chapter 5 presents the major conclusions of this thesis, contributions made to the field of peptide-based scaffolds for promoting wound healing and bone regeneration, and future perspectives, which includes future research directions and potential clinical applications.

List of Publications

1. **Vatan Chawla**, Sakshi Sharma, and Yashveer Singh*, Yttrium oxide nanoparticle-loaded, self-assembled peptide gel with antibacterial, anti-inflammatory, and proangiogenic properties for wound healing, *ACS Biomaterials Science and Engineering*, **2023**, *9*, 2647-2662. (**Chapter 2**).
2. **Vatan Chawla**, Soumyajit Roy, John Raju, Durba Pal and Yashveer Singh*, Proangiogenic cyclic peptide nanotubes for diabetic wound healing, *ACS Applied Biomaterials* **2024 (Chapter 3, manuscript submitted**).
3. **Vatan Chawla** and Yashveer Singh*, ALP-Mimetic Cyclic Peptide Nanotubes: A Multifunctional Strategy for Osteogenesis and Bone Regeneration, *ACS Biomacromolecules* **2024 (Chapter 4, manuscript under revision)**.
4. Moumita Haldar, **Vatan Chawla**, Yashveer Singh*, Ceria nanoparticles immobilized with self-assembling peptide for biocatalytic applications, *Nanoscale* **2024,** *16*, 16887-16899.
5. Pruthviraj Bundel, **Vatan Chawla**, Ankur J. Saikia, and Yashveer Singh*, Hydroxyapatite-loaded, Antibacterial Peptide Gels for Osteogenic Applications, *ACS Applied Nano Materials,* **2024,** *7*, 22334–22348.
6. Dimpy Bhardwaj, **Vatan Chawla**, Aastha Gupta, Ankita Dhiman, Yashveer Singh, Garima Agrawal*, Fe/Se nanocomposite-loaded chitosan/alginate-based antibacterial films for wound healing application, *ACS Applied Biomaterials,* **2024 (Manuscript submitted).**
7. Neeraj Kumar Yadav, **Vatan Chawla**, and Rakesh Kumar Maurya*, Toxicological assessment of particulate and unregulated emissions from methanol and gasoline fueled reactivity-controlled compression ignite engines, *Journal of Engine Research,* **2024 (Manuscript submitted)**.
8. Shrishthi Rawat, **Vatan Chawla**, Yashveer Singh, Inderbir Singh*, Development and Evaluation of Chitosan/HMPC/PVA Biocomposite Hydrogel Films of Norfloxacin for Wound Healing Applications **(Manuscript under preparation)**.

Conferences

1. **Vatan Chawla**, Soumyajit Roy, John Raju, Durba Pal, Yashveer Singh, Proangiogenic Cyclic Peptide Nanotubes for Diabetic Wound Healing, *12th World Biomaterial Congress, WBC 2024,* Exco, Daegu, Republic of Korea, 26-31 May 2024 **(Poster presentation).**
2. **Vatan Chawla**, Soumyajit Roy, John Raju, Durba Pal, Yashveer Singh, Proangiogenic Cyclic Peptide Nanotubes for Diabetic Wound Healing, *International Conference and Start-up Summit on Functional Biomaterials and Synthetic Biology (FBSB- 2023)*, PSG Institute of Advanced Studies, Coimbatore, 31 Aug-1 Sep 2023 **(Oral presentation, best oral presentation award).**
3. **Vatan Chawla**, Sakshi Sharma, Yashveer Singh, Yttrium Oxide Nanoparticle-Loaded, Self-Assembled Peptide Gel with Antibacterial, Anti-Inflammatory, and Proangiogenic Properties for Wound Healing, *9th Indian Peptide Symposium*, BITS Pilani, K K Birla Campus, Goa, 23-24 Feb 2023 **(Poster presentation).**
4. **Vatan Chawla**, Sakshi Sharma, Yashveer Singh, Yttrium Oxide Nanoparticle-Loaded, Self-Assembled Peptide Gel with Antibacterial, Anti-Inflammatory, and Proangiogenic Properties for Wound Healing, *Asian Polymer Association Bioforum,* Virtual mode*,* 14- 16 July 2022 **(Oral and poster presentation).**
5. **Vatan Chawla**, Sakshi Sharma, Yashveer Singh, Yttrium Oxide Nanoparticle-Loaded, Self-Assembled Peptide Gel with Antibacterial, Anti-Inflammatory, and Proangiogenic Properties for Wound Healing, *29th CRSI National Symposium in Chemistry & CRSI- ACS Symposium Series in Chemistry, Department of Chemical Sciences*, IISER Mohali, Mohali, 7-9 July 2022 **(Poster presentation).**

Table of Contents

List of Figures

List of Tables

Notations and Abbreviations

Acronym	Name
0D/1D/2D/3D	Zero/one/two/three-dimensional.
ABTS	(2,2′-azino-bis-(3-ethylbenzothiazoline-6-sulfonic) acid.
ACN	Acetonitrile.
ALP	Alkaline phosphatase.
AMP	Antimicrobial peptides.
ARS	Alizarin Red S.
ATR	Attenuated total reflection.
BET	Brunauer–Emmett–Teller.
BMHP-1	Bone marrow homing peptide 1.
BMP	Bone morphogenetic protein.
Boc	tert-Butyloxycarbonyl.
BSA	Bovine serum albumin.
CCL-2/5	Chemokine (C-C motif) ligand 2/5.
CD31	Cluster of differentiation 31.
DAPI	4′,6-Diamidino-2-phenylindole.
DCF	Dichlorofluorescein.
DCFDA	2′,7′-Dichlorodihydrofluorescein diacetate.
DCM	Dichloromethane.
DFO	Deferoxamine.
DFT	Density functional theory.
DFU	Diabetic foot ulcers.
DIEA	N,N-diisopropylethylamine.
DLS	Dynamic light scattering.
DMEM	Dulbecco's modified eagle medium.
DMF	Dimethylformamide.
DNA	Deoxyribonucleic acid.
DPPH	1´-Diphenyl-2-picrylhydrazyl.
EBM	Endothelial basal medium.
ECM	Extracellular matrix.
EGFR	Epidermal growth factor receptor.
EGM-2	Endothelial growth medium-2.
EMT	Endothelial to mesenchymal transition.

eNOS	Endothelial nitric oxide synthase.
ETV2	ETS variant transcription factor 2.
FBS	Fetal bovine serum.
FE-SEM	Field emission scanning electron microscopy.
FGF2	Fibroblast growth factor 2.
FGFR	Fibroblast growth factor receptor.
FT-IR	Fourier transform infrared spectroscopy.
HA	Hydroxyapatite.
HATU	1-[Bis(dimethylamino)methylene]-1H-1,2,3-triazolo[4,5-b] pyridinium 3-oxide hexafluorophosphate.
HOBt	Hydroxybenzotriazole.
HBTU	Hexafluorophosphate benzotriazole tetramethyl uronium.
HFIP	1,1,1,3,3,3-Hexafluoroisopropanol.
HG	Hyperglycemic.
HGF	Hepatocyte growth factor.
HIF-1	Hypoxia-inducible factor.
HR-MS	High-resolution mass spectrometry.
HR-TEM	High-resolution transmission electron microscopy.
HUVEC	Human umbilical vein endothelial cells.
IL-1/4/6/10/15	Interleukin-1/4/6/10/15.
iNOS	Inducible nitric oxide synthase.
LPS	Lipopolysaccharide.
MAPK	Mitogen-activated protein kinase.
MEM-α	Minimum essential medium (MEM)- α.
MHC-II	Major histocompatibility complex-II.
MIC	Minimum inhibitory concentration.
MMP	Matrix metalloproteinase.
MRSA	Methicillin-resistant *Staphylococcus aureus*.
MSC	Mesenchymal stem cells.
MTT	(3-(4,5-Dimethylthiazol-2-yl)-2,5-diphenyltetrazolium bromide.
NAD(P)H	Nicotinamide adenine dinucleotide phosphate hydrogen.
NF-KB	Nuclear factor kappa-light-chain-enhancer of activated B cells.
NG	Non-glycemic.
NP	Nanoparticles.
NPN	N-Phenyl-1-naphthylamine.

OCN	Osteocalcin.
OD	Optical density.
OPN	Osteopontin.
PBST	1X phosphate-buffered saline with Tween® detergent.
PCL	Polycaprolactone.
PDA	Photo diode array.
PDGF	Platelet-derived growth factor.
PGA	Polyglycolic acid.
PLA	Polylactic acid.
PRP	Platelet-rich plasma.
PVDF	Polyvinylidene fluoride.
RANKL	Receptor activator of nuclear factor kappa beta ligand.
RBC	Red blood cells.
rhBMP-2	Recombinant human bone morphogenetic protein-2.
rhTGF-β1	Recombinant human transforming growth factor-beta1
RNPT	Regulated negative pressure-assisted wound therapy.
ROS	Reactive oxygen species.
RP-HPLC	Reverse-phase high-pressure liquid chromatography.
RPMI	Roswell Park Memorial Institute medium.
RT-PCR	Reverse transcription polymerase chain reaction.
RUNX2	Runt-related transcription factor 2.
SAP	Self-assembled peptides.
SDS-PAGE	sodium dodecyl sulfate–polyacrylamide gel electrophoresis
SPPS	Solid-phase peptide synthesis.
TBST	Tris-buffered saline with 0.1% Tween® 20 detergent.
TCP	Tricalcium phosphate.
TFA	Trifluoroacetic acid.
TGF-α/β	Transforming growth factor α and β.
THF	Tetrahydro furan.
TIS	Triisopropyl silane.
TLC	Thin layer chromatography.
TLR-2	Toll-like receptor 2.
TMST	Trimethyl amine sulfur trioxide complex.
TNF-α	Tumor necrosis factor-α.
TRAP	Tartrate-resistant acid phosphatase.

VE-Cad	Vascular endothelial cadherin.
VEGF	Vascular endothelial growth factor.
VEGFR	Vascular endothelial growth factor receptor.
VLU	Venous leg ulcer.
vWF	Von Willebrand factor.
XRD	X-Ray diffraction.
Zeb1	Zinc finger E-box-binding homeobox 1.

CHAPTER - 1

Introduction

Chapter 1
Introduction

1. Introduction

1.1. Molecular self-assembly

Molecular self-assembly is the development of nanostructures through the organization of molecular building blocks by intra- and inter-molecular interactions. The potential of the self-assembled structures is as vast as the types of molecules being studied, as it allows for the facile production of materials with tailored properties and performance.[1] Molecular self-assembly broadly refers to a bottom-up assembly approach, in which molecular building blocks engage primarily through non-covalent interactions, leading to the formation of hierarchical, supramolecular structures endowed with specific functions.[2] The non-covalent interactions involved in the self-assembly are hydrogen bonding, van der Waal's forces, electrostatic interactions, π-π, metal-π, and hydrophobic interactions.[3] Additionally, the strategically formed covalent bonds like disulfide linkages have also been exploited to drive the supramolecular self-assembly.[4] The individual molecular units can be assembled via multiple reversible or irreversible pathways,[5,6,7] with the ability to tune the interactions to drive the desired molecular organization into materials with targeted structure and function.

In nature, self-assembly is ubiquitous in systems like DNA double helix, collagen triple helical structure, and folding of other proteins, which play a crucial role not only in carrying out various physiological functions but also inspiring the design of multiple synthetic functional, dynamic, and reversible architectures.[8,9] Natural and synthetic molecules like DNA,[10] proteins, peptides,[11] phospholipids,[12,13] polysaccharides[14] and polymers[15] have been employed to design self-assembled architectures. The self-assembling peptide systems, however, have attracted the most attention due to the advantages they offer, from their ease of design and synthesis to industrial-level scaling-up. [16] They have an inherent biological origin, structural programmability, good biocompatibility and biodegradability, low immunogenicity, versatile functionality, easy availability, and cost-effectiveness. In addition, their biodegradation products, which are amino acids, are non-toxic to the surrounding cells and tissues.[17]

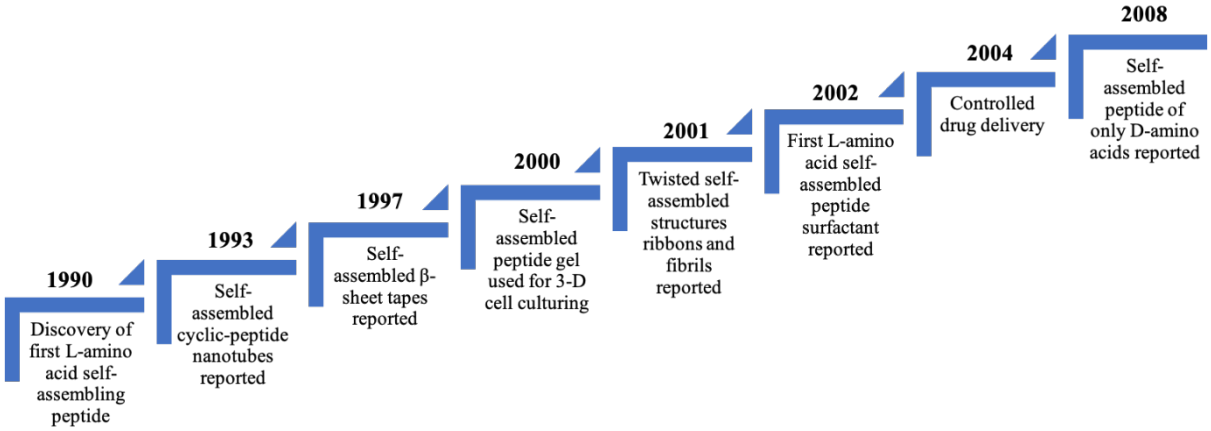

Figure 1.1. The timeline showcasing the development and applications of self-assembling peptides since their discovery in 1990s.

1.2. Self-assembled peptides

Peptides are the short amino acid sequences that form the structural and functional domain in naturally occurring proteins. Peptide-based self-assembled nanomaterials are considered highly versatile owing to their inherent advantages and broad application prospects in biomaterials science. The amino acid sequences can be modified with different functional groups at the molecular level, yielding biomaterials with customized properties.[18] Since the accidental discovery of the first self-assembling peptide EAK16-II by Zhang *et al.* over 30 years ago in the 1990s from the baker's yeast protein zuotin, a flurry of interest has been seen in the field of peptide self-assembly.[19] EAK16-II was referred to as "peptide Lego" as, like Lego bricks, it has hydrophilic pegs and hydrophobic holes, allowing them to form complementary ionic bonds and self-assemble into larger structures.[20] During a similar period in 1993, Ghadiri and co-workers reported for the first time a class of organic nanotubes derived from cyclic peptides with an even number of alternating D-and L-amino acids.[21] The field has grown enormously since then (**Figure 1.1**), and multiple research groups worldwide are working on self-assembled peptides and exploring their potential in various applications ranging from electronics to nanomedicine. Self-assembled peptides (SAPs) have found significant applications in drug delivery,[22] biosensors,[23] biocatalysis,[24] bioimaging,[25] phototherapy,[26] gene therapy[27] and tissue engineering.[28]

Peptide self-assembly is an efficient method of fabricating functional biomaterials with hierarchical structures. Self-assembly of peptides is governed by the folding of individual peptides in the solution, which determines whether the self-assembly occurs or not. Secondary

structures like α-helices, β-sheets, β-hairpin, and random coils promote self-assembly by constructing morphologies at the nanoscale with well-defined 0-D (nanospheres and nanoparticles), 1-D (nanofibers and nanowires), 2-D (nanosheets and nanoribbons), and 3-D (hydrogel/gels) architectures. The rational modulation of intrinsic and external factors serves as a measure for controlling the peptide self-assembly, thereby, affecting the size and morphology of the formed biomaterials. The inherent factor includes the sequence, number of amino acids, and the functional groups on the side chains of amino acids. In contrast, the external factors include the temperature, pH, and solvent.

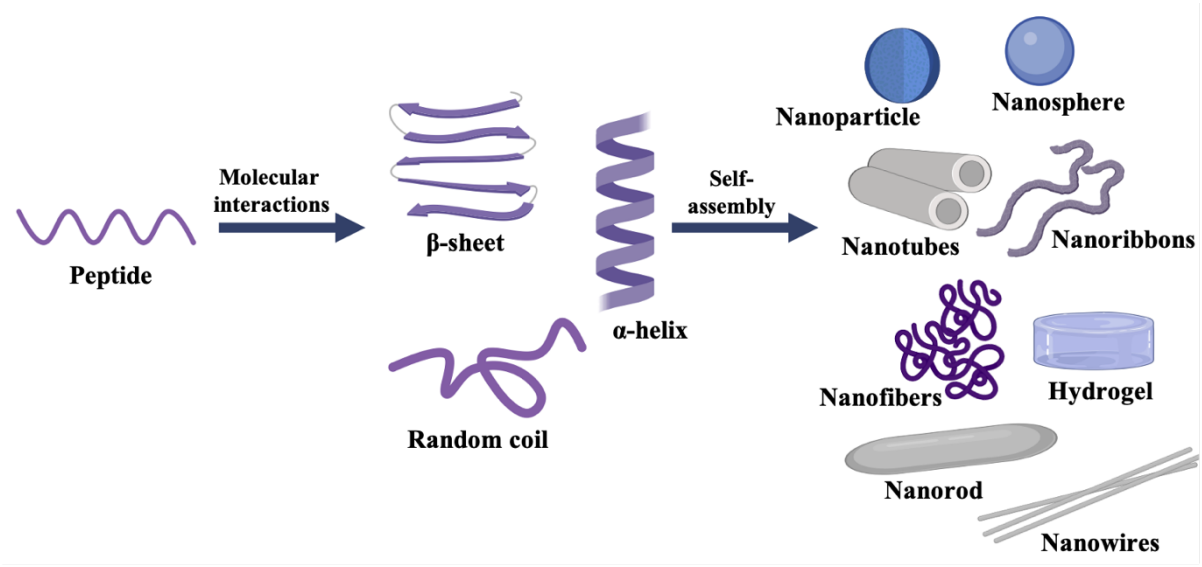

Figure 1.2. Peptide self-assembly into different secondary structures, leading to the formation of various nano-assemblies.

1.2.1. Secondary structures

The secondary structure of peptides represents the first level of folding beyond the primary sequence of amino acids, forming recurring patterns that contribute to the overall 3D architecture.[29] These are specific local conformations of the peptide backbone, stabilized primarily by hydrogen bonds. The most common secondary structures in peptides are α-helices, β-sheets, β-hairpin, and random coils (**Figure 1.2**).

α-Helix. Alpha helices are the right-handed coils where each backbone N-H group forms a hydrogen bond with the C=O group of the amino acid four residues earlier. The helical structure has a periodicity of 3.6 residues per turn, with side chains projecting outward, thus, minimizing steric hindrance and allowing for various interactions with the surrounding environment.[30] When two or more alpha-helices wound around each other, a supercoiled structure stabilized by

hydrophobic interactions and ionic bonds between the helices is formed, which are called coiled-coil structures.

β-Sheets. Beta sheets consist of beta-strands connected laterally by at least two or three backbone hydrogen bonds, forming a sheet-like array.[31] Strands can run in parallel or anti-parallel directions, with the side chains alternating above and below the plane of the sheet. This structure is stabilized by the extensive hydrogen bonding network between the strands, contributing to its rigidity and strength.

β-Hairpins. Beta hairpin structures consist of two anti-parallel beta strands connected by a short loop or turn. This loop typically consists of a few residues, creating a sharp, hairpin-like turn that brings the strands close together. The beta-strands are stabilized by hydrogen bonds between the carbonyl oxygen and amide hydrogen of the backbone. Beta hairpin structures can drive the self-assembly of peptides into more extensive, ordered aggregates, such as fibrils and beta-barrels.

Random coils. Random coil peptide structures lack a fixed or regular secondary structure, such as alpha-helices or beta-sheets.[32] The backbone dihedral angles of random coils vary widely, and there is no consistent pattern of hydrogen bonding. Despite their lack of defined structure, they play essential roles in the functioning of SAPs by providing flexibility for molecular interactions and enabling conformational changes necessary for biological activity.

1.2.2. Self-assembled peptide nanomaterials

Amino acid residues and their sequence in peptide chains affect the self-assembly of peptides through different arrangements and combinations to form different nanostructures, including 0-D nanoparticles and nanospheres, 1-D nanofibers, nanowires, nanotubes, and nanorods, 2-D nanosheets and nanoribbons, as well as 3-D peptide hydrogels/gels.[33] These nanostructures exhibit structural stability, biocompatibility, and tunable properties, making them ideal for various biological applications.

1.2.2.1. 0-D peptide nanostructures

Zero-dimensional peptide nanostructures are compact assemblies formed when peptides self-assemble into discrete, three-dimensional shapes at the nanoscale. These structures, typically ranging from a few to several nanometres in size, are meticulously engineered through controlled interactions between peptide molecules. These nanostructures include peptide nanoparticles and nanospheres. An example of this is the fabrication of self-assembled peptide nanoparticles of diphenylalanine amide. The nanoparticles were prepared by the cross-linking

of diphenylalanine derivatives with glutaraldehyde in hexafluoroisopropanol (HFIP). The resulting nanoparticles modified with pencil graphite electrodes have been utilized for electrochemical cytosensing of DLD-1 cancer cells.[34] Zhang *et al*. employed ultrasound to induce the self-assembly of soybean peptides, resulting in peptide nanoparticles that were utilised as a stabilizer for the O/W emulsion system.[35]

1.2.2.2. 1-D peptide nanostructures

One-dimensional (1D) peptide nano-assemblies are elongated nanostructures formed by the self-assembly of peptides into linear or filamentous shapes. These structures are characterized by their extended length in one dimension while being confined in the other two, typically at the nanoscale. Their formation is driven by specific interactions like hydrogen bonding, hydrophobic interactions, and van der Waals forces, often guided by the intrinsic properties of the peptide sequences**.** It includes the assemblies like, nanofibers, nanotubes, and nanowires. Nanofibers are formed by the alignment of beta-sheets or alpha-helices in a linear arrangement, resulting in long, thread-like structures. Peptide nanotubes are the cylindrical structures formed by amphiphilic peptides aligned in a circular arrangement. Self-assembling cyclic peptides stack into supramolecular cyclic peptide nanotubes, driven by β-sheet-like hydrogen bonding. The larger surface area and aspect ratio of these nanostructures provides them with greater number of bioactive sites making them ideal candidates for drug delivery. Peptide nanofibers can mimic the extracellular matrix and support the cell growth and tissue regeneration. The surfaces of peptide nanowires and nanotubes can be functionalized to design sensitive biosensors for biomolecules, pathogens, or environmental toxins. Wei *et al.* fabricated peptide nanofibers of different lengths from KIIIIKYWYAF peptide, and hybridized them with other materials to form biomaterials with specific functions, which demonstrated their ability in photothermal therapy, and as colorimetric and electrochemical sensors.[36,37]

1.2.2.3. 2-D peptide nanostructures

Two-dimensional (2D) peptide nanostructures are flat, sheet-like assemblies formed by the self-organization of peptides into extended, planar arrays. The inherent properties of the peptide sequences and lateral alignment of beta-strands are responsible for the formation of flat and layered structures of 2D beta nanosheets and nanoribbons. The surface of 2D peptide nanostructures is rich in functional groups that provide excellent platforms for the fabrication of hybrid nanomaterials. The 2D peptide nanostructures have diverse applications like biosensing, catalysis, tissue engineering, and drug delivery due to their unique planar morphology and surface properties. Their self-assembly can also be regulated by the external environment as Montenegro and co-workers demonstrated that 1D peptide nanotubes formed by the self-assembly of cyclic peptides with alternating D- and L-amino acids can be further

assembled into 2D nanosheets by heating the cyclic peptide solution to 80 ℃ for 1.5 h and then allowing its self-assembly at room temperature.[38]

1.2.2.4. 3-D peptide nanostructures

Three-dimensional (3D) peptide nanostructures comprise self-assembling nanofibrous hydrogels/gels, which are developed by the entanglement of peptide nanofiber networks to form a gel-like matrix that retains structural integrity while holding a significant quantity of water. The 3D nanostructures also include peptide nanocrystals and nanocages formed through the precise intermolecular interactions. These 3D nanofibrous peptide gels can mimic the extracellular matrix and have been explored widely for wound healing, tissue regeneration, and drug delivery vehicles. $RADA_{16}$ peptide self-assembles to form nanostructured scaffolds in phosphate-buffered saline, which can mimic the extracellular matrix. These self-assembled nanoscaffolds have been used to culture mouse neural stem cells.[39] Cui *et al*. reported the fabrication of instant self-assembled peptide hydrogel as a dual drug delivery system. The hydrogel fabricated from the Nap-Gly-Phe-Phe-Lys-His self-assemble outside the microfluidic-based alginate microfibers at a pH of 6. The hydrogel was applied as a delivery vehicle for recombinant bovine basic fibroblast growth factor (FGF-2) and antibiotics (ampicillin and lincomycin).[40]

1.3. Fabrication of peptide self-assembly

Peptide self-assembly can be induced by various strategies like pH-switch, temperature variation, **enzymatic triggering,** ionic strength variation, co-solvent approach**,** and **ultrasonication**, **which** provides further avenues for directing peptide assembly with precision, enabling the creation of tailored nanostructures for specific applications.

pH-switch. The pH-triggered self-assembly mechanism in peptides involves the molecular dissolution of peptides with charged side chains in a solvent, which exist freely due to the repulsion between similar charges.[41] A change in pH initiates protonation or deprotonation of side chains, leading to the reduction in the overall charge and consequent decrease in repulsion. As a result of the decreased repulsion, the peptides start to come closer and engage in interactions like aromatic stacking and hydrophobic interactions, contributing to peptide self-assembly.

Temperature-triggered. Temperature-induced peptide self-assembly is a technique that relies on the influence of temperature changes on the peptide's intermolecular interactions.[42] The temperature affects the thermodynamics of the assembly process by either promoting or disrupting the formation of ordered structures.

Enzymatic triggering. Enzymes can trigger the self-assembly of peptides by converting a non-assembling peptide precursor into a self-assembling peptide either by causing some cleavage or inducing a conformational change that promotes assembly.[43] This approach allows for site-specific or condition-specific assembly.

Ionic strength variation. The concentration of ions substantially impacts the stacking of molecules and the structure and functionality of peptides.[44] Elevating the ionic strength through the addition of salt ions can lead to the neutralization of charged repulsive forces, thereby resulting in reduced electrostatic interactions between molecules and facilitating the self-assembly.

Co-solvent approach. Changing the solvent composition can alter peptide solubility, leading to the self-assembly.[45] Peptides are typically dissolved in an appropriate solvent, maintaining them in a monomeric or unassembled state. The gradual introduction of a poorer solvent decreases the solubility of peptides. This reduction in solubility forces the peptides to aggregate and self-assemble into ordered structures.

Ultrasonication. Ultrasound presents a non-invasive external stimulus capable of modulating peptide self-assemblies through adjustable mechanical perturbation.[46] The process of ultrasonication can initiate the nucleation for self-assembly either by disrupting intra-molecular bonds or by energizing self-assembling peptides (SAPs) to enter a metastable state. Moreover, ultrasound not only impacts the kinetics of peptide assembly but also the capability to induce morphological transformations. It can break down large aggregates, thus, allowing for the controlled assembly.

1.4. Characterization of peptide self-assembly

The characterization of peptide self-assembly holds significant importance in comprehending the structure, characteristics, and functioning of the resultant nanostructures. A variety of methodologies are employed to examine the morphology, molecular interactions, and mechanical properties of self-assembled peptides.

Microscopy techniques. Electron microscopic techniques like scanning electron microscopy (SEM) and transmission electron microscopy (TEM) provide insight into the surface morphology, shape, size, and organization of peptide-based assemblies at nanoscale. Atomic force microscopy (AFM) allows for the 3D imaging of peptide assemblies on surfaces, giving insights into their height, roughness, and mechanical properties. AFM can also be used in force spectroscopy mode to measure the stiffness and elasticity of peptide assemblies.[47]

Spectroscopic techniques. Fourier-Transform Infrared Spectroscopy (FTIR) and Circular Dichroism (CD) Spectroscopy are used to analyze the secondary structure of peptides within the assemblies. CD spectroscopy can also provide the information about the overall conformation of the peptides by measuring the differential absorption of left- and right-handed circularly polarized light.[48] FTIR can be further employed to analyze the chemical bonds and molecular interactions between peptide chains. Nuclear Magnetic Resonance (NMR) Spectroscopy provides detailed information on the molecular structure and dynamics of peptides in solution or within assembled states. It is particularly useful for studying the interactions between peptide monomers in assemblies. Further, Raman spectroscopy has also been used for the analysis of amino acids (composition) or structural features (secondary structure).[49]

Rheological analysis. Rheology measurements determines the mechanical properties of peptide-based hydrogels.[50] By applying shear stress, the viscoelastic properties, such as storage modulus (G') and loss modulus (G"), can be determined, providing insights into the stiffness and gelation behavior of the material.

Zeta potential measurements. The surface charge of the peptide-based nano-assemblies in the solution can be determined using zeta potential. It provides insights into the stability of the nanomaterial.[47]

Dynamic Light Scattering. DLS determines the size distribution of peptide assemblies in solution by investigating the scattered light from particles moving in Brownian motion.[51] It is used for the estimation of hydrodynamic radius of peptide based-nanoparticles, micelles, and vesicles.

1.5. Factors affecting peptide self-assembly

Peptide self-assembly is governed by various intrinsic and external parameters that determine the final structure and properties of the nanostructures.[52] Understanding these factors is crucial for designing peptides that can form desired nanostructures with specific functions.

1.5.1. Intrinsic factors

Amino acid side chain. Amino acid side chains significantly influence the self-assembly of peptides by dictating the types of interactions that can occur between individual peptide molecules. The interactions between the side chains affect the morphology of nanostructures, mechanical properties, and speed of self-assembly. The side chains can be categorized based on their chemical properties into hydrophobic, hydrophilic, charged, and aromatic groups. Peptides with both hydrophobic and hydrophilic residues can form amphiphilic structures that self-assemble into micelles or bilayers, with hydrophobic cores and hydrophilic surfaces. Peptides

with complementary charged residues can form highly stable, ordered structures through ionic interactions and hydrogen bonding. The presence of aromatic residues can enhance the stability of these assemblies and introduce specific binding sites or structural motifs. Gazit *et al*. reported the effect of the side chain on the self-assembly, where the spherical nano assemblies were formed by diphenylglycine, whereas the diphenylalanine and its analogs self-assemble into nanotubes.[53] While they have similar chemical properties but the side chain of phenylglycine is more rigid than that of phenylalanine as it lacks the methylene group, which provides diphenylalanine the ability for lateral growth.

Sequence of amino acids. The specific arrangement or order of amino acids in a peptide sequence plays a pivotal role in determining the self-assembly process. It regulates the ability of peptides to form specific secondary structures, interact among themselves, environment, and ultimately aggregate into higher-order nanostructures. Specific sequences are known to stabilize particular secondary structures. For example, sequences with repeated alanine residues tend to form alpha-helices, while alternating hydrophobic and hydrophilic residues can promote beta-sheet formation.[54] By strategically designing the sequence, the morphology, stability, and properties of nanostructures can be controlled. Lee *et al*. studied the effect of the order of amino acid sequences on the morphology of self-assembled structure. Peptides with sequences Ac-$(FKFE)_2$-NH_2 and Ac-$(FK)_2(FE)_2$-NH_2 self-assemble into β-sheet nanoribbons under acidic conditions, while Ac-FFKEKEFF-NH_2 peptide form micelle-like aggregates.[55]

Number of amino acids. The number of amino acids in a peptide, often referred to as peptide length, significantly influences its self-assembly behaviour.[52] The length of a peptide can determine its ability to form stable secondary structures, influence its solubility, and affect the interactions that drive the self-assembly process. Longer peptides have more interaction sites and have a greater propensity to form stable secondary structures, such as alpha-helices and beta-sheets. The loss of conformational entropy upon assembly is compensated by a favorable enthalpic gain from intermolecular interactions. Wang *et al*. studied the dynamic self-assembly of peptides A_6K and A_9K.[56] They observed that with the increase in the hydrophobic chain length, A_9K self-assembles faster and form nanorod morphology, while A_6K forms nanoaggregates, which act as building blocks for short nanofibers.

1.5.2. External factors

pH. The self-assembly of peptides into nanostructures is influenced by the pH of the surrounding environment, which affects the ionization state of amino acid residues in the peptide sequences.[57] This, in turn, impacts intermolecular interactions like hydrogen bonding, electrostatic interactions, and hydrophobic effects. As a result, different morphologies of peptide assemblies can be achieved based on the pH levels. Zhao *et al*. observed the pH-responsive self-

assembling behaviour of RATEA16 peptide hydrogel. RATAE16 peptide sequence is composed for four cationic and two anionic amino acids residues. It has exhibited pH reversible transitions, changing from viscous solution to elastic hydrogel to precipitated state.[58] Stupp *et al*. studied the change in the morphology of self-assembled $C_{16}H_{31}O$-VEVEGRGD at different pH conditions.[59] At low pH, multi-layered nanobelts are formed because most of the COOH groups are protonated. At high pH, the deprotonation of COOH was increased, leading to nanobelt dissociation in response to electrostatic repulsion among glutamate side chains and generates the 2 nm grooves on the surfaces of the nanobelts.

Temperature. Temperature plays a crucial role in the self-assembly of peptides by influencing the kinetic and thermodynamic properties of the assembly process.[60] The effect of temperature on peptide self-assembly is complex, as it can impact various interactions, such as hydrogen bonding, hydrophobic interactions, and van der Waals forces that drive the self-assembly process. The elevated temperature weakens the hydrogen bonds while strengthens the hydrophobic interactions. Moreover, at low temperatures, the kinetic energy of peptide molecules is reduced, slowing down the self-assembly process, which can lead to the formation of highly ordered and stable structures. Temperature-induced reversible self-assembly of diphenylalanine peptide was observed by Huang *et al*. where a clear solution in ACN/H_2O was formed at 90 ℃, which turned into self-assembled nanowires as the temperature gets reduced to 25 ℃.[42] In another study, Luo *et al*. reported the structural dynamics of d-EAK16 peptide, where at 25 ℃ peptide showed a β-sheet structure while with increase in temperature to 80 ℃, it transitioned to typical α-helix structure.[61]

Solvent. Solvents influence the self-assembly by affecting the peptide solubility and interactions, which are key determinants of the self-assembly process.[62] Aqueous solvents drive the aggregation of hydrophobic residues, promoting the formation of nanostructures. Polar solvents can disrupt intramolecular and intermolecular hydrogen bonds within peptides, while non-polar solvents allow stable hydrogen-bonded structures to form. Mixed solvents provide a tunable environment by balancing these interactions to control the self-assembly process and resulting structures. Huang *et al*. reported a solvent based approach for controlling the self-assembly of diphenylalanine peptide.[63] They observed the structural transition of peptide microtubes assembled in the aqueous phase into nanofibers by introducing acetonitrile as a co-solvent. Similarly, Li and co-workers investigated the effect of solvent on the self-assembly of dipeptide sodium salts of L- and D-alanine, where a twisted nanoribbon morphology was observed in both water and THF.[64] However, the handedness of nanoribbons is opposite in both solvents, which was due to the change in the interlayer distance in different solvents.

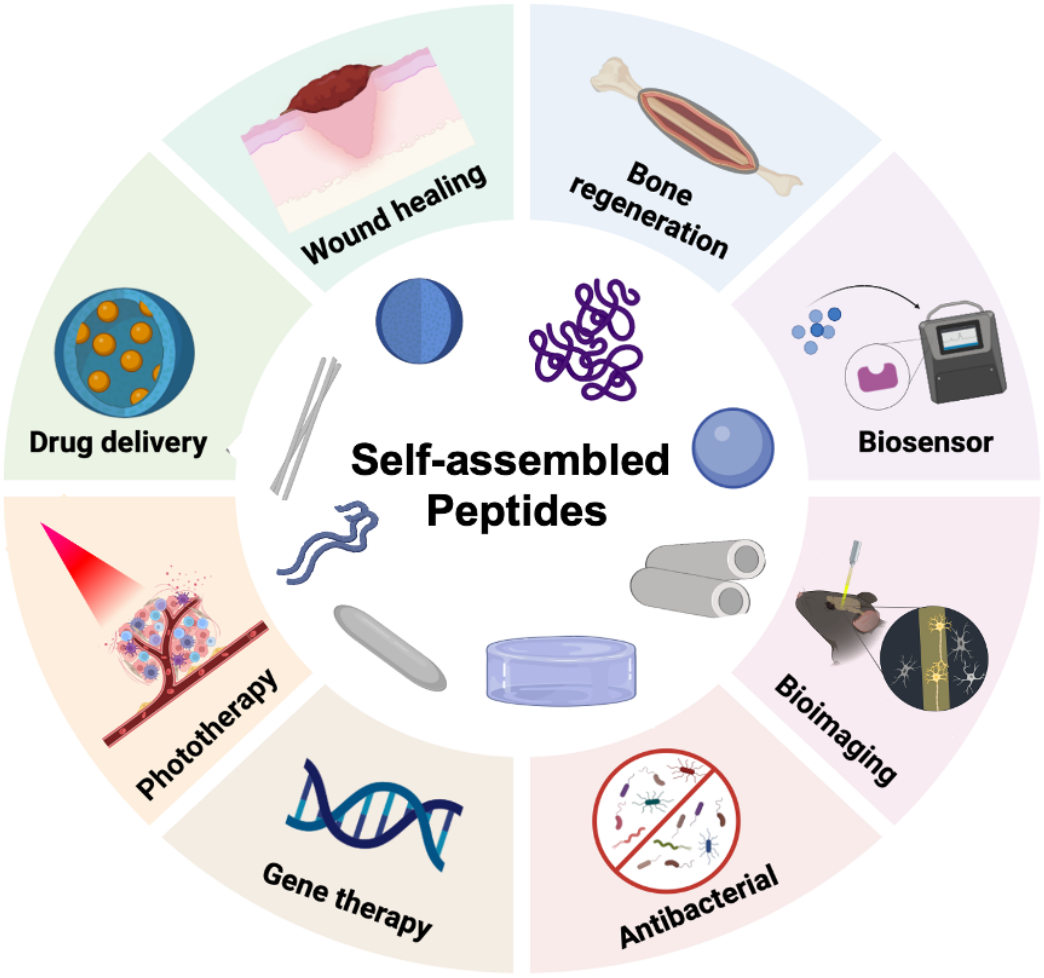

Figure 1.3. Various biomedical applications of self-assembled peptide-based nano-assemblies.

1.6. Biomedical applications

Self-assembled peptides (SAPs) are versatile molecules to generate diverse supramolecular structures with tunable functionality.[29] Their properties can be finely tuned by altering the amino acid sequence, allowing for precise control over their physical, chemical, and mechanical characteristics. A wide range of functional domains like cell attachment sequences, targeting groups, signaling domains, vaccine epitopes, and therapeutic moieties into the SAPs, making them effective for various biomedical applications like targeted and controlled drug delivery, biosensing, bioimaging, antimicrobials, therapeutics, vaccination, and tissue regeneration (**Figure 1.3**).[65] Their stimuli-responsive behaviour enables controlled drug release in response to specific environmental triggers, while their ability to mimic natural extracellular matrix structures supports the tissue regeneration. The best example of a commercially available self-assembling peptide hydrogel is RADA16-I, which is used as cell matrix for tissue engineering

and sustained drug delivery under the name of PuraMatrix™.[66] Hydrogels of P11-4 peptide are available in market as Curodont™ for the repair of early dental lesions.[67] Topical palmitoyl pentapeptide (pal-KTTKS), Matrixyl is present in many skin care products available commercially and provides improvements in photoaged facial skin.[68] SAP-based functional materials have garnered significant research interest due to their versatility and potential applications across various fields. However, this thesis specifically concentrates on exploring the potential of self-assembling peptide-based biomaterials for chronic wound healing and bone regeneration. The focus on these two areas underscores the potential of peptide-based materials to address critical challenges in regenerative medicine.

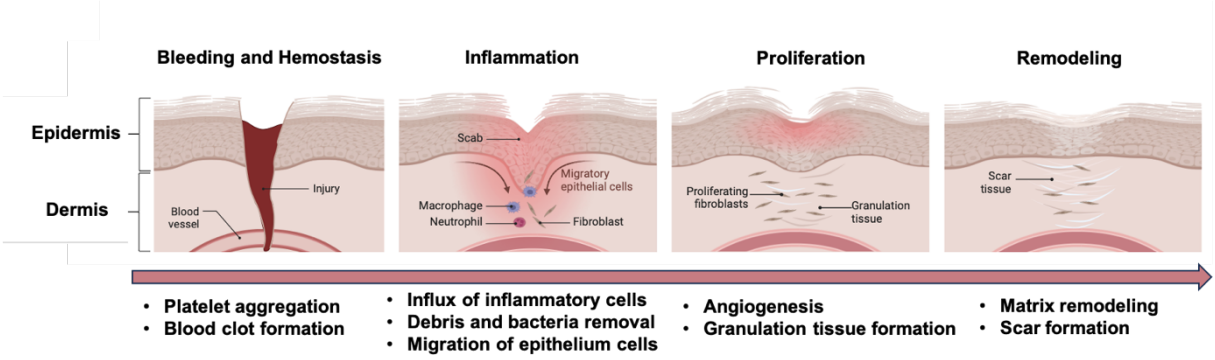

Figure 1.4. Phases of wound healing: hemostasis, inflammation, proliferation, and remodeling.

1.6.1. Wound healing

A wound constitutes damage or a disruption to the typical anatomical structure and function.[69] This damage can vary widely, from a mere breach in the skin's epithelial layer to more severe injuries that penetrate the subcutaneous layer, affecting various structures, including tendons, muscles, blood vessels, nerves, parenchymal organs, and bones. A wound can be caused by an accidental trauma, surgery, or a disease. Irrespective of the etiology, wound damages the tissue along with the local microenvironment. Immediately following an injury or trauma, the healing process begins, which involves the coordinated interaction between various resident and migrating cells, signalling molecules, and extracellular matrix. This intricate interplay ensures that the wound healing progresses efficiently through four overlapping but well-orchestrated phases called hemostasis, inflammation, proliferation, and remodelling **(Figure 1.4**). Hemostasis involves the vasoconstriction and formation of a fibrin plug to prevent the blood loss and keep the vasculature intact. Platelet aggregation and clot formation provide a provisional matrix for the cell's migration in subsequent phases. The Inflammatory phase involves the infiltration of neutrophils at the wound site to prevent infection and remove the damaged tissue. Neutrophils destroy foreign materials and bacteria by releasing proteolytic enzymes and reactive oxygen species (ROS). In the later inflammatory stage, monocytes

infiltrate and differentiate to macrophages to continue the phagocytosis. However, macrophages have a dual role, as they also release various cytokines and growth factors like TGFβ, TGF-α, heparin-binding epidermal growth factor (EGF), fibroblast growth factor (FGF), collagenase, which activate the keratinocytes, fibroblasts, and endothelial cells. Thus, they promote the transition to the proliferative phase. Proliferative phase is characterized by the migration and proliferation of epithelial cells over the provisional matrix. The prominent cell types present are fibroblast and endothelial cells, which facilitate the capillary formation, collagen synthesis, and accumulation of extracellular matrix (ECM). Finally wound enters to the remodelling phase, which involves the remodelling of ECM along with the synthesis and breakdown of collagen fibres. Matrix metalloproteinase (MMPs) enzymes are responsible for this activity, which is tightly regulated and synchronized by inhibitory factors. Gradually, there is a drop in the activity of MMPs promoting the accumulation of new matrix. Initially, the deposition of collagen bundles is disorganized, which becomes oriented and crosslinked. Moreover, ECM architecture approaches to that of the normal tissue during the remodelling phase. The physical contraction of the wound occurs throughout the healing process, which is facilitated by the contractile fibroblasts or myofibroblasts. As the wound heals, the density of fibroblasts, macrophages is reduced by the apoptosis. The growth of capillaries and metabolic activity at wound site decreases. The end result is the formation of a scarred tissue with around 80% recovered tensile strength but the original strength of a tissue can never be regained.[70,71]

1.6.1.1. Chronic wounds

Chronic wounds are characterized by their inability to progress through normal stages of healing in a timely and orderly manner, ultimately failing to re-establish the anatomical and functional integrity of tissue, even after a duration of three months.[72] Typically, chronic wounds are classified into four categories on the basis of etiology: arterial, diabetic, pressure, and venous ulcers. Despite the differences in etiology at molecular level, chronic wounds have various common features, including elevated levels of proinflammatory cytokines, proteases, ROS, and senescent cell population along with the persistent infection, drug resistant biofilms, degradation of ECM and growth factors, impaired angiogenesis, poor cell migration, and dysfunctional stem cells (**Figure 1.5**).[72] Chronic wounds have become a major burden for patients as well as the health care system. Worldwide, the problem of chronic wound has been growing like a silent epidemic due to the aging population and the increase in comorbidities and lifestyle diseases, such as diabetes, obesity, venous hypertension, and peripheral vascular diseases. According to an estimation, in developed countries, 1-2 % of the population will experience chronic wounds in their lifetime.[73] For instance, 6.5 million people in the USA suffer from chronic wounds, and the healthcare system spends more than US$25 billion annually treating wound-related problems.[73] In developing countries like India, the problem of wounds is worsened by factors

such as limited access to quality healthcare, inadequate health infrastructure, lack of medical equipment, and affordability. Only a few regional studies, with limited population sizes, have reported on the prevalence and causes of chronic wounds in specific areas of India. A study by Shukla *et al*. in India on the epidemiology of chronic wounds found a prevalence rate of 4.5 per 1,000 population.[74] In light of the present situation, it is imperative to manage chronic wound issues efficiently and develop cutting-edge biomaterials and therapeutic techniques to enhance patient's life quality and lessen the cost of healthcare.

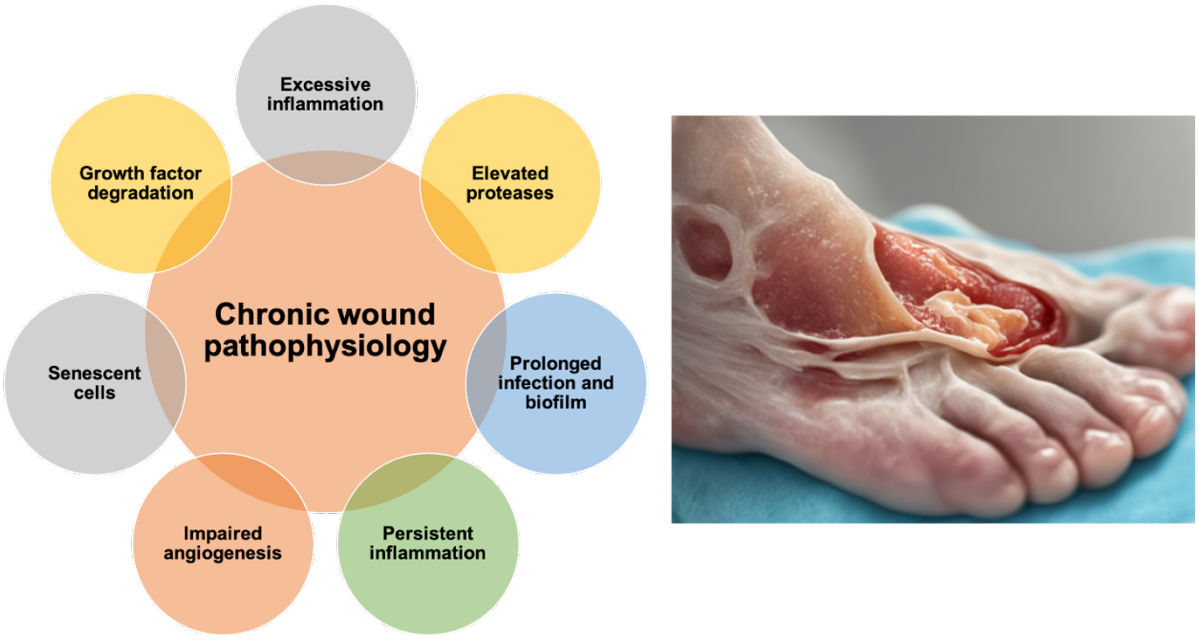

Figure 1.5. Pathophysiology of chronic wounds.

1.6.1.2. Strategies for chronic wound healing

Chronic wound healing is complex and multifaceted mechanism, involving multiple impediments to the healing process. Therefore, it requires a comprehensive and individualized approach that extends beyond traditional wound care strategies, such as sutures, gauges, staples, and bandages, which merely serve as a physical barrier and lack any kind of bioactivity to promote wound healing.[75] Clinical treatments includes the surgical debridement, topical application of antibiotics, and frequent change of dressings. Other techniques include the use of regulated negative pressure wound therapy (RNPT)[76] to enhance the local blood supply, hyperbaric oxygen therapy (HBOT)[77] to raise the oxygen level at wound site, and platelet-rich plasma (PRP) therapy[78] to enhance cytokines and nutritional factors. However, these approaches are only the adjuvant treatments that do not alter the wound microenvironment.[79] Moreover, the development of multi drug-resistant bacteria and biofilm formation, restrict the use of antibiotics.[80]

In view of these limitations, recent times have seen extensive research on the development of functionally bioactive materials that can interact with the wound environment and target the different factors impairing the chronic wound healing.[81,82] For a biomaterial to be optimal for wound healing, it must exhibit excellent biocompatibility, biodegradability, tunable mechanical properties, and the ability to sustain a moist environment at the site of the wound. Further, the properties like, ability to host living cells, deliver drugs and therapeutically active components, inherent antimicrobial, bioadhesive, anti-inflammatory, and proangiogenic ability can help in producing promising results in the healing of chronic wounds. Over time, a range of bioactive materials, including nanoparticles, microneedles, membranes, films, hydrogels, and nanofibers, have been developed from various polymers, peptides, ceramics, metals and their combination for employment as scaffolds in wound healing.[82] These scaffolds are engineered to simulate the extracellular matrix, offering a supportive framework that facilitates cellular migration and proliferation. Moreover, their integration with cells, growth factors, and pharmaceutical agents has been shown to substantially improve the outcomes of wound healing. Various natural (collagen, fibrin, silk fibroin, keratin, gelatin, hyaluronan, cellulose, alginate, chondroitin, and chitosan) and synthetic polymers (polylactic acid, polyvinyl alcohol, polycaprolactone, and polyglycolic acid) along with their composites have been implemented extensively to fabricate scaffolds for wound healing.[83] ++

Peptide-based biomaterials have drawn a significant attention as they can be specifically designed and synthesized to incorporate the bioactive sequences that can stimulate particular cellular responses. For example, peptides can be engineered to include sequences that mimic growth factors or adhesion motifs, directly influencing cellular behaviour, and accelerating the healing process. This level of precision in bioactivity is challenging to achieve with polymeric scaffolds. Their optimal biodegradability ensures that the material provides a temporary support without the need for removal. Biodegradation products of peptides, amino acids, are in general, non-toxic to surrounding cells and tissues. Additionally, peptides are widely distributed throughout the body and are less likely to provoke an immune response compared to some synthetic polymers, which can sometimes be seen as foreign bodies by the immune system. Furthermore, the ease of design and synthesis ensures that peptide sequences can be easily tailored to exhibit intrinsic antibacterial, anti-inflammatory, and angiogenic capabilities.[84,85]

1.6.1.3. Self-assembled peptides for wound healing (literature survey)

Peptides have been self-assembled into different nanostructures like spheres, vesicles, micelles, nanofibers, nanotubes, and hydrogels/gels, which can be functionalized and modified with bioactive motifs to enhance their wound healing efficacy.[86] Moreover, these nanostructures can be incorporated with therapeutic cargos, such as growth factors, cells, antibiotics, and small

molecule drugs for the effective treatment by addressing the challenges at various stages of wound healing.[85,33]

Haemostatic peptides. Following a trauma or surgery, the failure to achieve effective hemostasis can result in uncontrollable bleeding, leading to significant blood loss and potential mortality. A variety of hemostatic agents, such as silicates, fibrin sealants, collagen, and coagulation proteins have been designed to facilitate rapid hemostasis. Nonetheless, these agents often exhibit limited effectiveness in halting severe hemorrhage and lack properties that promote wound healing. In recent years, peptides with self-assembling characteristics have been developed with inherent capabilities to promote both fast hemostasis and rapid wound healing. Supramolecular hydrogels composed of PuraStat®/PuraBond® have demonstrated high hemostasis efficacy in a number of different surgical procedures by the synergistic effect of biofunctional peptides and natural polysaccharide hydrogels.[87] Xu *et al*. have developed platelet-mimicking C_6KL peptide nano-particles and fibrin-mimicking C_6KG peptide nanoparticles to promote the natural coagulation for enhanced hemostasis and wound healing.[88] Zeng *et al.* reported the fabrication of two 12-residue peptides containing pro-cell adhesion sequence Arg-Gly-Asp, RGD to promote rapid and efficient hemostasis.[89] RATEA16, a half-sequence ionic-complementary self-assembled peptide, composed of regular repeating residues containing arginine (Arg), alanine (Ala), threonine (Thr) and glutamic acid (Glu) showed excellent hemostatic performance and biocompatibility. It forms a nanofibrous network, which provides a matrix to entrap the blood components and accelerate the clotting.[90]

Antimicrobial peptides. Bacterial infection is a common impediment to the wound healing, leading to chronicity.[91] In chronic wounds, bacterial infection advances through three stages: contamination, colonization, and infection. Contamination involves the transfer of microbes from the surrounding environment to the site of injury. Colonization occurs when bacteria replicate and attach to the wound without impeding the healing process. Infection develops when the continued growth of bacteria overwhelms the patient's immune system, resulting in damage to healthy cells. Common type of bacterial pathogens found at the infected wounds are *Pseudomonas aeruginosa*, *Staphylococcus aureus*, *Acinetobacter baumannii*, *Escherichia coli*, *Proteus mirabilis* and Gram-positive, anaerobic Cocci. Self-assembled peptide gels can be endowed with the antibacterial properties by incorporating antibiotics, nanoparticles, and small drug molecules into their 3D scaffold either by covalent linkage or passive loading. Their encapsulation within peptide nanostructures prevents the premature degradation of antibiotics, ensuring their stability and prolonged activity in the wound environment. It will also aid in their controlled and sustained release. Hwang *et al*. developed elastin and collagen-like peptide nanovesicles tethered to collagen-containing matrices for the controlled release of vancomycin against *methicillin-resistant S. aureus* (MRSA).[92] Binaymotlagh *et al*. reported the fabrication of Ag nanoparticles incorporated in a peptide gel exhibiting antibacterial activity against

laboratory strain and clinical isolate of *S. aureus*.[93] However, over and misuse of antibiotics has led to the rise of drug-resistant infections, which leads to the exploration of antimicrobial peptides (AMPs) as alternative antimicrobial agents. Their primary structure is typically characterized by a net positive charge, which enables electrostatic interactions with the anionic phospholipids of microbial cell membranes. This interaction leads to the perturbation of the membrane potential and disintegration, ultimately resulting in cell death. It circumvents the need to encapsulate therapeutics to prevent or kill the existing infection. Amphipathic antimicrobial peptides (AMPs) can form supramolecular hydrogels through pH adjustments. For instance, Azoulay *et al*. developed self-assembling AMP hydrogel with a net cationic character, using the sequence Phe–Lys–Phe (FKF). The self-assembly process occurs within minutes at a pH range of 3.3 to 4.3. Antimicrobial studies showed a significant reduction in the presence of *E. coli, P. aeruginosa*, *A. baumannii*, and *S. epidermidis*, indicating a broad spectrum of activity.[94] In another study, Cao and co-workers developed an injectable AMP hydrogel PAF26 from hexapeptide (Ac-RKKWFW-NH2), that gelates at physiological pH and permeabilizes the cell wall, resulting in microbial death.[95] Moreover, the proteolytically stable cyclic peptide-based nanostructures have been explored for their antimicrobial activity. In 2001, Fernandez-Lopez *et al*. demonstrated that self-assembling cyclic D, L-α-peptide nanotubes with suitable functional groups on the outer surface exhibited antibacterial activity against *E. coli* and *methicillin-resistant S. aureus*.[96] As per their report, peptide nanotubes align parallel to the cell membrane, with their hydrophobic side chains inserted into the lipid components of the membrane. At the same time, the hydrophilic residues remain exposed to the hydrophilic components of the cell membrane. Nanotubes permeate the cell membrane using carpet-like mechanism and collapse the transmembrane potential.

***Anti-inflammatory peptides*.** Prolonged, elevated inflammation is hallmark for the chronic non-healing wounds.[97] Excessive neutrophil infiltration increases the expression of proteases and reactive oxygen species, which impairs healing by degrading growth factors, the extracellular matrix and its components. Topical formulations of the self-assembled peptide gels can encapsulate anti-inflammatory drugs in their assemblies to achieve the controlled drug release, improved bioavailability, and decreased side effects. Another strategy includes the co-assembly and modification of the peptides with anti-inflammatory drugs. Webber *et al.* have reported the fabrication of Dex-releasing peptide amphiphile, where dexamethasone has been conjugated using a hydrazone linkage.[98] A nanofibrous gel was fabricated for the controlled release of dexamethasone over several weeks. Enzymatic release of the anti-inflammatory drug ibuprofen from the ibuprofen-conjugated GFFY peptide hydrogel was reported by Yu and co-workers.[99] The drug was conjugated to peptide with ester linkage using hydroxybenzoic acid as an enzymatically cleavable linkage. Further, Tang *et al*. employed the enzyme-instructed self-assembly to co-assemble dephosphorylated dexamethasone sodium phosphate and hydrogelator

precursor Nap-Phe-Phe-Tyr(H_2PO_3)-OH.[100] The dephosphorylation and co-assembly are carried out inside the cells by alkaline phosphatase, which is overexpressed on LPS-stimulated inflammatory macrophages.

Angiogenic peptides. Angiogenesis, the process of forming new blood vessels from existing ones, plays a crucial role in delivering oxygen, nutrients, and vital cells to the site of the wound.[101] Any impediment in this process can lead to defective granulation tissue formation, eventually causing failure of the wound healing to progress through the proliferation phase. The disruption of microvasculature during an injury or trauma leads to fluid accumulation, inflammation, and hypoxia. While the normal angiogenesis depends mainly on endothelial cell migration, proliferation, and matrix deposition by fibroblasts, in chronic wounds the cell functions are altered by the degradation of ECM, growth factors, and impaired cytokines activity and signal transduction. Self-assembled peptide-based biomaterials have emerged as a viable option for proangiogenic treatment techniques owing to their ability to mimic the natural extracellular matrix (ECM) and incorporate the bioactive motifs like growth factors to augment their activity. Huang *et al*. have developed self-assembling peptide hydrogel with proteoglycan heparan sulfate-assisted for the sustained delivery of proangiogenic growth factors, VEGF and HGF.[102] In another work, Jian *et al*. investigated the angiogenic potential of a PDGF-BB-derived supramolecular peptide gel.[103] They developed a PDGF-mimicking peptide using the PDGF epitope VRKIEIVRKK and a self-assembling motif. The exposed hydrophilic epitope on the nanofibrils' surface aid the binding and activation of PDGF receptors, thus promoting vascularization. Hartgerink *et al*. reported the fabrication of a self-assembled peptide gel from a multidomain peptide sequence conjugated with a VEGF-165 mimic to promote angiogenesis.[104] Heparin-mimetic peptide nanofibers have been fabricated by Mammadov and co-workers, which promotes the binding of angiogenesis-promoting growth factors to their receptors.[105] These growth factors and proteoglycans-mimetic peptide scaffolds eliminate the need for the exogenous supply of these molecules. If supplied exogenously, heparin, an animal-derived supplement, may induce an immunogenic response and have potential side effects. The usage of self-assembled peptide-based scaffolds has easily overcome this challenge.

Designing self-assembled peptides for wound healing applications involves several critical factors to ensure they are effective, biocompatible, and conducive to healing.[106] Peptides should promote the cellular responses essential for healing, such as cell adhesion, migration, and proliferation, often by incorporating bioactive motifs like the RGD sequence. They must respond to the wound environment, potentially through stimuli-responsive elements that adapt to changes in pH, temperature, or enzymatic activity at the wound site. Moreover, chronic wounds present a multifaceted challenge as they often suffer from persistent inflammation, infection, impaired angiogenesis, and inadequate extracellular matrix (ECM) remodelling. All of this impairs the healing process and necessitates the multifunctional materials for effective

healing. Since the self-assembled peptide scaffolds can be tailored with diverse functionalities to provide a multidimensional approach towards these impediments, they can offer a holistic approach to promote the wound healing.[107]

1.6.2. Bone regeneration

Bone is a dynamic, mineralized tissue composed primarily of a matrix that provides structural support and is constantly remodelled by various cell types.[108] Bones protect the internal organs, enable mechanical movements, regulate mineral homeostasis, and endocrine functions. Bone cells are enveloped by an extracellular matrix (ECM) consisting of two crucial elements: hydroxyapatite nanoparticles and type-I collagen fibrils. It comprises 40% organic and 60% inorganic compounds, where the organic ECM primarily consists of collagen type I (90%).[109] The hydroxyapatite nanocrystals are organized along the collagen fibrils in a regular and staggered pattern. This unique combination of hard hydroxyapatite and flexible collagen fibrils along with the hierarchical microstructure, gives bone tissue an optimal blend of strength and toughness. The principal cells involved are osteoblasts, osteocytes, osteoclasts, and bone lining cells. Of these, 4–6% of the resident cell population in bone cells are osteoblasts. Through the synthesis, secretion, and mineralization of the osteoid, they play a critical role in bone development. After completing their biosynthetic role, osteoblasts undergo apoptosis or mature into osteocytes, which are dormant cells embedded in the extracellular matrix of the bone. In the meanwhile, the primary cell type in charge of bone resorption is osteoclasts. They accomplish this by lowering the pH and releasing lysosomal enzymes, which break down the protein matrix and cause the mineral components to dissolve.[110] Bone regeneration is a complex yet regulated process in which multiple cell types and chemical signals are employed to heal and restore the physical structure and function of an injured bone tissue. The process of bone regeneration typically involves three overlapping phases, inflammation, repair and remodelling (**Figure 1.6**).[111]

Inflammation. Following a bone fracture or injury, blood vessel gets ruptured in the bone and neighbouring soft tissue leading to bleeding.[112] Damage to surrounding cells and tissues promotes the initiation of an inflammatory cascade, which involves the vasodilation and migration of leukocytes. Inside the fracture gap, there is a conversion of fibrinogen to fibrin, leading to the formation of hematoma (blood clot). This clot stabilizes the injury and provides a matrix for cell migration. The infiltrating inflammatory cells, like neutrophils, macrophages, and lymphocytes, clear the debris and pathogens through phagocytosis. Various signalling molecules including interleukins, tumour necrosis factor-alpha (TNF-α), and bone morphogenetic proteins (BMPs) are released by these cells, which leads to the recruitment of mesenchymal stem cells (MSCs) to initiate the healing process.[113]

Reparative phase. Capillary ingrowth, along with mononuclear cells and fibroblasts, initiates the conversion of haematoma to granulation tissue over a span of a few days. This initial phase of the healing is accompanied by a moderate gain in mechanical strength. As granulation tissue transforms into connective tissue, the presence of collagen fibres increases. While types I, II, and III collagen are initially deposited, type I collagen gradually becomes the predominate form as the maturation process progresses.[111] MSCs undergo differentiation into chondroblasts, which fill the gaps between the broken bone ends with a fibrocartilaginous matrix called soft callus. This soft callus provides initial mechanical stability and support to the fracture site. The soft callus undergoes gradual infiltration by new blood vessels, playing a crucial role in providing nutrients and oxygen to the proliferating cells and facilitating the removal of metabolic waste. Osteoblasts and hypertrophic chondrocytes express high levels of VEGF, thereby promoting the invasion of blood vessels and transforming the avascular cartilaginous matrix into a vascularized osseous tissue. Further, bone regeneration progresses by resorption of soft cartilaginous callus and its replacement by hard callus. Chondrocytes grow hypertrophic and go through apoptosis, while the cartilage matrix progressively calcifies. The calcification mechanism involves mitochondria, which store calcium-containing granules formed in the hypoxic fracture environment. Calcium granules are transferred into the extracellular matrix, where they precipitate with phosphate forming early mineral deposits. These calcium and phosphate deposits serve as the nucleus for homogenous nucleation and apatite crystal formation. MSCs and periosteal cells differentiate into osteoblasts, which lay down new bone matrix (osteoid) over the calcified cartilage. The osteoid mineralizes to form a hard callus of woven bone, which replaces the soft callus and provides mechanical stability.[114]

Remodelling. While the hard callus forms a rigid structure that provides biomechanical stability, it does not completely replicate the biomechanical properties of an intact bone.[115] To address this, the fracture healing process initiates a secondary resorptive phase to remodel the hard callus into an organized lamellar bone featuring a central medullary cavity. High expression levels of IL-1 and TNF-α biochemically mediate this remodelling phase. The process involves the removal of disorganized woven bone by osteoclasts, followed by the deposition of lamellar bone by osteoblasts, which is structurally more robust and organized. The newly formed bone gradually adapts to mechanical loads and remodel according to the stresses placed upon it.

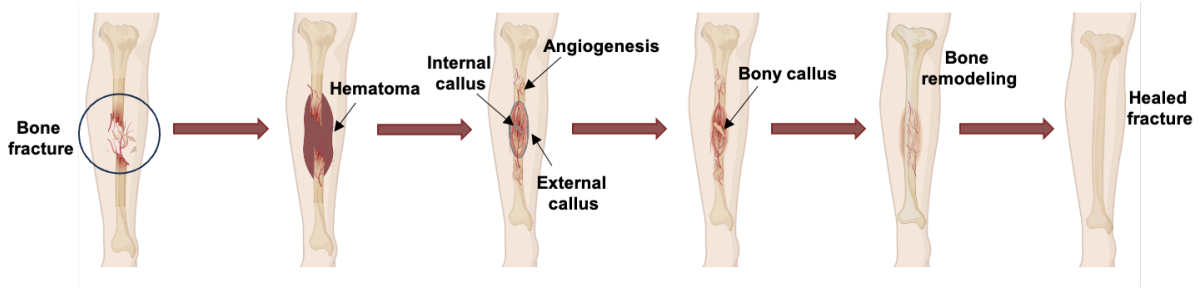

Figure 1.6. Stages of bone regeneration.

1.6.2.1. Strategies for bone regeneration

Bones have an inherent ability to regenerate in response to an injury. Most bone injuries heal without scar tissue formation and are regenerated with their pre-existing properties primarily restored. However, various conditions like, complex fractures with severely damaged surrounding environment, ageing, and musculoskeletal diseases, like tumours, scoliosis, congenital malformations, osteoporosis, bone infection, and osteoarthritis, require external intervention. Understanding the underlying factors is crucial for developing effective strategies that address the specific challenges posed by each condition. The key strategies that are used for the bone regeneration includes the following:

Bone grafts. Bone grafting is an effective surgical procedure for regenerating bone, particularly in cases involving large bone defects, non-union fractures, or the need for additional structural support.[116] The main objective of bone grafting is to create a framework for new bone growth, promote osteogenesis, and improve the healing process. There are different types of bone grafts, including autografts (taken from the patient's body), allografts (taken from another person), and xenografts (taken from non-human species, commonly bovine or porcine). Autologous bone grafts are considered as the "gold standard" in the bone defect treatment due to excellent bone conduction, osteoinduction, osteogenesis, available source, ideal biocompatibility, and three-dimensional structures.[117] They contain living osteogenic cells, such as osteoblasts and osteoprogenitor cells, which directly contribute to new bone formation and accelerate the healing process. Additionally, autologous bone grafts possess various growth factors, including bone morphogenetic proteins (BMPs) that promote the differentiation of mesenchymal stem cells into osteoblasts, enhancing the body's natural healing response. Since the graft is harvested from the patient's own body, there is no risk of immune rejection or disease transmission. Nevertheless, the need of subsequent surgeries, donor site morbidity, substantial costs, and limited availability are the disadvantages that necessitate the consideration of alternative materials. Additionally, with allografts and xenografts, there is are complications regarding immune rejection and disease transmission.[118]

Growth factors. Growth factors play an auxiliary role in bone tissue engineering.[119] Growth factors used for bone regeneration include bone morphogenetic protein-2 (BMP-2), fibroblast growth factor-2 (FGF-2), and vascular endothelial growth factor (VEGF), platelet-derived growth factor (PDGF), and transforming growth factor-beta (TGF-β), etc. BMPs, particularly BMP-2 and BMP-7, are powerful osteoinductive agents that stimulate the differentiation of mesenchymal stem cells (MSCs) into osteoblasts, promoting new bone formation. PDGF and VEGF are critical for the proliferation and recruitment of osteoprogenitor cells and promote

angiogenesis, ensuring the adequate supply of oxygen and nutrients for the bone regeneration. TGF-β regulates the production of extracellular matrix components and contributes the bone remodelling. Growth factors can be delivered at the site of injury using impregnated scaffolds like microspheres, nanoparticles, and hydrogels/gels for their controlled release. Different viral or non-viral vectors are widely used to deliver the genes encoding the growth factors and promote osteogenesis with accelerated vascularization in the defect areas.[120]

Stem cells. Stem cell therapy holds great promise for bone regeneration owing to its remarkable regenerative potential and versatility of stem cells.[121] Mesenchymal stem cells (MSCs) induced pluripotent stem cells (iPSCs), and embryonic stem cells (ESCs) can differentiate into osteoblasts and release bioactive molecules that facilitate tissue repair and angiogenesis. MSCs, commonly harvested from bone marrow, adipose tissue, or umbilical cord blood, are favoured for their immunomodulatory effects and ability to improve the healing microenvironment. Stem cells can be delivered using biocompatible scaffolds or advanced techniques such as 3D bioprinting, which provide structural support and optimize cell attachment and differentiation. Despite their advantages, such as reduced morbidity and potential for personalized treatments, there are some significant challenges associated with it, including safety concerns, as there is a risk of tumour formation in case of uncontrolled differentiation. Standardization and reproducibility of the therapeutic outcomes are challenging, as variations in cell source, culture conditions, and handling can impact therapeutic outcomes.[122,121]

Scaffolds and synthetic bone substitutes. Scaffolds are the three-dimensional structures, providing a temporary matrix for cell attachment, proliferation, and differentiation.[123] Key properties of an ideal scaffold for bone regeneration include biocompatibility, biodegradability, appropriate mechanical strength, and a conducive architecture for cell infiltration and vascularization. Natural materials, such as collagen, chitosan, and alginate are biocompatible and have ability to mimic the natural extracellular matrix. Their scaffolds promote cell attachment and proliferation but may lack mechanical strength. **Synthetic polymers like** polylactic acid (PLA), polyglycolic acid (PGA), and polycaprolactone (PCL) offer customizable properties and controlled degradation rates. They can be engineered to have suitable mechanical properties for bone regeneration. Moreover, synthetic bone substituents like **hydroxyapatite and beta-tricalcium phosphate** are commonly used because of their biocompatibility and osteoconductive properties. These are being used as adjuncts or alternatives to autologous bone grafts, as they promote the migration, proliferation, and differentiation of bone cells for bone regeneration.[124,125]

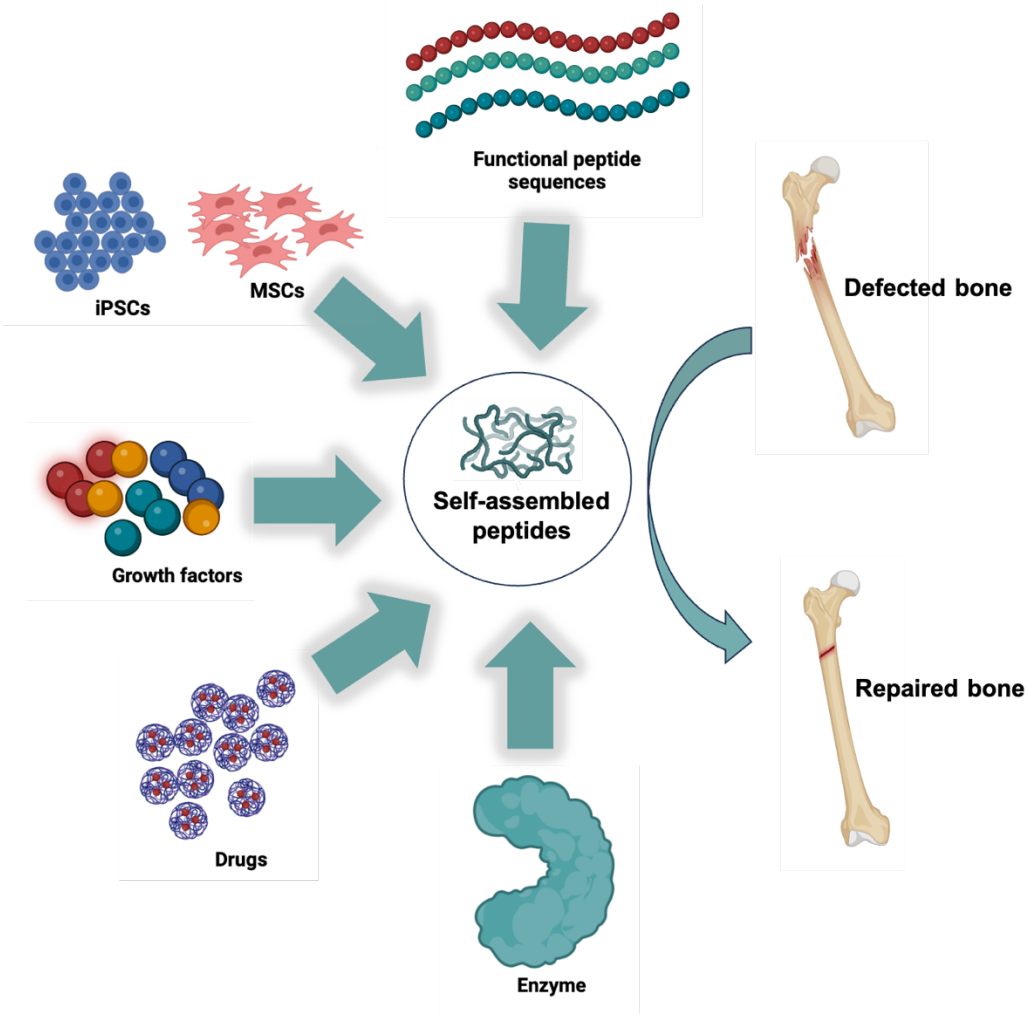

Figure 1.7. Self-assembled peptide-based strategies for bone regeneration.

1.6.2.2. Self-assembled peptide for bone regeneration (literature survey)

Bone tissue regeneration consists of three critical components: "seed cells" that produce the target tissue, growth factors that provide the required guiding signals to the "seed cells," and a three-dimensional scaffold that promotes tissue formation.[126] Scaffolds are usually supplied with growth factors, cells, and drugs to target the impairments to bone regeneration in different ways. A scaffold is the immediate environment for the cells and is essential to bone regeneration. Excellent biocompatibility, non-toxicity, affordability, lack of carcinogenicity, and the ability to effectively induce and enhance osteoconduction and osteoinduction in bone formation are desirable qualities in a scaffold material. Peptide-based scaffolds can be endowed with specific properties by adjusting the composition and introducing biologically active functional groups into the peptide chain. Modification strategies like employing growth factor-mimicking fragments, cell adhesion sequences, and side chain modifications (phosphorylation) can promote the cell proliferation, bone mineralization, enhance alkaline phosphatase activity, direct the differentiation of osteoblasts and regenerate new bone tissue to fill the defect sites. Here are

some key strategies for the use of self-assembled peptide scaffolds in bone regeneration (**Figure 1.7**):

Functional peptide-based scaffolds. Peptide-based biomaterials can serve as temporary cellular scaffolds, offering a microscopic three-dimensional environment at the injury site to assist in mineral deposition and osteoconduction.[127] Incorporating bioactive peptide sequences like arginine-glycine-aspartic acid (RGD) enhances cell adhesion by interacting with integrin receptors on cell surfaces, fostering cell attachment, proliferation, and differentiation. The RGD tripeptide sequence found in fibronectin is a minimal cell adhesion peptide and is extensively studied due to its binding with multiple integrins, stimulating cell adhesion and differentiation. Phosphorylation of the peptide chain aids its binding to calcium ions, providing nucleation sites for the deposition of calcium phosphate, facilitating the formation and maturation of hydroxyapatite crystals. Thus, they contribute to biomineralization. Hartgerink *et al*. developed amphiphilic peptide nanofibers with a hydrophilic polypeptide head and a hydrophobic alkyl tail.[128] These peptide fibres can self-assemble into a hydrogel, with the hydrophilic head containing a phosphorylated serine residue that can interact with calcium ions to promote the formation of HA. Additionally, an RGD sequence has been incorporated to facilitate integrin-mediated cell adhesion. Sugino *et al*. reported the fabrication of a covalently cross-linked polyglutamic acid gel with osteoconductive ability and bioresorbability.[129] It has been reported earlier that glutamic acid-rich sequences in osteonectin (a non-collagenous bone protein), act as binding sites for hydroxyapatite crystals. Segman-Magidovic and co-workers have designed acidic β-sheet peptide nanofibrous matrices and explored them as a negatively charged template for calcium phosphate mineralization.[130] PuraMatrix™, a commercially available matrix is obtained from 16-amino acid peptide sequence (AcN-RADARADARADARADA-CNH_2), has been reported for bone regeneration applications. The RAD repeating sequence in PuraMatrix™ is similar to that of ubiquitous integrin binding sequence RGD and promotes the cell adhesion, proliferation, and differentiation.[131] Moreover, these injectable peptide hydrogels promote the bone repair by rapid hemostasis and osteosis as reported by Wu *et al*. by experiments on rabbit iliac defects.[132] Additionally, a number of functional peptides have been designed that mimic the growth factors and bind to their receptors, functioning similarly to growth factors as osteogenic promoters. Tavakol *et al*. developed a nanofibrous self-assembling peptide gel (R-BMHP1) by integrating bone marrow homing peptide 1 (BMHP1) and RADA16.[133] They observed that the R-BMHP1 sequence exhibited stronger electrostatic interactions with the BMPR1A receptor than bone morphogenic protein 2 (BMP2). It promotes downstream signaling far more effectively than BMP2, leading to improved cell proliferation, osteogenesis, and bone repair. In another work, Zhang *et al.* reported the fabrication of designer peptide nanofiber scaffold by functionalization of RADA16 with three other short motifs, osteogenic growth peptide (OGP) ALKRQGRTLYGFGG, osteopontin cell adhesion

motif (DGRGDSVAYG) and a designed two-unit RGD binding sequence (PRGDSGYRGDS).[134] This designer peptide scaffold significantly enhanced the osteoblast 3-D migration, proliferation, and differentiation.

Delivery system using peptide-based scaffolds. Bone regeneration is tightly regulated by the interactions between various cells, cytokines, and growth factors.[135] Therefore cells, growth factors, drugs, and other bioactive substances can be delivered exogenously by using self-assembled peptide-based scaffolds to promote the bone regeneration. The major concern with stem cell therapy is administration of its suspension into the bone defect using a syringe, where it can be difficult to keep a sufficient number of cells viable at the defect site. Peptide scaffolds can act as carriers for the cells to be delivered at site of injury and prevent the side effects to the neighbouring tissues and organs. Quan *et al*. fabricated a scaffold comprising of bioactive molecules like bone morphogenetic protein-2 biomimetic peptide, cell adhesion factor (RGDS), phosphoserine, and polyaspartic acid and incorporated it with rat marrow mesenchymal stem cells (rMSCs).[136] The scaffold was found to be promoting cell proliferation, calcium deposition, and differentiation of rMSCs towards the osteogenic lineage. Similarly, Hayashi *et al*. reported the improved bone regeneration in a rat cranial defect with self-assembled peptide nanofiber hydrogel incorporating human-induced pluripotent stem cells.[137]

Further, the growth factors like vascular endothelial growth factor (VEGF), bone morphogenic proteins (BMPs), and platelet-derived growth factors (PDGF) can be loaded or covalently attached to the peptide gel to construct a sustained release system. In a study reported by Phipps *et al*. researchers have investigated the use of RADA16, an injectable hydrogel as a vehicle for intraosseous delivery of BMP-2 into the pig femoral head model.[138] A longer thermos-responsive peptide chain, poly(VPAVG)$_{220}$, which self assembles into spherical nanoparticles, have been explored for the encapsulation and delivery of BMP-2 and BMP-14.[139] BMP-14 is an essential growth factor for bone regeneration, playing a key role in promoting angiogenesis activity for bone regeneration. Sulfated glycosaminoglycans, such as heparan sulfate, enhance BMP signaling by assisting in the localization and binding of growth factors to their receptors. Building on this Lee *et al*. developed a sophisticated delivery system for BMP-2 using an amphiphilic peptide-based approach, incorporating heparin-binding peptide amphiphile and heparan sulfate[140]. They postulated that heparin-binding peptide amphiphiles would bind to heparan sulfate, which would, in turn, bind to BMP-2 and present it to cell receptors. Moreover, the presence of heparan sulfate slowed down the release of BMP-2 from the peptide hydrogel in a rat model with a critical femoral defect, leading to a significant enhancement of bone regeneration even with a reduced amount of BMP-2. In another work by He *et al*. developed basic-fibroblast growth factor (bFGF) loaded D-RADA16 peptide gel and investigated it for its bone regeneration and osteogenic properties.[141] Zhou *et al.* have reported the fabrication of D-RADA16 and D-RADA16-RGD peptide scaffolds containing transforming growth factor beta

1 (TGF-β1).[142] Peptide scaffolds were explored for the controlled release of TGF-β1 to promote osteogenesis, chondrogenesis, and blood vessel regeneration. Native enzyme immobilization has also been investigated as a method of inducing ossification. Stupp *et al*. used the native alkaline phosphatase and a phosphorylated, anionic peptide amphiphilic nanofiber gel matrix to template hydroxyapatite nanocrystals that resemble actual bone mineral.[143]

Infection within bone defects constitutes a considerable clinical obstacle that can significantly impede the healing trajectory, potentially resulting in chronic conditions. Such infections may necessitate the removal of internal fixation and lead to an increase in the size of the bone defect. They initiate an inflammatory response that can adversely affect the natural bone healing process by impeding the formation of new bone tissue. In clinical practice, controlled release of antibiotics at the at the site is a common strategy. Peptide-based scaffolds can act as carrier for antibiotic drugs. Baral *et al*. designed a thixotropic injectable peptide hydrogels in phosphate buffer of pH 7.46 for the encapsulation and slow and sustained release of vancomycin and vitamin B_{12} for 2 days at physiological pH and temperature.[144] Koch and co-workers demonstrated the incorporation of tetracycline, ciprofloxacin, and doxycycline in two self-assembled peptide hydrogels and observed their release for around 120 hours.[145] Further, peptides with inherent antimicrobial activity have received a significant attention in the recent years due to development of antibiotic-resistant bacterial strains. Yang *et al*. have employed RADA16 for the sustained release of antimicrobial peptides (Tet213) for the treatment of bone infection and osteomyelitis.[146] The release was analysed for over 28 days and resulted in improved bone regeneration as compared to control group. The simultaneous delivery of multiple bioactive substances can create a synergistic/additive effect and enhance the overall efficacy of the treatment. In this context, Ryoko and co-workers investigated the capability of PuraMatrix as a scaffold for bone regeneration in combination with dog mesenchymal stem cells (dMSCs) and platelet-rich plasma (PRP), and it showed the accelerated maturation of bone along this the enhanced bone volume.[147]

Designing a scaffold for bone regeneration involves creating a multifunctional platform that integrates biocompatibility, structural support, and bioactivity to effectively promote bone healing.[148] Peptide-based scaffolds have significantly contributed by offering a versatile and effective platform. These scaffolds are designed to emulate the complex natural extracellular matrix, delivering a biocompatible and biodegradable environment that supports cell adhesion, proliferation, and differentiation. Integrating specific bioactive peptides, such as RGD sequences, enhances the attachment and activity of osteoblasts, which are crucial for bone formation. Furthermore, these scaffolds can be tailored to administer various growth factors like BMPs, bFGF, and VEGF, which promote bone and blood vessel formation. These scaffolds have been used as transport carriers for antibiotics to prevent infection and anti-inflammatory agents to reduce inflammation, creating an ideal environment for bone healing. The mechanical

properties of the scaffold are tailored by adjusting the cross-linking density and peptide concentration to match the stiffness and strength of the target bone tissue, thus, ensuring the scaffold can provide adequate support while gradually degrading as new bone forms. This comprehensive approach ensures that the peptide-based scaffold not only supports structural integrity but also actively participates in the biological processes essential for effective bone regeneration.[126]

1.7. Knowledge gaps

Chronic wounds present multifaceted challenges, where multiple systemic and local factors like bacterial infections, elevated ROS, impaired vascularization, growth factor degradation, enhanced proteases, and defective re-epithelialization impede wound healing. The majority of the currently existing strategies target only one of the many impaired processes, which hampers their overall effectiveness. There is a growing need to develop multifunctional scaffolds that can interact with the wound milieu to address diverse facets of the intricate wound healing process. While the incorporation of antibiotics into wound healing scaffolds has been extensively investigated as a means to combat infection and promote healing, the increasing prevalence of antibiotic resistance has notably diminished its effectiveness. Impaired angiogenesis is a hallmark of diabetic wounds, where the elevated proteases compromise the process by degrading growth factors, signaling molecules, and other components of the extracellular matrix, leading to dysfunctional cellular pathways. The therapeutic potential of administering naturally occurring biomolecules, including growth factors, proteins, glycosaminoglycans, and genes, directly at the site of chronic wounds, while promising, is significantly hindered by several challenges. These challenges encompass aspects, such as the short half-lives of these molecules, the degradation of growth factors, and the inherent risks associated with gene therapies, including tumorigenicity, variable patient responses, and immunogenic reactions. Consequently, there is a pressing need to explore functional biomaterials capable of endogenously modulating factors to promote angiogenesis in diabetic wounds, thereby circumventing the necessity for the external administration of growth factors or supplements. Lastly, the application of native growth factors, proteins, and enzymes in promoting bone mineralization, though potentially beneficial, is mired in issues related to the laborious, costly processes required for their purification, handling, and processing coupled with their poor stability, short half-life, and variations in batch-to-batch efficacy. Therefore, developing enzyme-like artificial scaffolds that mimic the active sites and biological roles of model enzymes is crucial to promote bone regeneration.

1.8. Objectives

Wound healing and bone regeneration are intricate, multi-stage processes that share several critical challenges. These processes entail a precisely regulated sequence of phases like, hemostasis, inflammation, cellular proliferation, tissue remodeling, and matrix formation, which are essential for the restoration of tissue integrity and function. However, conditions like wound chronicity, underlying diseases or significant bone defects frequently disrupt these processes due to factors, such as microbial infection, chronic inflammation, impaired angiogenesis, and inadequate cell migration and proliferation. These challenges are compounded by maladaptive immune responses and imbalanced cytokine signaling, which further obstructs the progression to the later phases of healing or regeneration. These complications underscore the necessity of biomaterials capable of addressing the diverse facets of the healing process.

In recent years, the domain of regenerative medicine has embraced innovative biomaterials, notably self-assembled peptides, to overcome the intricate challenges associated with wound healing and bone regeneration. Self-assembling peptides offer significant benefits for multiple applications in wound healing and bone regeneration due to their modularity, biocompatibility, and ability to address several therapeutic challenges in a single platform. Their customizable structure enables them to integrate specific bioactive motifs, allowing them to be designed for antimicrobial, pro-angiogenic, anti-inflammatory, or cell-adhesion functions. This versatility means that self-assembling peptides can be designed to combat infection, support cell proliferation, modulate inflammation, and promote vascularization, which are critical in both chronic wound and bone healing environments. In wound healing, self-assembling peptides can be tailored to support soft tissue repair by enhancing keratinocyte and fibroblast migration, which is necessary for skin regeneration, while reducing the risk of infection at the wound site. For bone regeneration, peptide scaffolds can be designed to promote osteoblast differentiation and bone mineralization while sustaining a stable structure for new bone formation. Their structural similarity to the extracellular matrix (ECM) further supports cell attachment, growth, and differentiation, thus, creating an optimal microenvironment for both soft and hard tissue healing. This adaptability, combined with their inherent biocompatibility and low toxicity, makes self-assembling peptides an ideal biomaterial for wound healing and bone repair applications, which offers a comprehensive approach to address the biological challenges in tissue repair.

The critical knowledge gaps in the design of biomaterials aimed at addressing the intricate therapeutic challenges associated with wound healing and bone regeneration has been delineated earlier. This thesis seeks to mitigate these gaps by developing multifunctional peptide-based nanoarchitectures encompassing nanofibrous hydrogels and cyclic peptide nanotubes to concurrently target therapeutic requirements in chronic diabetic wounds and bone defects

(Figure 1.8). These peptide-based systems are meticulously engineered to exhibit intrinsic bioactivity, effectively combat infections, modulate inflammation, promote angiogenesis, enhance cellular migration, and facilitate tissue regeneration without necessitating the incorporation of drugs or exogenous growth factors. This drug- and growth factor-free approach not only reduces the potential side effects but emphasizes the inherent bioactivity and adaptability of peptide-based biomaterials for supporting a comprehensive strategy for tissue repair.

Self-assembled peptide hydrogels have been widely used as carrier for antibiotics and anti-inflammatory drugs. However, these delivery strategies come with the limitation like potential side effects of the drugs and rise of antibiotic-resistant bacteria. Moreover, the multifactorial nature of chronic wounds requires a comprehensive treatment approach that can simultaneously address these diverse pathophysiological factors. Therefore, the first objective of my thesis was to develop a multifunctional, nanofibrous self-assembled peptide gel, LA-^{L}Lys-^{D}Phe-^{L}Lys-NH_2 loaded with Y_2O_3 nanoparticles for antibacterial, ROS-scavenging, and proangiogenic properties. The inclusion of basic amino acid residues in the peptide sequence will give the gel a net positive charge, enabling it to damage bacterial cell membranes by disrupting their membrane potential. Additionally, the electron pairs on lysine amines will act as a shield against ROS-induced cellular damage. The Y_2O_3 nanoparticles can confer proangiogenic properties by inducing temporary hypoxia and stimulating the expression of hypoxia-inducible factor (HIF-1), which, in turn, can amplify the angiogenic signalling. This multifaceted approach aims to effectively promote wound healing by addressing various aspects associated with wound healing.

Elevated proteases and dysfunctional cellular pathways in diabetes compromise angiogenesis. While the exogenously delivered growth factors and genes suffer from various challenges like their degradation and immunogenic response and, therefore, my second objective is to develop a material that can endogenously manipulate the angiogenic signalling. We have developed heparan sulfate-mimicking self-assembled cyclic-hexapeptide (PWLSEKs) nanotubes that can promote angiogenesis, without using a growth factor and drug. Under chronic wound conditions, these nanotubes can interact with the proangiogenic growth factors, thus, preventing their proteolytic degradation and facilitating their binding to their cognate receptors to induce angiogenic signalling. Thus, they can restore the dysfunctional activity of hyperglycemic endothelial cells and promote diabetic wound healing.

In clinical practice, about 2.2 million bone transplants are done yearly, with pathological fractures and accidental traumas being the most prevalent cause of injuries. Although bone possesses a remarkable capacity for self-healing, complicated cases like large defects at load-bearing site, tumour, scoliosis, congenital malformation, osteoporosis, bone infection, and

osteoarthritis necessitate external intervention to ensure effective bone regeneration. Most current therapeutic approaches centre on bone grafts, which present several innate drawbacks, including immunological rejection, material scarcity, donor site morbidity, and the need for subsequent surgeries. The use of natural enzymes and growth factors in regenerative scaffolds is hampered by their vulnerability to denaturation, time, cost, and effort required for their purification and processing. Thus, there is a pressing need to develop synthetic biomaterials mimicking enzymes for tissue regeneration. The third objective of my thesis was to develop alkaline phosphatase (ALP)-mimicking cyclic peptide nanotubes to induce osteogenesis and bone mineralization. The cyclic peptides in the nanotubes contain the histidine residues, which provide the multiple imidazole rings in close proximation, a critical group in the functional domain of ALP. By emulating ALP, these mimetic nanotubes aim to augment phosphatase activity, thus, facilitating the formation of bone-like nodules indicative of osteogenic differentiation and bone mineralization.

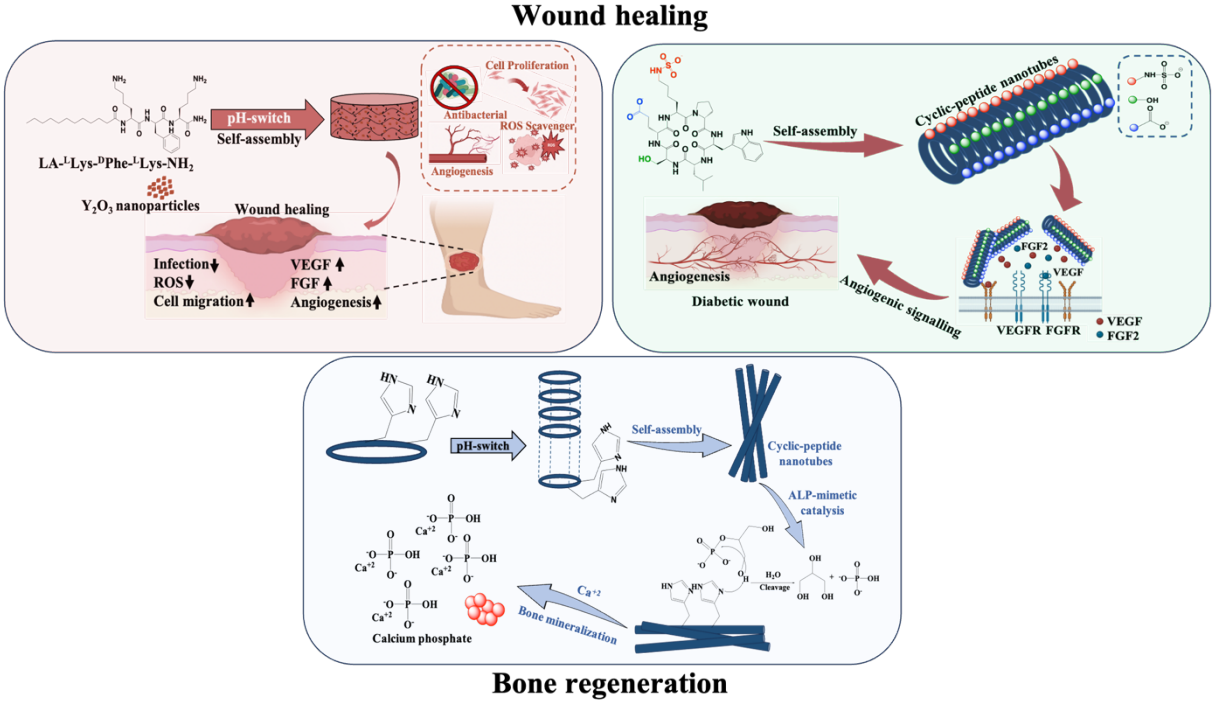

Figure 1.8. Objectives of the thesis- development of self-assembled peptide-based nanostructures for chronic wound healing and bone regeneration.

1.9. Thesis outline

The aim of this thesis was to develop self-assembled peptide-based biomaterials for chronic wound healing and bone regeneration by harnessing their inherent biological properties, without the reliance on exogenous drugs and growth factors, thus, minimizing potential side effects and limitations. The first chapter of the thesis discusses the molecular self-assembly, with a focus on peptide-based scaffolds. It thoroughly explores interactions between peptide chains and the

secondary structures they adopt, facilitating the formation of various nanoarchitectures. The discussion extends to cover both intrinsic and external factors that influence peptide self-assembly. Moreover, the chapter provides an overview of the biomedical applications of self-assembled peptides, particularly highlighting their potential in wound healing and bone regeneration. This includes an extensive review of related literature, identifying existing knowledge gaps, and presenting challenges, along with clearly defined objectives and scope for further research. The second chapter describes the development of a multifunctional, yttrium oxide nanoparticle-loaded, self-assembled peptide gel with antibacterial, ROS-scavenging, and proangiogenic characteristics for wound healing. The third chapter discusses the fabrication of proangiogenic cyclic-hexapeptide nanotubes with heparin-inspired functional groups for diabetic wound healing. The fourth chapter presents the development of alkaline phosphatase-mimetic cyclic peptide nanotubes to stimulate bone mineralization and osteogenic differentiation, hence promoting bone regeneration. Chapter five discusses the major conclusions of this thesis, contributions made to the field of peptide-based scaffolds for promoting wound healing and bone regeneration, and future prospective, which includes future research directions and potential clinical applications.

References

(1) Pochan, D.; Scherman, O. Introduction: Molecular Self-Assembly. *Chem. Rev.* **2021**, *121* (22), 13699–13700.

(2) Sinha, N. J.; Langenstein, M. G.; Pochan, D. J.; Kloxin, C. J.; Saven, J. G. Peptide Design and Self-Assembly into Targeted Nanostructure and Functional Materials. *Chem. Rev.* **2021**, *121* (22), 13915–13935.

(3) Whitesides, G. M.; Grzybowski, B. Self-Assembly at All Scales. *Science* **2002**, *295* (5564), 2418–2421.

(4) Stenzel, M. H. Bioconjugation Using Thiols: Old Chemistry Rediscovered to Connect Polymers with Nature's Building Blocks. *ACS Macro Lett.* **2013**, *2* (1), 14–18.

(5) Averick, S.; Karácsony, O.; Mohin, J.; Yong, X.; Moellers, N. M.; Woodman, B. F.; Zhu, W.; Mehl, R. A.; Balazs, A. C.; Kowalewski, T.; Matyjaszewski, K. Cooperative, Reversible Self-Assembly of Covalently Pre-Linked Proteins into Giant Fibrous Structures. *Angew Chem Int Ed* **2014**, *53* (31), 8050–8055.

(6) Pochan, D. J.; Schneider, J. P.; Kretsinger, J.; Ozbas, B.; Rajagopal, K.; Haines, L. Thermally Reversible Hydrogels via Intramolecular Folding and Consequent Self-Assembly of a *de Novo* Designed Peptide. *J. Am. Chem. Soc.* **2003**, *125* (39), 11802–11803.

(7) Berger, J.; Reist, M.; Mayer, J. M.; Felt, O.; Peppas, N. A.; Gurny, R. Structure and Interactions in Covalently and Ionically Crosslinked Chitosan Hydrogels for Biomedical Applications. *European Journal of Pharmaceutics and Biopharmaceutics* **2004**, *57* (1), 19–34.

(8) Das, R.; Gayakvad, B.; Shinde, S. D.; Rani, J.; Jain, A.; Sahu, B. Ultrashort Peptides—A Glimpse into the Structural Modifications and Their Applications as Biomaterials. *ACS Appl. Bio Mater.* **2020**, *3* (9), 5474–5499.

(9) Kisiday, J.; Jin, M.; Kurz, B.; Hung, H.; Semino, C.; Zhang, S.; Grodzinsky, A. J. Self-Assembling Peptide Hydrogel Fosters Chondrocyte Extracellular Matrix Production and Cell Division: Implications for Cartilage Tissue Repair. *Proc. Natl. Acad. Sci. U.S.A.* **2002**, *99* (15), 9996–10001.

(10) Gerling, T.; Wagenbauer, K. F.; Neuner, A. M.; Dietz, H. Dynamic DNA Devices and Assemblies Formed by Shape-Complementary, Non–Base Pairing 3D Components **2015**, *347*(6229), 1446–1452.

(11) Matsuurua, K. Rational Design of Self-Assembled Proteins and Peptides for Nano- and Micro-Sized Architectures. *RSC Adv.* **2014**, *4* (6), 2942–2953.

(12) Yu, Z.; Erbas, A.; Tantakitti, F.; Palmer, L. C.; Jackman, J. A.; Olvera De La Cruz, M.; Cho, N.-J.; Stupp, S. I. Co-Assembly of Peptide Amphiphiles and Lipids into

Supramolecular Nanostructures Driven by Anion−π Interactions. *J. Am. Chem. Soc.* **2017**, *139* (23), 7823–7830.

(13) Israelachvili, J. N.; Mitchell, D. J.; Ninham, B. W. Theory of Self-Assembly of Lipid Bilayers and Vesicles. *Biochimica et Biophysica Acta (BBA) - Biomembranes* **1977**, *470* (2), 185–201.

(14) Nie, J.; Pei, B.; Wang, Z.; Hu, Q. Construction of Ordered Structure in Polysaccharide Hydrogel: A Review. *Carbohydrate Polymers* **2019**, *205*, 225–235.

(15) Pochan, D. J.; Chen, Z.; Cui, H.; Hales, K.; Qi, K.; Wooley, K. L. Toroidal Triblock Copolymer Assemblies. *Science* **2004**, *306* (5693), 94–97.

(16) Zhang, J.; Zhao, Y.; Han, S.; Chen, C.; Xu, H. Self-Assembly of Surfactant-like Peptides and Their Applications. *Sci. China Chem.* **2014**, *57* (12), 1634–1645.

(17) Ravichandran, R.; Griffith, M.; Phopase, J. Applications of Self-Assembling Peptide Scaffolds in Regenerative Medicine: The Way to the Clinic. *J. Mater. Chem. B* **2014**, *2* (48), 8466–8478.

(18) Paradís-Bas, M.; Tulla-Puche, J.; Albericio, F. The Road to the Synthesis of "Difficult Peptides." *Chem. Soc. Rev.* **2016**, *45* (3), 631–654.

(19) Zhang, S. Spontaneous Assembly of a Self-Complementary Oligopeptide to Form a Stable Macroscopic Membrane. *Proc. Natl. Acad. Sci. USA* **1993,** *90*(8), 3334–3338.

(20) Zhang, S. Fabrication of Novel Biomaterials through Molecular Self-Assembly. *Nat Biotechnol* **2003**, *21* (10), 1171–1178.

(21) Ghadiri, M. R.; Granja, J. R.; Milligan, R. A.; McRee, D. E.; Khazanovich, N. Self-Assembling Organic Nanotubes Based on a Cyclic Peptide Architecture. *Nature* **1993**, *366* (6453), 324–327.

(22) Yan, J.; He, W.; Yan, S.; Niu, F.; Liu, T.; Ma, B.; Shao, Y.; Yan, Y.; Yang, G.; Lu, W.; Du, Y.; Lei, B.; Ma, P. X. Self-Assembled Peptide–Lanthanide Nanoclusters for Safe Tumor Therapy: Overcoming and Utilizing Biological Barriers to Peptide Drug Delivery. *ACS Nano* **2018**, *12* (2), 2017–2026.

(23) Yuan, L.; Liu, L. Peptide-Based Electrochemical Biosensing. *Sensors and Actuators B: Chemical* **2021**, *344*, 130232.

(24) Han, J.; Gong, H.; Ren, X.; Yan, X. Supramolecular Nanozymes Based on Peptide Self-Assembly for Biomimetic Catalysis. *Nano Today* **2021**, *41*, 101295.

(25) Qi, G.-B.; Gao, Y.-J.; Wang, L.; Wang, H. Self-Assembled Peptide-Based Nanomaterials for Biomedical Imaging and Therapy. *Adv. Mater.* **2018**, *30* (22), 1703444.

(26) Kong, H.; Han, J.; Yang, M.; Lai, L.; Sun, Y.; Luan, X.; Ren, W.; Wu, A.; Wei, G. Two-Dimensional Peptide Nanosheets Functionalized with Gold Nanorods for Photothermal Therapy of Tumors. *J. Mater. Chem. B* **2023**, *11* (15), 3445–3452.

(27) Luo, K.; Li, C.; Li, L.; She, W.; Wang, G.; Gu, Z. Arginine Functionalized Peptide Dendrimers as Potential Gene Delivery Vehicles. *Biomaterials* **2012**, *33* (19), 4917–4927.

(28) Cheng, B.; Yan, Y.; Qi, J.; Deng, L.; Shao, Z.-W.; Zhang, K.-Q.; Li, B.; Sun, Z.; Li, X. Cooperative Assembly of a Peptide Gelator and Silk Fibroin Afford an Injectable Hydrogel for Tissue Engineering. *ACS Appl. Mater. Interfaces* **2018**, *10* (15), 12474–12484.

(29) Rad-Malekshahi, M.; Lempsink, L.; Amidi, M.; Hennink, W. E.; Mastrobattista, E. Biomedical Applications of Self-Assembling Peptides. *Bioconjugate Chem.* **2016**, *27* (1), 3–18.

(30) Dieckmann, G. R.; Dalton, A. B.; Johnson, P. A.; Razal, J.; Chen, J.; Giordano, G. M.; Muñoz, E.; Musselman, I. H.; Baughman, R. H.; Draper, R. K. Controlled Assembly of Carbon Nanotubes by Designed Amphiphilic Peptide Helices. *J. Am. Chem. Soc.* **2003**, *125* (7), 1770–1777.

(31) Toksöz, S.; Guler, M. O. Self-Assembled Peptidic Nanostructures. *Nano Today* **2009**, *4* (6), 458–469.

(32) Sinha, N. J.; Langenstein, M. G.; Pochan, D. J.; Kloxin, C. J.; Saven, J. G. Peptide Design and Self-Assembly into Targeted Nanostructure and Functional Materials. *Chem. Rev.* **2021**, *121* (22), 13915–13935.

(33) Zhu, D.; Kong, H.; Sun, Z.; Xu, Y.; Han, P.; Xi, Y.; Wei, G. Recent Advance in Tailoring the Structure and Functions of Self-Assembled Peptide Nanomaterials for Biomedical Applications. *Coordination Chemistry Reviews* **2023**, *494*, 215374.

(34) Yaman, Y. T.; Akbal, Ö.; Bolat, G.; Bozdogan, B.; Denkbas, E. B.; Abaci, S. Peptide Nanoparticles (PNPs) Modified Disposable Platform for Sensitive Electrochemical Cytosensing of DLD-1 Cancer Cells. *Biosensors and Bioelectronics* **2018**, *104*, 50–57.

(35) Zhang, Y.; Zhou, F.; Zhao, M.; Lin, L.; Ning, Z.; Sun, B. Soy Peptide Nanoparticles by Ultrasound-Induced Self-Assembly of Large Peptide Aggregates and Their Role on Emulsion Stability. *Food Hydrocolloids* **2018**, *74*, 62–71.

(36) Chen, Y.; Kong, H.; Guo, L.; Wei, G. Biomimetic Organic-Inorganic Hybrid Membranes for Removal of Fluoride Ions. *Materials* **2022**, *15* (10), 3457.

(37) Liu, B.; Yao, J.; Xing, J.; Yang, M.; Zhu, D.; Ren, W.; Xiang, L.; Wang, Y.; Wu, A.; Wei, G. Design, Biomimetic Synthesis, and Tumor Photothermal Therapy of Peptide-Based Two-Dimensional Photothermal Conversion Nanomaterials. *Mol. Syst. Des. Eng.* **2022**, *7* (11), 1549–1560.

(38) Insua, I.; Montenegro, J. 1D to 2D Self Assembly of Cyclic Peptides. *J. Am. Chem. Soc.* **2020**, *142* (1), 300–307.

(39) Cunha; Villa; Silva; Gelain; Panseri, S. 3D Culture of Adult Mouse Neural Stem Cells within Functionalized Self-Assembling Peptide Scaffolds. *IJN* **2011**, 6, 943–955.

(40) Cui, T.; Li, X.; He, S.; Xu, D.; Yin, L.; Huang, X.; Deng, S.; Yue, W.; Zhong, W. Instant Self-Assembly Peptide Hydrogel Encapsulation with Fibrous Alginate by Microfluidics for Infected Wound Healing. *ACS Biomater. Sci. Eng.* **2020**, *6* (9), 5001–5011.

(41) Li, Z.; Zhu, Y.; Matson, J. B. pH-Responsive Self-Assembling Peptide-Based Biomaterials: Designs and Applications. *ACS Appl. Bio Mater.* **2022**, *5* (10), 4635–4651.

(42) Huang, R.; Wang, Y.; Qi, W.; Su, R.; He, Z. Temperature-Induced Reversible Self-Assembly of Diphenylalanine Peptide and the Structural Transition from Organogel to Crystalline Nanowires. *Nanoscale Res Lett* **2014**, *9* (1), 653.

(43) Criado-Gonzalez, M.; Loftin, B.; Rodon Fores, J.; Vautier, D.; Kocgozlu, L.; Jierry, L.; Schaaf, P.; Boulmedais, F.; Harth, E. Enzyme Assisted Peptide Self-Assemblies Trigger Cell Adhesion in High Density Oxime Based Host Gels. *J. Mater. Chem. B* **2020**, *8* (20), 4419–4427.

(44) Gao, Y.; Wang, L.; Zhang, X.; Zhou, Z.; Shen, X.; Hu, H.; Sun, R.; Tang, J. Advances in Self-Assembled Peptides as Drug Carriers. *Pharmaceutics* **2023**, *15* (2), 482.

(45) Kashyap, S.; Pal, V. K.; Mohanty, S.; Roy, S. Exploring a Solvent Dependent Strategy to Control Self-Assembling Behavior and Cellular Interaction in Laminin-Mimetic Short Peptide Based Supramolecular Hydrogels. *ChemBioChem* **2024**, *25* (8), e202300835.

(46) Ni, R.; Liu, J.; Chau, Y. Ultrasound-Facilitated Assembly and Disassembly of a pH-Sensitive Self-Assembly Peptide. *RSC Adv.* **2018**, *8* (51), 29482–29487.

(47) Edwards-Gayle, C. J. C.; Wychowaniec, J. K. Characterization of Peptide-Based Nanomaterials. In *Peptide Bionanomaterials*; Elsawy, M. A., Ed.; Springer International Publishing: Cham, 2023; pp 255–308.

(48) Beychok, S. Circular Dichroism of Biological Macromolecules. **1966,** *154*(3754), 1288–1299.

(49) Tuma, R. Raman Spectroscopy of Proteins: From Peptides to Large Assemblies. *J Raman Spectroscopy* **2005**, *36* (4), 307–319.

(50) Yan, C.; Pochan, D. J. Rheological Properties of Peptide-Based Hydrogels for Biomedical and Other Applications. *Chem. Soc. Rev.* **2010**, *39* (9), 3528.

(51) Stetefeld, J.; McKenna, S. A.; Patel, T. R. Dynamic Light Scattering: A Practical Guide and Applications in Biomedical Sciences. *Biophys Rev* **2016**, *8* (4), 409–427.

(52) Li, T.; Lu, X.-M.; Zhang, M.-R.; Hu, K.; Li, Z. Peptide-Based Nanomaterials: Self-Assembly, Properties and Applications. *Bioactive Materials* **2022**, *11*, 268–282.

(53) Reches, M.; Gazit, E. Formation of Closed-Cage Nanostructures by Self-Assembly of Aromatic Dipeptides. *Nano Lett.* **2004**, *4* (4), 581–585.

(54) Zhuang, Y.; Bureau, H. R.; Lopez, C.; Bucher, R.; Quirk, S.; Hernandez, R. Energetics and Structure of Alanine-Rich α-Helices via Adaptive Steered Molecular Dynamics. *Biophysical Journal* **2021**, *120* (10), 2009–2018.

(55) Lee, N. R.; Bowerman, C. J.; Nilsson, B. L. Effects of Varied Sequence Pattern on the Self-Assembly of Amphipathic Peptides. *Biomacromolecules* **2013**, *14* (9), 3267–3277.

(56) Wang, J.; Han, S.; Meng, G.; Xu, H.; Xia, D.; Zhao, X.; Schweins, R.; Lu, J. R. Dynamic Self-Assembly of Surfactant-like Peptides A6K and A9K. *Soft Matter* **2009**, *5* (20), 3870.

(57) Goldberger, J. E.; Berns, E. J.; Bitton, R.; Newcomb, C. J.; Stupp, S. I. Electrostatic Control of Bioactivity. *Angew Chem Int Ed* **2011**, *50* (28), 6292–6295.

(58) Zhao, Y.; Yokoi, H.; Tanaka, M.; Kinoshita, T.; Tan, T. Self-Assembled pH-Responsive Hydrogels Composed of the RATEA16 Peptide. *Biomacromolecules* **2008**, *9* (6), 1511–1518.

(59) Cui, H.; Muraoka, T.; Cheetham, A. G.; Stupp, S. I. Self-Assembly of Giant Peptide Nanobelts. *Nano Lett.* **2009**, *9* (3), 945–951.

(60) Tiné, M. R.; Alderighi, M.; Duce, C.; Ghezzi, L.; Solaro, R. Effect of Temperature on Self-Assembly of an Ionic Tetrapeptide. *J Therm Anal Calorim* **2011**, *103* (1), 75–80.

(61) Luo, Z.; Zhao, X.; Zhang, S. Structural Dynamic of a Self-Assembling Peptide d-EAK16 Made of Only D-Amino Acids. *PLoS ONE* **2008**, *3* (5), e2364.

(62) Cui, J.; Liu, A.; Guan, Y.; Zheng, J.; Shen, Z.; Wan, X. Tuning the Helicity of Self-Assembled Structure of a Sugar-Based Organogelator by the Proper Choice of Cooling Rate. *Langmuir* **2010**, *26* (5), 3615–3622.

(63) Huang, R.; Qi, W.; Su, R.; Zhao, J.; He, Z. Solvent and Surface Controlled Self-Assembly of Diphenylalanine Peptide: From Microtubes to Nanofibers. *Soft Matter* **2011**, *7* (14), 6418.

(64) Li, Y.; Li, B.; Fu, Y.; Lin, S.; Yang, Y. Solvent-Induced Handedness Inversion of Dipeptide Sodium Salts Derived from Alanine. *Langmuir* **2013**, *29* (31), 9721–9726.

(65) Qin, S.-Y.; Feng, J.-Q.; Cheng, Y.-J.; Liu, W.-L.; Zhang, A.-Q.; Wang, L.; Wang, H.; Zhang, X.-Z. A Comprehensive Review on Peptide-Bearing Biomaterials: From Ex Situ to in Situ Self-Assembly. *Coordination Chemistry Reviews* **2024**, *502*, 215600.

(66) Koutsopoulos, S.; Unsworth, L. D.; Nagai, Y.; Zhang, S. Controlled Release of Functional Proteins through Designer Self-Assembling Peptide Nanofiber Hydrogel Scaffold. *Proc. Natl. Acad. Sci. U.S.A.* **2009**, *106* (12), 4623–4628.

(67) Kirkham, J.; Firth, A.; Vernals, D.; Boden, N.; Robinson, C.; Shore, R. C.; Brookes, S. J.; Aggeli, A. Self-Assembling Peptide Scaffolds Promote Enamel Remineralization. *J Dent Res* **2007**, *86* (5), 426–430.

(68) Robinson, L. R.; Fitzgerald, N. C.; Doughty, D. G.; Dawes, N. C.; Berge, C. A.; Bissett, D. L. Topical Palmitoyl Pentapeptide Provides Improvement in Photoaged Human Facial Skin [1]. *Intern J of Cosmetic Sci* **2005**, *27* (3), 155–160.

(69) Velnar, T.; Bailey, T.; Smrkolj, V. The Wound Healing Process: An Overview of the Cellular and Molecular Mechanisms. *J Int Med Res* **2009**, *37* (5), 1528–1542.

(70) Sharifi, S.; Hajipour, M. J.; Gould, L.; Mahmoudi, M. Nanomedicine in Healing Chronic Wounds: Opportunities and Challenges. *Mol. Pharmaceutics* **2021**, *18* (2), 550–575.

(71) Wilkinson, H. N.; Hardman, M. J. Wound Healing: Cellular Mechanisms and Pathological Outcomes. *Open Biol.* **2020**, *10* (9), 200223.

(72) Frykberg, R. G.; Banks, J. Challenges in the Treatment of Chronic Wounds. *Advances in Wound Care* **2015**, *4* (9), 560–582.

(73) Sen, C. K.; Gordillo, G. M.; Roy, S.; Kirsner, R.; Lambert, L.; Hunt, T. K.; Gottrup, F.; Gurtner, G. C.; Longaker, M. T. Human Skin Wounds: A Major and Snowballing Threat to Public Health and the Economy. *Wound Repair Regeneration* **2009**, *17* (6), 763–771.

(74) Shukla, V. K.; Ansari, M. A.; Gupta, S. K. Wound Healing Research: A Perspective From India. *The International Journal of Lower Extremity Wounds* **2005**, *4* (1), 7–8.

(75) Chen, Y.; Wang, X.; Tao, S.; Wang, Q.; Ma, P.-Q.; Li, Z.-B.; Wu, Y.-L.; Li, D.-W. Research Advances in Smart Responsive-Hydrogel Dressings with Potential Clinical Diabetic Wound Healing Properties. *Military Med Res* **2023**, *10* (1), 37.

(76) Huang, C.; Leavitt, T.; Bayer, L. R.; Orgill, D. P. Effect of Negative Pressure Wound Therapy on Wound Healing. *Current Problems in Surgery* **2014**, *51* (7), 301–331.

(77) Huang, X.; Liang, P.; Jiang, B.; Zhang, P.; Yu, W.; Duan, M.; Guo, L.; Cui, X.; Huang, M.; Huang, X. Hyperbaric Oxygen Potentiates Diabetic Wound Healing by Promoting Fibroblast Cell Proliferation and Endothelial Cell Angiogenesis. *Life Sciences* **2020**, *259*, 118246.

(78) Gonchar, I. V.; Lipunov, A. R.; Afanasov, I. M.; Larina, V.; Faller, A. P.; Kibardin, A. V. Platelet Rich Plasma and Growth Factors Cocktails for Diabetic Foot Ulcers Treatment: State of Art Developments and Future Prospects. *Diabetes & Metabolic Syndrome: Clinical Research & Reviews* **2018**, *12* (2), 189–194.

(79) Zhang, X.; Shu, W.; Yu, Q.; Qu, W.; Wang, Y.; Li, R. Functional Biomaterials for Treatment of Chronic Wound. *Front. Bioeng. Biotechnol.* **2020**, *8*, 516.

(80) Wang, Y.; Shi, J.; Wang, M.; Zhang, L.; Wang, R.; Zhang, J.; Qing, H.; Duan, J.; Zhang, X.; Pu, G. pH-Responsive Co-Assembled Peptide Hydrogel to Inhibit Drug-Resistant Bacterial Infection and Promote Wound Healing. *ACS Appl. Mater. Interfaces* **2024**, *16* (15), 18400–18410.

(81) Kaur, G.; Narayanan, G.; Garg, D.; Sachdev, A.; Matai, I. Biomaterials-Based Regenerative Strategies for Skin Tissue Wound Healing. *ACS Appl. Bio Mater.* **2022**, *5* (5), 2069–2106.

(82) Ali Zahid, A.; Chakraborty, A.; Shamiya, Y.; Ravi, S. P.; Paul, A. Leveraging the Advancements in Functional Biomaterials and Scaffold Fabrication Technologies for Chronic Wound Healing Applications. *Mater. Horiz.* **2022**, *9* (7), 1850–1865.

(83) Oliveira, C.; Sousa, D.; Teixeira, J. A.; Ferreira-Santos, P.; Botelho, C. M. Polymeric Biomaterials for Wound Healing. *Front. Bioeng. Biotechnol.* **2023**, *11*, 1136077.

(84) Gelain, F.; Luo, Z.; Rioult, M.; Zhang, S. Self-Assembling Peptide Scaffolds in the Clinic. *npj Regen Med* **2021**, *6* (1), 9.

(85) Guan, T.; Li, J.; Chen, C.; Liu, Y. Self-Assembling Peptide-Based Hydrogels for Wound Tissue Repair. *Advanced Science* **2022**, *9* (10), 2104165.

(86) Edwards-Gayle, C. J. C.; Hamley, I. W. Self-Assembly of Bioactive Peptides, Peptide Conjugates, and Peptide Mimetic Materials. *Org. Biomol. Chem.* **2017**, *15* (28), 5867–5876.

(87) Yang, Z.; Chen, L.; Liu, J.; Zhuang, H.; Lin, W.; Li, C.; Zhao, X. Short Peptide Nanofiber Biomaterials Ameliorate Local Hemostatic Capacity of Surgical Materials and Intraoperative Hemostatic Applications in Clinics. *Advanced Materials* **2023**, *35* (39), 2301849.

(88) Xu, H.-G.; Liang, Q.-L.; Li, L.; Qi, G.-F.; Wang, L.; Zhan, L.-N.; Ding, M.-R.; Zhang, K.; Cui, X. Biomimetic Peptide Nanoparticles Participate in Natural Coagulation for Hemostasis and Wound Healing. *Biomater. Sci.* **2022**, *10* (10), 2628–2637.

(89) Zeng, L.; Luo, G.; Yue, Z.; Tang, Y.; Wang, Z.; Chang, Y. Experimental Study on Rapid Hemostasis Using Peptide Hydrogels. *ACS Omega* **2024**, *9* (8), 9247–9255.

(90) Wei, S.; Chen, F.; Geng, Z.; Cui, R.; Zhao, Y.; Liu, C. Self-Assembling RATEA16 Peptide Nanofiber Designed for Rapid Hemostasis. *J. Mater. Chem. B* **2020**, *8* (9), 1897–1905.

(91) Falcone, M.; De Angelis, B.; Pea, F.; Scalise, A.; Stefani, S.; Tasinato, R.; Zanetti, O.; Dalla Paola, L. Challenges in the Management of Chronic Wound Infections. *Journal of Global Antimicrobial Resistance* **2021**, *26*, 140–147.

(92) Hwang, J.; Huang, H.; Sullivan, M. O.; Kiick, K. L. Controlled Delivery of Vancomycin from Collagen-Tethered Peptide Vehicles for the Treatment of Wound Infections. *Mol. Pharmaceutics* **2023**, *20* (3), 1696–1708.

(93) Binaymotlagh, R.; Del Giudice, A.; Mignardi, S.; Amato, F.; Marrani, A. G.; Sivori, F.; Cavallo, I.; Di Domenico, E. G.; Palocci, C.; Chronopoulou, L. Green In Situ Synthesis of Silver Nanoparticles-Peptide Hydrogel Composites: Investigation of Their Antibacterial Activities. *Gels* **2022**, *8* (11), 700.

(94) Azoulay, Z.; Aibinder, P.; Gancz, A.; Moran-Gilad, J.; Navon-Venezia, S.; Rapaport, H. Assembly of Cationic and Amphiphilic β-Sheet FKF Tripeptide Confers Antibacterial Activity. *Acta Biomaterialia* **2021**, *125*, 231–241.

(95) Cao, F.; Mei, L.; Zhu, G.; Song, M.; Zhang, X. An Injectable Molecular Hydrogel Assembled by Antimicrobial Peptide PAF26 for Antimicrobial Application. *RSC Adv.* **2019**, *9* (53), 30803–30808.

(96) Fernandez-Lopez, S.; Kim, H.-S.; Choi, E. C.; Delgado, M.; Granja, J. R.; Khasanov, A.; Kraehenbuehl, K.; Long, G.; Weinberger, D. A.; Wilcoxen, K. M.; Ghadiri, M. R. Antibacterial Agents Based on the Cyclic D,L- a-Peptide Architecture. **2001,** *412*(6845), 452–455.

(97) Schilrreff, P.; Alexiev, U. Chronic Inflammation in Non-Healing Skin Wounds and Promising Natural Bioactive Compounds Treatment. *IJMS* **2022**, *23* (9), 4928.

(98) Webber, M. J.; Matson, J. B.; Tamboli, V. K.; Stupp, S. I. Controlled Release of Dexamethasone from Peptide Nanofiber Gels to Modulate Inflammatory Response. *Biomaterials* **2012**, *33* (28), 6823–6832.

(99) Yu, X.; Zhang, Z.; Yu, J.; Chen, H.; Li, X. Self-Assembly of a Ibuprofen-Peptide Conjugate to Suppress Ocular Inflammation. *Nanomedicine: Nanotechnology, Biology and Medicine* **2018**, *14* (1), 185–193.

(100) Tang, W.; Yang, J.; Zhao, Z.; Lian, Z.; Liang, G. Intracellular Coassembly Boosts the Anti-Inflammation Capacity of Dexamethasone. *Nanoscale* **2017**, *9* (45), 17717–17721.

(101) Abdulkadir, S.; Li, C.; Jiang, W.; Zhao, X.; Sang, P.; Wei, L.; Hu, Y.; Li, Q.; Cai, J. Modulating Angiogenesis by Proteomimetics of Vascular Endothelial Growth Factor. *J. Am. Chem. Soc.* **2022**, *144* (1), 270–281.

(102) Huang, L.-C.; Wang, H.-C.; Chen, L.-H.; Ho, C.-Y.; Hsieh, P.-H.; Huang, M.-Y.; Wu, H.-C.; Wang, T.-W. Bioinspired Self-Assembling Peptide Hydrogel with Proteoglycan-Assisted Growth Factor Delivery for Therapeutic Angiogenesis. *Theranostics* **2019**, *9* (23), 7072–7087.

(103) Jian, K.; Yang, C.; Li, T.; Wu, X.; Shen, J.; Wei, J.; Yang, Z.; Yuan, D.; Zhao, M.; Shi, J. PDGF-BB-Derived Supramolecular Hydrogel for Promoting Skin Wound Healing. *J Nanobiotechnol* **2022**, *20* (1), 201.

(104) Kumar, V. A.; Taylor, N. L.; Shi, S.; Wang, B. K.; Jalan, A. A.; Kang, M. K.; Wickremasinghe, N. C.; Hartgerink, J. D. Highly Angiogenic Peptide Nanofibers. *ACS Nano* **2015**, *9* (1), 860–868.

(105) Mammadov, R.; Mammadov, B.; Toksoz, S.; Aydin, B.; Yagci, R.; Tekinay, A. B.; Guler, M. O. Heparin Mimetic Peptide Nanofibers Promote Angiogenesis. *Biomacromolecules* **2011**, *12* (10), 3508–3519.

(106) Li, J.; Xing, R.; Bai, S.; Yan, X. Recent Advances of Self-Assembling Peptide-Based Hydrogels for Biomedical Applications. *Soft Matter* **2019**, *15* (8), 1704–1715.

(107) Hu, Y.; Yu, L.; Dai, Q.; Hu, X.; Shen, Y. Multifunctional Antibacterial Hydrogels for Chronic Wound Management. *Biomater. Sci.* **2024**, *12* (10), 2460–2479.

(108) Florencio-Silva, R.; Sasso, G. R. D. S.; Sasso-Cerri, E.; Simões, M. J.; Cerri, P. S. Biology of Bone Tissue: Structure, Function, and Factors That Influence Bone Cells. *BioMed Research International* **2015**, *2015*, 1–17.

(109) Lin, X.; Patil, S.; Gao, Y.-G.; Qian, A. The Bone Extracellular Matrix in Bone Formation and Regeneration. *Front. Pharmacol.* **2020**, *11*, 757.

(110) Florencio-Silva, R.; Sasso, G. R. D. S.; Sasso-Cerri, E.; Simões, M. J.; Cerri, P. S. Biology of Bone Tissue: Structure, Function, and Factors That Influence Bone Cells. *BioMed Research International* **2015**, *2015*, 1–17.

(111) Bigham-Sadegh, A.; Oryan, A. Basic Concepts Regarding Fracture Healing and the Current Options and Future Directions in Managing Bone Fractures. *International Wound Journal* **2015**, *12* (3), 238–247.

(112) Kolar, P.; Schmidt-Bleek, K.; Schell, H.; Gaber, T.; Toben, D.; Schmidmaier, G.; Perka, C.; Buttgereit, F.; Duda, G. N. The Early Fracture Hematoma and Its Potential Role in Fracture Healing. *Tissue Engineering Part B: Reviews* **2010**, *16* (4), 427–434.

(113) Bastian, O.; Pillay, J.; Alblas, J.; Leenen, L.; Koenderman, L.; Blokhuis, T. Systemic Inflammation and Fracture Healing. *Journal of Leukocyte Biology* **2011**, *89* (5), 669–673.

(114) Stamnitz, S.; Klimczak, A. Mesenchymal Stem Cells, Bioactive Factors, and Scaffolds in Bone Repair: From Research Perspectives to Clinical Practice. *Cells* **2021**, *10* (8), 1925.

(115) Gerstenfeld, L. C.; Cullinane, D. M.; Barnes, G. L.; Graves, D. T.; Einhorn, T. A. Fracture Healing as a Post-natal Developmental Process: Molecular, Spatial, and Temporal Aspects of Its Regulation. *J of Cellular Biochemistry* **2003**, *88* (5), 873–884.

(116) Dimitriou, R.; Jones, E.; McGonagle, D.; Giannoudis, P. V. Bone Regeneration: Current Concepts and Future Directions. *BMC Med* **2011**, *9* (1), 66.

(117) Agarwal, R.; García, A. J. Biomaterial Strategies for Engineering Implants for Enhanced Osseointegration and Bone Repair. *Advanced Drug Delivery Reviews* **2015**, *94*, 53–62.

(118) Ye, G.; Bao, F.; Zhang, X.; Song, Z.; Liao, Y.; Fei, Y.; Bunpetch, V.; Heng, B. C.; Shen, W.; Liu, H.; Zhou, J.; Ouyang, H. Nanomaterial-Based Scaffolds for Bone Tissue Engineering and Regeneration. *Nanomedicine (Lond.)* **2020**, *15* (20), 1995–2017.

(119) Xue, N.; Ding, X.; Huang, R.; Jiang, R.; Huang, H.; Pan, X.; Min, W.; Chen, J.; Duan, J.-A.; Liu, P.; Wang, Y. Bone Tissue Engineering in the Treatment of Bone Defects. *Pharmaceuticals* **2022**, *15* (7), 879.

(120) Oliveira, É. R.; Nie, L.; Podstawczyk, D.; Allahbakhsh, A.; Ratnayake, J.; Brasil, D. L.; Shavandi, A. Advances in Growth Factor Delivery for Bone Tissue Engineering. *IJMS* **2021**, *22* (2), 903.

(121) Quek, J.; Vizetto-Duarte, C.; Teoh, S. H.; Choo, Y. Towards Stem Cell Therapy for Critical-Sized Segmental Bone Defects: Current Trends and Challenges on the Path to Clinical Translation. *JFB* **2024**, *15* (6), 145.

(122) Perez, J. R.; Kouroupis, D.; Li, D. J.; Best, T. M.; Kaplan, L.; Correa, D. Tissue Engineering and Cell-Based Therapies for Fractures and Bone Defects. *Front. Bioeng. Biotechnol.* **2018**, *6*, 105.

(123) Alshehri, S.; Susapto, H. H.; Hauser, C. A. E. Scaffolds from Self-Assembling Tetrapeptides Support 3D Spreading, Osteogenic Differentiation, and Angiogenesis of Mesenchymal Stem Cells. *Biomacromolecules* **2021**, *22* (5), 2094–2106.

(124) Lee, S. S.; Du, X.; Kim, I.; Ferguson, S. J. Scaffolds for Bone-Tissue Engineering. *Matter* **2022**, *5* (9), 2722–2759.

(125) Donnaloja, F.; Jacchetti, E.; Soncini, M.; Raimondi, M. T. Natural and Synthetic Polymers for Bone Scaffolds Optimization. *Polymers* **2020**, *12* (4), 905.

(126) Fan, Y.; Ren, G.; Cui, Y.; Liu, H.; Li, S.; Tian, Y.; Wang, G.; Peng, C.; Wang, Y.; Wu, D. Peptide-Based Hydrogel for Enhanced Bone Repair. *Materials & Design* **2023**, *229*, 111862.

(127) Segman-Magidovich, S.; Grisaru, H.; Gitli, T.; Levi-Kalisman, Y.; Rapaport, H. Matrices of Acidic β -Sheet Peptides as Templates for Calcium Phosphate Mineralization. *Advanced Materials* **2008**, *20* (11), 2156–2161.

(128) Hartgerink, J. D.; Beniash, E.; Stupp, S. I. Self-Assembly and Mineralization of Peptide-Amphiphile Nanofibers. *Science* **2001**, *294* (5547), 1684–1688.

(129) Sugino, A.; Miyazaki, T.; Ohtsuki, C. Apatite-Forming Ability of Polyglutamic Acid Hydrogels in a Body-Simulating Environment. *J Mater Sci: Mater Med* **2008**, *19* (6), 2269–2274.

(130) Segman-Magidovich, S.; Grisaru, H.; Gitli, T.; Levi-Kalisman, Y.; Rapaport, H. Matrices of Acidic β -Sheet Peptides as Templates for Calcium Phosphate Mineralization. *Advanced Materials* **2008**, *20* (11), 2156–2161.

(131) Misawa, H.; Kobayashi, N.; Soto-Gutierrez, A.; Chen, Y.; Yoshida, A.; Rivas-Carrillo, J. D.; Navarro-Alvarez, N.; Tanaka, K.; Miki, A.; Takei, J.; Ueda, T.; Tanaka, M.; Endo, H.; Tanaka, N.; Ozaki, T. PuraMatrix^{TM} Facilitates Bone Regeneration in Bone Defects of Calvaria in Mice. *Cell Transplant* **2006**, *15* (10), 903–910.

(132) Wu, M.; Ye, Z.; Zhu, H.; Zhao, X. Self-Assembling Peptide Nanofibrous Hydrogel on Immediate Hemostasis and Accelerative Osteosis. *Biomacromolecules* **2015**, *16* (10), 3112–3118.

(133) Tavakol, S.; Rasoulian, B.; Ramezani, F.; Hoveizi, E.; Tavakol, B.; Rezayat, S. M. Core and Biological Motif of Self-Assembling Peptide Nanofiber Induce a Stronger Electrostatic Interaction than BMP2 with BMP2 Receptor 1A. *Materials Science and Engineering: C* **2019**, *101*, 148–158.

(134) Horii, A.; Wang, X.; Gelain, F.; Zhang, S. Biological Designer Self-Assembling Peptide Nanofiber Scaffolds Significantly Enhance Osteoblast Proliferation, Differentiation and 3-D Migration. *PLoS ONE* **2007**, *2* (2), e190.

(135) Bai, X.; Gao, M.; Syed, S.; Zhuang, J.; Xu, X.; Zhang, X.-Q. Bioactive Hydrogels for Bone Regeneration. *Bioactive Materials* **2018**, *3* (4), 401–417.

(136) Quan, C.; Zhang, Z.; Liang, P.; Zheng, J.; Wang, J.; Hou, Y.; Tang, Q. Bioactive Gel Self-Assembled from Phosphorylate Biomimetic Peptide: A Potential Scaffold for Enhanced Osteogenesis. *International Journal of Biological Macromolecules* **2019**, *121*, 1054–1060.

(137) Hayashi, K.; Ochiai-Shino, H.; Shiga, T.; Onodera, S.; Saito, A.; Shibahara, T.; Azuma, T. Transplantation of Human-Induced Pluripotent Stem Cells Carried by Self-Assembling Peptide Nanofiber Hydrogel Improves Bone Regeneration in Rat Calvarial Bone Defects. *BDJ Open* **2016**, *2* (1), 15007.

(138) Phipps, M. C.; Monte, F.; Mehta, M.; Kim, H. K. W. Intraosseous Delivery of Bone Morphogenic Protein-2 Using a Self-Assembling Peptide Hydrogel. *Biomacromolecules* **2016**, *17* (7), 2329–2336.

(139) Bessa, P. C.; Machado, R.; Nürnberger, S.; Dopler, D.; Banerjee, A.; Cunha, A. M.; Rodríguez-Cabello, J. C.; Redl, H.; Van Griensven, M.; Reis, R. L.; Casal, M. Thermoresponsive Self-Assembled Elastin-Based Nanoparticles for Delivery of BMPs. *Journal of Controlled Release* **2010**, *142* (3), 312–318.

(140) Lee, S. S.; Huang, B. J.; Kaltz, S. R.; Sur, S.; Newcomb, C. J.; Stock, S. R.; Shah, R. N.; Stupp, S. I. Bone Regeneration with Low Dose BMP-2 Amplified by Biomimetic Supramolecular Nanofibers within Collagen Scaffolds. *Biomaterials* **2013**, *34* (2), 452–459.

(141) He, B.; Ou, Y.; Chen, S.; Zhao, W.; Zhou, A.; Zhao, J.; Li, H.; Jiang, D.; Zhu, Y. Designer bFGF-Incorporated d -Form Self-Assembly Peptide Nanofiber Scaffolds to Promote Bone Repair. *Materials Science and Engineering: C* **2017**, *74*, 451–458.

(142) Zhou, A.; Chen, S.; He, B.; Zhao, W.; Chen, X.; Jiang, D. Controlled Release of TGF-Beta 1 from RADA Self-Assembling Peptide Hydrogel Scaffolds. *DDDT* **2016**, *10*, 3043–3051.

(143) Spoerke, E. D.; Anthony, S. G.; Stupp, S. I. Enzyme Directed Templating of Artificial Bone Mineral. *Advanced Materials* **2009**, *21* (4), 425–430.

(144) Baral, A.; Roy, S.; Dehsorkhi, A.; Hamley, I. W.; Mohapatra, S.; Ghosh, S.; Banerjee, A. Assembly of an Injectable Noncytotoxic Peptide-Based Hydrogelator for Sustained Release of Drugs. *Langmuir* **2014**, *30* (3), 929–936.

(145) Koch, F.; Ekat, K.; Kilian, D.; Hettich, T.; Germershaus, O.; Lang, H.; Peters, K.; Kreikemeyer, B. A Versatile Biocompatible Antibiotic Delivery System Based on Self-Assembling Peptides with Antimicrobial and Regenerative Potential. *Adv Healthcare Materials* **2019**, *8* (13), 1900167.

(146) Yang, G.; Huang, T.; Wang, Y.; Wang, H.; Li, Y.; Yu, K.; Dong, L. Sustained Release of Antimicrobial Peptide from Self-Assembling Hydrogel Enhanced Osteogenesis. *Journal of Biomaterials Science, Polymer Edition* **2018**, *29* (15), 1812–1824.

(147) Yoshimi, R.; Yamada, Y.; Ito, K.; Nakamura, S.; Abe, A.; Nagasaka, T.; Okabe, K.; Kohgo, T.; Baba, S.; Ueda, M. Self-Assembling Peptide Nanofiber Scaffolds, Platelet-Rich Plasma, and Mesenchymal Stem Cells for Injectable Bone Regeneration With Tissue Engineering. *Journal of Craniofacial Surgery* **2009**, *20* (5), 1523–1530.

(148) Szwed-Georgiou, A.; Płociński, P.; Kupikowska-Stobba, B.; Urbaniak, M. M.; Rusek-Wala, P.; Szustakiewicz, K.; Piszko, P.; Krupa, A.; Biernat, M.; Gazińska, M.; Kasprzak, M.; Nawrotek, K.; Mira, N. P.; Rudnicka, K. Bioactive Materials for Bone Regeneration: Biomolecules and Delivery Systems. *ACS Biomater. Sci. Eng.* **2023**, *9* (9), 5222–5254.

CHAPTER - 2

Yttrium Oxide Nanoparticle-loaded, Self-assembled Peptide Gel with Antibacterial, Anti-inflammatory, and Proangiogenic Properties for Wound Healing

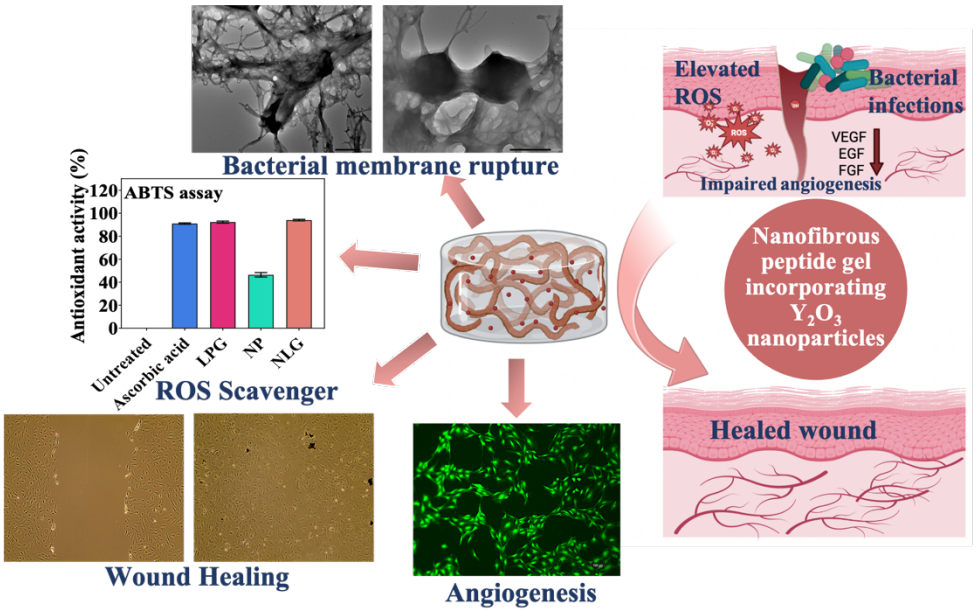

ToC graphic

Chapter 2

Nanoparticle-loaded self-assembled peptide gel for wound healing

2.1. Introduction

2.1.1. Chronic wounds

Body wounds are prevalent and can lead to significant disability, often necessitate a prolonged rehabilitation period. In individuals with no underlying health issues, the process of wound healing unfolds through four distinct stages: hemostasis, inflammation, proliferation, and remodeling.[1] This healing process is intricate but highly coordinated. Acute wounds transform into chronic wounds when they fail to follow the typical healing phases and remain in a perpetually disordered state of inflammation. The defining characteristic of a chronic wound is its failure to heal within the expected timeframe. Comorbidities, such as diabetes, immune suppression, vasculitis, specific conditions leading to neuropathy, poor circulation, ischemia, and reduced mobility significantly increase the risk of wounds becoming chronic.[2] Chronic wounds, including diabetic foot ulcers, venous leg ulcers, and pressure ulcers, pose significant healthcare challenges.[3] The global incidence of DFUs is estimated to be between 9.1 and 26.1 million annually, with about 15-25% of diabetic patients likely to develop a chronic ulcer at some stage of their life. Alarmingly, 1% of those patients might undergo amputation due to the severity of the condition.[4] VLUs exhibit high recurrence rates of 54-78%, which prolong suffering and adversely affect the patient's quality of life.[5] The estimated yearly direct cost for conservatively managing VLUs in developed countries is approximately US $5527 per patient.[6] Pressure ulcers primarily affect individuals with decreased mobility, diminished protective sensation, and less elastic skin, risks that escalate with age.[7]

2.1.2. Challenges

Chronic wounds are characterized by prolonged inflammation, persistent infections, biofilm formation, high proteolytic activity, impaired vascularization, downregulated growth factors, and ECM degradation.[3] Bacterial infections and their associated endotoxins play a significant role in the perpetuation of the inflammatory response, notably through the sustained elevation of proinflammatory cytokines, such as interleukin-1 (IL-1) and tumour necrosis factor-α (TNF-α). This prolonged inflammatory phase can ultimately lead to a chronic nonhealing state of wounds. Infected wounds commonly present with diverse microbiota, including, *Staphylococcus aureus*, *Enterococcus faecalis*, and *Pseudomonas aeruginosa*.[8] These bacteria, once established within a wound, tend to become resistant to conventional antimicrobial treatments.[9] A significant factor in this resistance is the ability of the bacteria to secrete extracellular polymeric substances, leading to the formation of a biofilm. This 3-dimensional

biofilm structure not only provides a physical barrier that protects the bacteria but also facilitates the adherence of pathogens, thereby enhancing their resistance to antimicrobial and antiseptic treatments.[10] One of the key challenges underlying wound chronicity is the degradation of the extracellular matrix and its components by elevated and unchecked expression of matrix metalloproteases (MMPs), and reactive oxygen species (ROS). Degradation of growth factors, like VEGF, FGF2, and EGF along with their receptors impair the signalling pathway, leading to poor cell migration, proliferation, and impediment in angiogenesis.[11] Developing biomaterials for chronic wound healing requires an understanding of the factors that cause an acute wound to become a chronic wound as well as how body changes the wound microenvironment from a non-healing to a healing state.

2.1.3. Research gap

Conventional wound care approaches, such as bandages, gauges, sutures, and staples, are notably inadequate for the treatment of chronic wounds since they merely serve as a barrier against further damage and fail to provide the bioactive functional elements needed to promote wound healing.[12,13] A wide range of strategies, such as the administration of antibiotics,[14,15] drugs,[16,17] growth factors,[18,19,20] and cells,[21] gene therapy,[22] immunomodulation,[23] and hyperbaric oxygen therapy,[24] have been studied to address the impediments associated with delayed wound healing. However, there are several challenges that limit their overall efficacy. Despite their effectiveness at the wound site, the exogenous supply of growth factors and proteins faces limitations regarding their stability under high protease activity prevalent in wound environments, resulting in a drastically shortened half-life. Additionally, the administration of these bioactive molecules is fraught with complications, such as the potential for immune reactions, difficulties in determining the appropriate dosage, and variable efficacy among individuals.[25] Current clinical practices involve topical or systemic delivery of antibiotics to combat the infections, but the emergence of antibiotic-resistant strains is a hurdle to this approach.[9] Hyperbaric oxygen therapy requires sophisticated instruments that are expensive and lack portability. Moreover, there is a risk of oxygen poisoning, adding to the complexity of its application.[26] The insufficient gene uptake, and inflammatory and immunogenic response raises the safety concerns with the gene therapy.[27]

The multifaceted nature of chronic wound pathophysiology necessitates a comprehensive treatment strategy. However, the majority of current biomaterials either target a singular aspect of the healing process or rely on complex multicomponent systems to address multiple factors simultaneously. A previous study by Gao *et al*. showed a double-layered antibacterial and proangiogenic patch loaded with tetracycline hydrochloride and deferoxamine (DFO) for wound healing.[28] Similarly, Hu *et al*. investigated a smart wound healing hydrogel incorporated with the antibiotic amikacin and micelles loaded with the anti-inflammatory drug naproxen.[29] A dual growth factor-releasing nanoparticle-in-nanofiber system was developed by Xie *et al*. for the

controlled release of VEGF and PDGF-BB.[30] While these approaches have yielded impressive results, the complexity of multicomponent systems makes it difficult to predict their biological response. The multiplicity of components complicates their design, synthesis, and clinical translation. This presents a significant gap in wound care, urging the need for innovative solutions that can effectively promote the healing of chronic wounds by addressing their underlying complexities.

2.1.4. Self-assembled peptide gels

It is imperative to consider a spectrum of characteristics that a biomaterial should embody to be optimal for wound healing applications. Self-assembled peptide-based hydrogels offer a promising platform for wound healing due to their excellent biocompatibility and optimal biodegradation, which ensures that its breakdown products are non-toxic and elicit no adverse immune reactions.[31] They seamlessly integrate with the surrounding tissues and mimic the extracellular matrix, thus, providing a supportive scaffold that promotes cell attachment, proliferation, and migration. Their porous morphology facilitates the vital exchange of cells, gases, nutrients, and waste between the healing tissue and the biomaterial. Moreover, the versatility of these biomaterials extends to their potential as carriers for therapeutic agents like drugs, growth factors, or other bioactive molecules. Additionally, their ability to get functionalized, enable them to actively participate in the healing process beyond passive support with enhanced anti-inflammatory, angiogenic, antibacterial, and adhesive capabilities, which are essential for mitigating infection risks and promoting wound repair.[32,33]

2.2. Objectives

To address the challenges discussed, we designed a yttrium oxide (Y_2O_3) nanoparticle-loaded multifunctional, self-assembled peptide gel (NLG) with bactericidal, ROS scavenging, cell proliferative and angiogenic properties. A self-assembled peptide gel was fabricated from a lauric acid conjugated peptide sequence ^{L}Lys-^{D}Phe-^{L}Lys-NH_2. The 12-carbon-containing alkyl chain of lauric acid and an aromatic phenylalanine group provide sufficient hydrophobic and π-π interactions to form a self-assembled nanofibrous gel. The basic lysine residues impart a net positive charge to the sequence and endow the material with antibacterial properties. The negatively charged phospholipids in bacterial membranes interact with these chains, damaging their membrane potential and disrupting them. Moreover, as the peptide chains are prone to proteolytic degradation, we have included a non-natural amino acid residue, D-phenyl alanine, which provides additional stability. In addition, we integrated the metal oxide nanoparticles into the peptide gel, as they are known to serve as versatile multifunctional agents across various biomedical applications. Metal oxide nanoparticles, like cerium oxide are reported for their ability to modulate the intracellular redox environment, which may enhance cell proliferation

and angiogenesis.[34] Yttrium oxide (Y_2O_3) nanoparticles possess biological activities similar to CeO_2 and have been recognized for their antioxidant properties and their ability to scavenge radicals under various conditions.[35] Given these characteristics, we hypothesized that the incorporation of Y_2O_3 nanoparticles within the self-assembled peptide scaffolds will induce a transient hypoxic environment. This condition is likely to activate hypoxia-inducible cellular pathways, consequently stimulating the production of factors that promote cell proliferation and vascularization. Moreover, it can prevent the drug-related side effects like stability, dosage complexities, off-targeting, and complex synthesis procedures. Thus, we decided to fabricate a peptide gel loaded with Y_2O_3 nanoparticles and investigate its efficacy in enhancing cell proliferation and angiogenesis to facilitate wound healing.

The peptide conjugate LA-^{L}Lys-^{D}Phe-^{L}Lys-NH_2 was synthesized by solid-phase peptide synthesis and characterized by RP-HPLC, mass spectrometry, and ^{1}H-NMR. The peptide was self-assembled into the gel using the pH-switch method in water with a passive incorporation of Y_2O_3 nanoparticles. The nanoparticle-loaded gel (NLG) was investigated for its surface morphology, self-healing ability, viscoelastic character, swelling and degradation, and antibacterial and antioxidant properties. The cell viability studies were performed on murine fibroblast L929 and human umbilical vein endothelial cell lines. The material was further investigated for its ROS scavenging and angiogenic potential.

2.3. Experimental Section

2.3.1. Materials

The analytic grade reagents were utilized without further purification. The supplier of the rink amide AM resin (200–400 mesh, 0.8 mmol/g loading) was Novabiochem. Triisopropylsilane (TIS), trifluoroacetic acid (TFA), HATU, Fmoc-^{L}Lys(Boc)-OH, Fmoc-^{D}Phe-OH, Fmoc-^{L}Phe-OH, lauric acid, N,N-diisopropylethylamine (DIEA), and 1-N-phenylnaphthylamine (NPN) were obtained from TCI. The 2,4-pentadione and anhydrous dimethylformamide (DMF) were purchased from Avra. We bought yttrium(III) nitrate hexahydrate from GLR innovations. Sigma-Aldrich provided Pluronic P-123. We acquired acetonitrile (ACN), ethanol, HPLC grade methanol, and dichloromethane (DCM) from Merck. Piperidine was bought from Spectrochem. Rankem was the supplier of diethyl ether. All studies utilized deionized (DI) water (18.2 MΩ·cm Bio-Rad). Bio-Rad PolyPrep chromatography columns were used for solid-phase peptide synthesis (SPPS). We acquired *E. Coli* and *S. aureus* from CSIR- IMTECH, Chandigarh, with accession numbers MTCC 1687 and MTCC 7443. Antibacterial studies were carried out using Luria broth and bacteriological agar powder (HiMedia). Thermo Fisher Scientific supplied fetal bovine serum (FBS), MTT reagent, DMEM, and RPMI for cell culture investigations. Dr. Durba Pal, Assistant Professor, DBME, IIT Ropar, gifted the murine fibroblast cell line (L929). We purchased the endothelial cell growth medium-2 (EGM 2) Bullet Kit and the endothelial cell line (HUVECs) from Lonza.

2.3.2. Methods

A Tecan Infinite Pro multimode plate reader was used to determine the UV–vis absorbance. FTIR spectra have been obtained using OPUS software in ATR mode (Bruker Tensor 27) in 400–4000 cm^{-1} region. A RIGAKU Mini-Flex diffractometer with a Cu Kα (λ = 0.154 nm, 40 kV, 15 mA) radiation source was used to record powdered XRD. Both the surface potential and the particle size distribution were measured using DLS Microtrac/Nanotrac Flex. Using a Quantachrome QUADRASORB-SI automatic volumetric instrument, the BET analysis was performed to assess the surface area and pore size of nanoparticles. The XEVO G2-XS QTOF was used to collect the HR-MS. The NMR spectra were recorded using a 400 MHz JEOL JNM-ECS NMR. A circular dichroism spectrophotometer (JASCO J-1500) was used to determine the secondary structure. Waters system with BEH 300 RP C_{18} column (250 × 4.6 mm, 5 µm), pump, degasser, injector with 100 µL loop, PDA, and UV–vis detectors was used for RP-HPLC. Empower 3 software was utilized in isocratic mode to analyze the data, and the mobile phase used was 50:50 ACN:H_2O with 0.1% TFA at a flow rate of 1 mL/min. A JEOL JSM-6610 LV microscope equipped with a tungsten filament and an accelerating voltage of 10 kV was used to take SEM images. HR-TEM pictures were acquired at 200 kV with a JEM-2100 Plus instrument. For the rheological investigations, an Anton Paar MCR 102 rheometer was utilized. A Leica DMi8 fluorescence microscope was used to capture fluorescence images.

2.3.3. Synthesis of lauric acid-peptide conjugate (LPC)

The LPC was synthesised using solid-phase peptide synthesis (SPPS) on rink amide AM resin (200-400 mesh, 0.8 mM/g loading) in Bio-Rad PolyPrep chromatography columns. The 100 mg of rink amide resin beads were swelled in 1 mL of DMF before being used. The synthesis followed the Fmoc approach, using 2.85 and 5.7 equivalents of HATU and DIEA for coupling of each amino acid, where each coupling step took around 4 hours. Fmoc deprotection was carried out using 20% v/v piperidine in DMF solution. After every stage, the resin was rinsed three times with DMF and DCM (1 mL each). Side-chain Boc-group deprotection and peptide cleavage from the resin were performed using a TFA:TIS mixture in 95:2.5:2.5 ratio i.e. 4.75 mL TFA, 125 µL TIS, and 125 µL H_2O for 3 hours at room temperature. The peptide conjugate was then precipitated in ice-cold diethyl ether and vacuum dried. The purity of peptide was determined using RP-HPLC, and it was further characterized using FTIR, CD, HR-MS, and ^1H NMR.

2.3.4. Fabrication of yttrium oxide (Y_2O_3) nanoparticles

As previously reported, Y_2O_3 nanoparticles were fabricated using the sol-gel approach.[36] Using strong magnetic stirring, 0.0026 mol (~0.99 g) of yttrium nitrate hexahydrate [$Y(NO_3)_3 \cdot 6H_2O$] was dispersed in methanol (MeOH) at a molar ratio of 123:1 (MeOH:Y) for a duration of 15 minutes. The sol was stabilized with acetylacetone, and the development of mesoporous structures was facilitated by the addition of poloxamer P-123 in a 2:1 molar ratio (P-

123:Y). After heating the mixture for 24 hours at 90 °C to form a xerogel, it was heated for an additional hour at 900 °C in a furnace to form a dense material and induce crystallization. Powder X-ray diffraction (PXRD), Fourier-transform infrared spectroscopy (FT-IR), and UV-visible spectroscopy were used to analyze the nanoparticles. FE-SEM and HR-TEM were used to examine the size and surface morphology of Y_2O_3 nanoparticles. Brunauer-Emmett-Teller (BET) plots were used for estimating the pore size and surface area.

2.3.5. Fabrication of nanoparticle-loaded peptide gel

The NP-loaded gel (NLG) was fabricated using the pH switch approach. In a 5 mM solution of Y_2O_3 nanoparticles in DI water, lauric acid-^{L}Lys-^{D}Phe-^{L}Lys-NH_2 conjugate (LPC) was added to prepare a solution of 1% w/v. Next, 2-3 drops of 0.2 M NaOH solution were added to the solution while sonicating it constantly, resulting in gel formation in 10-15 minutes. Afterwards, the gel was kept unperturbed at 37 °C for a few hours before being employed for further analyses. Likewise, another gel, lauric acid-peptide conjugate gel (LPG), was fabricated without incorporating nanoparticles for control studies.

2.3.6. Surface morphology

SEM and HR-TEM were used to assess the surface morphology of gel and Y_2O_3 nanoparticles. An ethanol-dispersed sample of Y_2O_3 NPs was drop-cast onto a metal stub and air-dried before SEM analysis. While the gel was placed directly on stub and dried overnight under vacuum. The samples were sputtered with platinum and micrographs were taken with a JEOL JSM-6610LV microscope equipped with a tungsten filament and an acceleration voltage of 10 kV. Samples were prepared on a copper grid for HR-TEM analysis, and images were taken at various magnifications using an HR-TEM JEM-2100 Plus instrument running at 200 kV.

2.3.7. Rheology

An Anton Paar MCR 102 modular rheometer, featuring a 25 mm parallel plate configuration, was utilized for conducting rheological experiments. Prior to rheological analysis, both NLG and LPG were kept unperturbed overnight. At a fixed angular frequency of 10 rad/s and a varying strain between 0.01−100 %, the dynamic amplitude sweep test was performed. Further, the frequency sweep analysis was performed by keeping the strain constant at 1%, with a frequency varying between 0.1 to 100 rad/s. High-viscosity paraffin oil was applied around the plates to prevent the evaporation of water from the gels.

2.3.8. Self-healing analysis

Time-dependent recovery experiments on an MCR 102 modular rheometer (Anton Paar) were used to examine the self-healing characteristics of LPG and NLG gels. The gel was subjected to six consecutive cycles of 200 s each, with a periodic strain of 0% and 30% applied to it. Additionally, the macroscopic examination of self-healing was carried out by slicing the gel in half using a surgical blade. Rhodamine B was applied to one half of the gel and the other half

remained unstained. The dye diffusion was monitored for up to 24 hours while both halves were stacked together.

2.3.9. Proteolytic stability

In order to study the resistance of the gel to protease enzymes, LPG (without NPs) was placed in a 1 mL solution of proteolytic enzymes in 10 mM PBS. The solution contained 1.65 units of each proteinase K, chymotrypsin, and pepsin.[37,38] The gel was then exposed to the enzyme mixture for 0, 12, 24, and 36 hours at 37 °C. At specific time points, the samples were centrifuged at 10,000 rpm for 10 minutes while maintaining a temperature of 4 °C. The samples were rinsed three times with DI water and freeze-dried. After the freeze-dried gel was dissolved in 500 µL of methanol, it was syringe-filtered (0.2 µm) and subjected to RP-HPLC analysis, using a 10 µL injection volume. A control peptide conjugate gel was used as well, with a sequence of LA-^{L}Lys-^{L}Phe-^{L}Lys-NH_2, containing L-phenylalanine in place of D-phenylalanine. Following equation was used to determine the percentage stability of peptide:

$$\% \text{ Remaining peptide} = \frac{Area\ under\ the\ peak\ at\ time\ t}{Area\ under\ the\ peak\ at\ 0\ h} \times 100 \qquad Equation\ 1$$

where, t = 12, 24, and 36 h.

2.3.10. Swelling and degradation

NLG and LPG were investigated for their swelling and degradation analysis in the buffer solutions with pH 7 and 8.4. The gels were placed in an incubator at 37 °C and 100 rpm, where gel degradation was estimated through gravimetric analysis after 24, 48, and 72 hours. After each interval, the media was removed, and the gels were weighed. Gravimetric assessment of stability was performed using the formula given below:[39]

$$\text{Swelling/Degradation } (\%) = \frac{(W_i - W_f)}{W_i} \times 100 \qquad \textbf{Equation 2}$$

where, w_i is the initial weight of the gel and w_f is the weight of gel at a particular time interval.

2.3.11. Antioxidant activity

The antioxidant activity of the material was investigated by DPPH and ABTS assays,[40,41] as discussed below:

ABTS assay. It was performed by preparing a stock solution of ABTS radical, where 1 ml of 7.38 mM ABTS salt (3.8 mg) solution was mixed with 1 mL of 2.58 mM potassium persulfate (0.7 mg) in DI water. For the generation of ABTS radical, the solution was placed in dark for 12 h. The absorbance of the solution was taken at 415 nm and was adjusted to 0.75 by dilution with PBS. The 200 µL of this diluted solution with absorbance value of 0.75 was added to each sample and control. We have taken 1 mg/mL solution of ascorbic acid as the positive control and untreated ABTS radical solution as negative control. All the samples were then incubated at 37 °C and 100 rpm for 1 h. After 1 h, the samples were centrifuged at 700 rpm for 5 minutes and the absorbance reading at 415 nm were taken.

DPPH assay. The 1′-diphenyl-2-picrylhydrazyl (DPPH) radical scavenging ability of the material was analyzed by DPPH assay. Samples and controls were incubated with the 200 µL solution of DPPH radical solution (0.1 mM) in methanol at 37 °C for 2 h. Trolox (25 µM) in methanol was taken as the positive control while the untreated DPPH radical solution was taken as the negative control. After 2 h, the absorbance readings for each sample at 517 nm were taken using a plate reader. The following equation was used to quantify antioxidant activity:

$$\% \text{ Radical Scavenging Effect} = \frac{(A_c - A_s)}{A_c} \times 100 \qquad \textbf{Equation 3}$$

where, A_c and A_s are the absorbance value of control and samples.

2.3.12. Antibacterial activity

The antibacterial activity of the NLG and LPG was investigated against *S. aureus* and *E. coli* by optical density method (OD_{600}) and Live−Dead fluorescence imaging.

Optical density method. The gels were freeze-dried and sterilized under UV-radiations prior to the experiment. Bacterial cultures of *E. Coli* and *S. aureus* were maintained in Luria broth until the midlog phase in a shaker incubator set to 100 rpm and 37 °C. OD_{600} was then adjusted to 0.01 AU (1×10^6 cfu/mL) by diluting it with luria broth. We have taken Gentamicin Sulfate (50 μg/mL) as positive control and the untreated bacterial samples were used as negative controls. Samples and control sets were then incubated with the 500 μL bacterial culture for 24, 48, and 72 h. After each specified interval, OD_{600} value of each sample was recorded. The percentage antibacterial activity of the material was determined by comparing it against the untreated bacterial samples.[42]

$$\text{Bacterial inhibition (\%)} = \frac{(A_c - A_s)}{A_c} \times 100 \qquad \textbf{Equation 4}$$

Where, A_c is the OD_{600} value of untreated control samples and A_s is the OD_{600} value of samples.

Live−dead assay. Similarly, for live-dead analysis, the samples are prepared and UV-sterilized prior to treatment. Both Gram-positive bacteria and Gram-negative bacterial strains were cultured in Luria broth until midlog phase and their OD_{600} was adjusted to 0.01 AU, i.e. 1×10^6 cfu/ml. The sample and control sets were incubated for 24 h with the bacterial cultures in an orbital shaker kept at 100 rpm and 37 °C. Gentamicin was used as positive control with the untreated bacterial samples as negative control. After 24 h of incubation, 100 μL of culture from each set was costained with a 1:1 v/v mixture of propidium iodide (Ex/Em = 535/617 nm) and SYTO 9 (Ex/Em = 483/503 nm). The stained samples were then kept in dark for 20 minutes and placed on a glass slide for the microscopic analysis. Leica microscope at 20X magnification was used to capture the fluorescence images.

2.3.13. Mechanistic analysis of antibacterial activity

HR-TEM images of the NLG-treated bacterial samples were taken for the mechanistic analysis of antibacterial activity. We have taken 6 sets of *E. coli* and *S. aureus* bacterial strains with the OD_{600} value adjusted to 0.01, as discussed earlier. Both the strains were treated with NLG for 24 h. After 24 h, bacterial cultures from all the sets were centrifuged (5500 RPM, 4 °C, 10 min), and the pellet collected at the bottom was washed thrice with PBS (pH: 7.4). The bacterial cells were then fixed overnight using 2.5% glutaraldehyde. Following fixation, the cells were rinsed with PBS and stained with osmium tetroxide (1%) for 30 minutes. A repeated ethanol washing (30%, 50%, 70%, and 90%) was performed to dehydrate the bacterial cells. The cells were suspended in the pure ethanol, and around 5 µL of it was drop cast onto a carbon-coated copper grid (mesh size: 300). The samples were air-dried before the images were captured using an HR-TEM. The untreated bacterial cells were used as a negative control.

2.3.14. 1-*N*-phenylnaphthylamine (NPN) assay

The NPN assay was used to quantitatively determine the impact of NLG on the integrity of bacterial cell membranes. As discussed earlier, *E. coli* and *S. aureus* were cultured, and their OD_{600} was adjusted to 0.01 AU (1×10^6 cfu/mL). The bacterial samples were then incubated with NLG for 24 hours. After the incubation, 100 µL of the suspensions were taken from each sample and centrifuged (3500g, 4 °C, 5 min). The collected pellet was washed twice and suspended in 100 µL of PBS. Next, the suspension was transferred to a 96-well plate, and 8 µL of NPN (0.5 mM) solution prepared in 50:50 acetone:PBS was added. The fluorescence spectrum was recorded between 375 and 600 nm, with the excitation wavelength set at 356 nm. Any change in the fluorescence intensity at 425 nm (λ_{em}) was then observed.[43]

2.3.15. Cell viability analysis

Cell viability analysis of the fabricated materials, NLG, LPG and NP was performed by the MTT assay and live-dead fluorescence imaging. The study was performed on murine fibroblast L929 and human umbilical vein endothelial cell lines. L929 cells were grown in the RPMI media, which was supplemented with 10% fetal bovine serum and 1% antibiotic. HUVECs were cultured in endothelial basal medium (EBM), which was supplemented with EGM-2 bullet kit and 1% antibiotic.

MTT Assay. Cell lines were grown in Nunc-coated T-25 flasks and incubated at 37 °C in a humidified atmosphere with 5% CO_2 until 80-90% confluence was attained. The subconfluent cells were taken out using a trypsin-EDTA solution and collected for further analysis. The freeze-dried samples were sterilized for 30 min using UV radiation. The LPG and NLG samples were incubated in the incomplete medium at a concentration of 1 mg/mL for 24 h at 37 °C. After incubation, the sample extracts were collected using a 0.2 µm syringe filter and diluted three times to obtain the working concentration of 330 µg/mL, as optimized by the dose-dependent MTT assay of gel extracts in the concentration ranging from 100-1000 µg/mL. The

nanoparticles were also dispersed in the incomplete media at a concentration of 5 mM and diluted thrice. In a Nunc-coated 96-well plate, the cells were seeded with a density of 10,000 cells/well and kept in the incubator for cell fixation. After 24 h, the media in the wells was replaced with the 100 µL of sample extracts. Following the treatment, the cells were again incubated for another 24 hours. The cells without treatment were considered positive control, and the wells containing only media without cells were taken as blank. Following the treatment period of 24 h, each well was added with the 20 µL of MTT solution (5 mg/mL) prepared in the incomplete media. The cells were then incubated for 3.5 hours at 37 ℃ to allow for the formation of formazan crystals. These crystals were dissolved in the 100 µL DMSO, and the absorbance of the samples (n=3) was taken at 570 nm. The ratio of the sample-treated cells and untreated cells determined the cell viability.[44]

Live-dead assay. The cell viability analysis by live-dead assay involved the fluorescent imaging of the cells after treatment with the samples for 24 h. A working dye solution of calcein AM (2 μM) and ethidium homodimer 1-red (4 μM) was prepared for the staining. Both HUVECs and L929 cells were cultured in a 35 mm disc with a cell density of 1.2×10^6 cells/disc in their respective media solutions. The cell were grown in a humidified environment at 37 ℃ and 5% CO_2. The cells were treated with the NLG and LPG gel extracts at concentration of 330 µg/mL for 24 h. After treatment, the cells were stained with the 500 μL dye solution that was prepared earlier and kept in dark for 45-60 minutes. The images of the cells were then captured using Leica fluorescence microscope and the intensity of live and dead cells was observed.

2.3.16. ROS scavenging

In a Nunc-treated 6-well plate, murine fibroblast L929 cells were seeded in a concentration of 1.2×10^6 cells/well and kept in a humidified environment with 5% CO_2 and 37 °C temperature. The cells were treated with 0.5 mM of H_2O_2 for an hour to induce ROS stress. Following the induction of ROS stress, the cells were treated with the sample extracts and incubated for 24 hours. After 24 h of incubation, the 25 µM DCFDA dye solution was added to each well, and the plate was placed in the dark for around 30 minutes. The ROS stress in the cells was then observed by fluorescence imaging, where the intensity of green fluorescence determined the oxidative stress. Moreover, the viability of ROS-stressed cells on treatment with the NLG was also investigated by MTT assay. The cells were seeded in a 96-well plate at 1×10^4 cells/well for this analysis. Cells were treated with the sample extracts, and 0.5 mM of H_2O_2 was added to each well. The cells were incubated for 24 h, and viability was assessed using an MTT assay. The wells with no NLG treatment and only H_2O_2 were considered positive control, and wells without H_2O_2 were taken as negative control.[45]

2.3.17. Cell migration and *in vitro* wound healing

Scratch assay was performed to investigate the cell migration and *in vitro* wound healing ability of HUVEC and L929 cells on treatment with the NLG and LPG. In a 6-well plate, the cells (1.2×10^6 cells/well) were seeded in their respective media and incubated in a humidified environment containing 5% CO_2 at 37 °C until 80-90% confluency was achieved. Upon attaining the desired confluency, a scratch was made on the monolayer of cells using a sterile tip. The debris was removed with the continuous washing using incomplete media. The cells were then treated with the sample extracts with a concentration of 330 µg/mL and the healing of scratch was observed at different time intervals. The images were captured under a light microscope at 12, 24 and 48 hours and area of scratch healing was observed using ImageJ software.[46]

2.3.18. Angiogenesis

The angiogenic ability of the NLG was determined by the *in vitro* angiogenesis assay following the protocol reported by Hauser *et al*.[47] Endothelial cells (HUVECs) with a cell density of 40,000 cells/well were cultured on the NLG in a 24-well plate. The cells were immersed in incomplete Endothelial Growth Media (EGM-2) and incubated for 24 hours at 37 °C in a humid environment containing 5% CO_2. After 24 h of incubation, the cells were stained with the working concentration of calcein AM and ethidium homodimer solution for 40 min. The images were captured using a fluorescence microscope and analyzed using ImageJ with Angiogenesis Analyzer.[47]

2.3.19. Gene expression analysis

The expression of various proangiogenic genes like VEGF, FGF2, EGFR and HIF-1 was analyzed using qRT-PCR analysis. The HUVECs cultured in 35 mm discs were treated with LPG and NLG for 24 h. Next, RNA was isolated from the cells using trizol and was quantified using NanoDrop One/One Microvolume UV−vis spectrophotometer (Thermo Fisher Scientific, USA). Further, cDNA was synthesized from the 600 ng RNA using the Bio-Rad cDNA synthesis kit. RT-qPCR analysis was performed on Quant- Studio 3 Real-Time PCR System (Applied Biosystem, USA) using SYBR Universal. The expression level of VEGF, FGF2, HIF-1, and EGFR were investigated by taking actin as reference gene, which served as the standard for data normalization. The cells without the NLG treatment were taken as control.

2.3.20. Statistical analysis

The student's t test was used to evaluate the data. The experiments were performed in triplicates and data presented as mean values along with the standard deviations. Result significance was determined with *P* values, where < 0.05 (*), < 0.01 (**), and < 0.001 (***) indicated significant differences, and "*ns*" indicated non-significant difference.

2.4. Results and discussion

This work aimed to develop a multifunctional, self-assembled peptide-based gel loaded with nanoparticles to address the challenges of chronic wound healing. The strategy was to leverage the inherent properties of the materials developed, rather than delivering exogenous growth factors, drugs, or adjuvants. We have fabricated a Y_2O_3 nanoparticle-loaded lauric acid-peptide conjugate gel, LA-^{L}Lys-^{D}Phe-^{L}Lys-NH_2 (NLG) with inherent antibacterial, ROS scavenging, and proangiogenic properties **(Figure 2.1)**. The rationale behind incorporating the basic lysine residues with an amine side chain within our conjugate was to impart antibacterial and anti-inflammatory properties to the gel. The positively charged lysine side chains engage in electrostatic interactions with negatively charged bacterial cell membranes, leading to the disruption of membrane integrity and consequently exerting antimicrobial effects.[48] Moreover, the lone pair on amine shields the cells from oxidative damage.[49] The hydrophobic phenylalanine (Phe) was selected to enhance the self-assembly of the peptide into a stable gel structure, attributable to its aromatic (π-π) interactions and hydrophobic characteristics, which contribute to maintaining structural integrity and improving the physical robustness of the gel, which is crucial for wound dressings. In addition, the hydrophobic nature of lauric acid further promotes peptide self-assembly into nanofibrous structures. The short length of the peptide sequence (LA-^{L}Lys-^{D}Phe-^{L}Lys-NH_2) was strategically taken to balance the ease of synthesis and self-assembly capabilities and was found sufficient to allow self-assembly into a gel structure, avoiding the need for longer, more complex peptides. The simplicity of this trimeric sequence also minimizes potential immunogenicity, a critical factor for applications in wound healing.[50] Furthermore, we capitalized on the redox-active properties of Y_2O_3 NPs. These nanoparticles induce a temporary hypoxic environment conducive to promote the hypoxia-induced angiogenesis and activates the cellular pathways to promote cell migration and proliferation. Thus, the nanoparticle loaded peptide gel (NLG) presents a promising approach to wound healing. The obtained results were compared with the lauric acid-peptide conjugate gel (LPG) without the nanoparticle entrapment.

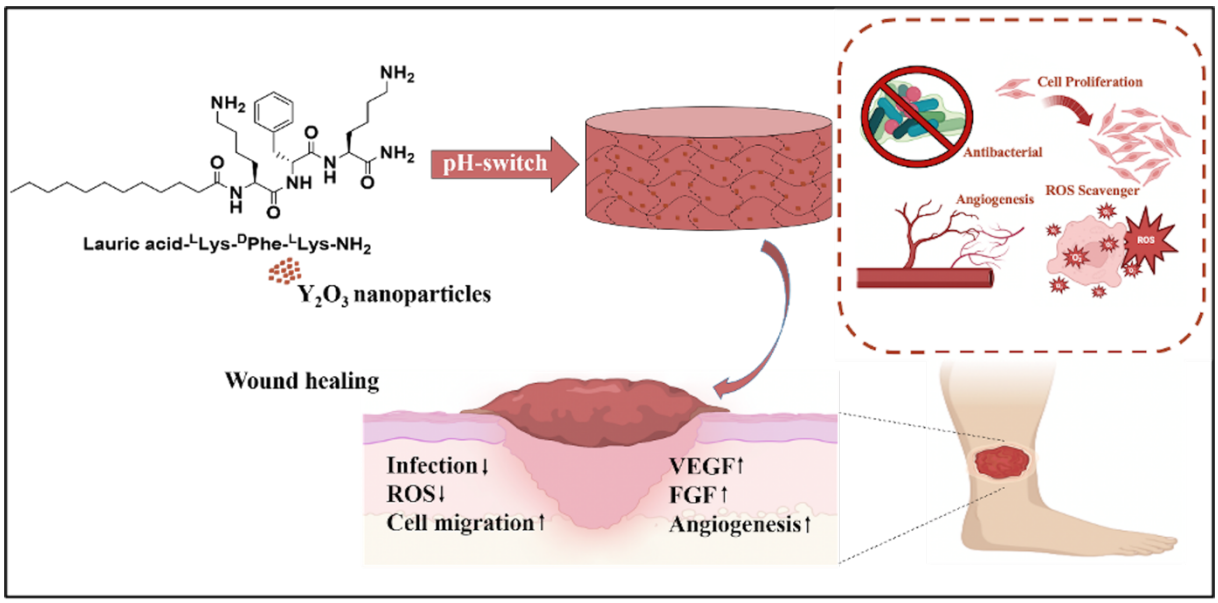

Figure 2.1. Self-assembly of Y_2O_3 nanoparticles-loaded peptide-based gel, LA-^{L}Lys-^{D}Phe-^{L}Lys-NH_2, and its wound healing activity.

2.4.1. Lauric acid-peptide conjugate

The solid phase peptide synthesis (SPPS) technique was used to fabricate the LA-^{L}Lys-^{D}Phe-^{L}Lys-NH_2 **(Figure A1, Appendix)**. The synthesis followed a Fmoc-based approach, and the lauric acid was conjugated to the peptide chain using amide linkage. RP-HPLC, ^{1}H NMR and HR-MS were performed for the peptide characterization. RP-HPLC determined the 95% purity of the peptide, and the observed retention time (R_t) was 4.5 min **(Figure A3, Appendix**). The molecular weight determined by HR-MS (603 Da) was consistent with the theoretical value **(Figure A2, Appendix)**. Further, the assigned NMR peaks have been provided in **Figure A4, Appendix**. FT-IR and CD-spectroscopy were performed to investigate the secondary structure of the peptide conjugate. The amide I peak identified at 1642 cm^{-1} corresponds to stretching vibrations of C-O, and the amide II peak observed at 1543 cm^{-1} corresponds to the N−H bending peak **(Figure A5, Appendix**). Peaks corresponding to amide III were observed in the 1229−1301 cm^{-1} region, which were attributed to N-H bending coupled with C−N stretching. The FT-IR data indicated a random coil configuration for the peptide conjugate, which was supported by CD spectroscopy results showing a minimum at 196 nm **(Figure A6, Appendix**).[51,52] Additionally, the peptide chain exhibited a net positive zeta potential of +1.5 mV, likely due to the presence of basic lysine residues.

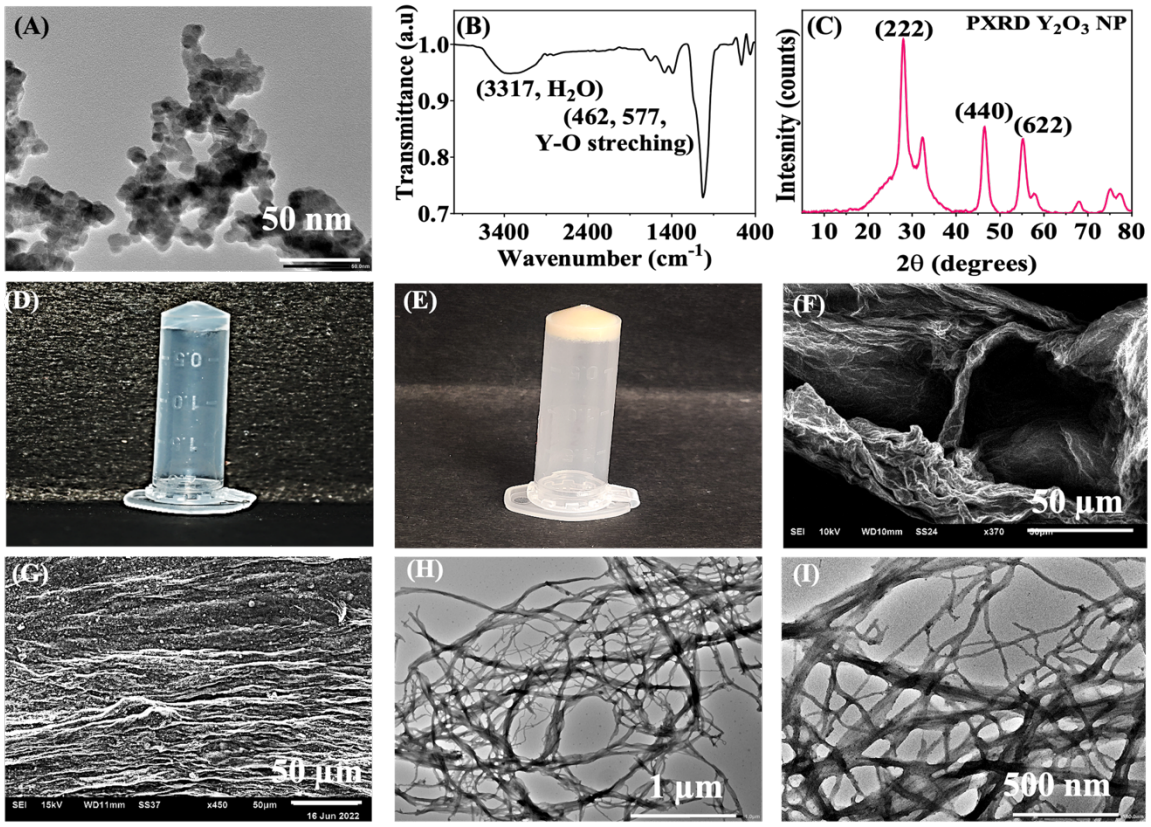

Figure 2.2. Characterization of Y_2O_3 NPs and NP-loaded peptide gel (NLG). (A-C) HR-TEM, FT-IR spectrum and powdered X-ray diffraction data of Y_2O_3 NPs. (D) Lauric acid-peptide conjugate gel (LPG). (E) Nanoparticle-loaded peptide-conjugate gel (NLG). (F, G) Scanning electron microscopy (SEM) images of LPG and NLG. Scale bar: 50 µm. (H, I) HR-TEM images of nanofibrous gel. Scale bar: 1 µm and 500 nm.

2.4.2. Yttrium oxide (Y_2O_3) nanoparticles

The sol-gel technique was employed to fabricate the Y_2O_3 nanoparticles using yttrium nitrate hexahydrate as a precursor, where poloxamer P-123 was added to provide the mesoporosity. The nanoparticles were characterized by FT-IR, UV-visible spectroscopy, PXRD, DLS, zeta potential, HR-TEM, FE-SEM, and BET **(Figure 2.2)**. The HR-TEM images revealed that the nanoparticles possess a cubic morphology that was further validated by FE-SEM analysis **(Figure A10, Appendix)**. The hydrodynamic radius was measured at 80.4 ± 3.34 nm (n = 3) by DLS **(Figure A9, Appendix)**, whereas the HR-TEM analysis determined the size to be around 20 nm. Moreover, the surface potential of nanoparticles was observed about +5.16 ± 0.05 mV, indicating a mild positive charge on their surface.

UV-visible spectroscopy exhibited a strong absorption band at 290 nm, which was consistent with the literature, confirming the fabrication of Y_2O_3 NPs **(Figure A7, Appendix)**.[53] The FT-IR spectra peaks at 462 and 577 cm^{-1} corresponded to Y-O stretching **(Figure 2.2B).** The presence of moisture was indicated by a broad peak at 3317 cm^{-1}, while the peaks at 1490 and

1396 cm^{-1} suggested the -COOH stretching. The Powder X-ray Diffraction (PXRD) pattern for the NPs showcased three distinct peaks at 2θ positions of 28.04, 46.46, and 55.2, corresponding to the (222), (440), and (622) crystal planes, respectively **(Figure 2.2C)**. This PXRD data aligns well with the existing literature and the JCPDS card, thereby, corroborating the formation of cubic-structured Y_2O_3 NPs.[54] Further, the Brunauer-Emmett-Teller (BET) study conducted at 77 K yielded an estimated surface area of 98 m^2/g for the NPs **(Figure A8, Appendix)**. After calculating the pore size using the DFT approach, the mesoporous structure of the NPs was confirmed with a pore size of 17 Å.

2.4.3. Y_2O_3 NP-loaded lauric acid-peptide conjugate gel (NLG)

The peptide chains self-assembled in an alkaline environment to form the gel. A 1% w/v solution of lauric acid-^{L}Lys-^{D}Phe-^{L}Lys-NH_2 peptide conjugate was prepared using 100 µL of 5 mM dispersion of Y_2O_3 NPs in DI water, followed by 2-3 drops of 0.2 M NaOH. The gel formation process required approximately 15 to 20 min, resulting in a loading of approximately 50 µg of nanoparticles. Peptide gels with different concentration of Y_2O_3 (1-15 mM) were prepared to optimize the effective loading concentration. We used the inverted vial technique to confirm its formation **(Figure 2.2D, E).** We examined the morphology of the scaffold using SEM **(Figures 2.2F, G)** and HR-TEM **(Figure 2.2H)**, which showed a nanofibrous structure. The gelation process was facilitated by interactions, such as cation-π stacking, H-bonding, π−π stacking, and hydrophobic interactions.

2.4.4. Rheology studies

Rheology analyses were performed to examine the viscoelastic properties and self-healing ability of NLG and LPG **(Figure 2.3)**. In the frequency sweep experiment, the study was carried out at a constant 1% strain and varying angular frequency from 0.1 to 100 rad/s, while the amplitude sweep experiment was conducted at a constant angular frequency of 10 rad/s and the strain varying between 0.01% to 100% **(Figure 2.3A, D)**. For both gels, within the frequency range of 0.1−100 rad/s, there were no crossovers, and the G′ values remained stable, indicating that the viscoelastic behaviour of the gel was consistent throughout this range. Gels had a linear viscoelastic range of up to 1%, with the crossover point determined at 24.8% for the peptide conjugate gel and 82.5% for the NP-loaded gel **(Figure 2.3B, E)**. The inclusion of NPs led to a significant increase in the mechanical strength of the gel because of the interaction between the amines on lysine and the metal ions, as indicated by the significant increase in the crossover points and a high storage modulus (~4 kPa). The gel's viscoelastic behaviour was validated by the higher storage modulus (G′) compared to the loss modulus (G″). To assess the self-healing properties, the gels were subjected to a constant angular frequency of 10 rad/s with alternating strains of 0.1% and 30% for six cycles, each lasting 200 seconds. Upon removal of the strain,

the gels were able to restore their original structure **(Figure 2.3C, F)**. The self-healing capacity of gels was also determined visually **(Figure A11, Appendix)**. A surgical blade was used to split the gel in two. The rhodamine B dye stained one half of the gel while the other half remained unstained. The self-healing ability was demonstrated by the diffusion of dye from the stained to unstained half of the gel, kept in contact under airtight conditions at 37 °C. Images were captured at 0, 6, 12, and 24 hours to monitor the dye diffusion.

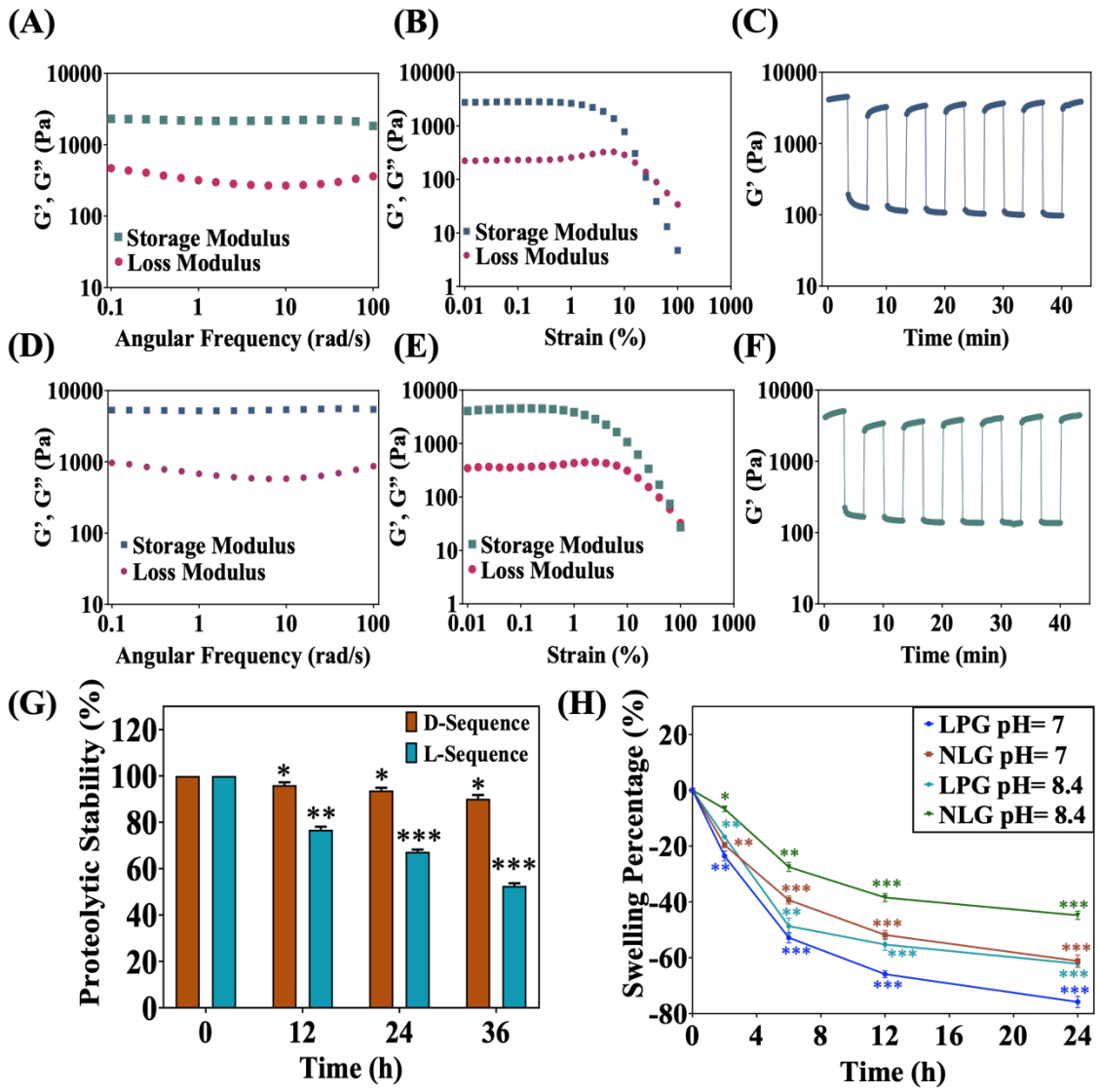

Figure 2.3. Rheological properties and stability profiles of gels. (A, D) Frequency sweep analysis of LPG and NLG at a constant strain of 1% with varying angular frequency from 0.1 to 100 rad/s. (B, E) Amplitude sweep of LPG and NLG at a 10 rad/s constant angular frequency with a varying strain of 0.01-100%. (C, F) Self-healing analysis of gel for 6 cycles by using the periodic strains of 0.1% and 30%. (G) Proteolytic stability studies of LPG, LA-^{L}Lys-^{D}Phe-^{L}Lys-NH_2 at physiological pH. Peptide conjugate gel, LA-^{L}Lys-^{L}Phe-^{L}Lys-NH_2, with L-Phe instead of D-Phe was taken as a control. (H) Degradation study of LPG and NLG in the buffer solutions

of pH 7 and 8.4. The data is provided as mean ± standard deviation (n = 3), with P values of <0.05 (*), 0.01 (**), and 0.001 (***) indicating significant differences.

2.4.5. Stability of gels

The proteolytic stability of the lauric acid-peptide conjugate gel (LPG) was assessed using an enzyme cocktail consisting of chymotrypsin, pepsin, and proteinase K. For comparison, a conjugate gel, LA-^{L}Lys-^{L}Phe-^{L}Lys-NH_2, containing L-Phe instead of D-Phe was used as a control. A 1% gel solution was incubated with the enzyme mixture, and its proteolytic stability was measured at 0-, 12-, 24-, and 36-hours using RP-HPLC **(Figure 2.3G)**. The stability was quantified by estimating the area under the RP-HPLC peak. After 36 hours, the gel containing D-Phe showed only 10% degradation, whereas the gel made entirely of L-amino acids exhibited approximately 48% degradation. Incorporating D-amino acids into the peptide sequence alters its spatial conformation, affecting the recognition of peptide by enzymes and, thereby, enhancing the proteolytic stability of the peptide gels. Images of both gels were taken at specific time intervals following the removal of the proteolytic mixture **(Figure A12, A13, Appendix)**.

The stability of the peptide conjugate (LPG) and NP-loaded peptide conjugate (NLG) gels was further assessed by examining their swelling and degradation profiles at neutral and slightly alkaline pH levels of 7 and 8.4 **(Figure 2.3H)**. Considering the pH of a chronic wound is typically alkaline (7.2−8.9), we focused on the stability of the gels under these conditions. Compared to the NLG gel (~45%), the LPG gel showed a greater degradation rate (~62%). The side chain amines on lysine and the cationic metal ions interact with the nanoparticles to improve the mechanical stability of the NLG. Additionally, less degradation was observed in NLG at alkaline pH 8.4 (~45%) compared to pH 7 (~61%). The positive charge on the peptide chains decreases as the pH becomes more alkaline, reducing repulsion between peptide chains and thus increasing the gel's stability.

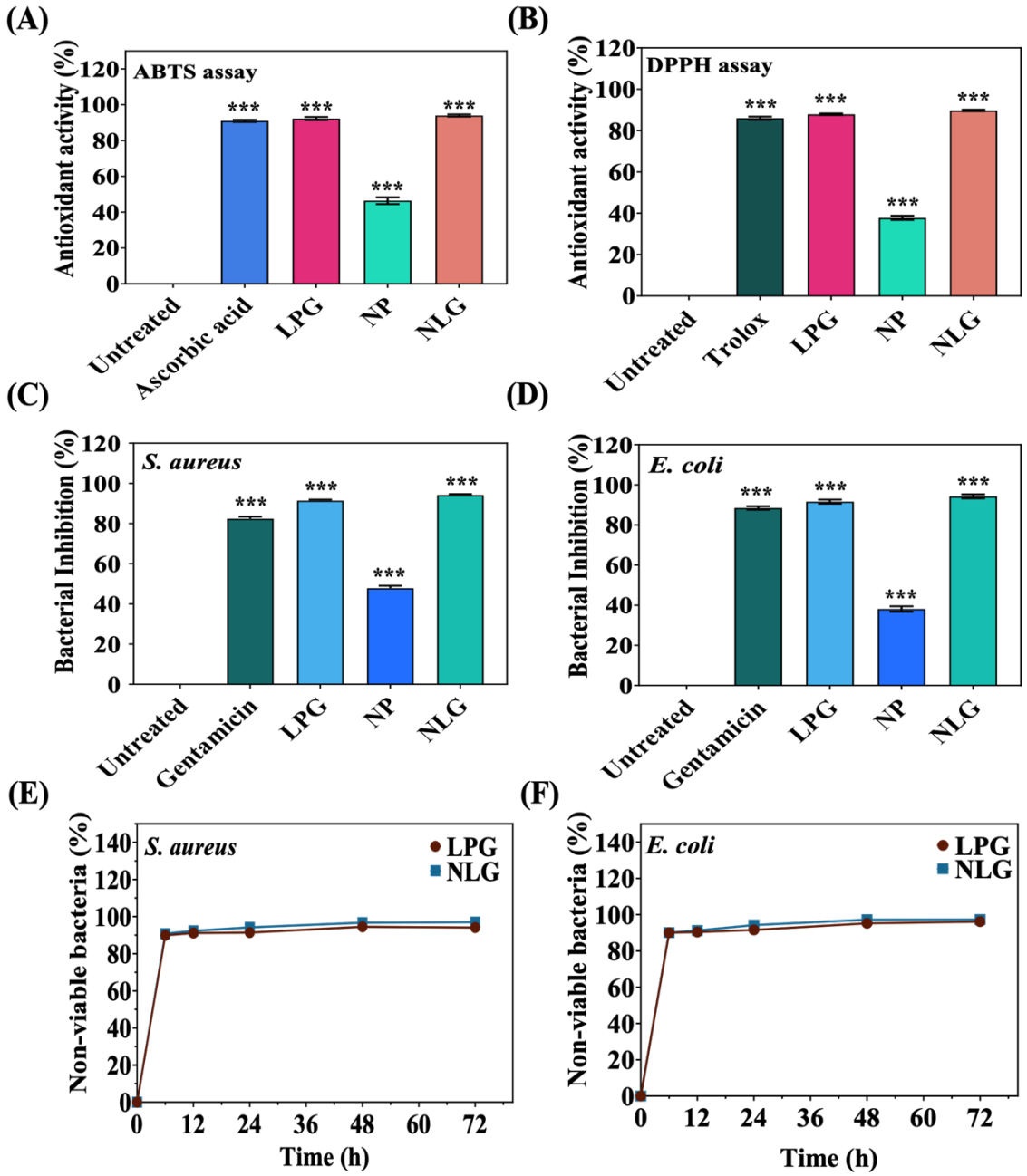

Figure 2.4. Evaluation of the antioxidant and antibacterial potential of NPs, LPG, and NLG. (A, B) Antioxidant activity. (A) ABTS assay. (B) DPPH assay. Ascorbic acid and trolox served as controls. (C, D) Percentage antibacterial activity estimation using OD_{600nm} method. (C) *S. aureus.* (D) *E. coli*. (E, F) Investigation of sustained antibacterial activities for up to 72 h. (E) *S. aureus.* (F) *E. coli*. The data is provided as mean ± standard deviation (n = 3), with P values of <0.05 (*), 0.01 (**), and 0.001 (***) indicating significant differences.

2.4.6. Antioxidant properties

Reactive oxygen species (ROS) serve as critical agents in host defense mechanisms during wound healing. They are released by phagocytic neutrophils and macrophages to combat bacterial infections by leveraging their reactive and damaging properties. However, excessive ROS activity damages the extracellular matrix (ECM) and its components, like growth factors

and proteins. It adversely affects the functionality of dermal fibroblasts and keratinocytes, causes cellular damage, and impedes the healing process. The prolonged presence of hydroxyl radicals ($OH^{\cdot}$), superoxide (O^{2-}), and hydrogen peroxide (H_2O_2) in high concentrations at the site of injury extends the inflammatory phase. These radicals must be neutralized for the healing to take place efficiently. The lone pair of electrons on the lysine side chains in NLG and LPG peptide chains shield the cells from damage by ROS and provide a protective mechanism.

DPPH and ABTS assays determined the antioxidant activity of the materials **(Figure 2.4A, B)**. The material demonstrated its effectiveness in the ABTS assay by reducing the $ABTS^{\cdot+}$ radical from a coloured to a colourless solution, with LPG and NPs serving as controls. The absorbance was measured at 415 nm. The NP-loaded gel (NLG) exhibited remarkable antioxidant activity, achieving 93.9% in 1 hour, whereas LPG and NPs showed 92% and 46% activity, respectively. The DPPH assay further affirmed the NLG's effectiveness, demonstrating around 89% activity, with the control LPG and NPs showing around 87% and 38% activity. In both assays, the efficacy of NLG stood on par with established positive controls, ascorbic acid for the ABTS and Trolox for the DPPH assay.

This study underscored the antioxidant potential of NP-loaded gel (NLG), highlighting its excellent radical scavenging capacity, surpassing that of previously reported materials in literature by Hao et al.,[41] Wei et al.,[55,] and Zhang et al.[56] Interestingly, the antioxidant activity of gels was largely unaffected by the addition of NPs, which had no discernible effect on the antioxidant activity of the gels.

2.4.7. Antibacterial activity

Optical density (OD_{600}) method was used to investigate the antibacterial potential of NP-loaded gel. The efficacy of material was assessed against Gram-positive (*S. aureus*) and Gram-negative (*E. coli*) bacterial strains (**Figure 2.4**). We compared the results with the gentamicin sulfate (50 μg/mL), while the untreated bacterial samples were used a negative control. The gels were fabricated as mentioned earlier and were further analyzed. The NP-loaded gel (NLG) exhibited a 94.2% antibacterial activity against both *E. coli* and *S. aureus* (**Figure 2.4C, D**). Remarkably, an approximate 90% level of antibacterial effectiveness was observed at just 6 hours of incubation for both bacterial strains, an effect that was sustained up to 72 hours (**Figure 2.4E, F**). These results align with the recent antibacterial materials reported by Atefyekta *et al*.[57] and Veiga[58] *et al*. An intriguing observation was that the LPG gel, lacking nanoparticles (NPs), still manifested over 90% antibacterial activity, underscoring the gel's inherent antimicrobial properties. While the nanoparticles alone showed a lesser degree of effectiveness, with under 50% activity against the both bacterial strains. The bactericidal properties of the gel can be attributed to its ability to interact with bacterial membranes, which are predominantly composed

of phospholipids and phosphatidylglycerol, containing negatively charged head groups. The basic functional groups within the peptide chains are drawn to these charges. The lysine residues with positively charged side chains demonstrate a strong attraction to the bacterial membrane. The integration of the lauric acid chain notably elevates the hydrophobic nature of the peptide chain. This increase in hydrophobicity significantly boosts the interaction of peptide with the lipid bilayer, thereby augmenting its antibacterial efficacy. Thus, peptide chain disrupts the integrity of the bacterial membrane, leading to a collapse of its potential and consequent cell death.[48] MIC_{90} is the minimum concentration capable of inhibiting at least 90% of the bacterial population. The determination of the minimum inhibitory concentration (MIC_{90}) for lauric acid-peptide conjugate (LPC) against *S. aureus* and *E. coli* was conducted through the standard dilution method. Luria broth was used to prepare samples at varying concentrations (2.5, 1.25, 0.625, 0.312, 0.156, 0.078, 0.039, 0.0195, 0.0097, 0.00485, and 0.00242 mg/mL), which were then incubated with the bacterial cultures at 37 °C for a duration of 24 hours. Utilizing a UV-visible spectrophotometer, the optical density (OD) was measured at 600 nm for both bacterial strains, which gave the MIC_{90} as 0.312 mg/mL (31.2 μg/100 μL) **(Figure A14, Appendix)**.

Live−Dead fluorescence imaging was further performed to demonstrate the antibacterial activity of NLG against *S. aureus* **(Figure 2.5A)** and *E. coli* **(Figure A15, Appendix)**. The method utilized SYTO 9 and propidium iodide (PI) dyes to co-stain the bacteria after being exposed to NP-loaded gel for a period of 24 hours. SYTO 9, which binds to both DNA and RNA regardless of the cell's membrane integrity, produces a green fluorescent signal indicating live cells. PI, which preferentially binds to the DNA of cells with compromised membrane integrity, emits a red fluorescence, signaling dead cells.[59] The observed fluorescence from the NLG-treated bacterial cells predominantly exhibited red, indicating a higher presence of dead cells in populations treated with the gel. In contrast, the control group of untreated bacterial cells displayed mainly green fluorescence, pointing towards a predominantly live cell population. Semi-quantitative analysis further validated these observations, with red and green fluorescence intensity measurements indicating that NLG treatment led to a substantial decrease in bacterial viability **(Figure 2.5B)**. We observed 3.2- and 0.15-time increase in red and green fluorescence, respectively, compared to the untreated control. This enhanced red fluorescence with the diminished presence of green fluorescence corroborate with the efficacious antibacterial activity of NLG, highlighting its potential as a therapeutic agent against bacterial infections.

The antibacterial efficacy of NLG gel on both Gram-positive and Gram-negative bacteria was mechanistically analyzed through HR-TEM analysis **(Figure 2.5C-N)**. Initial observations of bacteria cells in untreated conditions showed their typical spherical or rod-shaped structures, with the cell membrane and cytoplasm remaining unblemished. However, upon treatment with NLG, the bacterial cell membranes appeared ruptured, resulting in the expulsion of cytoplasmic content and, ultimately, cell death. This disruption of cell integrity was further substantiated

through a N-phenylnaphthylamine (NPN) uptake assay. The assay evidenced a marked increase in NPN fluorescence at 425 nm (λ_{em}) for NLG-treated *E. coli* (3.59-fold increase) and *S. aureus* (2.85-fold increase), compared to the control groups **(Figure 2.5O, P)**. NPN is known to exhibit enhanced fluorescence in phospholipid environments. However, under normal conditions, an intact outer cell membrane acts as a barrier to NPN entry. Therefore, the observed increase in fluorescence suggests that NLG gel facilitates NPN uptake by destabilizing and disrupting the bacterial membrane. This disruption is indicative of NLG gel compromising the membrane structure, providing direct evidence of its antibacterial mechanism through membrane perturbation.

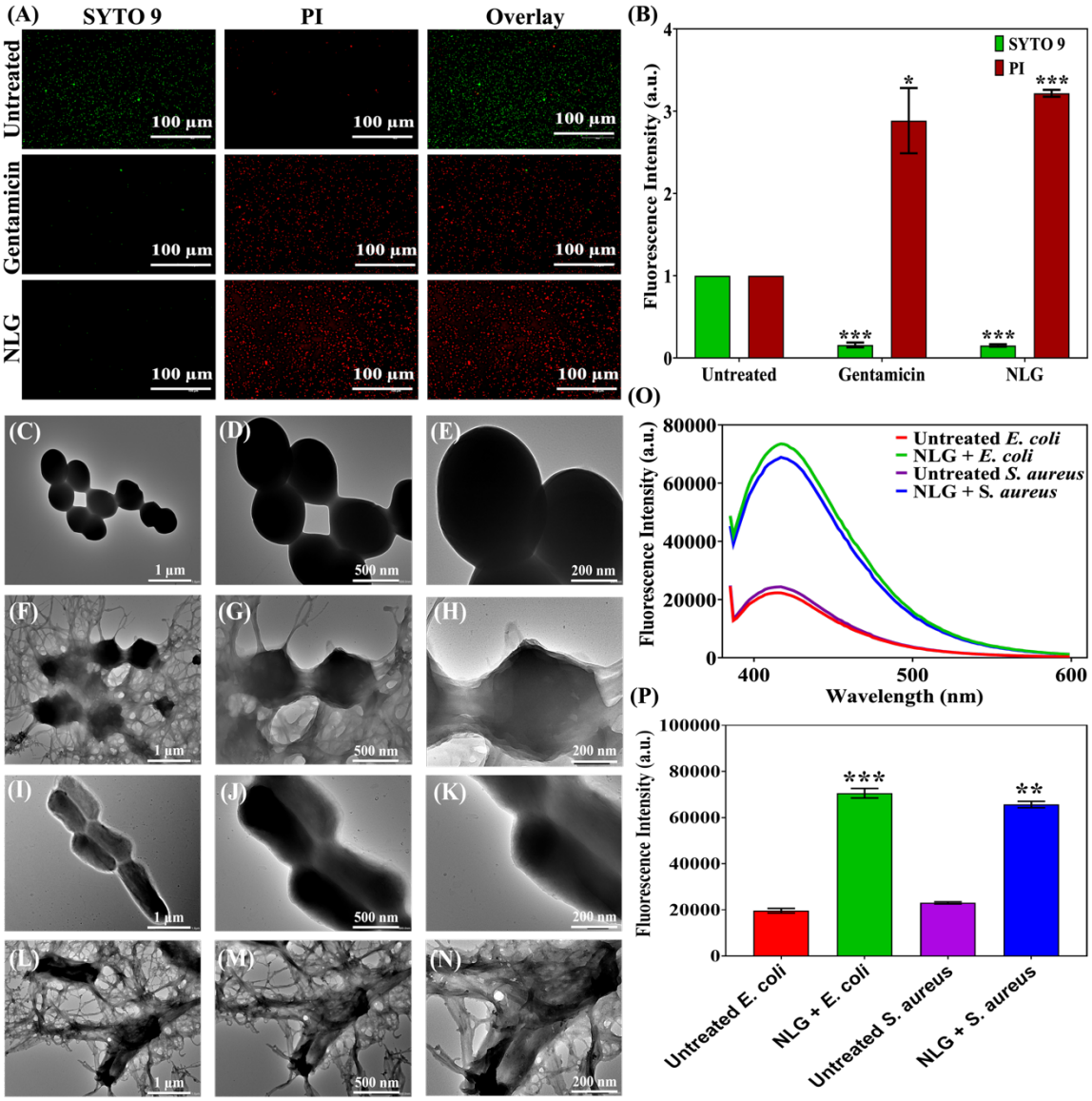

Figure 2.5. Bactericidal potential of NLG and its mechanistic investigation. (A) Live/dead fluorescence imaging of *S. aureus.* (B) Semiquantitative analysis of SYTO 9 and propidium iodide channels' fluorescence intensity. Gentamicin sulfate was used as a positive control for comparison and untreated bacterial samples served as a negative control. Scale bar: 100 µm. (C-

N) Mechanistic analysis with HR-TEM imaging and NPN assay. (C-E) HR-TEM images of untreated *S. aureus*. (F-H) NLG-treated *S. aureus*. (I-K) HR-TEM imaging of untreated *E. coli*. (L-N) NLG-treated *E. coli*. (O, P) NPN assay showing enhanced fluorescence at 425 nm (λ_{em}) in treated bacteria. The data is provided as mean ± standard deviation (n = 3), with P values of <0.05 (*), 0.01 (**), and 0.001 (***) indicating significant differences.

2.4.8. Cell viability studies

When employing biomaterials for wound healing applications, one of the most important things to consider is their biocompatibility. The MTT test was used to evaluate the cell viability of human umbilical vein endothelial cells (HUVECs) and the murine fibroblast cell line (L929) **(Figure 2.6)** on treatment with NP-loaded gel (NLG). The working concentration of NLG (330 µg/mL) **(Figure A16, Appendix)**. and the loading amount of Y_2O_3 nanoparticles **(Figure A17, Appendix)** was optimized by dose-dependent cell viability studies using MTT assay. The cell viability of L929 cells was investigated in the presence of peptide gel fabricated using Y_2O_3 nanoparticles dispersion ranging from 1-15 mM of concentration. The scaffolds showed no cytotoxicity to cells at lower concentration. We observed an effective proliferation in the presence of NLG extracts obtained from peptide gel fabricated using 5 mM concentration of Y_2O_3 nanoparticles. However, above 8 mM concentration, the cell viability reduced significantly. After being incubated with NLG gel (5 mM Y_2O_3) for 24 h, the cell viability of L929 cells was observed to be 151% **(Figure 2.6A)** compared to untreated cells. However, only 93.9% of the cells treated with gel without NPs were viable. After being incubated with NLG for 24 h, HUVECs showed 119.9% viability **(Figure 2.6B)**, whereas cells treated with gel without NPs (LPG) showed around 94% viabilities. In this study, the metabolic-based MTT assay revealed the increased viability in NLG-treated cells, which suggest enhanced cellular proliferation and metabolic activity due to the therapeutic effects of the peptide gel. However, to further validate these findings and address any concerns about potential stress responses that could influence MTT readings, we conducted live/dead fluorescence imaging as a complementary analysis. The live/dead assay provided additional confirmation of cell viability by allowing for the direct visual assessment of cell health.

Live-dead fluorescence assay evaluated the cytocompatibility of NLG **(Figure 2.6C, D)**. The assay involved incubating L929 and HUVEC cells with NLG and LPG for a 24-hour period, with untreated cells serving as the control group. Following the incubation, the cells were simultaneously stained with calcein AM and ethidium homodimer-1 red. Ethidium homodimer selectively marks the dead cells due to its inability to permeate live cell membranes, whereas calcein AM can penetrate live cells, producing a green fluorescence following ester hydrolysis by cellular esterases. Fluorescence microscopy revealed a predominance of green fluorescence

in both cell lines, indicating a majority of live and proliferating cells. These results obtained were consistent with the MTT assay and support our observations that NLG treatment fosters a favorable cell environment rather than inducing stress-related metabolic changes. Furthermore, these observations can be supported by the recent literature report where Y_2O_3 nanoparticles have been demonstrated to possess the ability to modify the redox environment, leading to the induction of transient hypoxic conditions.[35] This process stimulates the production of Hypoxia-Inducible Factor 1 (HIF-1), which subsequently enhance the expression of pro-angiogenic genes, including Vascular Endothelial Growth Factor (VEGF), Epidermal Growth Factor Receptor (EGFR), and Fibroblast Growth Factor 2 (FGF2), thereby facilitating cell proliferation.

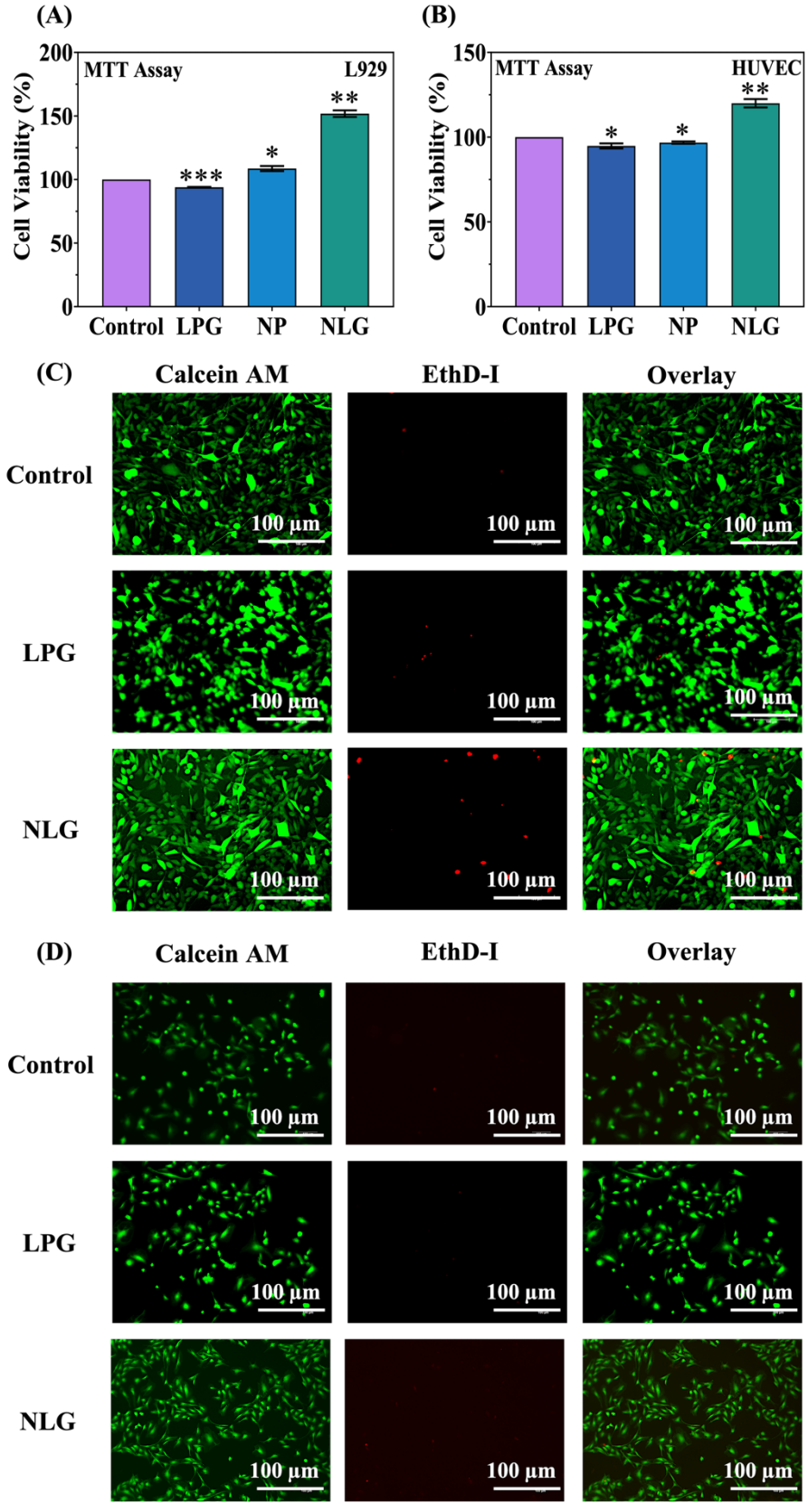

Figure 2.6. Cell viability analysis of LPG and NLG on murine fibroblast (L929) and human umbilical vein endothelial (HUVEC) cells on 24 h incubation. (A-B) MTT assay. (A) L929 cells. (B) HUVECs. (C-D) Live/dead assay. (C) L929 cells. (D) HUVECs. Untreated cells were

used as a control. Scale bar: 100 µm. The data is provided as mean ± standard deviation (n = 3), with P values of <0.05 (*), 0.01 (**), and 0.001 (***) indicating significant differences.

2.4.9. Scratch assay

Cell proliferation and migration are critical steps in wound healing, playing a significant role in tissue regeneration. To investigate the effects of NP-loaded gel (NLG) on wound closure, a scratch assay was performed on a monolayer of cells cultured in a 6-well plate. The scratch was created using a sterile tip, and both L929 and HUVEC cells were used in this study. Following the creation of the scratch, cells were given treatment with NLG and LPG, while a set of untreated cells served as the control group, **(Figure 2.7A, B).** Images were taken at regular intervals (0, 12, 24, and 48 hours) using a microscope to monitor the healing process. The analysis of the captured images indicated that cells treated with NLG exhibited a significantly faster rate of wound closure compared to both untreated cells and those treated with LPG **(Figure A18, Appendix)**. Notably, the L929 cells treated with NLG demonstrated complete wound healing within 24 hours, whereas it took approximately 48 hours for the wounds in HUVEC cells to heal. The extent of wound closure was quantitatively analyzed using ImageJ software, revealing that after 24 hours, only 8% of the scratch area in L929 cells remained unhealed following NLG treatment, in stark contrast to the 51% unhealed area observed in untreated cells **(Figure 2.7C)**. After 48 hours, the unhealed scratch area in HUVECs treated with NLG was reduced to just 10%, compared with 53% in the untreated HUVEC samples **(Figure 2.7D)**.

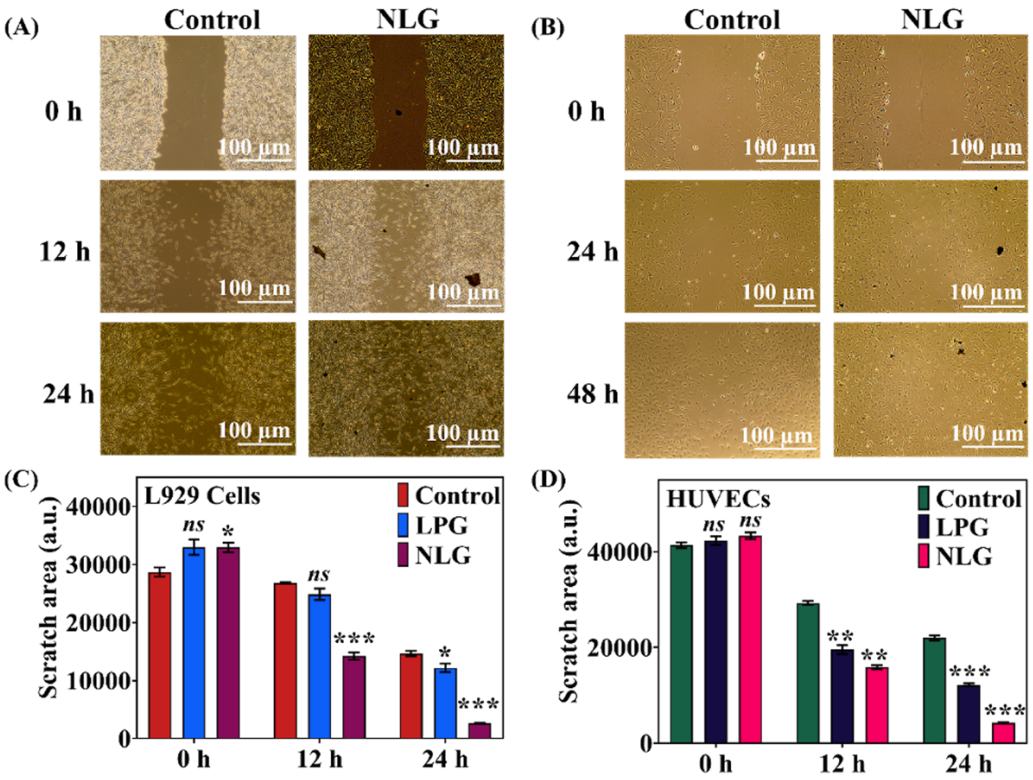

Figure 2.7. *In vitro* wound healing analysis on NLG-treated murine fibroblast cells (L929) and human umbilical vein endothelial cells (HUVEC) by scratch assay. (A-B) Microscopic images of scratch taken at 0, 12, 24, and 48 h. (A) L929 cells. (B) HUVECs. Scale bar: 100 µm. (C-D) Semiquantitative analysis of the unhealed scratch area. (C) L929. (D) HUVECs. Untreated samples were taken as a control. The data is provided as mean ± standard deviation (n = 3), with P values of <0.05 (*), 0.01 (**), and 0.001 (***) indicating significant differences.

2.4.10. Oxidative stress/ROS inhibition

The ability of NP-loaded gel (NLG) to confer protection against oxidative stress was investigated through the MTT assay on ROS-stressed L929 cells **(Figure 2.8A)**. Prior to NLG treatment, H_2O_2 was used to generate oxidative stress in cells. Cells with no induced oxidative stress were used as a negative control, while the cells incubated with H_2O_2 alone were taken as a positive control. Remarkably, cell viability was around 108% following a 24-hour incubation with NLG, which showed the ability of the gel to shield the cells from damage by reactive oxygen species. Further, the ROS-scavenging ability of NLG in cells treated with H_2O_2 was analyzed by DCFDA-based fluorescence assay **(Figure 2.8B)**. This assay elucidates the transformation of cell-permeant H_2DCFDA into 2′,7′-dichlorodihydrofluorescein (H_2DCF) through deacetylation by cellular esterases, which upon interaction with ROS, rapidly changes into the highly fluorescent 2′,7′- dichlorofluorescein (DCF),[60] as illustrated by the predominance of green fluorescence in H_2O_2-treated cells. However, a significant dip in green fluorescence was observed in the cells treated with the NP-loaded gel (NLG), signifying a reduction in ROS levels. These results align strongly with the earlier antioxidant studies performed with ABTS and DPPH assays.

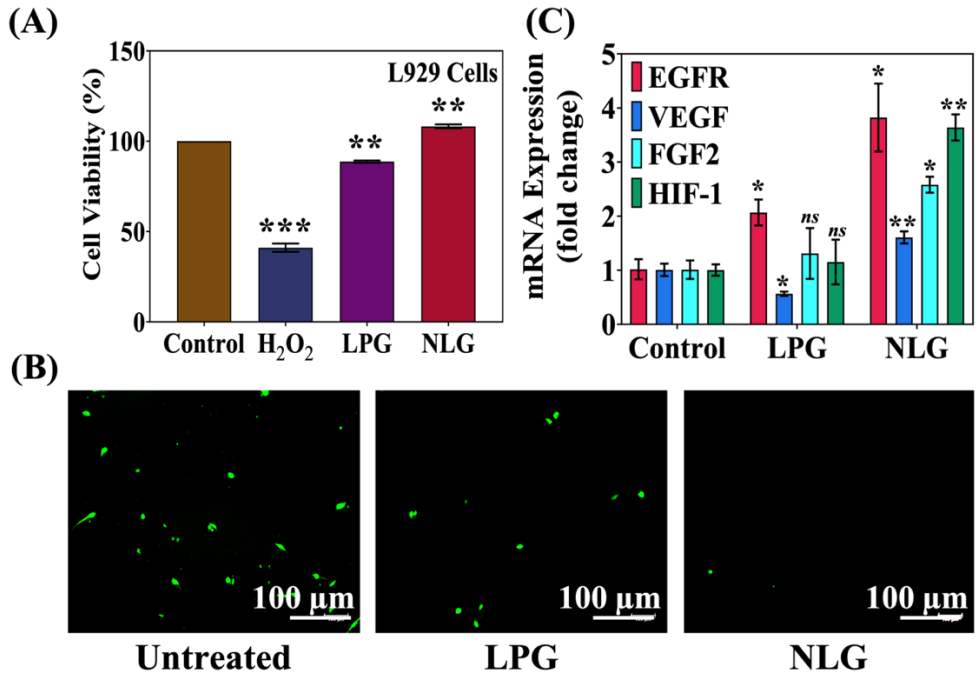

Figure 2.8. ROS-scavenging and gene expression analysis on NLG-treated cells (A) Cell viability assessment of ROS-induced cells on NLG treatment. (B) Evaluation of ROS-scavenging potential of NLG by DCFDA-based fluorescence assay on L929 cells. Scale bar: 100 μm. (C) qRT-PCR analysis determining the expression of EGFR, VEGF, FGF-2, and HIF-1 genes in HUVECs. The data is provided as mean ± standard deviation (n = 3), with P values of <0.05 (*), 0.01 (**), and 0.001 (***) indicating significant differences.

2.4.11. Angiogenesis

A key characteristic of non-healing chronic wounds is a diminished ability to rebuild the microvasculature by the process of angiogenesis. The growth of new blood vessels is essential for the development of granulation tissue as it facilitates the delivery of cells, nutrients, and oxygen to the site of the injury. The proangiogenic potential of NP-loaded peptide gel (NLG) was investigated by *in vitro* angiogenesis assay on human umbilical vein endothelial cells (HUVECs) (**Figure 2.9).** As demonstrated in Figure 2.9, after a 24-hour culture period with NLG, human umbilical vein endothelial cells (HUVECs) were subjected to staining with calcein AM and ethidium homodimer-I. Subsequent microscopic observation revealed the formation of dense, network-like structures. These findings are consistent with the observations documented by Hauser *et al*.[47] regarding the angiogenic hydrogel (IVFK). Furthermore, in comparison to cells treated with LPG hydrogel and untreated cells, the NLG exhibited a statistically significant increase in the number of nodes, junctions, and tube lengths, which were quantitatively assessed using the angiogenesis analyzer tool within ImageJ software. The ability of Y_2O_3 nanoparticles to induce the transient hypoxia upregulate the expression of various proangiogenic genes and promote the angiogenesis.

2.4.12. Gene expression analysis

Gene expression of various proangiogenic genes, like VEGF, FGF2, EGFR and HIF-1 were investigated by qRT-PCR analysis to understand the underlying mechanism for enhanced cell migration, proliferation, and angiogenesis **(primer sequences listed in Table 1, Appendix**). VEGF and FGF2 are well-reported to be critically involved in stimulating angiogenesis and can be activated in response to hypoxic conditions. Similarly, EGFR is known to play a pivotal role in cell migration and proliferation, and recent literature suggests that hypoxia-induced activation of HIF-1 may lead to elevated expressions of EGFR, VEGF, and FGF2. Notably, cerium oxide nanoparticles have been reported to induce transient hypoxia, resulting in the upregulation of these proangiogenic genes.[34,61,62] Owing to their similar properties, Yttrium Oxide (Y_2O_3) nanoparticles were hypothesized to embody a parallel mechanism. The results unveiled that a 24 h incubation of HUVECs with nanoparticle (NP)-embedded gel (NLG) significantly amplified the expression levels of VEGF, FGF2, EGFR, and HIF-1, achieving expression folds of 1.6, 2.58, 3.8, and 3.63 respectively **(Figure 2.8C).** While the cells treated with LPG (without nanoparticles), did not exhibit a statistically significant upregulation in these proangiogenic

genes. Thus, the augmented cell proliferation, migration, and angiogenesis observed in Y_2O_3-containing scaffolds, as compared to the control scaffolds, is ascribed to the enhanced expression of these key proangiogenic genes.

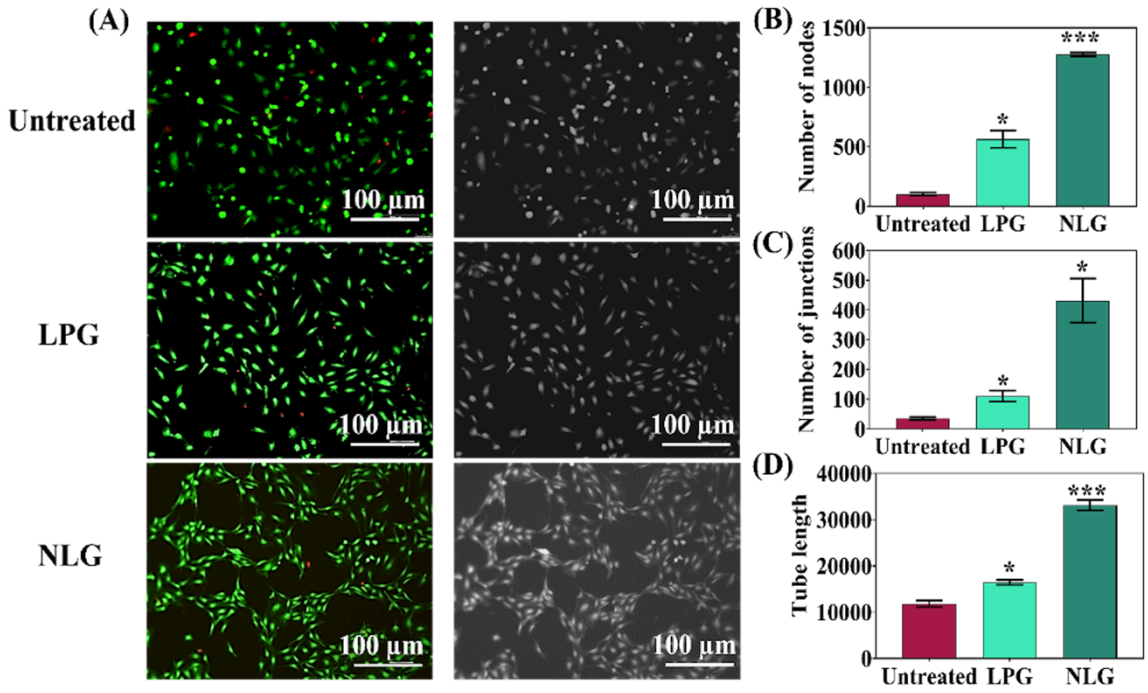

Figure 2.9. In vitro angiogenesis assay on LPG and NLG-treated HUVECs. (A) Fluorescence and bright field images of HUVECs on incubation with LPG and NLG for 24 h. Untreated cells were taken as a control. Scale bar: 100 µm. (B-D) Quantitative analysis of number of nodes, junctions, and tube length by using angiogenesis analyzer in ImageJ software. The data is provided as mean ± standard deviation (n = 3), with P values of <0.05 (*), 0.01 (**), and 0.001 (***) indicating significant differences.

2.5. Conclusions

Chronic wound healing is a multifaceted challenge and presents various complications like persistent inflammation, infection, growth factor degradation, impaired angiogenesis and healing. Thus, it requires a comprehensive approach targeting diverse impediments to the healing process. Therefore, we developed a multifunctional peptide-based gel, lauric acid-^{L}Lys-^{D}Phe-^{L}Lys-NH_2 loaded with Y_2O_3 nanoparticles. The material exhibited antibacterial, ROS-scavenging, cell proliferative and angiogenic properties without the need for exogenously supplied drugs and growth factors. This approach will address the challenges associated with the side effects of drugs and rise of antibiotic resistant bacterial strains. Since, we used nanoparticles with angiogenic ability, the concerns regarding the degradation and biostability of growth factors and proteins were also addressed. With the significant ROS scavenging potential, the material can reduce the oxidative stress and minimize the inflammatory responses.

Moreover, the gel provided a three-dimensional matrix for providing a conducive environment for cell migration and proliferation, which promotes the wound healing. Overall, our multifunctional peptide gel, with its antibacterial, anti-inflammatory, and angiogenic properties, offers a potential therapeutic approach for chronic wound healing by targeting several key challenges commonly encountered in chronic wounds. Following the establishment of its efficacy in *in vivo* animal models and subsequent clinical trials, this multifunctional peptide gel can be utilized as a primary dressing for chronic wound management. Upon application at the wound site, it would deliver localized antibacterial, anti-inflammatory, and pro-angiogenic effects, thus, addressing critical factors that impede healing in chronic wounds. As observed in the stability studies, the gel demonstrated only 45% degradation even after 24 h at alkaline pH 8.4. This controlled biodegradation of gel is likely to facilitate sustained therapeutic action while minimizing the need for frequent dressing changes or removal. Once validated in clinical settings, this peptide gel can be incorporated into standard wound care protocols, either as a standalone treatment or in combination with adjunctive therapies, to enhance the healing process in chronic wound environments. The intrinsic wound-healing potential of the peptide-based scaffold developed in this work aligns with our thesis objective for a drug- and growth factor-free approach. The third chapter explored this concept further by focusing on addressing the impaired angiogenesis in diabetic wounds using inherently angiogenic cyclic-peptide nanotubes.

References

(1) Saghazadeh, S.; Rinoldi, C.; Schot, M.; Kashaf, S. S.; Sharifi, F.; Jalilian, E.; Nuutila, K.; Giatsidis, G.; Mostafalu, P.; Derakhshandeh, H.; Yue, K.; Swieszkowski, W.; Memic, A.; Tamayol, A.; Khademhosseini, A. Drug Delivery Systems and Materials for Wound Healing Applications. *Advanced Drug Delivery Reviews* **2018**, *127*, 138–166.

(2) Bettle, G.; Bell, D. P.; Bakewell, S. J. A Novel Comprehensive Therapeutic Approach to the Challenges of Chronic Wounds: A Brief Review and Clinical Experience Report. *Adv Ther* **2024,** *41*, 492-508.

(3) Frykberg, R. G.; Banks, J. Challenges in the Treatment of Chronic Wounds. *Advances in Wound Care* **2015**, *4* (9), 560–582.

(4) Edmonds, M.; Manu, C.; Vas, P. The Current Burden of Diabetic Foot Disease. *Journal of Clinical Orthopaedics and Trauma* **2021**, *17*, 88–93.

(5) Abbade, L. P. F.; Lastória, S. Venous Ulcer: Epidemiology, Physiopathology, Diagnosis and Treatment. *Int J Dermatology* **2005**, *44* (6), 449–456.

(6) Kolluri, R.; Lugli, M.; Villalba, L.; Varcoe, R.; Maleti, O.; Gallardo, F.; Black, S.; Forgues, F.; Lichtenberg, M.; Hinahara, J.; Ramakrishnan, S.; Beckman, J. A. An Estimate of the Economic Burden of Venous Leg Ulcers Associated with Deep Venous Disease. *Vasc Med* **2022**, *27* (1), 63–72.

(7) Agale, S. V. Chronic Leg Ulcers: Epidemiology, Aetiopathogenesis, and Management. *Ulcers* **2013**, *413604*, 1–9.

(8) Price, L. B.; Liu, C. M.; Frankel, Y. M.; Melendez, J. H.; Aziz, M.; Buchhagen, J.; Contente-Cuomo, T.; Engelthaler, D. M.; Keim, P. S.; Ravel, J.; Lazarus, G. S.; Zenilman, J. M. Macroscale Spatial Variation in Chronic Wound Microbiota: A Cross-sectional Study. *Wound Repair Regeneration* **2011**, *19* (1), 80–88.

(9) Munita, J. M.; Arias, C. A. Mechanisms of Antibiotic Resistance. *Microbiol Spectr* **2016**, *4* (2), 10.1128.

(10) Darvishi, S.; Tavakoli, S.; Kharaziha, M.; Girault, H. H.; Kaminski, C. F.; Mela, I. Advances in the Sensing and Treatment of Wound Biofilms. *Angew Chem Int Ed* **2022**, *61* (13), e202112218.

(11) Auf Dem Keller, U.; Sabino, F. Matrix Metalloproteinases in Impaired Wound Healing. *Metalloproteinases In Medicine.* **2015**, *2*, 1-8.

(12) Dart, A.; Bhave, M.; Kingshott, P. Antimicrobial Peptide-Based Electrospun Fibers for Wound Healing Applications. *Macromolecular Bioscience* **2019**, *19* (9), 1800488.

(13) Zhong, Y.; Wei, E.; Wu, L.; Wang, Y.; Lin, Q.; Wu, N.; Chen, H.; Tang, N. Novel Biomaterials for Wound Healing and Tissue Regeneration. *ACS Omega* **2024,** *9*(30), 32268–32286.

(14) Radhakumary, C.; Antonty, M.; Sreenivasan, K. Drug Loaded Thermoresponsive and Cytocompatible Chitosan Based Hydrogel as a Potential Wound Dressing. *Carbohydrate Polymers* **2011**, *83* (2), 705–713.

(15) Huan, Y.; Kong, Q.; Tang, Q.; Wang, Y.; Mou, H.; Ying, R.; Li, C. Antimicrobial Peptides/Ciprofloxacin-Loaded O-Carboxymethyl Chitosan/Self-Assembling Peptides Hydrogel Dressing with Sustained-Release Effect for Enhanced Anti-Bacterial Infection and Wound Healing. *Carbohydrate Polymers* **2022**, *280*, 119033.

(16) Wang, Y.; Wu, Y.; Long, L.; Yang, L.; Fu, D.; Hu, C.; Kong, Q.; Wang, Y. Inflammation-Responsive Drug-Loaded Hydrogels with Sequential Hemostasis, Antibacterial, and Anti-Inflammatory Behavior for Chronically Infected Diabetic Wound Treatment. *ACS Appl. Mater. Interfaces* **2021**, *13* (28), 33584–33599.

(17) Zhong, H.; Fang, Y.; Luo, M.; Wang, L.; Huang, J.; Dai, G.; Liu, K.; Wu, J.; Du, J. Deferoxamine-Loaded Injectable Chitosan-Grafted Chlorogenic Acid/Oxidized Hyaluronic Acid Hybrid Hydrogel with Antibacterial, Anti-Inflammatory, and Angiogenesis-Promoting Properties for Diabetic Wound Repair. *ACS Appl. Mater. Interfaces* **2024**, *16* (22), 28209–28221.

(18) Yu, Y.; Chen, J.; Chen, R.; Cao, L.; Tang, W.; Lin, D.; Wang, J.; Liu, C. Enhancement of VEGF-Mediated Angiogenesis by 2- *N* ,6- *O* -Sulfated Chitosan-Coated Hierarchical PLGA Scaffolds. *ACS Appl. Mater. Interfaces* **2015**, *7* (18), 9982–9990.

(19) Vijayan, A.; A., S.; Kumar, G. S. V. PEG Grafted Chitosan Scaffold for Dual Growth Factor Delivery for Enhanced Wound Healing. *Sci Rep* **2019**, *9* (1), 19165.

(20) Jin, N.; Wu, J.; Ye, S.; Xue, J.; Meng, T.; Hu, L.; Jiang, S.; Xu, H.; Yu, Y.; Hu, D.; Zhang, G. Injectable Dynamic ROS-Responsive COF-Modified Microalgae Gels for In Vivo bFGF Delivery to Treat Diabetic Wounds. *ACS Appl. Mater. Interfaces* **2024**, *16* (15), 18608–18626.

(21) Fu, J.; Zhang, Y.; Chu, J.; Wang, X.; Yan, W.; Zhang, Q.; Liu, H. Reduced Graphene Oxide Incorporated Acellular Dermal Composite Scaffold Enables Efficient Local Delivery of Mesenchymal Stem Cells for Accelerating Diabetic Wound Healing. *ACS Biomater. Sci. Eng.* **2019**, *5* (8), 4054–4066.

(22) Romano Di Peppe, S.; Mangoni, A.; Zambruno, G.; Spinetti, G.; Melillo, G.; Napolitano, M.; Capogrossi, M. C. Adenovirus-Mediated VEGF165 Gene Transfer Enhances Wound Healing by Promoting Angiogenesis in CD1 Diabetic Mice. *Gene Ther* **2002**, *9* (19), 1271–1277.

(23) Raghavan, J. V.; Dorai, V. K.; Sagar, S. K.; Sivaraman, A.; R, K. S.; Jhunjhunwala, S. Immunomodulatory Bandage for Accelerated Healing of Diabetic Wounds. *ACS Bio Med Chem Au* **2022**, *2* (4), 409–418.

(24) Teguh, D. N.; Bol Raap, R.; Koole, A.; Knippenberg, B.; Smit, C.; Oomen, J.; Van Hulst, R. A. Hyperbaric Oxygen Therapy for Nonhealing Wounds: Treatment Results of a Single Center. *Wound Repair Regeneration* **2021**, *29* (2), 254–260.

(25) Zheng, S.-Y.; Wan, X.-X.; Kambey, P. A.; Luo, Y.; Hu, X.-M.; Liu, Y.-F.; Shan, J.-Q.; Chen, Y.-W.; Xiong, K. Therapeutic Role of Growth Factors in Treating Diabetic Wound. *World J Diabetes* **2023**, *14* (4), 364–395.

(26) Heyboer, M.; Sharma, D.; Santiago, W.; McCulloch, N. Hyperbaric Oxygen Therapy: Side Effects Defined and Quantified. *Advances in Wound Care* **2017**, *6* (6), 210–224.

(27) Branski, L. K.; Pereira, C. T.; Herndon, D. N.; Jeschke, M. G. Gene Therapy in Wound Healing: Present Status and Future Directions. *Gene Ther* **2007**, *14* (1), 1–10.

(28) Gao, S.; Zhang, W.; Zhai, X.; Zhao, X.; Wang, J.; Weng, J.; Li, J.; Chen, X. An Antibacterial and Proangiogenic Double-Layer Drug-Loaded Microneedle Patch for Accelerating Diabetic Wound Healing. *Biomater. Sci.* **2023**, *11* (2), 533–541.

(29) Hu, C.; Zhang, F.; Long, L.; Kong, Q.; Luo, R.; Wang, Y. Dual-Responsive Injectable Hydrogels Encapsulating Drug-Loaded Micelles for on-Demand Antimicrobial Activity and Accelerated Wound Healing. *Journal of Controlled Release* **2020**, *324*, 204–217.

(30) Xie, Z.; Paras, C. B.; Weng, H.; Punnakitikashem, P.; Su, L.-C.; Vu, K.; Tang, L.; Yang, J.; Nguyen, K. T. Dual Growth Factor Releasing Multi-Functional Nanofibers for Wound Healing. *Acta Biomaterialia* **2013**, *9* (12), 9351–9359.

(31) Guan, T.; Li, J.; Chen, C.; Liu, Y. Self-Assembling Peptide-Based Hydrogels for Wound Tissue Repair. *Advanced Science* **2022**, *9* (10), 2104165.

(32) Loo, Y.; Goktas, M.; Tekinay, A. B.; Guler, M. O.; Hauser, C. A. E.; Mitraki, A. Self-Assembled Proteins and Peptides as Scaffolds for Tissue Regeneration. *Adv Healthcare Materials* **2015**, *4* (16), 2557–2586.

(33) Koutsopoulos, S. Self-assembling Peptide Nanofiber Hydrogels in Tissue Engineering and Regenerative Medicine: Progress, Design Guidelines, and Applications. *J Biomedical Materials Res* **2016**, *104* (4), 1002–1016.

(34) Das, S.; Singh, S.; Dowding, J. M.; Oommen, S.; Kumar, A.; Sayle, T. X. T.; Saraf, S.; Patra, C. R.; Vlahakis, N. E.; Sayle, D. C.; Self, W. T.; Seal, S. The Induction of Angiogenesis by Cerium Oxide Nanoparticles through the Modulation of Oxygen in Intracellular Environments. *Biomaterials* **2012**, *33* (31), 7746–7755.

(35) Augustine, R.; Dalvi, Y. B.; Yadu Nath, V. K.; Varghese, R.; Raghuveeran, V.; Hasan, A.; Thomas, S.; Sandhyarani, N. Yttrium Oxide Nanoparticle Loaded Scaffolds with Enhanced Cell Adhesion and Vascularization for Tissue Engineering Applications. *Materials Science and Engineering: C* **2019**, *103*, 109801.

(36) Mellado-Vázquez, R.; García-Hernández, M.; López-Marure, A.; López-Camacho, P.; De Jesús Morales-Ramírez, Á.; Beltrán-Conde, H. Sol-Gel Synthesis and Antioxidant

Properties of Yttrium Oxide Nanocrystallites Incorporating P-123. *Materials* **2014**, *7* (9), 6768–6778.

(37) Baral, A.; Roy, S.; Ghosh, S.; Hermida-Merino, D.; Hamley, I. W.; Banerjee, A. A Peptide-Based Mechano-Sensitive, Proteolytically Stable Hydrogel with Remarkable Antibacterial Properties. *Langmuir* **2016**, *32* (7), 1836–1845.

(38) Asante, V.; Mortier, J.; Wolber, G.; Koksch, B. Impact of Fluorination on Proteolytic Stability of Peptides: A Case Study with α-Chymotrypsin and Pepsin. *Amino Acids* **2014**, *46* (12), 2733–2744.

(39) Huang, R.; Qi, W.; Feng, L.; Su, R.; He, Z. Self-Assembling Peptide–Polysaccharide Hybrid Hydrogel as a Potential Carrier for Drug Delivery. *Soft Matter* **2011**, *7* (13), 6222.

(40) Zheng, L.; Zhao, M.; Xiao, C.; Zhao, Q.; Su, G. Practical Problems When Using ABTS Assay to Assess the Radical-Scavenging Activity of Peptides: Importance of Controlling Reaction pH and Time. *Food Chemistry* **2016**, *192*, 288–294.

(41) Hao, T.; Li, J.; Yao, F.; Dong, D.; Wang, Y.; Yang, B.; Wang, C. Injectable Fullerenol/Alginate Hydrogel for Suppression of Oxidative Stress Damage in Brown Adipose-Derived Stem Cells and Cardiac Repair. *ACS Nano* **2017**, *11* (6), 5474–5488.

(42) Salick, D. A.; Kretsinger, J. K.; Pochan, D. J.; Schneider, J. P. Inherent Antibacterial Activity of a Peptide-Based β-Hairpin Hydrogel. *J. Am. Chem. Soc.* **2007**, *129* (47), 14793–14799.

(43) Gahane, A. Y.; Ranjan, P.; Singh, V.; Sharma, R. K.; Sinha, N.; Sharma, M.; Chaudhry, R.; Thakur, A. K. Fmoc-Phenylalanine Displays Antibacterial Activity against Gram-Positive Bacteria in Gel and Solution Phases. *Soft Matter* **2018**, *14* (12), 2234–2244.

(44) Zhang, F.; Hu, C.; Kong, Q.; Luo, R.; Wang, Y. Peptide-/Drug-Directed Self-Assembly of Hybrid Polyurethane Hydrogels for Wound Healing. *ACS Appl. Mater. Interfaces* **2019**, *11* (40), 37147–37155.

(45) Li, Y.; Sun, M.; Liu, Y.; Liang, J.; Wang, T.; Zhang, Z. Gymnemic Acid Alleviates Type 2 Diabetes Mellitus and Suppresses Endoplasmic Reticulum Stress *in Vivo* and *in Vitro*. *J. Agric. Food Chem.* **2019**, *67* (13), 3662–3669.

(46) Liang, C.-C.; Park, A. Y.; Guan, J.-L. In Vitro Scratch Assay: A Convenient and Inexpensive Method for Analysis of Cell Migration in Vitro. *Nat Protoc* **2007**, *2* (2), 329–333.

(47) Alshehri, S.; Susapto, H. H.; Hauser, C. A. E. Scaffolds from Self-Assembling Tetrapeptides Support 3D Spreading, Osteogenic Differentiation, and Angiogenesis of Mesenchymal Stem Cells. *Biomacromolecules* **2021**, *22* (5), 2094–2106.

(48) Li, J.; Koh, J.-J.; Liu, S.; Lakshminarayanan, R.; Verma, C. S.; Beuerman, R. W. Membrane Active Antimicrobial Peptides: Translating Mechanistic Insights to Design. *Front. Neurosci.* **2017**, *11*, 73.

(49) Xu, N.; Chen, G.; Liu, H. Antioxidative Categorization of Twenty Amino Acids Based on Experimental Evaluation. *Molecules* **2017**, *22* (12), 2066.

(50) Yang, S.; Wang, M.; Wang, T.; Sun, M.; Huang, H.; Shi, X.; Duan, S.; Wu, Y.; Zhu, J.; Liu, F. Self-Assembled Short Peptides: Recent Advances and Strategies for Potential Pharmaceutical Applications. *Materials Today Bio* **2023**, *20*, 100644.

(51) Bagińska, K.; Makowska, J.; Wiczk, W.; Kasprzykowski, F.; ChmurzyńSKI, L. Conformational Studies of Alanine-rich Peptide Using CD and FTIR Spectroscopy. *Journal of Peptide Science* **2008**, *14* (3), 283–289.

(52) Maia, L. F.; Soares, M. R.; Valente, A. P.; Almeida, F. C. L.; Oliveira, A. C.; Gomes, A. M. O.; Freitas, M. S.; Schneemann, A.; Johnson, J. E.; Silva, J. L. Structure of a Membrane-Binding Domain from a Non-Enveloped Animal Virus. *Journal of Biological Chemistry* **2006**, *281* (39), 29278–29286.

(53) Ahmad, S.; Faizan, M.; Ahmad, S.; Ikram, M. Synthesis and Characterization of Y2O3 Nano-Material: An Experimental and Theoretical Study; Mumbai, India, 2018; p 050013.

(54) Lin, L.; Starostin, S. A.; Li, S.; Khan, S. A.; Hessel, V. Synthesis of Yttrium Oxide Nanoparticles via a Facile Microplasma-Assisted Process. *Chemical Engineering Science* **2018**, *178*, 157–166.

(55) Wei, Q.; Duan, J.; Ma, G.; Zhang, W.; Wang, Q.; Hu, Z. Enzymatic Crosslinking to Fabricate Antioxidant Peptide-Based Supramolecular Hydrogel for Improving Cutaneous Wound Healing. *J. Mater. Chem. B* **2019**, *7* (13), 2220–2225.

(56) Zhang, S.; Hou, J.; Yuan, Q.; Xin, P.; Cheng, H.; Gu, Z.; Wu, J. Arginine Derivatives Assist Dopamine-Hyaluronic Acid Hybrid Hydrogels to Have Enhanced Antioxidant Activity for Wound Healing. *Chemical Engineering Journal* **2020**, *392*, 123775.

(57) Atefyekta, S.; Blomstrand, E.; Rajasekharan, A. K.; Svensson, S.; Trobos, M.; Hong, J.; Webster, T. J.; Thomsen, P.; Andersson, M. Antimicrobial Peptide-Functionalized Mesoporous Hydrogels. *ACS Biomater. Sci. Eng.* **2021**, *7* (4), 1693–1702.

(58) Veiga, A. S.; Sinthuvanich, C.; Gaspar, D.; Franquelim, H. G.; Castanho, M. A. R. B.; Schneider, J. P. Arginine-Rich Self-Assembling Peptides as Potent Antibacterial Gels. *Biomaterials* **2012**, *33* (35), 8907–8916.

(59) Rosenberg, M.; Azevedo, N. F.; Ivask, A. Propidium Iodide Staining Underestimates Viability of Adherent Bacterial Cells. *Sci Rep* **2019**, *9* (1), 6483.

(60) Tian, Y.-Y.; An, L.-J.; Jiang, L.; Duan, Y.-L.; Chen, J.; Jiang, B. Catalpol Protects Dopaminergic Neurons from LPS-Induced Neurotoxicity in Mesencephalic Neuron-Glia Cultures. *Life Sciences* **2006**, *80* (3), 193–199.

(61) Nethi, S. K.; Nanda, H. S.; Steele, T. W. J.; Patra, C. R. Functionalized Nanoceria Exhibit Improved Angiogenic Properties. *J. Mater. Chem. B* **2017**, *5* (47), 9371–9383.

(62) Augustine, R.; Dalvi, Y. B.; Dan, P.; George, N.; Helle, D.; Varghese, R.; Thomas, S.; Menu, P.; Sandhyarani, N. Nanoceria Can Act as the Cues for Angiogenesis in Tissue-Engineering Scaffolds: Toward Next-Generation in Situ Tissue Engineering. *ACS Biomater. Sci. Eng.* **2018**, *4* (12), 4338–4353.

CHAPTER - 3

Proangiogenic Cyclic Peptide Nanotubes for Diabetic Wound Healing

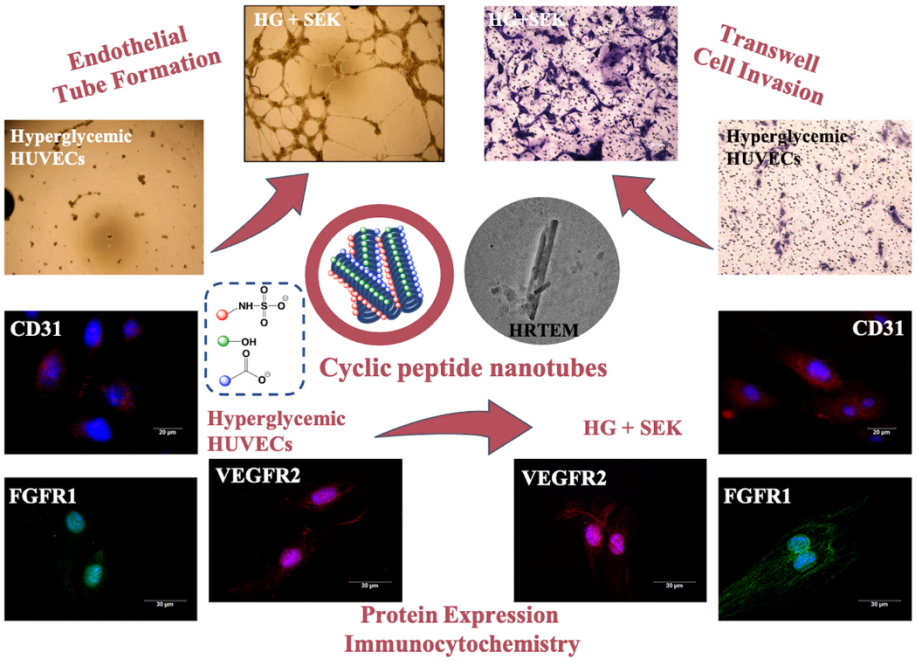

ToC graphic

Chapter 3

Cyclic peptide nanotubes for angiogenesis in diabetic wounds

3.1. Introduction

3.1.1. Diabetic wounds

Diabetes mellitus is a significant chronic metabolic disorder characterized by decline in the body's ability to metabolize glucose. According to the World Health Organization (WHO), there are 422 million individuals suffering from diabetes worldwide, accounting for 8.5% of the global population.[1] Type 2 diabetes, in particular, carries major global consequences, and it includes an annual financial burden exceeding 760 billion dollars. These statistics represents approximately 10% of the total annual healthcare budget designated for adults. The anticipated prevalence of diabetes is set to soar, with projections estimating over 700 million individuals affected by 2045. The year 2019 witnessed over 4 million fatalities attributed to diabetes-related complications, underscoring the gravity of the situation, with the global incidence of diabetes pegged at 9.3% for the same year. Given these dynamics, diabetes emerges as a critical global health challenge.[2,3] Impaired wound healing is a major concern in patients with diabetic hyperglycemia, which often suffers with high mortality, morbidity, and recurrence. Moreover, it is a leading cause of nontraumatic limb amputations worldwide. The prevalence of foot ulcers in patients with diabetes ranges from 19% to 34% over their lifetime, and approximately 20% of these cases result in some form of amputation.[4] Diabetic wound healing is influenced by over 100 known pathophysiological factors including high blood glucose levels (hyperglycemia), elevated oxidative stress, impaired growth factor production, poor angiogenic response, enhanced activity of proteases, nerve damage (neuropathy), microvascular complications like peripheral arterial disease and reduced oxygen supply (hypoxia), as well as complications with skin barrier and infections.[4,5]

3.1.2. Challenges

Normal wound healing is orchestrated through four critical phases: hemostasis, inflammation, proliferation, and remodeling. In contrast, wound healing in diabetic individuals is hindered due to dysfunctions occurring across all these stages, often precluding these wounds from achieving complete repair.[6,7] The pathogenesis of chronic, non-healing wounds in diabetic patients is multifaceted but can be largely attributed to inadequate vascular networking.[8] A critical factor in this disrupted healing process is angiogenesis, which is the development of new blood vessels from pre-existing structures, ensuring sufficient blood flow, nutrition and oxygenation for tissue growth and repair.[9] Angiogenesis involves a complex interplay between endothelial cells, macrophages, fibroblasts, and the surrounding extracellular matrix (ECM).[10] The process is mediated by a carefully maintained equilibrium between pro-angiogenic factors, such as Vascular Endothelial Growth Factor (VEGF), Fibroblast Growth Factor 2 (FGF2),

Transforming Growth Factor-beta (TGF-β), and angiopoietins, and anti-angiogenic factors, including angiostatin, endostatin, and thrombospondins.[11] However, in diabetic wounds, hyperglycemia exacerbates oxidative stress and inflammation, which leads to endothelial dysfunction, reduced production, and enhanced degradation of essential growth factors, impaired nitric oxide (NO) production, and ECM degradation, ultimately leading to compromised vascularization within the wound microenvironment.[12] There is also a marked reduction observed in syndecan-4 and glypican-1, cell surface heparan sulfate proteoglycans that are critical for the effective binding of angiogenic growth factors, like FGF-2 and VEGF to their receptors.[13,14]

Moreover, diabetic neuropathy further complicates wound healing by reducing sensory perception and motor control in the lower extremities. This reduction in sensory and motor function leads to decreased blood perfusion and hampers the supply of oxygen and nutrition to the wound sites.[15] Impaired angiogenesis prevents the efficient removal of necrotic tissue and debris, effective delivery of therapeutic agents, and granulation tissue formation. The diminished vascularization and capillary density constrain the migration of immune cells at the wound site, which weakens the immune response and makes the wound susceptible to infections.[16] Thus, impaired angiogenesis presents a significant challenge to diabetic wound healing, which needs to be addressed for effective treatment.

3.1.3. Research gap

The impairment of angiogenesis in diabetic wound healing has been the focus of several research efforts, highlighting its relevance in tissue regeneration. Various biomaterials, like nanoparticles,[17,18,19] nanofibers,[20,21] and hydrogels[22,23,24,25] have emerged, which aims to promote angiogenesis in diabetic wounds. These materials offer a high surface area and tunable release properties. Moreover, hydrogels have been known for their ability to mimic the extracellular matrix (ECM), providing a three-dimensional structure that not only supports the inclusion of growth factors, drugs, and cells but also helps maintain a moist wound environment.[26,27] The administration of exogenous growth factors such as VEGF, PDGF, EGF, and FGF-2 has been extensively studied and shown to effectively promote angiogenesis and wound healing.[28,29,30] However, despite their proven efficacy, the clinical application of these growth factors is hampered by drawbacks, such as their proteolytic instability and limited serum half-life, which significantly affect their therapeutic potential.[31] Gene regulation plays a critical role in angiogenesis.[32] Recently, a number of miRNA-based gene treatments have been developed that may have the potential to improve wound angiogenesis.[33,34,35] The targetable nature of miRNAs utilizing antagomir therapy makes these therapies intriguing. Their effectiveness is, however, limited by the challenges, such as determining the optimal dosage, stability, and effective administration.[36] Several stem cell types, including adipose-derived stem cells (ASCs), bone marrow-derived mesenchymal stem cells (MSCs), and induced pluripotent stem cells (iPSCs),

have been investigated for their potential to modulate the immune system, produce paracrine effects, and differentiate into vascular lineages that promote angiogenesis.[37] However, it has several downsides, such as immunological rejection, lower cell viability, proliferation, and differentiation capability in a hyperglycemic (HG) environment, which leads to the reduced efficiency of stem cells in DFU.[38] The challenges in using small drug molecules, like deferoxamine, is their short half-life, poor bioavailability, permeation, and potential side effects to non-target tissues.[39] Given the complications associated with the exogenous application of growth factors, proteins, cells, drugs and other adjuvants, there is a pressing need for the development of material that can manipulate the endogenous factors to promote the impaired angiogenesis in diabetic wounds.

3.1.4. Self-assembled peptide gel

Peptide-based scaffolds offer considerable benefits for wound healing due to their straightforward synthesis, customizable functionality, excellent biodegradability, biocompatibility, and the ability to present functional moieties at high density.[40.6] These scaffolds can be conveniently designed to transport drugs, cytokines, or cells to specific locations, after which they can break down into bioactive peptide sequences or natural amino acids, which can then assist in the surrounding tissue repair.[41] Huang *et al*. developed self-assembled peptide hydrogel with the proteoglycan assisted delivery of VEGF and HGF.[42] Similarly, Guo *et al*. reported a self-assembled peptide gel for sustained release of VEGF to stimulate angiogenesis.[43] Angiogenesis is an intricate process that involves several sequential steps. Angiogenic factors, along with MMPs and MMP-induced breakdown of the extracellular matrix (ECM) play crucial roles in the migration of endothelial cells (EC) and the maturation of blood vessels.[44] Through the manipulation of self-assembling peptides (SAPs), it is feasible to replicate the biological characteristics of the ECM and facilitate these steps. Incorporating MMP-sensitive motifs into SAPs increases their ability to break down naturally,[45] while including cell-binding sequences helps ECs adhere and migrate on the SAPs.[46] Furthermore, introducing peptides that mimic the growth factors' activity initiates angiogenesis and accelerates the maturation of blood vessels. Like, Hartgerink and co-workers developed a VEGF-mimicking highly angiogenic self-assembled multidomain peptide nanofibers for ischemic tissue disease.[47] Heparin-mimetic peptide nanofibers have been reported by Guler *et al*. to interact with the growth factors and promote angiogenesis.[48] Also, Liu *et al*. developed two designer self-assembled peptide scaffolds with one containing RGD cell adhesion sequence and other containing VEGF-mimicking sequence acting as VEGF agonist activating VEGF mediated signalling pathway.[49] Despite their promising ability to be customized and their functionality as scaffolds promoting angiogenesis, a significant limitation of using peptides in diabetic wounds is their susceptibility to degradation due to the heightened activity of proteolytic enzymes. This degradation can reduce their overall effectiveness, necessitating frequent treatments or additional modifications to enhance stability.[50]

3.2. Objectives

The challenges associated with the stability of peptides can be addressed by certain modifications with the sequence and structures, like modification of the N- or C- terminal, incorporation of D-amino acids, unnatural amino acids, cyclization of peptide chains, and insertion of non-peptidic backbones.[51] Moreover, Ghadiri *et al*. have reported that the cyclic peptides with alternating D- and L-residues and an even number of amino acids have a planar conformation with side chains positioned outside the ring structure. The amide groups are aligned perpendicular to the surface, facilitating hydrogen bonding and self-assembly into cyclic-peptide nanotubes.[52,] We aimed to explore the potential of cyclic peptide nanotubes (CPNTs) as a proangiogenic bioactive scaffold by incorporating heparan sulfate-inspired functional groups, hydroxyl, carboxylic acid, and sulfonate into the cyclic peptides. The CPNTs mimic the activity of heparan sulfate and aid the interactions of various proangiogenic growth factors like VEGF and FGF2 to their receptors.[48] The conformational rigidity of the cyclic peptides prevents the fast degradation of peptide chains in the wound microenvironment. Moreover, it addresses the challenges related to batch-to-batch variation in the efficacy, immunogenic response, stability and cost-effectiveness that arise with the administration of natural biomacromolecules, like growth factors, drugs and glycosaminoglycans exogenously.

We synthesized three cyclic-hexapeptides, ^{D}Pro-^{L}Trp-^{D}Leu-^{L}Ser-^{D}Glu-^{L}Lys, ^{D}Pro-^{L}Trp-^{D}Leu-^{L}Lys-^{D}Glu-^{L}Lys, and ^{D}Pro-^{L}Glu-^{D}Leu-^{L}Lys-^{D}Phe-^{L}Lys, and adorned them with the bioactive groups. The incorporated serine and glutamic acid provide hydroxyl and carboxylate groups, while the lysine side chain was functionalized with the sulfonate group. These cyclic peptides were then self-assembled into nanotubes using the pH-switch approach in ACN:H_2O. The CPNTs were investigated for cytocompatibility by cell viability analysis on murine fibroblast L929 and human umbilical vein endothelial cells, as well as hemocompatibility and immunotoxicity analysis. The material was then analyzed for its angiogenic potential by determining the expression of various angiogenic marker genes and proteins along with the cell migration, invasion, and tube formation potential.

3.3. Experimental section

3.3.1. Materials

Analytical-grade chemicals and reagents were utilized in the research work without further purification. The 2-chloro trityl resin with a mesh size of 200-400 and a loading capacity of 0.8 mmol/g was bought from Novabiochem. Bio-Rad PolyPrep chromatography columns were used for the solid-phase peptide synthesis (SPPS). Triisopropylsilane (TIS), trifluoroacetic acid (TFA), *N*-ethyl diisopropylamine (DIPEA), HATU, Fmoc-^{L}Lys(Boc)-OH, Fmoc-^{D}Phe-OH, Fmoc-^{D}Glu(OtBu)-OH, Fmoc-^{L}Trp-OH, and Fmoc-^{D}Pro-OH were obtained from TCI. We

acquired Fmoc-^{L}Glu(OtBu)-OH, Fmoc-^{D}Leu-OH, and Fmoc-^{L}Ser(OtBu)-OH from BLD Pharma. Avra supplied us with tributylamine and anhydrous dimethylformamide (DMF). Spectrochem was the supplier of piperidine. We purchased acetonitrile (ACN), sulfur trioxide trimethyl amine complex (TMST), ethanol, dichloromethane (DCM), HOBt, and HPLC grade methanol from Merck. The diethyl ether was provided by Rankem. All investigations utilized deionized water (DI, 18.2 MΩ•cm, Bio-Rad, Milli-Q). Lonza provided the Human Umbilical Vein Endothelial Cells (HUVECs) and the bullet kit including endothelial cell growth medium-2 (EGM 2). The NCCS, Pune provided the murine fibroblast L929 cells. Cell culture studies used fetal bovine serum (FBS), MTT reagent, DMEM, and RPMI from Thermo Fisher Scientific. Trolox was bought from Sigma-Aldrich. An Invitrogen live/dead kit was purchased for the study of cell viability. Studies on 3D cell migration, invasion, and endothelial tube development were conducted using Corning® Matrigel® matrix.

3.3.2. Methods

A Tecan Infinite Pro multiple plate reader was used to quantify the UV-Vis absorbance for the cell investigations. A Waters system with a BEH 300 RP C_{18} column (250 × 4.6 mm, 5 µm), a pump, a degasser, an injector with a 100 µL loop, PDA, and UV-vis detectors was used to perform the RP-HPLC study. Empower 3 software was used to process the data in an isocratic manner, where 20% acetonitrile (ACN) and 80% water along with 0.1% trifluoroacetic acid (TFA) formed the mobile phase. We used flow rate as 1 mL/min. The image acquisition was carried out using a scanning electron microscope (SEM, JEOL JSM-6610 LV model) with a tungsten filament and an accelerating voltage of 10 kilovolts (kV). A JEOL Model JSM7610F Plus equipment was used to conduct the FESEM investigation. The JEM-2100 Plus device, running at an acceleration voltage of 200 kilovolts (kV), was employed to take the high-resolution transmission electron microscopy (HR-TEM) images. On a Bruker Tensor 27 instrument, the Fourier transform infrared (FT-IR) spectra were acquired using the attenuated total reflection (ATR) mode. Fluorescence images were acquired using a Leica DMi8 fluorescence microscope.

3.3.3. Linear peptides

Peptide synthesis was carried out in Bio-Rad PolyPrep chromatography columns using solid-phase peptide synthesis (SPPS) with 2-chlorotrityl chloride (CTC) resin having a 1.00-1.80 mmol/g loading capacity. The 100 mg CTC resin beads were soaked in 1 mL of DCM for the whole night prior to use. The Fmoc strategy was used to synthesize the peptides. A 4.5 equivalents of DIPEA was added and the mixture was agitated for 10 minutes in order to activate the system for coupling of first amino acid to the resin. Subsequently, 10.5 equivalents of additional DIEA were added, and the mixture was agitated for another 3 hours to facilitate the complete coupling. After the completion of first coupling, the unreacted functional groups on the resin were passivated by adding methanol (0.8 mL/g of resin), and the mixture was shaken

for an additional 10 minutes. The sequential coupling of other amino acids was performed using 2.85 and 5.7 equivalents of HATU (~130 mg) and DIEA (~119 μL) for 4 h. A 20% v/v piperidine in DMF solution was employed to deprotect the Fmoc group of each amino acid. After each step, the resin was rinsed thrice using 1 mL of DMF and DCM each. A 4-5 mL solution of 1% TFA in DCM was used to cleave the peptide from the resin in 3.5-4 h. Ice cold ether was then used to precipitate the peptides. The peptides were dried under vacuum and characterized by mass spectrometry. We have synthesized three linear peptides, ^{D}Pro-^{L}Trp-^{D}Leu-^{L}Ser-^{D}Glu-^{L}Lys: PWLSEK, ^{D}Pro-^{L}Trp-^{D}Leu-^{L}Lys-^{D}Glu-^{L}Lys: PWLKEK, and ^{D}Pro-^{L}Glu-^{D}Leu-^{L}Lys-^{D}Phe-^{L}Lys: PELKFK.

3.3.4. Cyclic peptides

Cyclic peptides were synthesized from their linear counterparts using intramolecular cyclization performed at high dilution (0.5 mM solution in DCM) at 0 °C. Cyclization was performed using 6.5 equiv. of HBTU, 7.3 equiv. of HOBt, and 10.4 equiv. of DIPEA with a continuous stirring for 5 days. After the completion of reaction, the mixture was washed thrice with 40 mL of 0.1 M HCl and once with water and brine solution. DCM layer was collected and vacuum evaporated to collect the cylic peptide. We obtained three cyclic peptides, (PWLSEK), (PWLKEK), and (PELKFK) and characterized them using mass spectrometry.

3.3.5. Functionalization of cyclic peptides

The side chains of cyclic peptide were deprotected using a cocktail of TFA, H_2O, and TIS in the ratio of 95:2.5:2.5 (4.75 mL TFA, 125 μL H_2O, and 125 μL TIS). In a round-bottom flask, the protected cyclic peptide was mixed with the deprotection cocktail and stirred continuously for 4 h at room temperature. After precipitating the reaction mixture using a 30 mL of ice-cold diethyl ether, the completely deprotected cyclic peptide was isolated by centrifuging the mixture three times at 8000 rpm for 10 min and drying in vacuum. Using a mixture of tributylamine and trimethylamine sulfur trioxide complex (TMST), the amine (-NH2) side chains of deprotected cyclic peptides (CPs) were sulfonated by *in situ* production of tributylsulfoammonium betaine (TBSAB). At a concentration of 0.5 M, the cyclic peptide was dissolved in a mixture of MeCN and DMF, followed by the addition of tributylamine (4 equiv.) and trimethylamine sulfur trioxide complex (TMST). The reaction was carried out in an argon environment with constant stirring at 30 °C. The completion of the reaction (12 h) was validated using thin layer chromatography (TLC). Vacuum evaporation was used to remove the solvent once the reaction mixture had been cooled to room temperature. Ethanol was added to quench the reaction, followed by its filtration. Ice-cold ether was used to precipitate the sulfonated cyclic peptide. After the extraction, the precipitates were vacuum-dried. Mass spectrometry and RP-HPLC were used to characterize CPs. A JASCO J-1500 circular dichroism spectrophotometer was used to study the secondary structure of

peptides. We synthesized three functionalized cyclic peptides (PWLSEKs): SEK, (PWLKsEKs): KEK, and (PELKsFKs): KFK.

3.3.6. Fabrication of cyclic peptide nanotubes (CPNTs)

The functionalized cyclic peptides were dissolved in the 50/50 solution of ACN/H_2O at a concentration of 0.1 mg/mL. The pH of the solution was taken to 12 gradually by slow addition of 400 µL of 0.1 N NaOH to completely dissolve the peptides. To this solution, 0.1 M HCl was added dropwise until pH drops to 2. The solutions were kept unperturbed for 7-10 days to allow the self-assembly to take place. Prior to characterization, the solutions from each sample were sonicated in a bath sonicator for 30 minutes. FT-IR spectroscopy was used for characterization, while HR-TEM and FE-SEM images were used to assess surface morphology. Using a Bruker Tensor 27 instrument in the Attenuated Total Reflectance (ATR) mode, FT-IR spectra were acquired in the 400–4000 cm^{-1} region. OPUS software was used to process the collected data, and GraphPad Prism was used for analysis.

3.3.7. Surface morphology

The cyclic peptide nanotubes were subjected to field-emission scanning electron microscopy for surface morphology investigations using FE-SEM, JEOL Model JSM7610F Plus, with an accelerating voltage of 15 kV. The samples were drop-casted onto a silicon wafer and allowed to dry. HR-TEM analysis was further performed using the HR-TEM JEM-2100 Plus device at 200 kV, where samples were prepared on a copper grid and images were captured at different magnifications.

3.3.8. Stability analysis

The stability of SEK nanotubes was systematically investigated under different pH conditions and in environment containing proteolytic enzymes. Three buffer solutions at pH levels 5.8, 7, and 8.4 were prepared and incubated with nanotubes at a temperature of 37 °C. At designated time intervals of 0, 6, 12, and 24 hours, the nanotubes were subjected to centrifugation at 10,000 rpm for 10 minutes at 4 °C, followed by washing and dispersion in DI water. The stability of the nanostructure was assessed by measuring the average surface zeta potential using a Nanotrac Wave II zeta potential analyzer. Additionally, the stability was evaluated in a mixture of proteolytic enzymes by incubating the nanotubes at 37 °C in a mocktail of enzymes comprising of proteinase K, chymotrypsin, and pepsin, formulated in a 10 mM phosphate-buffered saline (PBS) solution. After the specified intervals, the nanotubes underwent centrifugation under the above-mentioned conditions and were subsequently dispersed in DI water for zeta potential analysis.

3.3.9. Cell culture studies

Murine macrophages (RAW264.7) and fibroblast cells (L929) were procured from the NCCS in Pune and grown in DMEM media containing 10% FBS and 1% antibiotic penicillin-

streptomycin. The cells were maintained at 37 °C in a CO_2-filled, humidified environment. HUVEC were cultured using an EGM-2 Bullet Kit supplemented with 1% penicillin-streptomycin. The cell lines were cultured in enclosed T-25 flasks, with medium replaced every 48 hours until 80-90% confluency was achieved. The impact of CPNTs on immunotoxicity and viability was assessed by treating macrophages and fibroblast cell lines at a dose of 350 µg/mL. The angiogenic potential of CPNTs was assessed on hyperglycemic HUVECs by nurturing cells in a medium comprising D-glucose (30 mM) for 24 hours and then treating them with CPNTs. Following the treatment, the cells were separated using a trypsin-EDTA solution or scrapped. For further experiments, the sub-confluent cells were extracted.

3.3.10. MTT assay

The MTT analysis was employed to assess the cellular viability of L929 and HUVEC cell lines following CPNT treatment.[53] The samples were sterilized using UV light for thirty minutes after being freeze-dried. Prior to cell incubation, the CPNTs were submerged in the incomplete medium. A 96-well plate coated with Nunc was used, with ten thousand cells added to each well. Each well received a 100 µL of sample extracts after 24 hours, and the treated cells were incubated for another 24 hours in a humidified incubator with 5% CO_2 enrichment at 37 °C. The control group consisted of untreated cells. After 24-hour treatment, 20 µL of 5 mg/mL MTT solution prepared in incomplete media was added to each well and kept in dark for around 4 h. After four hours, the MTT solution was taken out, and 100 µL of DMSO was used to dissolve the formazan crystals. Three repetitions of the experiment were conducted, and a plate reader set at 570 nm was used to determine absorbance. Cell viability was measured using the absorbance ratio between sample-treated and untreated control cells.

3.3.11. Live/dead assay

A LIVE/DEAD survival/cytotoxicity kit was used to assess the cell viability of L929 and HUVECs following their treatment with CPNTs. The functional dye solution for the live/dead assay was prepared, which contained 2 M calcein AM and 4 M ethidium homodimer 1-red in 5 mL of incomplete medium. In a Nunc-coated 6-well plate, the HUVECs and L929 cells were cultured at a density of 1.2 x 10^6 cells/well. The cells were treated with CPNTs at the previously mentioned dosages for 24 h at 37 °C in a humidified atmosphere with 5% CO_2. After treatment, the cells were stained with a 500 µL dye solution for 45–60 minutes. A Leica DMi8 fluorescent microscope was used to acquire images of both live and dead cells.

3.3.12. Oxidative stress analysis

The oxidative stress induced after CPNTs treatment has been examined using the DCFDA/H_2DCFDA-Cellular ROS Assay Kit.[54] A 6-well Nunc-coated plate was seeded with L929 cells, 1.2 x 10^6 cells per well, and incubated at 37 °C with 5% CO2. After reaching 90% confluency, cells were treated with 350 µg/mL CPNTs and incubated for 24 hours. As a positive control, cells were subjected to 50 mM H_2O_2 for two hours, whereas cells treated with the

complete media alone served as the negative control. The oxidative stress induced in the CPNT-treated cells was evaluated using 100 µL of 25 µM DCFDA dye in a serum-free medium. The dye solution was added to each well, and the plate was kept in the dark at room temperature for 30 minutes. Wells were cleaned with PBS after aspirating the media. The GFP fluorescence at Ex = 460-495 nm and Em >510 nm was detected using e-optical interference filters under a Leica DMi8 microscope.

3.3.13. Hemocompatibility

Healthy human donors provided fresh human blood in accordance with the Institutional Biosafety Committee's authorized procedure (#07/2021-II/IIT/IEC) to ascertain CPNTs hemocompatibility. Red blood cells (RBCs) were isolated via centrifugation at 1500 rpm for 20 minutes and subsequently washed thrice with PBS. Following the discarding of the supernatant, the pellet was reconstituted in 1 mL of PBS and then diluted with 9 mL of PBS. CPNTs at a concentration of 350 µg/mL were introduced to 1 mL of the diluted RBC solution and allowed to incubate at 37 °C for 4 hours. Post-incubation, the solution underwent centrifugation at 10,000 rpm for 10 minutes, following which a 200 µL aliquot of the supernatant was retrieved to quantify the degree of RBC lysis at 594 nm. PBS functioned as the negative control, while triton-X (0.1%) served as the positive control. The percentage of hemolysis was ascertained by correlating the sample's absorbance with that of the positive control.[55]

3.3.14. *In vitro* scratch/wound healing assay

A scratch-wound motility assay was employed to evaluate the impact of CPNTs on the migratory behaviour of L929 and HUVECs cells within a delineated scratch area.[56,57] A solution of CPNTs at a workable concentration of 350 µg/mL in serum-free media was meticulously prepared. The cells were cultivated in 6-well plates at a density of 1.2 x 10^6 cells/well until a monolayer was formed, reaching 80-90% confluency in an incubator maintained at 37 °C and 5% CO_2. Cells were cultured in a medium with 30 mM D-glucose for 24 hours to obtain hyperglycemic (HG) HUVECs. A cell-free zone was created by making a scratch in the cell monolayer using a sterile pipette tip after the culture media were removed. Cellular debris was removed by washing the wells with incomplete media. The CPNTs were then introduced to the wells and the healing of scratch was observed at different time intervals. ImageJ software was used to determine the scratch closure area.

3.3.15. Morphology assessment

Morphological alterations in murine fibroblast cells upon exposure to nanotubes were evaluated through cytoskeletal staining following a 24-hour treatment period. The cell morphology was visualized by staining cellular F-actin and nuclei with Alexa Fluor 488 phalloidin and DAPI, in accordance to a previously established protocol.[58] The cells were cultured on a coverslip and maintained in a humidified atmosphere containing 5% CO_2 at 37 °C for 24 hours. Subsequently,

the culture media was replaced with a solution of 350 µg/mL of CPNTs, and the treated cells were incubated for an additional 24 hours. Following a wash with phosphate-buffered saline (PBS), the cells were fixed using a 4% paraformaldehyde solution and permeabilized for 15 minutes with 0.1% Triton X-100. Alexa Fluor 488 phalloidin was then applied to stain the F-actin filaments, and the cells were incubated in the dark for 30 minutes. Thereafter, the cell nuclei were stained for 10 minutes with a 1 µg/mL DAPI solution, and the cells underwent another wash with PBS. The stained coverslips were carefully mounted onto glass slides with a suitable mounting solution, and images were acquired using a fluorescence microscope.

3.3.16. Gene expression analysis

To investigate the various gene expression profiles following CPNT treatment, two-step qRT-PCR was employed. Following the manufacturer's instructions, total RNA was isolated from several populations of Raw 264.7 and HUVECs using PureZOL RNA Isolation Reagent. Super Reverse Transcriptase (MuLV) was used reverse transcribe RNA after its quantification. A Quant Studio 3 Real-Time PCR System (Applied Biosystems, USA) was used to conduct quantitative real-time polymerase chain reaction (RT-qPCR) analysis employing gene-specific primers and Power Up SYBR Green Master Mix for qPCR (Applied Biosystems). By comparing the expression of the data to that of the housekeeping gene β-actin, the data were normalized.

3.3.17. Immunocytochemistry analysis

Cell lysis buffer containing 1% Halt protease and phosphatase inhibitor cocktail was used to lyse both control and treated cells. The Lowry technique was employed to determine the amount of protein in lysates.[59] Using the Trans-Blot Turbo Transfer System, cellular lysates containing 50 µg of protein were produced, separated on a 10% SDS-PAGE gel, and then transferred to PVDF membranes (Bio-Rad). The blocking buffer solution comprising of 5% BSA in TBST (1% tween 20 in Tris buffer) solution was initially applied to the membranes and left for one hour. Specific primary antibodies, at a dilution of 1:2000, were applied to the membranes and left to incubate overnight at 4 °C on a revolving shaker. Membranes were washed with TBST three times for 10 minutes each. After incubation with diluted (1:20.000) peroxidase-conjugated secondary antibodies for two hours at room temperature, membranes were washed with TBST. Subsequently, membranes were incubated at room temperature (RT) with Clarity Western ECL Substrate (Bio-Rad). Protein bands were observed using the Chemidoc XRS+ System (Bio-Rad), and Image-J software was used for analysis.[60]

Immunofluorescence was performed using antibodies on both treated and untreated HUVECs to evaluate the expression of pro-angiogenic proteins in CPNTs. A coverslip containing about 1 x 10^4 HUVECs was used to treat the cells with normal glucose (NG), high glucose (HG), and high glucose with SEK. Cells were fixed in cold methanol following the treatment. For three minutes, the cellular permeabilization buffer (0.1% Triton-X in PBS) was administered. The

cells were then washed once with PBS and treated with blocking buffer containing 1% BSA in PBST (0.5% Tween-20 in PBS) for one hour at room temperature. Primary antibody dilutions in PBST (1:100) were incubated overnight at 4 °C. Following three PBST washes, cells were incubated for two hours at a 1:1000 dilution with fluorescence-conjugated secondary antibodies in PBST. The nucleus was counterstained using Vector Laboratories' VECTASHIELD Vibrance Antifade Mounting Medium with DAPI. Leica DMi8 inverted fluorescent microscope and LAS X were utilized to get cellular images.[61]

3.3.18. Transwell migration and invasion assay

The study employed transwell inserts with 8.0 μm pores to evaluate the CPNT-induced cellular chemotactic activity. In a Nunc-coated 24-well plate, approximately 5 x 10^4 HUVEC cells/well were cultured for 24 hours in NG (5 mM) and HG (30 mM) media. After incubation, the cells were trypsinized and resuspended in FBS-free media. Transwell inserts containing cells were used for the migration assay, while invasion experiments were performed on cells in the upper chambers of transwell inserts covered with Matrigel Basement Membrane Matrix. Around 350 μL of medium containing 5% FBS was added to the lower compartment. The corresponding wells were filled with a predefined concentration of SEK in the lower chamber, and incubated for 24 hours. A cotton swab was used to clean off the top side of the membrane after the media was aspirated. The cells that have crossed across were fixed in 2.5% glutaraldehyde for 10 minutes. The cells were stained for two hours with 0.5% crystal violet solution, and Leica DMi8 microscope was used to capture 100x bright field images of migrating and invading cells at three randomly chosen fields per membrane. For a semi-quantitative evaluation, the stained cells were subjected to a 33% acetic acid solution for 10 minutes. After adding the eluent to a 96-well microplate, the absorbance at 590 nm was measured. A standard curve was created using various HUVEC cellular densities in order to determine the percentage of migrated or invaded cells.[62]

3.3.19. *In vitro* endothelial tube formation assay

In order to ascertain the angiogenic potential of hyperglycemic HUVECs treated with SEK CPNTs, capillary-like formations were examined on Matrigel Basement Membrane Matrix. HUVECs were grown in NG (5 mM) and HG (30 mM) media for 24 h. Matrigel (10 mg/mL) was applied to each well of 24-well plate in accordance with the manufacturer's instructions. Each Matrigel-coated well was seeded with 1.2 x 10^5 HUVECs over the gel in a total volume of 200 μL. At the predetermined doses, SEK was administered to the cells in the HG + SEK group for 24 hours at 37 °C. Following a 24-hour period of *in vitro* endothelial tubule development, three distinct fields of each set were captured. The SEK-treated, NG and HG sets of HUVECs were examined for their angiogenic characteristics using the Image-J software with its angiogenesis analyzer plugin.[63,64]

3.3.20. Statistical Analysis

The data was analyzed using GraphPad Prism 9.0 (GraphPad Software, La Jolla, CA). The data is represented as mean ± SD (n = 3). The student's t-test, one-way or multiple-t-test was used to determine the statistical significance. *P*-values less than 0.05 were regarded as significant.

3.4. Results and discussion

To address the challenges associated with impaired angiogenesis in the diabetic wounds, we have developed cyclic peptide nanotubes that mimic the glycosaminoglycan and assist in the binding of growth factors to their cognate receptors. We have synthesized, functionalized, and self-assembled cyclic peptides, ^{D}Pro-^{L}Trp-^{D}Leu-^{L}Ser-^{D}Glu-^{L}Lys$_s$ (SEK), ^{D}Pro-^{L}Trp-^{D}Leu-^{L}Lys$_s$-^{D}Glu-^{L}Lys$_s$ (KEK), and ^{D}Pro-^{L}Glu-^{D}Leu-^{L}Lys$_s$-^{D}Phe-^{L}Lys$_s$ (KFK) into nanotubes. Prior studies underscore the enhanced binding capacity to growth factors achieved through the addition of heparin-inspired functional groups to peptides and polymers.[65,66,67] Pursuant to this insight, we adorned the surface of these peptide nanotubes with carboxylic acid, hydroxyl, and sulfonate groups, with an aim to emulate the functionality of heparan sulfate. Serine (Ser) and glutamic acid (Glu) were integrated into the peptide sequence to incorporate hydroxyl and carboxylic acid side chains. Additionally, the amine group on the lysine (Lys) side chain was functionalized through sulfonation. This strategic surface modification is aimed at enhancing the peptides' ability to facilitate the binding of critical growth factors, such as Vascular Endothelial Growth Factor (VEGF) and Fibroblast Growth Factor 2 (FGF2), to their respective receptors, thereby promoting angiogenic activity **(Figure 3.1)**. Furthermore, the interaction between the growth factors and the HS-mimetic nanotubes is postulated to protect the enzymatic degradation of the growth factors.[48] The proline (Pro) residue within the peptide sequence serves to induce a bend in the peptide chain, which contributes to the stabilization of the cyclic conformation.[68] This stabilization, in turn, enhances the structural rigidity of the peptide, thereby impeding the action of proteolytic enzymes that are commonly overexpressed in diabetic wounds.[69] Tryptophan (Trp) and leucine (Leu) provide hydrophobic and aromatic interactions (π-π stacking) that further stabilizes the nanotube assembly. We have developed shorter peptide sequences comprising six residues, hypothesizing that it will increase the density of negatively charged functional groups and augment their interaction with the growth factors. Also, the shorter peptide chains will be straightforward and cost-effective in synthesizing, purifying, and scaling up compared to complex, longer sequences. Additionally, the expansive surface area of the nanotubes enables extensive interaction with the target sites, which is anticipated to significantly elevate both affinity and selectivity.

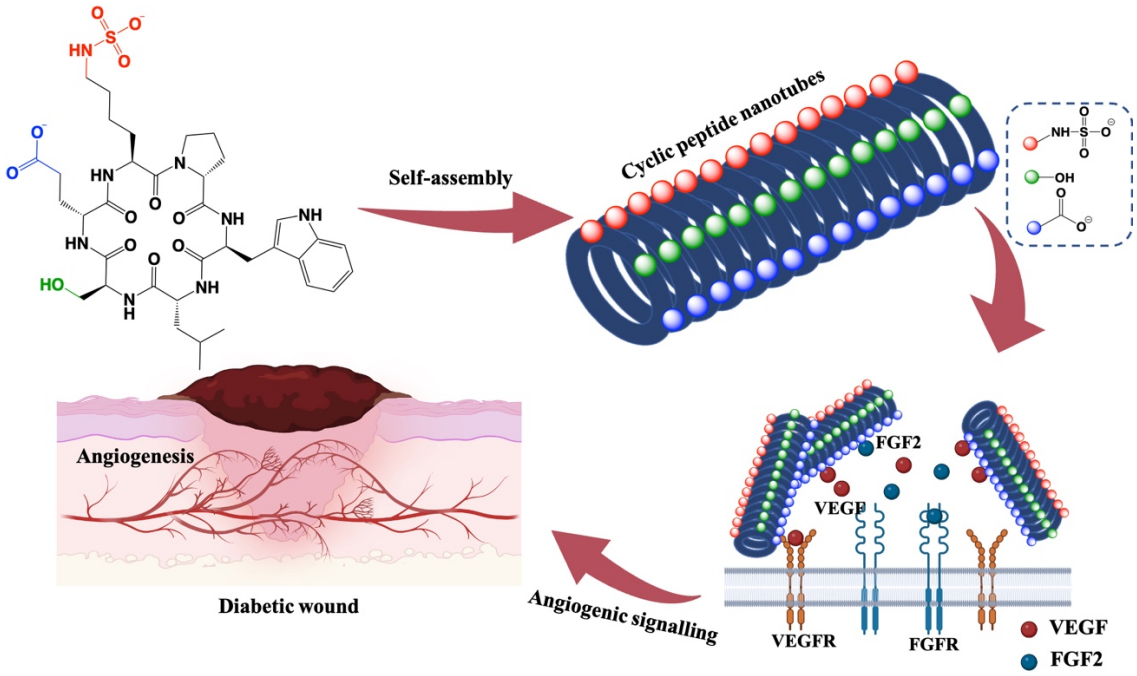

Figure 3.1. Diagrammatic illustration of cyclic peptide nanotubes derived from ^{D}Pro-^{L}Trp-^{D}Leu-^{L}Ser-^{D}Glu-^{L}Lys$_s$ (SEK) that aid in binding proangiogenic growth factors, such as FGF2 and VEGF, to their receptors to stimulate angiogenesis.

3.4.1. Synthesis of cyclic peptides

Solid-state peptide synthesis (SPPS) approach based on Fmoc chemistry was used to synthesize the linear peptides ^{D}Pro-^{L}Trp-^{D}Leu-^{L}Ser-^{D}Glu-^{L}Lys, ^{D}Pro-^{L}Trp-^{D}Leu-^{L}Lys-^{D}Glu-^{L}Lys, and ^{D}Pro-^{L}Glu-^{D}Leu-^{L}Lys-^{D}Phe-^{L}Lys **(Figure A19, Appendix)**. The linear peptides underwent cyclization at high a dilution (0.5 mM in DCM) and 0 °C temperature **(Figure A20, Appendix)**. Cyclic peptides were functionalized with sulfonate groups after the removal of side chain protecting groups (**Figure A21, Appendix**). The peptides were analyzed by mass spectrometry and reversed-phase high-performance liquid chromatography (RP-HPLC). RP-HPLC determined the purity of peptides, where ACN:H_2O (20:80) with 0.1% TFA was used as the mobile phase at 1 mL/min flow rate. SEK, KEK, and KFK were found to have retention times (R_t) of 2.3, 2.8, and 3.4 minutes, along with a purity of more than 95% (**Figure A23, Appendix**). Using mass spectrometry, the molar masses of the sulfonated cyclic peptides were determined to be 819, 901, and 949 Da for SEK, KEK, and KFK, respectively, which corresponded to their theoretical values (**Figure A22, Appendix**). FTIR and CD spectroscopy were used for evaluating the secondary structure of peptides. The FTIR spectra of SEK, KFK, and KEK showed the presence of amide I peaks at 1638, 1635, and 1630 cm^{-1} (**Figure A24, Appendix**), which corresponds the stretching vibrations of C=O functional group (**Figure 3.2H**). Further, the CD spectra revealed minimum values of 217, 216, and 214 nm for SEK, KFK, and KEK nanotubes **(Figure 3.2I)**. The results confirmed a secondary β-sheet structure of cyclic peptide nanotubes.

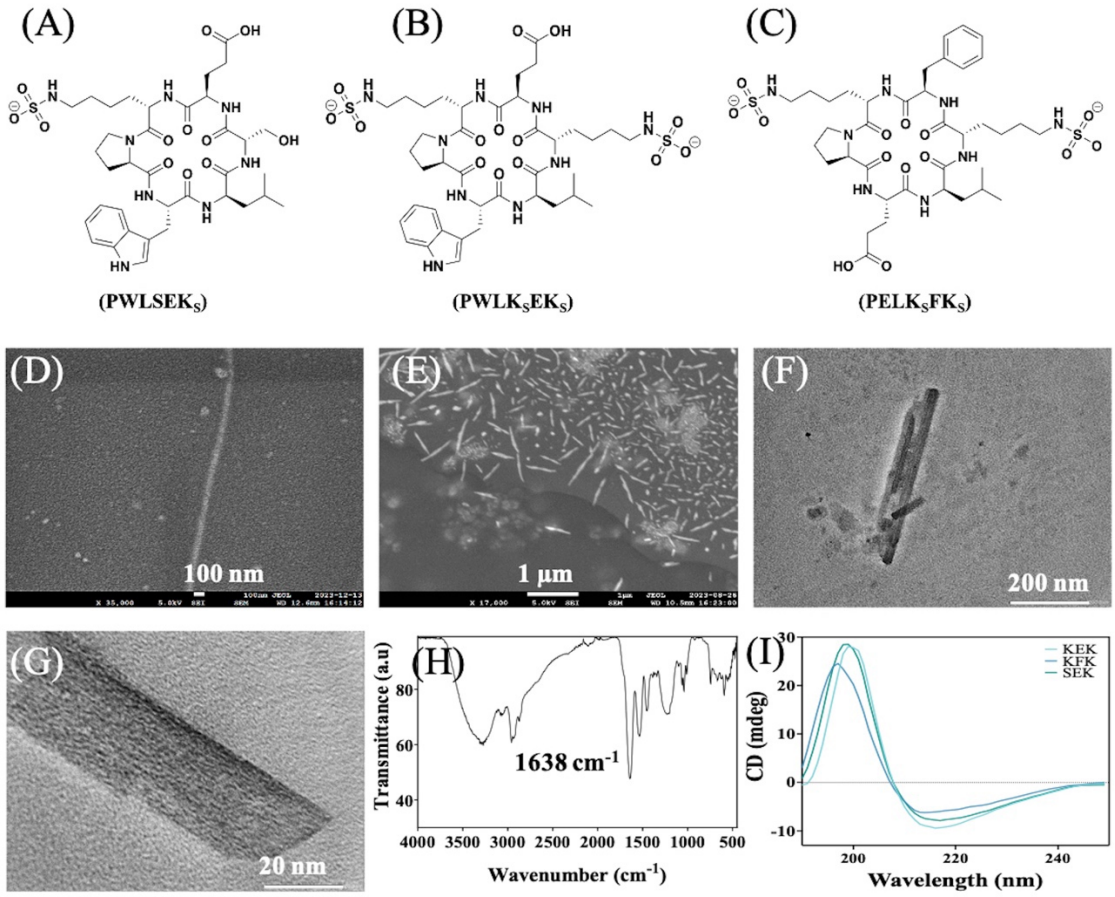

Figure 3.2. Cyclic peptide structures: (A) SEK, (B) KEK, and (C) KFK. (D-G) FESEM and HRTEM images depicting cyclic peptide nanotubes at different magnifications. (H, I) FT-IR and CD spectra determining a β-sheet like secondary structure.

3.4.2. Cyclic peptide nanotubes

Cyclic peptide nanotubes were fabricated by the self-assembly of cyclic peptides by switching the pH gradually. This strategy involves the solubilization of cyclic peptides in 50:50 mixture of ACN:H_2O at a 1% w/v concentration. The pH was raised to 12 by adding 0.1 N NaOH to ensure the complete solubility of peptide. Next, 0.1 M HCl was added dropwise to gradually drop the pH to 2. The solution was left unperturbed for around 7 days to encourage the self-assembly. Cyclic peptides composed of an even number of alternating D and L-amino acids demonstrate a unique structural characteristic by adopting a planar conformation. This configuration presents the side chains outside the ring while aligning the amide groups orthogonally to the plane. These amide groups are inclined to form hydrogen bonds, facilitating the stacking of the cyclic peptides into ordered structures and resulting in the formation of nanotubes. FESEM and HRTEM were used to examine the morphology of the nanotubes (**Figure 3.2D-G**). The results suggested a tubular shape with diameters ranging from 20 to 30

nm. Nanotubes were found to have zeta potentials of -10.8, -16.37, and -12.62 mV, indicating that their surface carries a net negative charge.

3.4.3. Stability analysis

The stability of cyclic peptide nanotubes was investigated using a mocktail of proteolytic enzymes comprising of chymotrypsin, pepsin, and proteinase K, and buffer solutions with slightly acidic, neutral, and basic and neutral pH of 5.8, 7 and 8.4 (**Figure A25, Appendix)**. SEK CPNTs were incubated in the solutions for 0, 6, 12 and 24 h. The assessment of their stability was conducted by measuring the average surface zeta potential using a Nanotrac Wave II zeta potential analyzer. Zeta potential serves as a significant parameter for elucidating the stability of nanostructures; a higher zeta potential correlates with enhanced stability, as it mitigates aggregation by balancing repulsive and attractive forces. As analyzed at specific time intervals, we observed that under acidic and neutral conditions, the average zeta potential exhibited minimal variation, even after 24 hours, thereby indicating the stability of the nanotubes. However, under the basic conditions (pH 8.4), a shift in the zeta potential from -12.23 to -8.63 was noted over the 24-hour period, suggesting a moderate decrease in stability, which may be attributed to an increase in repulsive interactions between the cyclic peptide rings under basic conditions. Furthermore, in the presence of proteolytic enzymes mocktail, the change in the surface potential was observed from -12.16 to -9.86, reflecting the overall stability of nanotubes under enzymatic conditions. This can be rationalized by the conformational rigidity of cyclic peptides, which effectively prevent their degradation in the presence of proteolytic enzymes.

3.4.4. Assessment of cytocompatibility

Assessing the cytocompatibility of CPNTs with mammalian cells is crucial for ensuring the safe integration of biomaterials in pharmaceutical applications. We evaluated the cytocompatibility of CPNTs towards murine fibroblast (L929) and human umbilical vein endothelial cells (HUVEC), which are substantially present in the wound ecosystem. MTT assay was employed to facilitate the assessment of cell viability, proliferation, and cytotoxicity on CPNT treatment. This assay measures the cellular metabolic activity based on the conversion of MTT, a yellow tetrazolium dye, to purple formazan crystals by metabolically active cells. This conversion is facilitated by the mitochondrial NAD(P)H-dependent oxidoreductase enzyme. The quantification of this reaction is achieved by measuring the absorbance of the solubilized formazan product in dimethyl sulfoxide (DMSO) at a wavelength of 570 nm. The colorimetric MTT assay was conducted on fibroblast cells (L929) following treatment with KEK, KFK, and SEK at varying dosages. The results revealed that the optimal dosage compatible with cells was 350 μg/mL across all treatments (**Figure A26, Appendix**). Subsequently, HUVEC endothelial cells treated with the same dosage of KEK, KFK, and SEK demonstrated no marked variations

in cell viability, indicating 350 μg/mL as the optimal dose for all CPNTs, and rendering them cytocompatible with both fibroblast and endothelial cells. SEK, KEK, and KFK treatment resulted in 108.37 ± 6.44, 112.84 ± 1.17, and 136.12 ± 6.59% viability of L929 cells, respectively. Moreover, after being treated for 24 hours with SEK, HUVECs showed a vitality of 103.52 ± 12.27%, whereas those treated with KEK and KFK showed viabilities of 108.69 ± 2.15% and 101.54 ± 5.13%, respectively (**Figure 3.3A, B)**.

Similar outcomes have been observed with live/dead staining of L929 and HUVECs following incubation (**Figure 3.3C, D**). SEK, KEK, and KFK were administered to L929 and HUVECs for a 24-hour incubation period. Untreated cells were used as the control group. Following incubation, ethidium homodimer 1-red and calcein AM were used to co-stain the cells. The fluorescence microscopy revealed that both cells exhibited predominantly green colour, indicating good cell viability. Semi-quantitative analysis revealed that the intensity of red fluorescence (dead cells) in CPNT-treated cells was equivalent to that of untreated cells (**Figure A27, Appendix)**. The cytocompatibility analysis of CPNTs was further elucidated by assessing the generation of intracellular reactive oxygen species (ROS) in L929 cells. This analysis was performed utilizing the DCFDA/H_2DCFDA- Cellular ROS Assay Kit post a 24-hour treatment, which revealed an absence of intracellular ROS activity post-CPNT treatment (**Figure 3.3E**). The assay's mechanism involves the conversion of H_2DCF into 2′,7′-dichlorofluorescein (DCF), a highly fluorescent compound, in the presence of ROS. For comparative analysis, the cells subjected to H_2O_2 treatment and those left untreated were taken as positive and negative controls, respectively. The H_2O_2-treated cells displayed a marked increase in green fluorescence, indicative of an enhanced ROS stress. In contrast, the cells treated with CPNTs showed only a minimal change in green fluorescence compared to the untreated cells. The hemocompatibility of CPNTs was also investigated by performing a hemolysis assay. It was observed that RBCs treated with CPNTs SEK (0.97), KEK (0.93), and KFK (0.95) did not exhibit significant alterations when compared to the control group containing PBS alone (**Figure 3.3F**). In contrast, RBCs treated with triton-X (positive control) experienced complete hemolysis, resulting in the formation of a red solution (**Figure A28, Appendix**).

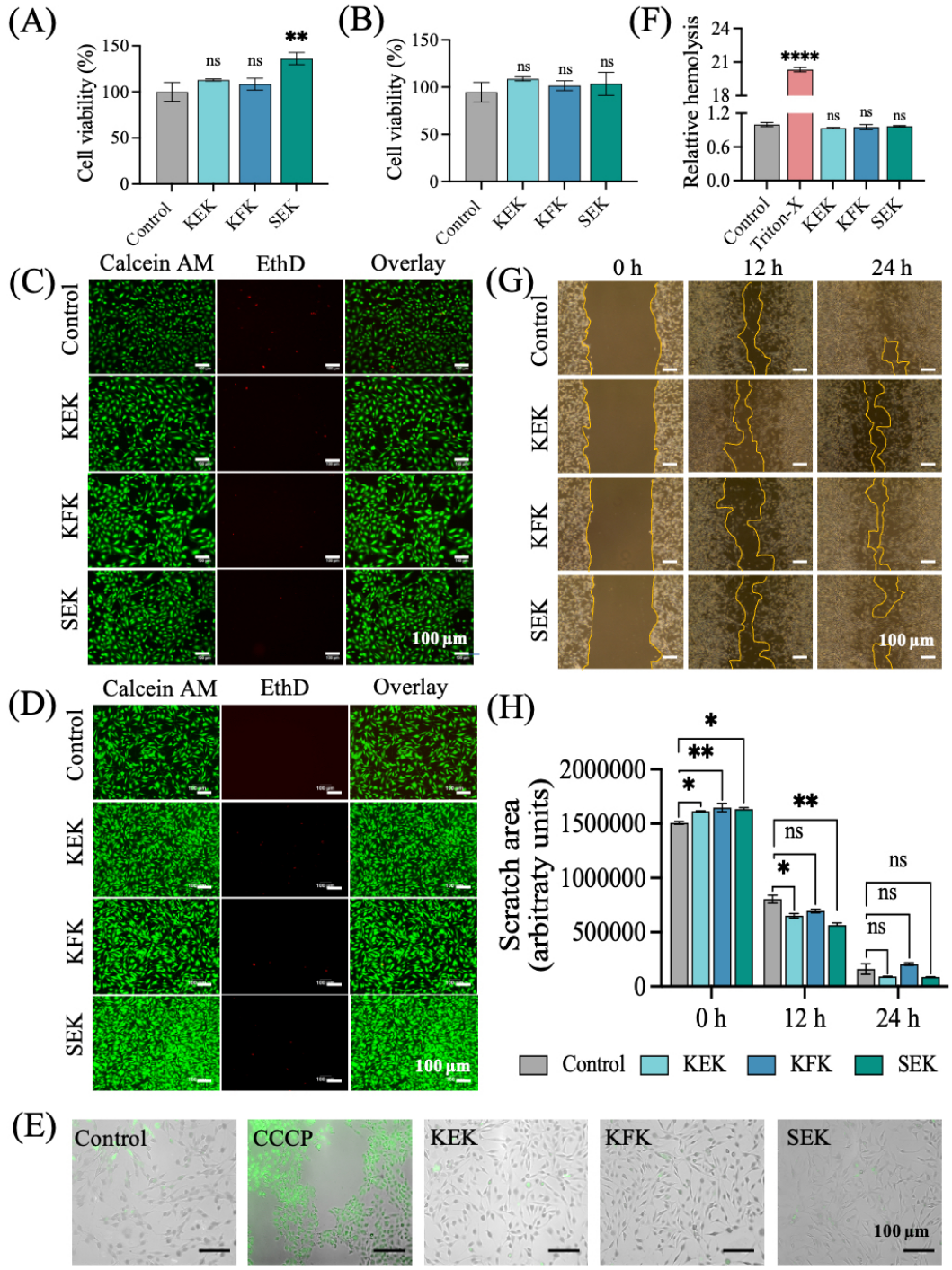

Figure 3.3. Cyclic peptide nanotubes' analysis for cell viability, ROS-induced stress, hemocompatibility and *in vitro* scratch healing. (A, B) MTT assay determining cell viability on 24 h treatment: (A) Murine fibroblast cells (L929), and (B) Human umbilical vein endothelial cells (HUVEC). (C, D) Live/dead fluorescence assay: (C) HUVECs, and (D) L929 cells. Scale bar: 100 µm. (E) Dichlorofluorescein diacetate (DCFDA) assay to investigate the ROS stress induced in L929 cells on treatment with nanotubes. Scale bar: 100 µm. (F) Hemocompatibility analysis of CPNTs, where triton X and PBS served as controls. (G) Scratch images of L929 cells taken at 0, 12, and 24 h to assess the *in vitro* wound healing potential of CPNTs. Scale bar: 100 µm. (H) Semiquantitative analysis of unhealed scratch area. Untreated cells were taken for

comparative analysis. The data has been shown as mean ± standard deviation (n = 3), with *ns* denoting the insignificant difference and *P* values <0.05 (*), 0.01 (**), and 0.001 (***) considered to be significant differences.

3.4.5. *In vitro* scratch assay

Cell migration plays a crucial role in the process of wound contraction and healing. The cell wound closure assay is utilized to evaluate the migratory and healing potential of CPNTs on L929 cells following an incision in a confluent cell plate. As a wound healing model, the progression of cell migration into the denuded region was tracked over a period in a scratched cell monolayer (**Figure 3.3G**). We observed that KEK, KFK, and SEK-treated cells exhibit migration within the scratch. The scratched areas were photographed at 0, 12, and 24 hours and the scratch closure were evaluated semi-quantitatively utilizing image J analysis tools. By comparing the scratch area at various time intervals to the original scratch area, the percentage of scratch closure was calculated (**Figure 3.3H**). About 95% of healing was observed by the migratory behaviour of L929 cells on SEK and KEK treatment, whereas KFK and untreated cells demonstrated 88% and 89% of healing. These results indicate that cyclic peptide nanotubes (CPNTs) provide a stable environment that moderately enhances cellular migration, thus, contributing positively to wound closure

3.4.6. Morphological assessment

Cytoskeletal staining was employed to examine the morphology of murine fibroblast cells following a 24-hour treatment with nanotubes (**Figure A29, Appendix**). The cells were stained using Alexa Fluor 488 phalloidin and DAPI (4',6-diamidino-2-phenylindole) stains. Alexa Fluor 488 phalloidin specifically stains the cytoskeleton by binding to filamentous actin (F-actin), while DAPI is a blue-fluorescent nuclear stain that exhibits fluorescence upon binding to adenine-thymine (AT) regions of double-stranded DNA (dsDNA). The observations revealed that the cells maintained a mononucleated, fibroblast-like morphology, characterized by extended cytoplasmic projections in response to nanotube treatment. This observation of intact and healthy cellular morphology demonstrates the cytocompatibility of the nanotubes.

3.4.7. Immunotoxicity analysis

The immunological response to the biomaterial has been investigated in order to comprehend its effect on the immune system. The expression level of proinflammatory cytokines in murine macrophages (RAW264.7) in response to nanotube exposure was investigated (**Figure 3.4**). by quantitative reverse transcription polymerase chain reaction (q-RT PCR). Proinflammatory cytokines (CCL5, CCL2, IL-15, iNOS, IL-1ß, IL-6), anti-inflammatory cytokines (IL-4, Ym1), and inflammation-induced cellular markers (MHCII, NfkB) were all evaluated for their expression levels (**Figure 3.4A**). After being exposed to CPNTs, the expression of CCL2, IL-1β, iNOS, IL-4, and Ym1 decreased significantly. However, we observed a significant increase

in MHCII expression across all groups treated with three CPNTs, which suggests that CPNTs may enhance the macrophages' ability to function as antigen-presenting cells by up taking peptides. Conversely, there was a noticeable reduction in the expression of CCL2, IL-1ß, iNOS, IL-4, and Ym1, thus, indicating the non-immunotoxic nature of CPNTs. The expression of other cytokines varied- CCL5, TLR2, and IL-15 levels were seen to decrease, while IL-6 levels increased significantly in the KEK and KFK-treated cells. This pattern was not observed in the SEK-treated group, where the expression demonstrated the opposite trend. Moreover, it was observed that the expression of NfkB, a pivotal regulator of cytokine production, remained unaffected on incubation with CPNTs. This was further supported by immunocytochemistry analyses for pro-inflammatory markers such as iNOS, CCL2, and IL-1β, where no notable increase in fluorescence intensity was observed, effectively indicating a lack of immunotoxicity (**Figure 3.4B-E**). This lack of altered gene and protein expression of inflammation-stimulated cytokines and cellular markers upon CPNTs treatment signifies their non-inflammatory action in RAW264.7, which suggests the potential of CPNTs in wound healing applications without augmenting any immunogenic response.

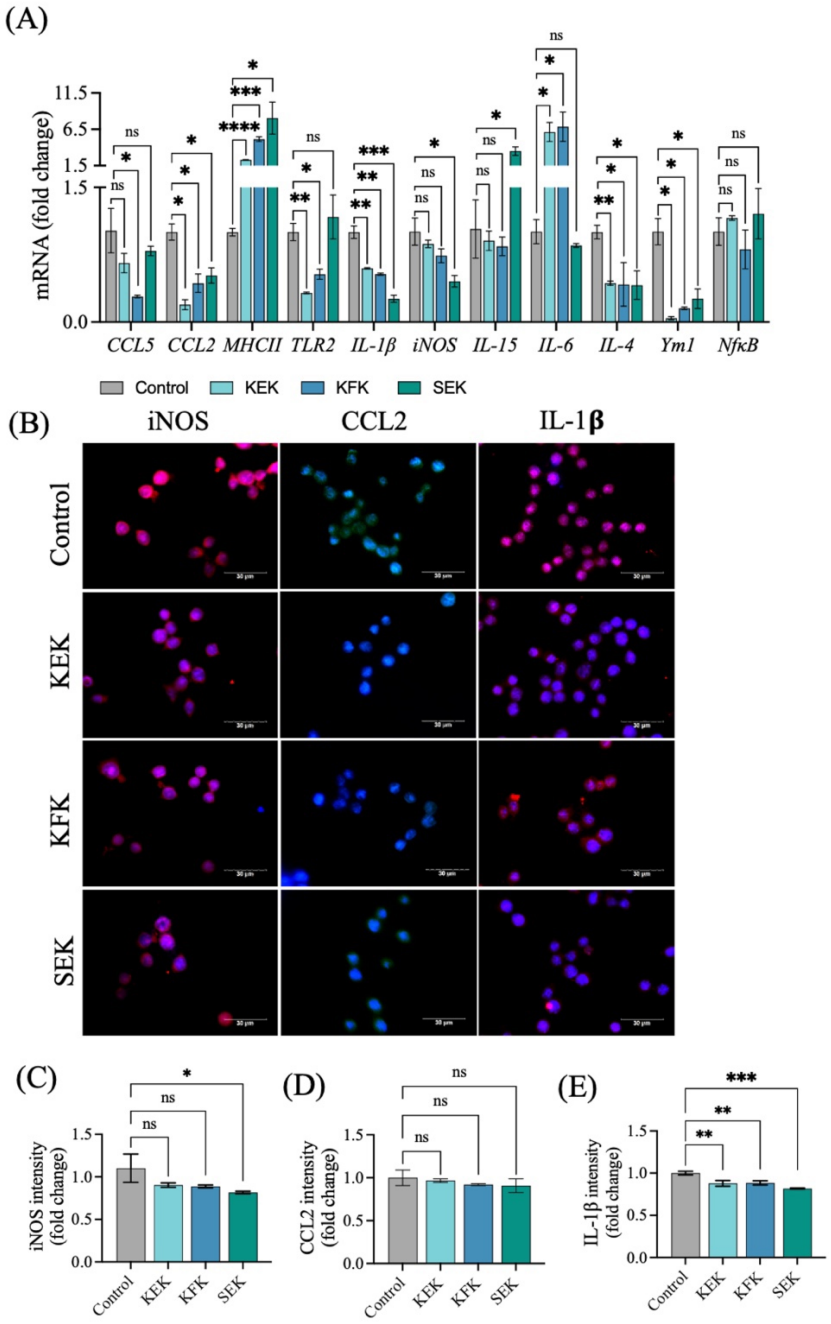

Figure 3.4. Investigation into immunotoxicity of CPNTs on murine RAW264.7 cells. (A) qRT-PCR analysis of pro- and anti-inflammatory cytokines after 24 h treatment. (B) Immunocytochemistry assessment for the expression of iNOS, CCL2, and IL-1β proteins. Scale bar: 30 µm. (C-E) Quantitative expression analysis of pro-inflammatory iNOS, CCL2, and IL-1β proteins. Untreated cells served as control. The data has been shown as mean ± standard deviation (n = 3), with *ns* denoting the insignificant difference and *P* values <0.05 (*), 0.01 (**), and 0.001 (***) were considered to be significant differences.

3.4.8. Proangiogenic potential of CPNTs in hyperglycemic (HG) conditions

Angiogenesis is a complex multifaceted process influenced by a myriad of factors and plays a crucial role in both physiological and pathological contexts. Impaired angiogenesis is prevalent

among diabetic vascular conditions because of the detrimental effects of hyperglycemia, causing upregulation of inflammatory factors, cytokines, and oxidative stress, which instigate endothelial dysfunction.[70,71] In concurrence with previous investigations, our studies have revealed that endothelial cells exhibit decreased expression of crucial proangiogenic genes when repeatedly exposed to hyperglycemic environment. These include Zeb1 (zinc finger E-box-binding homeobox 1), Tie2 (angiopoietin-1 receptor), FGF2 (fibroblast growth factor 2), vWF (von Willebrand factor), and eNOS (endothelial nitric oxide synthase) (**Figure A30, Appendix)**. Therefore, we employed cyclic peptide nanotubes against hyperglycemic endothelial cells and analyzed them for their proangiogenic potential.

3.4.8.1. Gene expression analysis

In the study, RT-PCR was utilized to evaluate the changes in gene expression associated with epithelial-mesenchymal transition (EMT) following the administration of CPNTs. This assessment covered an array of genes, including Zeb1, ETV2, vWF, eNOS, Tie2, TGF-β, VE-CAD, VEGF, FGF2, VEGFR2, and FGFR1(**Figure 3.5A**). The experiment involved treating HG HUVECs with CPNTs, KEK, KFK, and SEK for 24 hours. The results indicated a notable increase in Zeb1, ETV2, vWF, Tie2 and eNOS expression levels. Additionally, KEK and SEK treatments led to an enhanced expression of TGF-β. In contrast, a significant upregulation (14.40 ± 1.76, 2.23 ± 0.26, 2.54 ± 0.07, and 6.32 ± 1.01 folds) of VEGF, FGF2, VEGFR2, and FGFR1, respectively was exclusively observed in the SEK-treated cells (**Figure 3.5A**). Proangiogenic gene expression was markedly upregulated in HG HUVECs on incubation with SEK, indicating the production of EMT genes. As evidenced by the angiogenic gene profiling data, SEK nanotubes have pronounced angiogenic potential compared to others. The augmented gene expression observed upon treatment with SEK nanotubes can be attributed to the presence of heparin-mimicking functional groups, such as carboxylic acid, hydroxyl, and sulfonate, of which hydroxyl is not present in KEK and KFK. Interestingly, it was found that the mere presence of a sulfonate group is inadequate for achieving optimal angiogenic outcomes, emphasizing the significant contribution of the hydroxyl group to SEK's proangiogenic effects. Consequently, due to the heightened expression of proangiogenic genes in SEK-treated cells, the subsequent evaluations of the material's angiogenic potential focused exclusively on SEK.

3.4.8.2. Protein expression in hyperglycemic (HG) conditions

In HG HUVECs, the protein expression of VE-Cad, VEGFR2, FGFR1, and Zeb1 was downregulated (**Figure A31, Appendix)** but when exposed to SEK CPNTs, it became considerably elevated **(Figure 3.5B**). This upregulation was attributed to the modification of SEK with bioactive functional groups, specifically hydroxyl, carboxylic acid, and sulfate. These modifications were found to enhance the interaction between growth factors and their respective receptors, thereby initiating a sustained signaling pathway that effectively promotes

angiogenesis. Furthermore, these interactions serve to shield growth factors from degradation in chronic wound conditions and elevate their localized concentration for receptor-specific interactions. Based on immunoblotting study, the proteins VE-Cad, VEGFR2, FGFR1, and Zeb1 were found to have their expression elevated by 1.35 ± 0.08, 1.48 ± 0.06, 1.54 ± 0.085, and 1.17 ± 0.04 folds, respectively (**Figure 3.5C**). Proangiogenic protein expression in SEK-treated HG HUVECs was further investigated by immunocytochemistry analysis (**Figure 3.6**). The results indicated that SEK treatment effectively reinstated the expression of several critical angiogenic marker proteins, including Zeb1, a transcription factor associated with proangiogenic signaling, as well as endothelial cell surface markers, such as Tie2, CD31, and vWF. Furthermore, an augmented expression of the proangiogenic signaling molecule eNOS, as well as the growth factor receptors, VEGFR2 and FGFR2, was also observed. In comparison to untreated HG groups, we observed enhanced expression of Zeb1 by 10.20 ± 1.01 folds, Tie2 by 1.80 ± 0.03 folds, eNOS by 4.47 ± 0.23 folds, CD31 by 1.63 ± 0.14 folds, vWF by 3.73 ± 0.60 folds, VEGFR2 by 1.27 ± 0.03 folds, and FGFR2 by 1.20 ± 0.06 folds. These results underscore the potential of SEK in restoring angiogenic function in endothelial cells under chronic diabetic conditions and, thus, offering promising implications for therapeutic interventions targeting diabetes-related vascular complications.

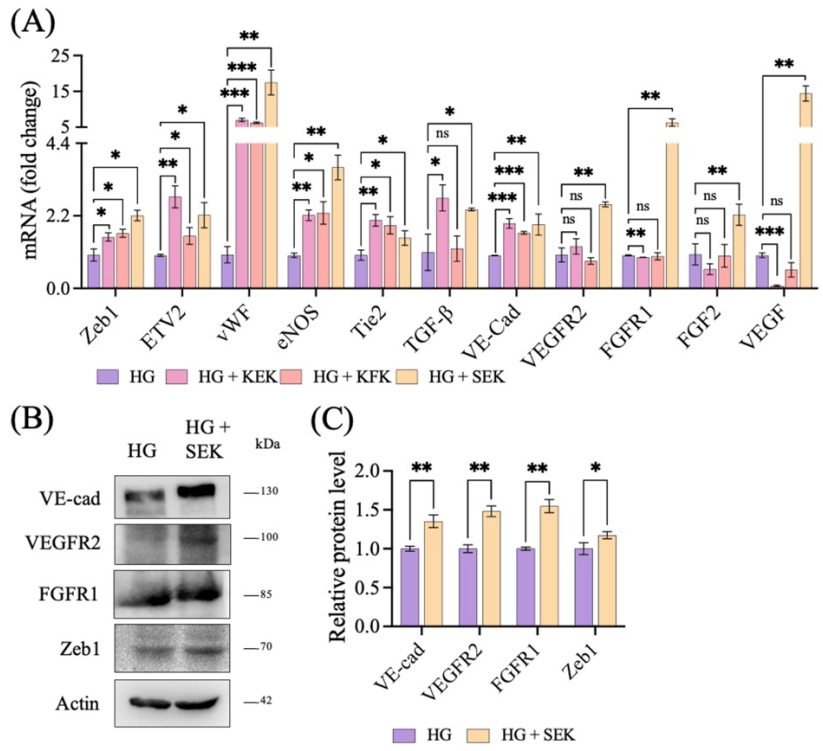

Figure 3.5. Expression profile of proangiogenic markers on SEK-treatment to hyperglycemic (HG) human umbilical vein endothelial cells (HUVECs). (A) Real-time qPCR investigation of proangiogenic genes after 24 h. (B, C) Immunoblotting and semiquantitative assessment of VE-cad, VEGFR2, FGFR1, and Zeb1 proteins expression. The data has been shown as mean ±

standard deviation (n = 3), with *ns* denoting the insignificant difference and *P* values <0.05 (*), 0.01 (**), and 0.001 (***) denoting significant differences

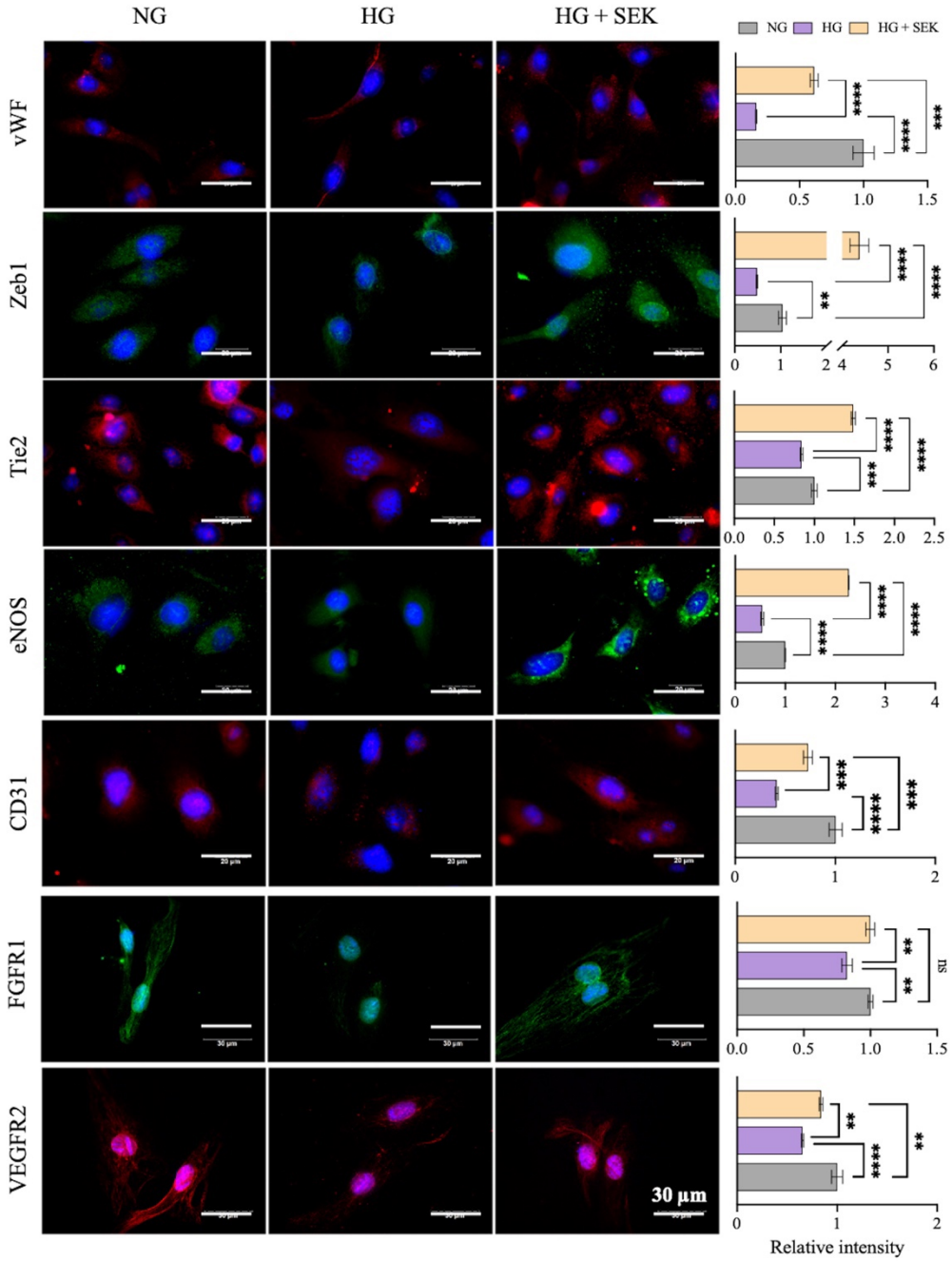

Figure 3.6. The expression profile of proangiogenic proteins in hyperglycemic (HG) human umbilical vein endothelial cells (HUVECs) using immunocytochemistry following a 24-hour incubation with SEK CPNTs. Scale bar: 30 µm. The data has been shown as mean ± standard deviation (n = 3), with *ns* denoting the insignificant difference and *P* values <0.05 (*), 0.01 (**), and 0.001 (***) denoting significant differences.

3.4.8.3. 2D and 3D cell migration in hyperglycemic (HG) conditions

The angiogenic signalling pathways, primarily mediated through the binding of vascular endothelial growth factor (VEGF) and fibroblast growth factor (FGF) to their respective receptors, have been shown to significantly influence cell migration, invasion, and proliferation. Therefore, a scratch-wound motility assay was performed to assess the impact of SEK nanotubes on cellular motility, focusing on the 2D-cell migration capabilities of HG HUVEC cells. The untreated HG HUVEC cells exhibited significantly reduced scratch healing abilities, which underscores a detrimental impact of high glucose levels on the natural healing and regeneration processes of endothelial cells. Conversely, when these HG cells were treated with SEK nanotubes, a noticeable improvement in scratch healing was observed within 48 hours. This improvement was attributed to the ability of SEK to augment cell migration by the activation of the angiogenic signaling pathways, a vital response for facilitating enhanced cellular migration and proliferation. The semiquantitative analysis by ImageJ software revealed that in the group treated with SEK nanotubes (HG + SEK), 62% healing of the scratch was observed, which was in contrast to the HG group, which showed only 38% healing (**Figure A32, Appendix**). The comparative analysis highlighted not only the detrimental effects of high glucose conditions on cell motility and wound healing but also underscored the potential therapeutic benefits of SEK nanotubes.

Further, the transwell cell migration and invasion analysis provided in-depth insights into the 3-D migratory behaviour of cells as they moved through physical barriers. The efficiency of HUVEC migration and invasion under HG conditions upon treatment with SEK was assessed using cell motility assays. Under HG circumstances, HUVECs' migratory and invasive activity was totally suppressed (**Figure 3.7A, C**); however, following the SEK administration for 24 hours, this activity improved. Crystal violet staining was used to quantify the increased cell migration and invasion. A plate reader was used to determine the absorbance at 590 nm after the sample was eluted with 33% acetic acid (**Figure A33, Appendix**). When treated with SEK, the proportion of invaded and migratory HUVECs in HG conditions increased by 16.42 and 35.93 times, respectively, in comparison to control HG cells. Transwell migration was found to be 2.19 times higher than in nonglycemic (NG) cells. Even in HG settings, the HG + SEK group demonstrated almost the same augmentation (1.12 times) of invaded cells as the NG group did in invasion experiments (**Figure 3.7B, D**), suggesting that SEK is actively stimulating angiogenesis in HG HUVECs.

3.4.8.4. Endothelial tube formation assay

Human umbilical vein endothelial cells (HUVECs) were grown on a Matrigel matrix in hyperglycemic (HG) conditions as shown in the schematic representation **(Figure A34, Appendix)** to explore the pro-angiogenic effects of SEK by assessing the tube formation ability. Consistent with the prior research, HG conditions were observed to deteriorate the endothelial

activity, as evidenced in the studied tube formation (**Figure 3.7E**). We observed that high glucose (HG) group compared with the normal glucose (NG) group, demonstrated a significant decrease in the several angiogenic markers, including the number of nodes formed, junctions, branches, and master junctions (**Figure 3.7F**), along with a reduction in the total length of master segments and tube length (**Figure 3.7G**). However, treatment with SEK resulted in a noticeable reversal of HG-induced impairments. The parameters indicative of tube formation showed a substantial increase in the SEK-treated group under HG conditions. Specifically, the number of nodes and junctions in SEK-treated HUVECs under HG conditions saw 7.75- and 9.5-fold increase, respectively, compared to untreated controls. Similarly, branch number, master segment length, and tube length saw improvements by factors of 3.4, 12.5, and 6.4, respectively, thus, showcasing the potent pro-angiogenic activity of SEK even under the stress of hyperglycemia.

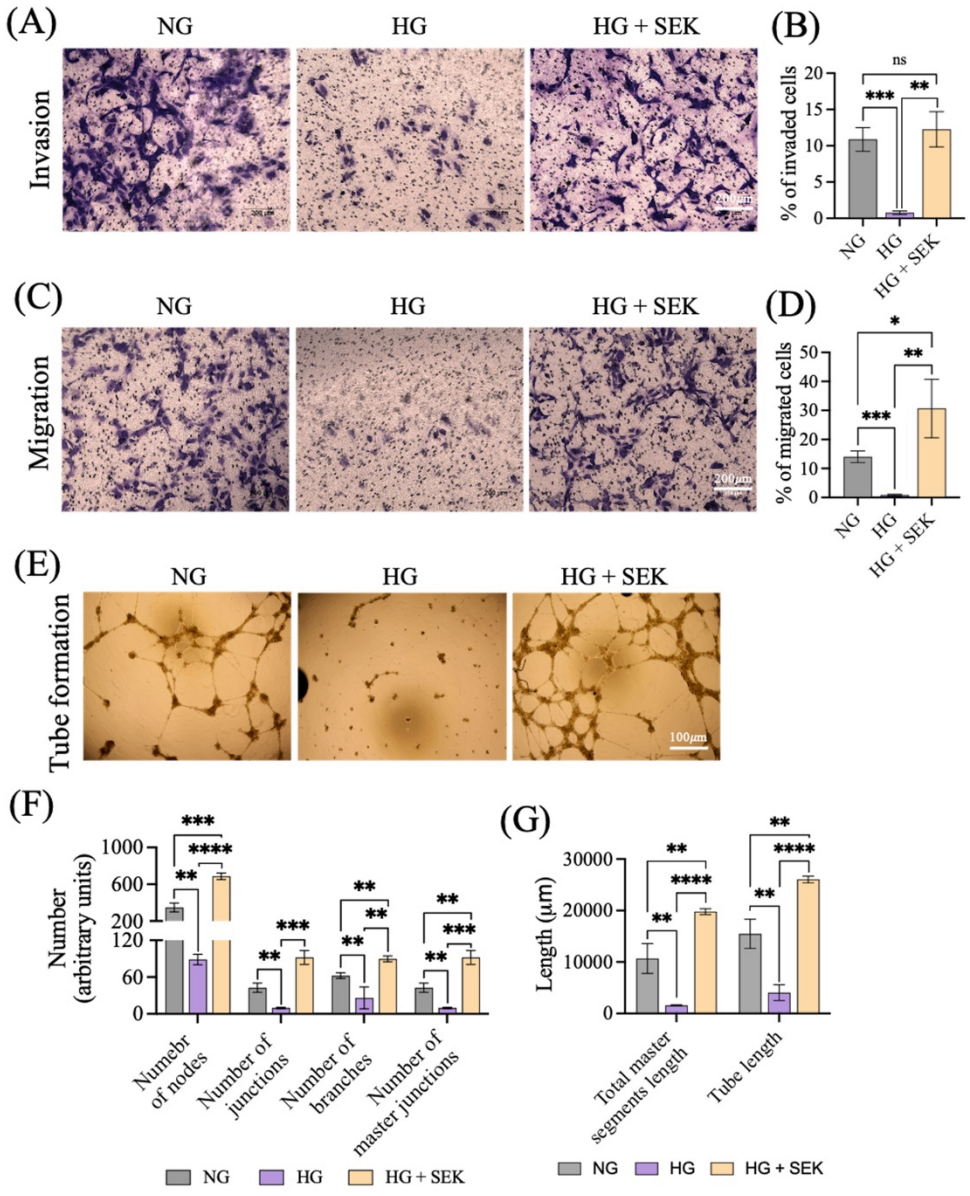

Figure 3.7. Transwell invasion/migration and endothelial tube formation assay upon 24 h treatment of HG HUVECs with SEK CPNTs. (A, C) Transwell invasion and migration assay. (B, D) Percentage increment in the cell invasion and migration compared to hyperglycemic HUVECs, taken as control. (E) Endothelial tube formation assay showcasing the increase in capillary tube structures. Scale bar: 100 μm. (F, G) Semiquantitative determination of capillary tube nodes, junctions, branches, master junctions, master segments length, and tube length. HG and non-glycemic (NG) served as controls. The data has been shown as mean ± standard deviation (n = 3), with *ns* denoting the insignificant difference and *P* values <0.05 (*), 0.01 (**), and 0.001 (***) denoting significant differences.

3.5. Conclusions

Compromised angiogenesis in diabetic wounds presents a substantial impediment to effective healing, as it constrains the genesis of new blood vessels pivotal for the delivery of nutrients and oxygen to the damaged tissue. This impairment not only retards the healing process but also escalates the susceptibility to infection and persistent inflammation. Recognizing this challenge, our research was directed to develop cyclic peptide nanotubes designed to foster angiogenesis independently of conventional drugs, growth factors or supplements, like heparin. The peptide nanotubes were functionalized with bioactive hydroxyl, carboxylic acid, and sulfonate groups, which provides the material with inherent ability to mimic the glycosaminoglycan, like heparan sulfate. Thus, by aiding the effective binding of proangiogenic growth factors, like VEGF and FGF2 to their receptors, these nanotubes can endogenously manipulate and promote the angiogenic signalling. The conformational rigidity of cyclic peptides will prevent its proteolytic degradation in chronic wound environment. Moreover, the cyclic peptide nanotubes did not induce ROS-stress, immunotoxicity, and exhibited optimal hemocompatibility. *In vitro* studies involving human umbilical vein endothelial cells showcased that SEK cyclic peptide nanotubes significantly upregulated the expression of crucial genes and proteins associated with angiogenesis. The angiogenic potential of these nanotubes is evidenced not only by their ability to stimulate the formation of capillary-like structures but also to exhibit the enhanced cell migration and invasion activities, even under hyperglycemic conditions. The studies conducted using KEK and KFK nanotubes has elucidated the influence of hydroxyl group on the angiogenic potential of heparan sulfate-mimicking biomaterials The observed results indicate that SEK nanotubes exhibited enhanced angiogenic properties in comparison to both KEK and KFK variants. The proangiogenic potential of the cyclic peptide nanotubes imitating heparan sulfate has never been explored. The attractiveness of this approach lies in its potential to obviate the need for external growth factors or other supplements, aligning in with the primary objective of this thesis. Building on the theme presented in Chapter 2, the peptide-based nanoassemblies developed here aim to simplify therapeutic strategies by addressing impaired angiogenesis, a

key factor in the delayed healing of chronic wounds. By leveraging their intrinsic properties, these systems have potential to reduce the complexities associated with the exogenously administered adjuvants and offer a potentially cost-effective alternative. However, the true efficacy and practical application of these peptide nanotubes in promoting angiogenesis will require further elucidation through comprehensive animal studies, thus, setting the stage for possible future clinical exploitation. Following the validation of biomaterial in pre-clinical and clinical models, these nanotubes can be used in conjunction with other dressing materials to comprehensively address the wound chronicity. The inherent complexity of chronic wounds frequently encompass multiple contributing factors and these nanotubes primarily aim to promote angiogenesis, effectively addressing one of the pivotal barriers to healing. Designed to degrade gradually over time, cyclic peptides will integrate seamlessly with the wound environment and facilitate the regenerative process, as their degradation products consist of amino acids that are naturally occurring in the body. Their application alongside existing therapeutic dressings would complement the broader therapeutic goals of standard wound care treatments.

References

(1) World Health Organization. *Global Report on Diabetes*; World Health Organization: Geneva, 2016.

(2) Saeedi, P.; Petersohn, I.; Salpea, P.; Malanda, B.; Karuranga, S.; Unwin, N.; Colagiuri, S.; Guariguata, L.; Motala, A. A.; Ogurtsova, K.; Shaw, J. E.; Bright, D.; Williams, R. Global and Regional Diabetes Prevalence Estimates for 2019 and Projections for 2030 and 2045: Results from the International Diabetes Federation Diabetes Atlas, 9th Edition. *Diabetes Research and Clinical Practice* **2019**, *157*, 107843.

(3) IDF Releases Report of Global Survey on Access to Medicines and Supplies for People with Diabetes. *Diabetes Research and Clinical Practice* **2017**, *129*, 224–225.

(4) Huang, C.; Yuan, W.; Chen, J.; Wu, L.-P.; You, T. Construction of Smart Biomaterials for Promoting Diabetic Wound Healing. *Molecules* **2023**, *28* (3), 1110.

(5) Brem, H.; Tomic-Canic, M. Cellular and Molecular Basis of Wound Healing in Diabetes. *J. Clin. Invest.* **2007**, *117* (5), 1219–1222.

(6) Ghosal, K.; Chakraborty, D.; Roychowdhury, V.; Ghosh, S.; Dutta, S. Recent Advancement of Functional Hydrogels toward Diabetic Wound Management. *ACS Omega* **2022**, *7* (48), 43364–43380.

(7) Mishra, A.; Kushare, A.; Gupta, M. N.; Ambre, P. Advanced Dressings for Chronic Wound Management. *ACS Appl. Bio Mater.* **2024**, *7* (5), 2660–2676.

(8) Okonkwo, U.; DiPietro, L. Diabetes and Wound Angiogenesis. *IJMS* **2017**, *18* (7), 1419.

(9) Dudley, A. C.; Griffioen, A. W. Pathological Angiogenesis: Mechanisms and Therapeutic Strategies. *Angiogenesis* **2023**, *26* (3), 313–347.

(10) Li, J.; Zhang, Y.; Kirsner, R. S. Angiogenesis in Wound Repair: Angiogenic Growth Factors and the Extracellular Matrix. *Microscopy Res & Technique* **2003**, *60* (1), 107–114.

(11) Rao, N.; Lee, Y. F.; Ge, R. Novel Endogenous Angiogenesis Inhibitors and Their Therapeutic Potential. *Acta Pharmacol Sin* **2015**, *36* (10), 1177–1190.

(12) Wang, X.; Li, R.; Zhao, H. Enhancing Angiogenesis: Innovative Drug Delivery Systems to Facilitate Diabetic Wound Healing. *Biomedicine & Pharmacotherapy* **2024**, *170*, 116035.

(13) Das, S.; Singh, G.; Majid, M.; Sherman, M. B.; Mukhopadhyay, S.; Wright, C. S.; Martin, P. E.; Dunn, A. K.; Baker, A. B. Syndesome Therapeutics for Enhancing Diabetic Wound Healing. *Adv Healthcare Materials* **2016**, *5* (17), 2248–2260.

(14) Monteforte, A. J.; Lam, B.; Das, S.; Mukhopadhyay, S.; Wright, C. S.; Martin, P. E.; Dunn, A. K.; Baker, A. B. Glypican-1 Nanoliposomes for Potentiating Growth Factor Activity in Therapeutic Angiogenesis. *Biomaterials* **2016**, *94*, 45–56.

(15) Zent, R.; Pozzi, A. Angiogenesis in Diabetic Nephropathy. *Seminars in Nephrology* **2007**, *27* (2), 161–171.

(16) Pal, D.; Das, P.; Mukherjee, P.; Roy, S.; Chaudhuri, S.; Kesh, S. S.; Ghosh, D.; Nandi, S. K. Biomaterials-Based Strategies to Enhance Angiogenesis in Diabetic Wound Healing. *ACS Biomater. Sci. Eng.* **2024**, *10* (5), 2725–2741.

(17) Shi, M.; Xia, L.; Chen, Z.; Lv, F.; Zhu, H.; Wei, F.; Han, S.; Chang, J.; Xiao, Y.; Wu, C. Europium-Doped Mesoporous Silica Nanosphere as an Immune-Modulating Osteogenesis/Angiogenesis Agent. *Biomaterials* **2017**, *144*, 176–187.

(18) Das, S.; Singh, S.; Dowding, J. M.; Oommen, S.; Kumar, A.; Sayle, T. X. T.; Saraf, S.; Patra, C. R.; Vlahakis, N. E.; Sayle, D. C.; Self, W. T.; Seal, S. The Induction of Angiogenesis by Cerium Oxide Nanoparticles through the Modulation of Oxygen in Intracellular Environments. *Biomaterials* **2012**, *33* (31), 7746–7755.

(19) Park, J. S.; Yang, H. N.; Yi, S. W.; Kim, J.-H.; Park, K.-H. Neoangiogenesis of Human Mesenchymal Stem Cells Transfected with Peptide-Loaded and Gene-Coated PLGA Nanoparticles. *Biomaterials* **2016**, *76*, 226–237.

(20) Mammadov, R.; Mammadov, B.; Toksoz, S.; Aydin, B.; Yagci, R.; Tekinay, A. B.; Guler, M. O. Heparin Mimetic Peptide Nanofibers Promote Angiogenesis. *Biomacromolecules* **2011**, *12* (10), 3508–3519.

(21) Yoo, S. Y.; Shrestha, K. R.; Jeong, S.-N.; Kang, J.-I.; Lee, S.-W. Engineered Phage Nanofibers Induce Angiogenesis. *Nanoscale* **2017**, *9* (43), 17109–17117.

(22) Burdick, J. A.; Prestwich, G. D. Hyaluronic Acid Hydrogels for Biomedical Applications. *Advanced Materials* **2011**, *23* (12).

(23) Wei, Z.; Volkova, E.; Blatchley, M. R.; Gerecht, S. Hydrogel Vehicles for Sequential Delivery of Protein Drugs to Promote Vascular Regeneration. *Advanced Drug Delivery Reviews* **2019**, *149–150*, 95–106.

(24) Daya, R.; Xu, C.; Nguyen, N.-Y. T.; Liu, H. H. Angiogenic Hyaluronic Acid Hydrogels with Curcumin-Coated Magnetic Nanoparticles for Tissue Repair. *ACS Appl. Mater. Interfaces* **2022**, *14* (9), 11051–11067.

(25) Li, M.-N.; Yu, H.-P.; Ke, Q.-F.; Zhang, C.-Q.; Gao, Y.-S.; Guo, Y.-P. Gelatin Methacryloyl Hydrogels Functionalized with Endothelin-1 for Angiogenesis and Full-Thickness Wound Healing. *J. Mater. Chem. B* **2021**, *9* (23), 4700–4709.

(26) Chen, H.; Cheng, R.; Zhao, X.; Zhang, Y.; Tam, A.; Yan, Y.; Shen, H.; Zhang, Y. S.; Qi, J.; Feng, Y.; Liu, L.; Pan, G.; Cui, W.; Deng, L. An Injectable Self-Healing Coordinative Hydrogel with Antibacterial and Angiogenic Properties for Diabetic Skin Wound Repair. *NPG Asia Mater* **2019**, *11* (1), 3.

(27) Wei, Z.; Volkova, E.; Blatchley, M. R.; Gerecht, S. Hydrogel Vehicles for Sequential Delivery of Protein Drugs to Promote Vascular Regeneration. *Advanced Drug Delivery Reviews* **2019**, *149–150*, 95–106.

(28) Augustine, R.; Hasan, A.; Dalvi, Y. B.; Rehman, S. R. U.; Varghese, R.; Unni, R. N.; Yalcin, H. C.; Alfkey, R.; Thomas, S.; Al Moustafa, A.-E. Growth Factor Loaded in Situ

Photocrosslinkable Poly(3-Hydroxybutyrate-Co-3-Hydroxyvalerate)/Gelatin Methacryloyl Hybrid Patch for Diabetic Wound Healing. *Materials Science and Engineering: C* **2021**, *118*, 111519.

(29) Long, G.; Liu, D.; He, X.; Shen, Y.; Zhao, Y.; Hou, X.; Chen, B.; OuYang, W.; Dai, J.; Li, X. A Dual Functional Collagen Scaffold Coordinates Angiogenesis and Inflammation for Diabetic Wound Healing. *Biomater. Sci.* **2020**, *8* (22), 6337–6349.

(30) Xiao, Z.; Zheng, X.; An, Y.; Wang, K.; Zhang, J.; He, H.; Wu, J. Zwitterionic Hydrogel for Sustained Release of Growth Factors to Enhance Wound Healing. *Biomater. Sci.* **2021**, *9* (3), 882–891.

(31) Whittam, A. J.; Maan, Z. N.; Duscher, D.; Wong, V. W.; Barrera, J. A.; Januszyk, M.; Gurtner, G. C. Challenges and Opportunities in Drug Delivery for Wound Healing. *Advances in Wound Care* **2016**, *5* (2), 79–88.

(32) Roy, S.; Sen, C. K. miRNA in Wound Inflammation and Angiogenesis. *Microcirculation* **2012**, *19* (3), 224–232.

(33) Devalliere, J.; Chang, W. G.; Andrejecsk, J. W.; Abrahimi, P.; Cheng, C. J.; Jane-wit, D.; Saltzman, W. M.; Pober, J. S. Sustained Delivery of Proangiogenic microRNA-132 by Nanoparticle Transfection Improves Endothelial Cell Transplantation. *FASEB j.* **2014**, *28* (2), 908–922.

(34) Gregory, P. A.; Bert, A. G.; Paterson, E. L.; Barry, S. C.; Tsykin, A.; Farshid, G.; Vadas, M. A.; Khew-Goodall, Y.; Goodall, G. J. The miR-200 Family and miR-205 Regulate Epithelial to Mesenchymal Transition by Targeting ZEB1 and SIP1. *Nat Cell Biol* **2008**, *10* (5), 593–601.

(35) Lucas, T.; Schäfer, F.; Müller, P.; Eming, S. A.; Heckel, A.; Dimmeler, S. Light-Inducible antimiR-92a as a Therapeutic Strategy to Promote Skin Repair in Healing-Impaired Diabetic Mice. *Nat Commun* **2017**, *8* (1), 15162.

(36) Shaabani, E.; Sharifiaghdam, M.; Faridi-Majidi, R.; De Smedt, S. C.; Braeckmans, K.; Fraire, J. C. Gene Therapy to Enhance Angiogenesis in Chronic Wounds. *Molecular Therapy - Nucleic Acids* **2022**, *29*, 871–899.

(37) Veith, A. P.; Henderson, K.; Spencer, A.; Sligar, A. D.; Baker, A. B. Therapeutic Strategies for Enhancing Angiogenesis in Wound Healing. *Advanced Drug Delivery Reviews* **2019**, *146*, 97–125.

(38) Hsieh, M.-C. W.; Wang, W.-T.; Lin, C.-Y.; Kuo, Y.-R.; Lee, S.-S.; Hou, M.-F.; Wu, Y.-C. Stem Cell-Based Therapeutic Strategies in Diabetic Wound Healing. *Biomedicines* **2022**, *10* (9), 2085.

(39) Shen, H.; Ma, Y.; Qiao, Y.; Zhang, C.; Chen, J.; Zhang, R. Application of Deferoxamine in Tissue Regeneration Attributed to Promoted Angiogenesis. *Molecules* **2024**, *29* (9), 2050.

(40) Li, Z.; Zhu, Y.; Matson, J. B. pH-Responsive Self-Assembling Peptide-Based Biomaterials: Designs and Applications. *ACS Appl. Bio Mater.* **2022**, *5* (10), 4635–4651.

(41) Chen, J.; Zou, X. Self-Assemble Peptide Biomaterials and Their Biomedical Applications. *Bioactive Materials* **2019**, *4*, 120–131.

(42) Huang, L.-C.; Wang, H.-C.; Chen, L.-H.; Ho, C.-Y.; Hsieh, P.-H.; Huang, M.-Y.; Wu, H.-C.; Wang, T.-W. Bioinspired Self-Assembling Peptide Hydrogel with Proteoglycan-Assisted Growth Factor Delivery for Therapeutic Angiogenesis. *Theranostics* **2019**, *9* (23), 7072–7087.

(43) Guo, H.; Cui, G.; Yang, J.; Wang, C.; Zhu, J.; Zhang, L.; Jiang, J.; Shao, S. Sustained Delivery of VEGF from Designer Self-Assembling Peptides Improves Cardiac Function after Myocardial Infarction. *Biochemical and Biophysical Research Communications* **2012**, *424* (1), 105–111.

(44) Carmeliet, P.; Jain, R. K. Molecular Mechanisms and Clinical Applications of Angiogenesis. *Nature* **2011**, *473* (7347), 298–307.

(45) Galler, K. M.; Aulisa, L.; Regan, K. R.; D'Souza, R. N.; Hartgerink, J. D. Self-Assembling Multidomain Peptide Hydrogels: Designed Susceptibility to Enzymatic Cleavage Allows Enhanced Cell Migration and Spreading. *J. Am. Chem. Soc.* **2010**, *132* (9), 3217–3223.

(46) Lee, S.-J.; Sohn, Y.-D.; Andukuri, A.; Kim, S.; Byun, J.; Han, J. W.; Park, I.-H.; Jun, H.-W.; Yoon, Y. Enhanced Therapeutic and Long-Term Dynamic Vascularization Effects of Human Pluripotent Stem Cell–Derived Endothelial Cells Encapsulated in a Nanomatrix Gel. *Circulation* **2017**, *136* (20), 1939–1954.

(47) Kumar, V. A.; Taylor, N. L.; Shi, S.; Wang, B. K.; Jalan, A. A.; Kang, M. K.; Wickremasinghe, N. C.; Hartgerink, J. D. Highly Angiogenic Peptide Nanofibers. *ACS Nano* **2015**, *9* (1), 860–868.

(48) Mammadov, R.; Mammadov, B.; Toksoz, S.; Aydin, B.; Yagci, R.; Tekinay, A. B.; Guler, M. O. Heparin Mimetic Peptide Nanofibers Promote Angiogenesis. *Biomacromolecules* **2011**, *12* (10), 3508–3519.

(49) Liu, X.; Wang, X.; Horii, A.; Wang, X.; Qiao, L.; Zhang, S.; Cui, F.-Z. In Vivo Studies on Angiogenic Activity of Two Designer Self-Assembling Peptide Scaffold Hydrogels in the Chicken Embryo Chorioallantoic Membrane. *Nanoscale* **2012**, *4* (8), 2720.

(50) Sarkar, B.; Nguyen, P. K.; Gao, W.; Dondapati, A.; Siddiqui, Z.; Kumar, V. A. Angiogenic Self-Assembling Peptide Scaffolds for Functional Tissue Regeneration. *Biomacromolecules* **2018**, *19* (9), 3597–3611.

(51) Wang, L.; Wang, N.; Zhang, W.; Cheng, X.; Yan, Z.; Shao, G.; Wang, X.; Wang, R.; Fu, C. Therapeutic Peptides: Current Applications and Future Directions. *Sig Transduct Target Ther* **2022**, *7* (1), 48.

(52) Hartgerink, J. D.; Granja, J. R.; Milligan, R. A.; Ghadiri, M. R. Self-Assembling Peptide Nanotubes. *J. Am. Chem. Soc.* **1996**, *118* (1), 43–50

(53) Diaferia, C.; Netti, F.; Ghosh, M.; Sibillano, T.; Giannini, C.; Morelli, G.; Adler-Abramovich, L.; Accardo, A. Bi-Functional Peptide-Based 3D Hydrogel-Scaffolds. *Soft Matter* **2020**, *16* (30), 7006–7017.

(54) Li, Y.; Sun, M.; Liu, Y.; Liang, J.; Wang, T.; Zhang, Z. Gymnemic Acid Alleviates Type 2 Diabetes Mellitus and Suppresses Endoplasmic Reticulum Stress *in Vivo* and *in Vitro*. *J. Agric. Food Chem.* **2019**, *67* (13), 3662–3669.

(55) Roy, S.; Halder, M.; Ramprasad, P.; Dasgupta, S.; Singh, Y.; Pal, D. Oxidized Pullulan Exhibits Potent Antibacterial Activity against S. Aureus by Disrupting Its Membrane Integrity. *International Journal of Biological Macromolecules* **2023**, *249*, 126049.

(56) Liang, C.-C.; Park, A. Y.; Guan, J.-L. In Vitro Scratch Assay: A Convenient and Inexpensive Method for Analysis of Cell Migration in Vitro. *Nat Protoc* **2007**, *2* (2), 329–333.

(57) Abdulkadir, S.; Li, C.; Jiang, W.; Zhao, X.; Sang, P.; Wei, L.; Hu, Y.; Li, Q.; Cai, J. Modulating Angiogenesis by Proteomimetics of Vascular Endothelial Growth Factor. *J. Am. Chem. Soc.* **2022**, *144* (1), 270–281.

(58) Zhang, Y.; Remy, M.; Leste-Lasserre, T.; Durrieu, M.-C. Manipulating Stem Cell Fate with Disordered Bioactive Cues on Surfaces: The Role of Bioactive Ligand Selection. *ACS Appl. Mater. Interfaces* **2024**, *16* (15), 18474–18489.

(59) Waterborg, J. H. The Lowry Method for Protein Quantitation. In *The Protein Protocols Handbook*; Walker, J. M., Ed.; Springer Protocols Handbooks; Humana Press: Totowa, NJ, 2009; pp 7–10.

(60) Banerjee, D.; Patra, D.; Sinha, A.; Roy, S.; Pant, R.; Sarmah, R.; Dutta, R.; Kanta Bhagabati, S.; Tikoo, K.; Pal, D.; Dasgupta, S. Lipid-Induced Monokine Cyclophilin-A Promotes Adipose Tissue Dysfunction Implementing Insulin Resistance and Type 2 Diabetes in Zebrafish and Mice Models of Obesity. *Cell. Mol. Life Sci.* **2022**, *79* (5), 282.

(61) Patra, D.; Roy, S.; Arora, L.; Kabeer, S. W.; Singh, S.; Dey, U.; Banerjee, D.; Sinha, A.; Dasgupta, S.; Tikoo, K.; Kumar, A.; Pal, D. *miR-210-3p* Promotes Obesity-Induced Adipose Tissue Inflammation and Insulin Resistance by Targeting SOCS1-Mediated NF-κB Pathway. *Diabetes* **2023**, *72* (3), 375–388.

(62) Nagabhishek, S. N.; Madan Kumar, A.; B., S.; Balakrishnan, A.; Katakia, Y. T.; Chatterjee, S.; Nagasundaram, N. A Marine Sponge Associated Fungal Metabolite Monacolin X Suppresses Angiogenesis by down Regulating VEGFR2 Signaling. *RSC Adv.* **2019**, *9* (46), 26646–26667.

(63) Carpentier, G.; Berndt, S.; Ferratge, S.; Rasband, W.; Cuendet, M.; Uzan, G.; Albanese, P. Angiogenesis Analyzer for ImageJ — A Comparative Morphometric Analysis of "Endothelial Tube Formation Assay" and "Fibrin Bead Assay." *Sci Rep* **2020**, *10* (1), 11568.

(64) Liu, Z.; Yang, S.; Li, X.; Wang, S.; Zhang, T.; Huo, N.; Duan, R.; Shi, Q.; Zhang, J.; Xu, J. Local Transplantation of GMSC-Derived Exosomes to Promote Vascularized Diabetic Wound Healing by Regulating the Wnt/β-Catenin Pathways. *Nanoscale Adv.* **2023**, *5* (3), 916–926.

(65) Freeman, I.; Kedem, A.; Cohen, S. The Effect of Sulfation of Alginate Hydrogels on the Specific Binding and Controlled Release of Heparin-Binding Proteins. *Biomaterials* **2008**, *29* (22), 3260–3268.

(66) Kim, S. H.; Kiick, K. L. Heparin-Mimetic Sulfated Peptides with Modulated Affinities for Heparin-Binding Peptides and Growth Factors. *Peptides* **2007**, *28* (11), 2125–2136.

(67) Christman, K. L.; Vázquez-Dorbatt, V.; Schopf, E.; Kolodziej, C. M.; Li, R. C.; Broyer, R. M.; Chen, Y.; Maynard, H. D. Nanoscale Growth Factor Patterns by Immobilization on a Heparin-Mimicking Polymer. *J. Am. Chem. Soc.* **2008**, *130* (49), 16585–16591.

(68) Ding, Y.; Lambden, E.; Peate, J.; Picken, L. J.; Rees, T. W.; Perez-Ortiz, G.; Newgas, S. A.; Spicer, L. A. R.; Hicks, T.; Hess, J.; Ulmschneider, M. B.; Müller, M. M.; Barry, S. M. Rapid Peptide Cyclization Inspired by the Modular Logic of Nonribosomal Peptide Synthetases. *J. Am. Chem. Soc.* **2024**, *146* (24), 16787–16801.

(69) Shivange, A. V.; Daugherty, P. S. De Novo Discovery of Bioactive Cyclic Peptides Using Bacterial Display and Flow Cytometry. In *Peptide Libraries*; Derda, R., Ed.; Methods in Molecular Biology; Springer New York: New York, NY, 2015; Vol. 1248, pp 139–153.

(70) Fadini, G. P.; Albiero, M.; Bonora, B. M.; Avogaro, A. Angiogenic Abnormalities in Diabetes Mellitus: Mechanistic and Clinical Aspects. *The Journal of Clinical Endocrinology & Metabolism* **2019**, *104* (11), 5431–5444.

(71) Singh, K.; Pal, D.; Sinha, M.; Ghatak, S.; Gnyawali, S. C.; Khanna, S.; Roy, S.; Sen, C. K. Epigenetic Modification of MicroRNA-200b Contributes to Diabetic Vasculopathy. *Molecular Therapy* **2017**, *25* (12), 2689–2704.

CHAPTER - 4

ALP-mimetic cyclic peptide nanotubes for osteogenic differentiation and bone mineralization

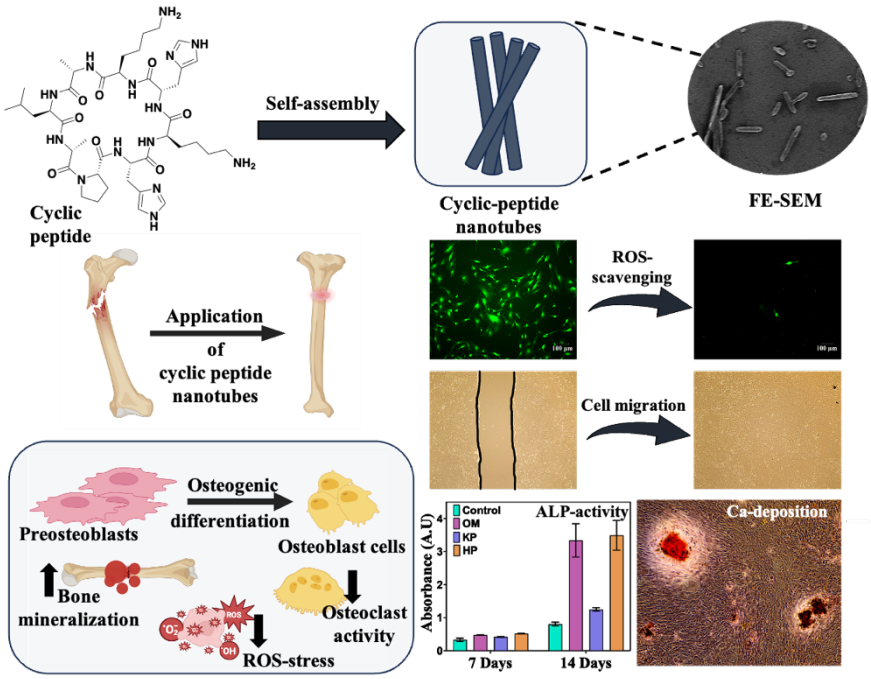

ToC graphic

Chapter 4

Cyclic peptide nanotubes for bone regeneration

4.1. Introduction

4.1.1. Bone regeneration

Bone, a dense connective tissue integral to the human structure, undergoes constant remodeling throughout the life of an individual to optimize its function and structure.[1] Its composition largely includes cells, extracellular matrix (ECM) primarily containing collagen fibrils, hydroxyapatite (HA), and various bound minerals.[2] Remarkably, collagen and HA encompass approximately 95% of bone's composition under dry conditions, illustrating the pivotal role these components play in bone's physical properties.[3] The dual nature of bone as both a supportive and protective element underscores its critical role by not only facilitating the movement by anchoring muscles but also by safeguarding vital organs from external threats. Additionally, it plays a key role in blood cell production, calcium homeostasis, and acid/base buffering.[4] The dynamic quality of bone facilitates an intrinsic regenerative capability, constantly balancing the resorption of old bone with the deposition of new bone.[5] Bone regeneration is a complex process involving diverse cell types, including osteogenic stem cells, osteoblasts, osteocytes, and osteoclasts. Osteoblasts play a pivotal role in bone growth and remodeling by synthesizing, depositing, and mineralizing the bone matrix by producing a protein composite known as osteoid. Osteocytes, originating from MSCs, are quiescent osteoblasts that become ensnared within the bone they have formed and are crucial for intercellular communication within bone tissue. Osteoclasts secrete enzymes and acids to dissolve and digest minerals in the bone, leading to the bone resorption.[6] The bone regeneration process typically initiates with the formation of a hematoma (blood clot) at the fracture site and infiltration of inflammatory cells, neutrophils, and macrophages at the fracture site. The next stage involves the invasion of fibroblasts and new capillaries to the hematoma leading to the formation of granulation tissue. Chondrocytes and fibroblasts produce collagen and cartilage, forming a soft callus around the fracture. Soft callus is gradually replaced by the hard callus (woven immature bone) by endochondral ossification. Osteoblasts produce new bone tissue, transforming the cartilage into woven bone. The woven immature bone is then remodeled into stronger, lamellar bone. Osteoclasts resorb the old bone, while osteoblasts form new bone, thus, restoring the bone's original shape and strength.[7]

4.1.2. Challenges

The natural bone remodeling process enables bones to heal autonomously in instances of minor damage without the necessity for medical intervention.[8,9] However, clinical interventions are required where the magnitude of bone loss or damage exceeds the natural regenerative capacity of bone.[10] Severe bone defects can be caused by the presence of diseases such as osteogenesis

imperfecta,[11] rheumatoid arthritis,[12] osteoporosis,[13] or conditions resulting from tumor resection,[14] severe trauma,[15] infection,[16] and congenital malformations.[17] Age and nutritional deficiencies also leads to decreased bone regeneration capacity due to the decline in cellular functions. Further, the comorbid conditions like diabetes impairs the inflammatory response, vascularization and also lead to infections affecting the bone regeneration.[18] Bone-specific diseases such as osteoporosis and bone tumors, as well as joint inflammatory diseases including rheumatoid arthritis and ankylosing spondylitis, are associated with increased levels of reactive oxygen species (ROS). The elevation in ROS stress within affected bones leads to the induction of cell death in both osteoblast precursors and mature osteoblasts, subsequently hindering the process of osteogenic differentiation.[19] These bone defects have become a serious public concern and a global burden, with an increase in the cases of fractures by 33·4% in 2019. Since 1990, 455 million cases of acute or long-term symptoms of a fracture have been reported. Globally, there were around 178 million new fractures in 2019.[20] Low bone mineral density and osteoporosis have increased the risk of severe fractures, with more than 8.9 million fractures annually occurring due to osteoporosis.[21]

4.1.3. Research gap

Current treatment modalities for bone repair and reconstruction primarily rely on auto/allo bone grafts, with autografts being regarded as the gold standard for small bone tissue reconstruction. Despite their widespread use, bone grafts present several challenges including the potential risk of immunological rejection, scarcity of graft materials, morbidity at the donor site, and the necessity for subsequent surgeries.[22] In recent years, various bioactive scaffolds obtained from the biomaterials like natural and synthetic polymers, metals, ceramics and their composites have emerged as pivotal means to replicate the structure and functionality of the natural bone extracellular matrix (ECM). These scaffolds offer a three-dimensional (3D) environment conducive for cellular adhesion, proliferation, and differentiation, all while possessing sufficient physical traits requisite for bone repair. Moreover, the integration of these scaffolds with various additives, including drugs, growth factors (GFs), and stem cells, has emerged as an effective treatment strategy, further enhancing their therapeutic potential in bone regeneration applications.[23] Jansen *et al*. have reported the fabrication of growth factors rhTGF-β1- and rhBMP-2- loaded Ti-fiber mesh and CaP cement scaffolds for increased regeneration of bones.[24] Similarly, Liu and coworkers developed Nb-Ti-Ta alloy scaffolds with different porosities for bone tissue engineering.[25] A microporous 3D collagen scaffold fabricated from fibrillated collagen for bone tissue regeneration has been reported by Lee *et al*.[26] Fielding *et a*l. have developed a 3D-printed osteoconductive β-tricalcium phosphate (TCP) scaffold supplemented with metal oxide dopants silica (SiO_2) and zinc oxide (ZnO) to promote osteoinduction.[27] VEGF-loaded gelatin/hydroxyapatite cryogel scaffold has been reported by Ozturk and coworkers for the treatment of bone defects in rabbit tibiae.[28] Raja *et al*. developed a 3D printed

bioceramic (α-TCP) and MC3T3-E1 cell laden alginate gel as core/shell scaffolds for the bone regeneration.[29]

These scaffolds have shown very promising results, however, there are certain associated challenges and disadvantages. The utilization of metal-based scaffolds is hindered by their non-biodegradable nature, necessitating additional surgery for removal. Additionally, there exists a risk of particle leaching and associated toxicity. Bioactive ceramics face limitations due to inconsistent degradation rates and osteogenic speed. Natural polymeric scaffolds exhibit low mechanical strength, whereas synthetic scaffolds degrade over a prolonged period, diminishing their effectiveness.[30] The challenges with the use of growth factors are their stability, dosage, high cost along with their controlled and sustained release.[31] The use of allogeneic cells can lead to immunogenic response and tumorigenesis.[32] The immobilized native enzyme-based scaffolds have also been explored in the bone regeneration studies. Osathanon *et al*. have shown the immobilization of alkaline phosphatase (ALP) onto the microporous nanofibrous fibrin scaffolds for bone regeneration.[33] The utilization of immobilized native enzyme-based scaffolds has been studied within the context of bone regeneration. Nevertheless, the complexities of processes associated with enzyme purification and handling, coupled with the notable variability in bioactivity observed across different batches of purified enzymes, serve as significant obstacles to their broad application as regenerative scaffolds. These challenges not only escalate the expense but also limit the practicality of employing native enzymes in tissue regeneration.[34]

4.1.4. Self-assembled peptides

Peptide-based scaffolds exhibit favorable biocompatibility due to their degradation products being primarily amino acids, which are readily metabolized by the body. This inherent compatibility underscores their potential in biomedical applications, particularly bone repair. However, the complex nature of bone defects necessitates that peptide-based hydrogels designed for bone repair possess controlled properties that are finely tuned to meet the specific requirements of bone regeneration. Achieving these tailored properties requires strategic modifications of the peptide chains constituting the biomaterial. By systematically altering the peptide structures, it is possible to significantly enhance the functional attributes of the hydrogels, such as improved mechanical stiffness, facilitation of drug delivery, and increased biological activity.[35] Peptide scaffolds have been explored as a carrier for the delivery of bioactive substances (drugs, growth factors, and cells) as well as the functional scaffolds for the bone regeneration. Quan *et al*. fabricated a self-assembled peptide gel from BMP-2 core sequence oligopeptide, cell adhesive RGDS peptide, phosphoserine, and polyaspartic acid, which incorporated rat marrow mesenchymal stem cells (rMSCs) to differentiate them towards osteogenic lineage.[36] Further, Stupp and coworkers reported peptide amphiphile nanofibers containing a BMP-2 binding domain that can bind the exogenous as well endogenous BMP-2 for use in bone regeneration.[37] Zhou *et al*. reported the controlled release of TGF-β1 from RADA

self-assembling peptide gel scaffolds.[38] Rapaport and group developed acidic rich β-sheet peptides as a templates to induce the adsorption or *in situ* nucleation of amorphous calcium phosphate.[39] Sugino *et al*. explored the ability of polyglutamic acid hydrogels to stimulate the formation of hydroxyapatite.[40] Moreover, the modification of the side chains of peptide by phosphorylation has also been reported to induce the bone mineralization.[41] Spoerke *et al*. developed a system that employed a phosphorylated, anionic nanofiber gel matrix and natural enzyme alkaline phosphatase to template HA nanocrystals.[42].

4.2. Objectives

In the previous sections, we have discussed the application and challenges with different scaffolds and bioactive molecules used for bone regeneration. The exogenous delivery of growth factors, cells, drugs and enzymes suffer from various drawbacks that limit their efficacy and have potential side effects as well. This highlights a dire need for the development of artificial enzyme-based nanostructures that can mimic the activity of enzymes by embedding active functional groups within their composition, thereby offering a promising avenue to overcome the aforementioned challenges. Therefore, our objective was to develop cyclic peptide nanotubes that mimic the activity of alkaline phosphatase to enhance osteogenic differentiation and bone mineralization. The cyclic peptide nanotubes were fabricated using cyclic octa peptide, ^{L}His-^{D}Lys-^{L}His-^{D}Lys-^{L}Ala-^{D}Leu-^{L}Ala-^{D}Pro, incorporating histidine residues in the sequence. Histidine amino acids present in the active domain of ALP strongly affects its catalytic activity as their significance lies in the versatility of their imidazole rings that at physiological pH can act as general bases or acids or even serve as nucleophiles with the assistance of metals.[43] These imidazole rings facilitate the complexation of organophosphates onto the enzyme and deprotonates the water, thus, converting it into a nucleophile. The deprotonated water then cleaves the phosphate monoester and starts the mineralization of hydroxyapatite.[44] Further, the fabrication of artificial proteinases with imidazole as a sole catalytic group requires the strategic positioning of two or more rings in close proximity.[43] The self-assembly of cyclic peptides into nanotubes will not only enhance the surface area but will also keep the multiple imidazole rings in close proximity, thereby augmenting the concentration of reaction loci. The nanotubes were fabricated from cyclic octapeptide by a pH-switch method in ACN/H_2O in 50:50 under alkaline conditions and investigated their morphology using FE-SEM and HR-TEM. The catalytic activity of the material was analyzed by pNPP hydrolysis. The material was assessed for its cytocompatibility on osteoblast precursor MC3T3-E1 cells. Cyclic peptide nanotubes were then investigated for their ROS scavenging ability using ABTS and DCFDA assay. The osteogenic differentiation and bone mineralization potential was evaluated by calcium deposition, ALP production and expression level of various osteogenic marker genes like Runx2, osteopontin, osteocalcin, and ALP by qRT-PCR. We also investigated the immunogenic response to the treatment with nanotubes using M1 and M2 phase marker expression analysis. An osteoblast

and macrophage co-culture approach has been used to demonstrate the osteogenic and anti-osteoclastogenic characteristics. Thus, the ALP-mimetic peptide-based nanotubes provide a promising approach to promote the bone regeneration.

4.3. Experimental section

4.3.1. Materials

Unless otherwise specified, all chemicals and solvents were of a high analytical standard and were used without further purification. For the synthesis of peptides, 2-chlorotrityl chloride resin with a mesh size of 200–400 and a loading capacity of 1.00–1.80 mmol/g was purchased from Novabiochem. BLD Pharmaceuticals provided the amino acids Fmoc-His(trt)-OH, Fmoc-^{D}Pro-OH, Fmoc-^{D}Lys(Boc)-OH, Fmoc-Ala-OH, and Fmoc-^{D}Leu-OH. Sigma Aldrich supplied the anhydrous N, N-dimethylformamide (DMF), 2′,7′-dichlorodihydrofluorescein diacetate (DCFDA), and 2,2′-azino-bis (3-ethylbenzothiazoline-6-sulfonic acid) diammonium salt (ABTS). Trifluoroacetic acid (TFA), triisopropyl silane (TIS), N,N-diisopropylethylamine (DIEA), HATU, and 4-nitrophenylphosphate (pNPP) were acquired from TCI Chemicals. We obtained dimethyl sulfoxide (DMSO) from Merck. Dichloromethane (DCM) and piperidine were procured from Spectrochem and Rankem Laboratories. Solid-phase peptide synthesis was carried out using Bio-Rad PolyPrep chromatography columns (SPPS). All of the studies utilized deionized water (DI, 18.2 MΩ cm), which was obtained from a Milli-Q system. The ATCC supplied MC3T3-E1 cells (CRL-2593, Subclone-4). Thermo Fisher Scientific provided MEM-α, 0.25% trypsin/EDTA, penstrep, SYBR^{TM} Green Master Mix, and trizol. Fetal bovine serum (FBS), ascorbic acid, 4',6-diamidino-2-phenylindole, dihydrochloride (DAPI), and (3-(4,5-dimethylthiazol)-2,5-diphenyltetrazolium bromide (MTT reagent) were obtained from Himedia. We purchased Phalloidin, Alexa Fluor^{TM} 488, and the LIVE/DEAD^{TM} Viability/Cytotoxicity Kit for mammalian cells from Invitrogen. Bio-Rad supplied the iScript^{TM} cDNA synthesis kit.

4.3.2. Synthesis of linear peptides

Solid-phase peptide synthesis (SPPS) was employed to synthesize linear peptides utilizing 2-chlorotrityl chloride (CTC) resin with a specific loading capacity ranging from 1.80–1.95 mmol/g. Bio-rad PolyPrep chromatography columns were used to carry out the synthesis. For overnight swelling, 100 mg of CTC resin beads were soaked in 1 mL of dichloromethane (DCM). Using DIPEA as a base, the first amino acid was attached to the solid support. After shaking the resin and amino acid with 4.5 eq of DIPEA for 10 min, 10.5 eq of additional DIPEA was added, and shaking was carried out for another 3 h. In order to cap the unreacted groups on the resin, methanol was added after 3 h, and the column was shaken for another 10 min. The remaining amino acids were coupled using 2.85 equiv of HATU as a coupling agent with 5.7 equiv of DIPEA as a base. The Fmoc deprotection was performed using 20% piperidine in DMF. Following a 3-4 h coupling reaction, Fmoc deprotection was carried out for 45 min. Each step was followed by three washings of resin with 1 mL of DMF and DCM. After the complete

synthesis, the peptide was cleaved from the resin using 1% TFA in DCM and precipitated in ice-cold diethyl ether. The centrifugation was performed at 8000 rpm for 10 min to collect the precipitates and then dried under vacuum. Following this protocol, we synthesized two octapeptides, ^{L}Ala-^{D}Lys-^{L}Ala-^{D}Lys-^{L}Ala-^{D}Leu-^{L}Ala-^{D}Pro and ^{L}Ala-^{D}Leu-^{L}Ala-^{D}Lys-^{L}His-^{D}Lys-^{L}His-^{D}Pro, and characterized them by mass spectrometry.

4.3.3. Synthesis and characterization of cyclic peptides

A 0.5 mM solution of the linear peptide was prepared in DCM to carry out cyclization using a high-dilution approach. The cyclization was performed using 6.5 eq. of HBTU and 7.36 eq. of HOBt with DIPEA as a base. The reaction was carried out at ice-cold temperature by stirring in a round bottom flask for five days. Thin-layer chromatography (TLC) indicated the completion of the reaction. Next, the reaction workup was performed using a separatory funnel employing brine solution (×1), DI H_2O (×2), and 0.1 M HCl (×3). The cyclic peptide was subsequently collected after vacuum evaporation of the DCM layer. A cleavage cocktail consisting of 95% TFA, 2.5% triisopropyl silane, and 2.5% H_2O was used to deprotect the side chains of the cyclic peptide following cyclization. Both the cyclic peptides, ^{L}Ala-^{D}Lys-^{L}Ala-^{D}Lys-^{L}Ala-^{D}Leu-^{L}Ala-^{D}Pro and ^{L}Ala-^{D}Leu-^{L}Ala-^{D}Lys-^{L}His-^{D}Lys-^{L}His-^{D}Pro, were synthesized by similar procedure. HR-MS (XEVO G2-XS QTOF) was then used to analyze the cyclic peptides. We employed the JASCO J-1500 circular dichroism spectrophotometer to ascertain the secondary structures of peptides. Fourier Transform Infrared (FT-IR) spectroscopy was carried out using a Bruker Tensor 27 instrument in the Attenuated Total Reflectance (ATR) mode, where the analysis was performed in the 400-4000 cm^{-1} range. The acquired data was processed using OPUS software, and the graphs were plotted using GraphPad Prism.

4.3.4. Fabrication and characterization of cyclic peptide nanotubes

Cyclic peptides were self-assembled into nanotubes by following a pH-switch approach. In this method, the cyclic peptides were completely solubilized in 50:50 ACN:H_2O containing 0.1% of TFA at 0.1% w/v concentration. Next, 0.2 N NaOH was added gradually to the solution until pH reached 9. The cyclic peptides were allowed to eventually self-assemble in the solution by leaving it unperturbed for 10 days. Field-emission scanning electron microscopy (FE-SEM) was then used to analyze the surface morphology of the resultant nano assemblies. For the FE-SEM investigation, a JEOL apparatus, Model JSM7610F Plus, operating at a 15 kV accelerating voltage was utilized. The HRTEM analysis was used to make the morphological assessment. For the analysis, the samples were appropriately fixed on a copper grid and images were obtained at various magnifications using the HR-TEM JEM-2100 Plus instrument operating at 200 kV.

4.3.5. Antioxidant activity

The ABTS assay was performed to evaluate the antioxidant properties of cyclic peptide nanotubes. A stock solution of ABTS radical was prepared by mixing 1 mL of 2.58 mM potassium persulfate solution and 7.38 mM ABTS salt solution in DI water, and keeping it in the dark for 8 h. The stock solution was diluted with PBS to adjust its absorbance to 0.75 at 415 nm. Subsequently, 200 µL of this solution was administered to each sample and control groups. A 1 mg/mL ascorbic acid solution was taken as a positive control, while the ABTS radical solution served as a negative control. The samples were then incubated at 37 °C and 100 rpm for 1 h. The solution was centrifuged at 700 rpm for 5 min after the incubation, and 100 µL from each set was taken to measure absorbance.

4.3.6. Alkaline phosphatase (ALP)-mimicking catalytic activity

The ALP-mimetic activity of HP-CPNTs was assessed by conducting the hydrolysis of p-nitro phenyl phosphate (pNPP). A dispersion of HP- and KP-CPNTs was prepared in a 20 mM phosphate buffer with a pH of 7 at a concentration of 1 mg/mL. The dispersion was vortexed for 10 min to achieve uniform suspension. Subsequently, 100 µL of the nanotube solution was added to a 96-well plate. The 12.5 mM solution of pNPP was prepared in a 25 mM tris buffer with a pH of 8, and 6 µL of this pNPP solution was combined with the 100 µL CPNTs solution in the 96-well plate. The catalytic efficiency of CPNTs was evaluated by measuring the absorbance of the solution at 405 nm at 15 min intervals for 150 min. The free imidazole was taken as control for the comparative analysis. Further, the absorbance of the substrate without CPNTs was analyzed to account for the self-hydrolysis effects.

4.3.7. Cell culture studies

The cell culture experiments were conducted using murine preosteoblast MC3T3-E1 cells. These cells were grown in MEM-α medium, which was further enhanced by adding 1% antibiotic (penicillin-streptomycin) and 10% fetal bovine serum (FBS) to support the cell growth. The cultured cells were maintained in a controlled environment, placed in a humidified atmosphere with a 5% CO_2 level and at a constant temperature of 37 °C. Covered T-25 flasks were employed for culture, and to ensure optimal growth conditions, the culture medium was renewed every 48 h. When the cell confluency reached approximately 80%, the cells were harvested using a trypsin-EDTA solution to detach them from the flask for further experimental use.

4.3.7.1. Cytocompatibility analysis

MTT assay. The cell viability of murine preosteoblast MC3T3-E1 cells following the treatment with nanotubes was assessed using the MTT assay, as previously reported.[45] Cells were seeded at a density of 10,000 cells/well in a Nunc-coated 96-well plate and allowed to grow. Subsequently, the cells were treated with 100 µL of CPNTs (330 µg/mL) dispersed in incomplete media and incubated for 24 h in a humidified atmosphere with 5% CO_2 at 37 °C.

The control group consisted of the untreated cells. Following a 24-hour incubation period, each well received 20 µL of MTT (5 mg/mL) solution, which was then incubated in the dark for 3.5 h at 37 °C. After extracting the MTT solution from each well, 100 µL of DMSO was applied to each well in order to dissolve the formazan crystals. In a plate reader, the absorbance of the dissolved crystals was determined at 570 nm. The cell viability was measured by comparing the absorbance of the sample sets to that of the control. Similarly, the cells were incubated with treatment samples for further 7 and 14 days to analyze the cell viability.

Live/dead assay. The cytocompatibility of MC3T3-E1 cells was further examined using live/dead fluorescence staining with a LIVE/DEAD cell viability/cytotoxicity kit. A working concentration of ethidium homodimer-1 (4 M) and calcein AM (2 M) was prepared in accordance with the manufacturer's instructions. In a humidified atmosphere with 5% CO_2 at 37 °C, the cells were cultured on a 6-well plate coated with Nunc at a density of 1.2 x 10^6 cells/well. Following the incubation, the cells were subjected to a 330 µg/mL working dose of peptide nanotube treatment and kept for another 24 h. The cells were stained for 45 min using the earlier-mentioned 500 µL dye solution. The Leica DMi8 fluorescent microscope was used to collect the fluorescence images of both alive and dead cells.

Cytoskeletal staining. To further assess the cytocompatibility of the material, MC3T3 -E1 cells were examined for their morphology after exposure to the CPNTs. Cell morphology was visualized by staining cellular F-actin and nucleus with Alexa Fluor 488 phalloidin and DAPI after 7 days of culture using previously described methods.[46] The cells were cultured over a coverslip and incubated in a humidified atmosphere with 5% CO_2 at 37 °C for 24 h. The media was then substituted with the 330 µg/mL solution of CPNTs, and the treated cells were incubated for 7 days. Following a PBS wash, the cells were fixed using 4% paraformaldehyde solution and permeabilized for 15 min with 0.1% triton X-100. Alexa Fluor 488 phalloidin was added to stain the F-actin filaments, and the cells were kept in the dark for 30 min. Subsequently, the cell nuclei were stained for 10 min with a 1 µg/mL DAPI solution, and the cells were again washed with PBS. The stained coverslips were carefully positioned onto a glass slide using a mounting solution and images were captured with a fluorescence microscope.

4.3.7.2. Immunogenic response

The immune response against the treatment of cyclic peptide nanotubes was assessed by examining the expression of M1 phenotype macrophage marker, *TNF-α*, *iNOS*, and M2 phenotype macrophage marker, *IL-10*, in murine macrophages RAW264.7 cell line. After incubating the cells with the nanotubes for 7-days, RNA was extracted from cells using TRIzol. The isolated RNA was quantified on NanoDrop One/One Microvolume UV–vis spectrophotometer and was taken for reverse transcription in order to synthesize cDNA using

Bio-Rad cDNA synthesis kit. The gene expression was analyzed. β-Actin was used as a house keeping gene for comparative analysis.

4.3.7.3. *In vitro* cell migration

To assess the migration of MC3T3-E1 cells on treatment with CPNTs, closure of a denuded area scratched in a confluent monolayer was monitored.[47] The cells were seeded in a 6-well plate (1×10^6 cells/well) and cultured at 37 °C temperature and 5% CO_2. On achieving confluency, a scratch was made in a straight line at the center of well using a 200 µL sterile tip. The detached cells were then removed by washing with PBS. The cells were incubated with the solution of cyclic peptide nanotubes at a concentration of 330 µg/mL. We have used untreated scratch as a control for the comparative analysis. The images of the scratch-healing in the treated and control samples were captured with an inverted microscope (Evos XL core, Invitrogen) at specified intervals of 0, 24, and 48 h. The unhealed scratch area was semi-quantitatively estimated using ImageJ software (n = 3).

4.3.8. Oxidative stress inhibition

To assess the *in vitro* efficacy of the nanotubes to regulate the elevated levels of ROS, we utilized murine preosteoblast MC3T3-E1 cells, which were grown in MEM-α supplemented with 10% FBS and 1% penstrep at 37 °C with 5% CO_2. DCFH-DA assay assessed the intracellular ROS stress in which 2,7-DCFDA dye reacts with ROS and becomes fluorescent. The cells with a density of 1.2×10^6 cells per well were grown in a 6-well plate coated with Nunc and incubated for 24 h. The ROS-stress was induced in the cells by exposing them to 0.5 mM of H_2O_2 for 1 h. Following the generation of ROS, the media was replaced by the nanotube samples and cells were further incubated for 24 h. The cells without the sample treatment (H_2O_2-treated) were considered as positive control, while the cells treated with 1 mg/mL ascorbic acid were taken as negative control. After 24 h incubation with the samples, 25 µM of DCFDA dye was added to the cells to investigate the ROS scavenging ability of samples. The cells were kept in dark for 30 min after addition of DCFDA dye and then observed under fluorescence microscope, where green fluorescence is the indicative of ROS stress. Further, the semi-quantitative determination of ROS-scavenging potential of CPNTs was performed by culturing MC3T3-E1 cells in a Nunc-coated 96-well black plate at a density of 1×10^4 cells/well. The cells were grown similarly as described and ROS-stress was generated by 1 h exposure to 0.5 mM H_2O_2. The cells were incubated for 24 h after treatment with the samples and then stained with DCFDA (25 µM). Fluorescent intensity was measured at excitation and emission wavelengths of 485 and 530 nm using a plate reader. The untreated cells were used as negative control while the ascorbic acid served as positive control.[48]

4.3.9. *In vitro* osteogenic activity

The osteogenic effect of CPNTs was evaluated by analyzing the ALP activity, which is an early osteogenic differentiation marker. Further, the bone mineralization potential was observed using alizarin red staining. We also investigated the expression profile of osteogenesis-related genes (ALP, OPN, Runx-2, and OCN) on 7- and 14-days of treatment with cyclic peptide nanotubes.

4.3.9.1. Alkaline phosphatase (ALP) estimation

ALP-estimation was performed by culturing the MC3T3-E1 cells (1×10^5/well) in complete MEM-α medium in a Nunc-coated 48-well plate. The cells were incubated for 24 h at 37 °C with 5% CO_2 and then treated with the sample extracts at the aforementioned concentration for 7- and 14-days. The treatment was repeated every 3 days during the course of the experiment. Sample set containing osteogenic media was considered as positive control, while the untreated cells were used a negative control. Osteogenic medium provides the ideal nutrition to promote the differentiation of MSCs into osteoblasts and is comprised of complete MEM-α, 50 μg/mL ascorbic acid, 10 mM β-glycerophosphate disodium salt hydrate, and 100 nM dexamethasone. After 7 days, the media was discarded, and the cells were rinsed with DPBS. Cell lysis was then induced by adding 200 μL of 0.2% Triton X for a 30 min to disrupt the cell membrane and facilitate the release of ALP molecules. Next, 200 μL of p-nitrophenyl phosphate (pNPP) solution was introduced to each well containing the lysate and incubated at 37 °C for 90 min in a light-protected environment. Subsequent to the incubation, absorbance at 405 nm was quantified utilizing a plate reader. Similar protocol was followed at 14 days of treatment to determine the ALP-activity.

4.3.9.2. Alizarin red staining

The degree of mineralization on MC3T3-E1 cells following the 7- and 14-days of culture with CPNTs was evaluated by using Alizarin Red S staining. The cells were cultured in Nunc-coated 48-well plate and treated with the samples as described earlier. On 7^{th} and 14^{th} day of treatment, the cells were washed with DPBS and fixed using 4% paraformaldehyde for 1 h. The cells were subsequently rinsed with PBS and kept for 1 h in a 500 μL solution of 40 mM Alizarin Red S (pH, 4.1). The unfixed dye was eliminated by gentle washing with DI water until a clear solution appeared. The cells were then observed using an inverted microscope to capture the images of red crystals formed. Further, the quantification of calcium deposition was performed by dissolving the obtained crystals in 200 μL of 10% cetyl pyridyl chloride solution. The plate was kept in dark for about 30 min and 100 μL of solution from each sample set was taken in a 96-well plate. The absorbance of dissolved crystals was measured at 562 nm to quantify the observed mineralization.

4.3.9.3. Gene expression of osteogenic marker genes

The murine preosteoblast MC3T3-E1 cells were cultured in a 6-well plate under the conditions mentioned earlier. The cells were incubated with 330 μg/mL of cyclic peptide nanotubes dispersed in incomplete media for 7-and 14-days. At specified time points, cells were lysed using TRIzol and total cellular RNA was isolated from each sample set. RNA was quantified using a NanoDrop One/One Microvolume UV–vis spectrophotometer (Thermo Fisher Scientific, USA) and reverse transcribed into cDNA with Bio-Rad cDNA synthesis kit. The relative mRNA expression levels of the osteogenic differentiation marker genes *ALP*, *OPN*, *Runx-2*, and *OCN* were quantified using RT-qPCR analysis with SYBR Universal in a Quant-Studio 3 Real-Time PCR System (Applied Biosystem, USA). The normalization of data was achieved by comparing its expression with that of the housekeeping gene β-actin.

4.3.9.4. Indirect co-culture of MC3T3-E1 and RAW 264.7 cells

The indirect co-culture studies were performed using the murine preosteoblasts (MC3T3-E1) and macrophage (RAW 264.7) cell lines. The studies were performed in a 12-well plate containing inserts with a pore size of 0.4 μm. RAW 264.7 cells were cultured at the bottom of 12-well plate in MEM- α with a cell density of 1×10^5 cells/well, while a similar concentration of MC3T3 cells were placed on the inserts. This plate was then incubated in humidified atmosphere with 5% CO_2 and 37 °C temperature for 24 h. Following the formation of monolayer, the co-culture system was kept in both basal and osteogenic conditions with and without 50 ng/mL receptor activator of nuclear factor kappa-B ligand (RANKL) protein. The MC3T3-E1 cells were treated with CPNTs and incubated further for 7 days, where treatment was repeated every 72 h. After 7 days, the qRT-PCR analysis was performed to evaluate the expression of osteoclast differentiation markers, *RANKL* and *TRAP*.

4.3.10. Statistical analysis

Student's t-test was used to analyze the data. The data collected were shown as mean ± standard deviation (n = 3), and *ns* denotes the nonsignificant difference, while *P* values < 0.05 (*), < 0.01 (**), and < 0.001 (***) denotes significant differences.

4.4. Results and discussions

The objective of this work was to develop self-assembled cyclic octapeptide, ^{L}His-^{D}Lys-^{L}His-^{D}Lys-^{L}Ala-^{D}Leu-^{L}Ala-^{D}Pro, nanotubes designed to mimic the activity of alkaline phosphatase (**Figure 4.1**). These nanotubes demonstrate both enzyme-mimetic and reactive oxygen species (ROS)-scavenging potential, which is likely to contribute to the improved osteogenic differentiation and bone regeneration. The fabricated material incorporates multiple histidine amino acid residues, which are integral to the functional domain of ALP. These histidine-presenting nanotubes can catalyze phosphate hydrolysis and induce bone mineralization.[34] The

imidazole ring in the histidine is a critical functional group in numerous enzymes, as it ionizes near neutral pH and functions as both an acid and a nucleophile in various catalytic processes.[49,50,51] Lysine (Lys) residue was hypothesized to further enhance the peptide's function by providing a basic environment that can stabilize negatively charged phosphate intermediates during catalysis, thus, complementing the ALP-mimetic activity. Additionally, it will aid in protecting the cells from oxidative damage due to the presence of lone pairs of electrons on the side-chain amine, which can effectively neutralize reactive oxygen species.[52] The induction of proline ensured the peptide to adopt a specific conformation conducive to cyclic assembly, while leucine and alanine residues have been integrated to foster hydrophobic interactions that support the self-assembly.[53] The cyclic structure of peptides will offer an enhanced resistance to enzymatic degradation when compared to linear peptides, rendering them particularly suitable for prolonged stability within the biological environment of bone tissue.[54] Additionally, the optimal length of octapeptides will facilitate both mechanical stability and effective self-assembly into nanotubular architectures, which are essential for supporting cellular migration and mineral deposition, as the longer sequence might increase synthesis complexity and introduce unnecessary flexibility.[55] Furthermore, positioning multiple imidazole rings in proximity within the nano scaffold amplifies the concentration of reaction loci, substantially enhancing the catalytic efficacy of the material by effective cooperation.[56,49] Thus, by incorporating the active enzyme component, we have developed bioinspired peptide nanotubes addressing several challenges associated with the direct use of native enzymes, including stability, immune response, handling, and batch-to-batch variance in efficacy.

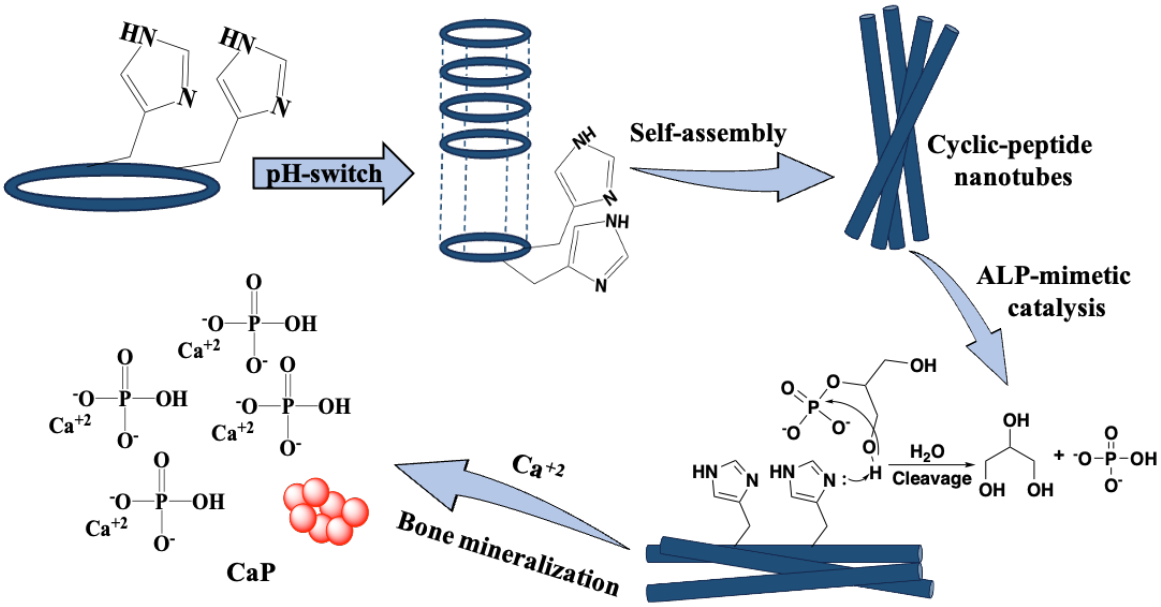

Figure 4.1. Self-assembly and alkaline phosphatase-mimicking activity of cyclic-octapeptide (^{L}Ala-^{D}Leu-^{L}Ala-^{D}Lys-^{L}His-^{D}Lys-^{L}His-^{D}Pro) nanotubes.

4.4.1. Cyclic peptides

Solid-phase peptide synthesis (SPPS) was employed to synthesize linear peptides ^{L}Ala-^{D}Lys-^{L}Ala-^{D}Lys-^{L}Ala-^{D}Leu-^{L}Ala-^{D}Pro and ^{L}Ala-^{D}Leu-^{L}Ala-^{D}Lys-^{L}His-^{D}Lys-^{L}His-^{D}Pro (**Figure A35, Appendix**). The linear peptides were synthesized on 2-chlorotrityl resin (2-CTC resin) using Fmoc chemistry approach, where Fmoc protected amino acids were utilized for synthesis. The synthesized peptides were cleaved from resin with 1% TFA in DCM and precipitated in ice-cold ether. After the vacuum drying of the linear peptides, they were cyclized in DCM at 0.5 mM concentration at 0 ℃ using HBTU and HOBt. The cyclic peptide side chains were then deprotected using 95% TFA along with 2.5% H_2O and 2.5% triisopropyl silane (TIS) (**Figure A36, Appendix**). The synthesized cyclic peptides ^{L}Ala-^{D}Lys-^{L}Ala-^{D}Lys-^{L}Ala-^{D}Leu-^{L}Ala-^{D}Pro: KP and ^{L}Ala-^{D}Leu-^{L}Ala-^{D}Lys-^{L}His-^{D}Lys-^{L}His-^{D}Pro: HP were characterized using mass spectrometry and their purity was determined by reversed-phase high-performance liquid chromatography (RP-HPLC). The mass of the KP and HP was found to be 750 KDa and 883 KDa respectively, which matched with their theoretical values (**Figure A37, Appendix**). The LC-MS data showed more than 90% purity of the cyclic peptides (**Figure A38, Appendix**). Next, we performed the FT-IR and circular dichroism analysis (**Figure 4.2C-E**) for the secondary structure determination of peptides, where the FT-IR peaks showed amide-1 peaks at 1632 and 1640 cm^{-1} for HP and KP, while amide-II peaks at 1536 and 1538 cm^{-1}, which indicated the β-sheet like secondary structure. Further, the CD-spectra confirmed our analysis with the minima produced at 216 and 217 nm.

4.4.2. Cyclic peptide nanotubes

Self-assembly of the cyclic peptides synthesized with even number of alternative D- and L-amino acids leads to the fabrication of cyclic peptide nanotubes. The nanotubes have their side-chains extending outwards with the perpendicular amide groups forming hydrogen bonding and supporting the stacking of cyclic peptides.[57] The cyclic peptides were self-assembled using pH-switch approach, where the peptides were initially dissolved in ACN/H_2O (50:50) with 0.1% TFA at a concentration of 0.1% v/v. Following the complete solubilization of peptides, the pH was inversed gradually by dropwise addition of 0.2 N NaOH until it reached 9. The self-assembly took place in around 10 days and the material was sonicated in a bath sonicator prior to its characterization. The surface morphology of the nanotubes was determined using HR-TEM and FE-SEM, which showed a tubular morphology with the size estimated to be between 100-130 nm (**Figure 4.2F-I**). Further, the zeta potential analysis was performed to evaluate the stability of material, where the surface potential for HP and LP was found to be +42.4 ± 2.31 and +34 ± 1.23 mV.

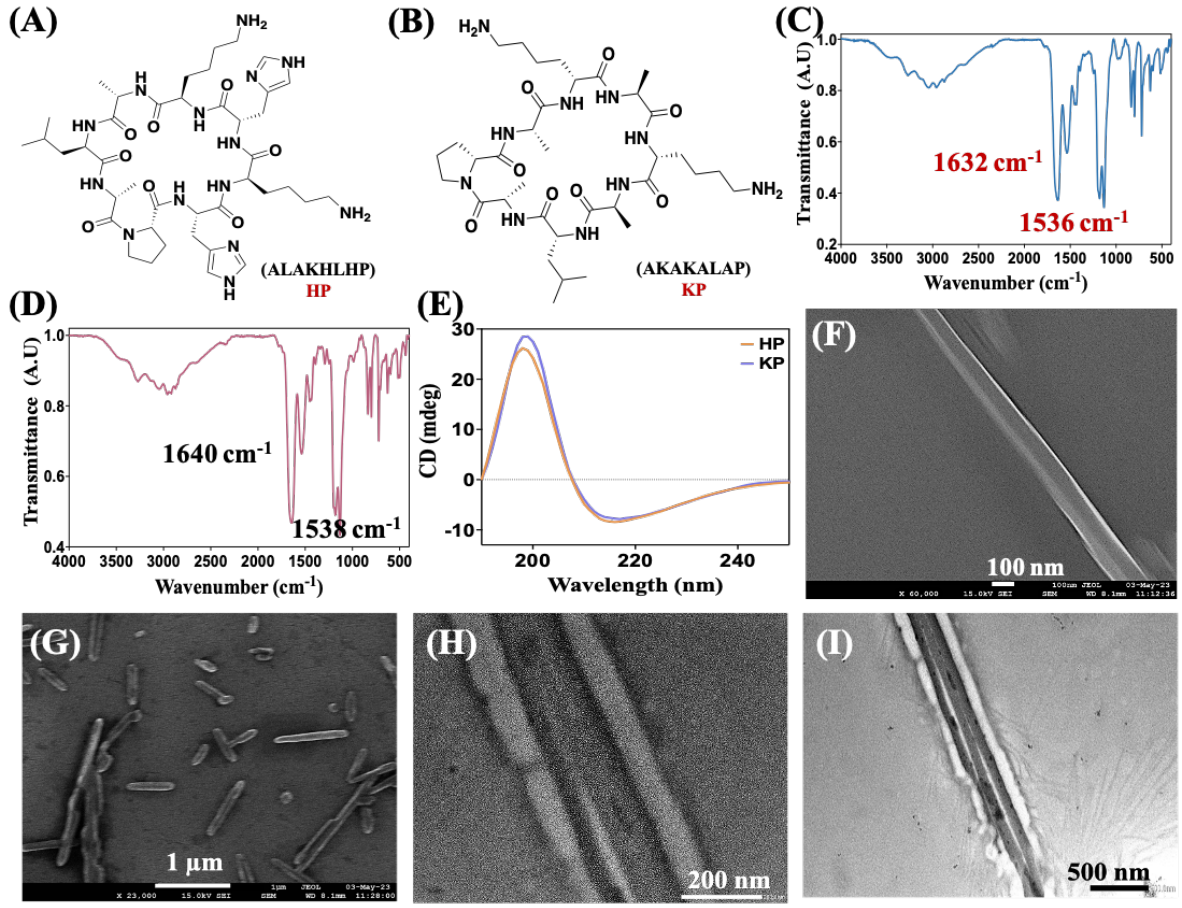

Figure 4.2. Structure and characterization of cyclic octapeptides and nanotubes. (A, B) Structure of cyclic octapeptides (^{L}Ala-^{D}Leu-^{L}Ala-^{D}Lys-^{L}His-^{D}Lys-^{L}His-^{D}Pro): HP and (^{L}Ala-^{D}Lys-^{L}Ala-^{D}Lys-^{L}Ala-^{D}Leu-^{L}Ala-^{D}Pro): KP. (C, D) FT-IR spectra of cyclic peptides: (C) HP, and (D) KP. (E) Circular dichroism spectra confirming the β-sheet like structure. (F, G) FE-SEM images of cyclic peptide nanotubes. Scale bar: 100 nm and 1 µm. (H, I) HR-TEM images of peptide nanotubes. Scale bar: 200 nm and 500 nm.

4.4.3. Antioxidant analysis

The excessive generation of reactive oxygen species on a bone fracture causes oxidative stress, stimulating osteoclastogenic activity and restricting osteoblast differentiation. During the inflammatory phase of bone healing, the immune and mesenchymal stem cells produce significant ROS to tackle any infection. This excessive production of ROS also damages the healthy cells and impairs the overall healing process.[58,59] The developed cyclic peptide nanotubes exhibited significant antioxidant ability, thus, lessening the undesired damage and speeding up the bone healing process. The presence of lone pair of electrons on the side chain of lysine in cyclic peptides will be more susceptible to ROS attack and shield the cells from oxidative damage. We determined the antioxidant activity of the material using colorimetric ABTS assay (**Figure 4.3A**). The colored solution of ABTS radical changes to colorless on reduction with the antioxidant materials and absorbance was measured at 415 nm. We employed

1 mg/mL solution of ascorbic acid as positive control, while the untreated samples served as negative controls. The antioxidant activity of HP and KP-CPNTs were observed to be 91.09 ± 1.59 and 90.89 ± 2.15%, which was comparable to the recent nonporous antioxidant scaffolds for bone regeneration reported by Asghar *et al.*[60] The antioxidant activity of both HP and KP was greater than 90%, and showed significant reduction in oxidative stress on treatment and a potential to enhance the bone regeneration by protecting the oxidative cellular damage.

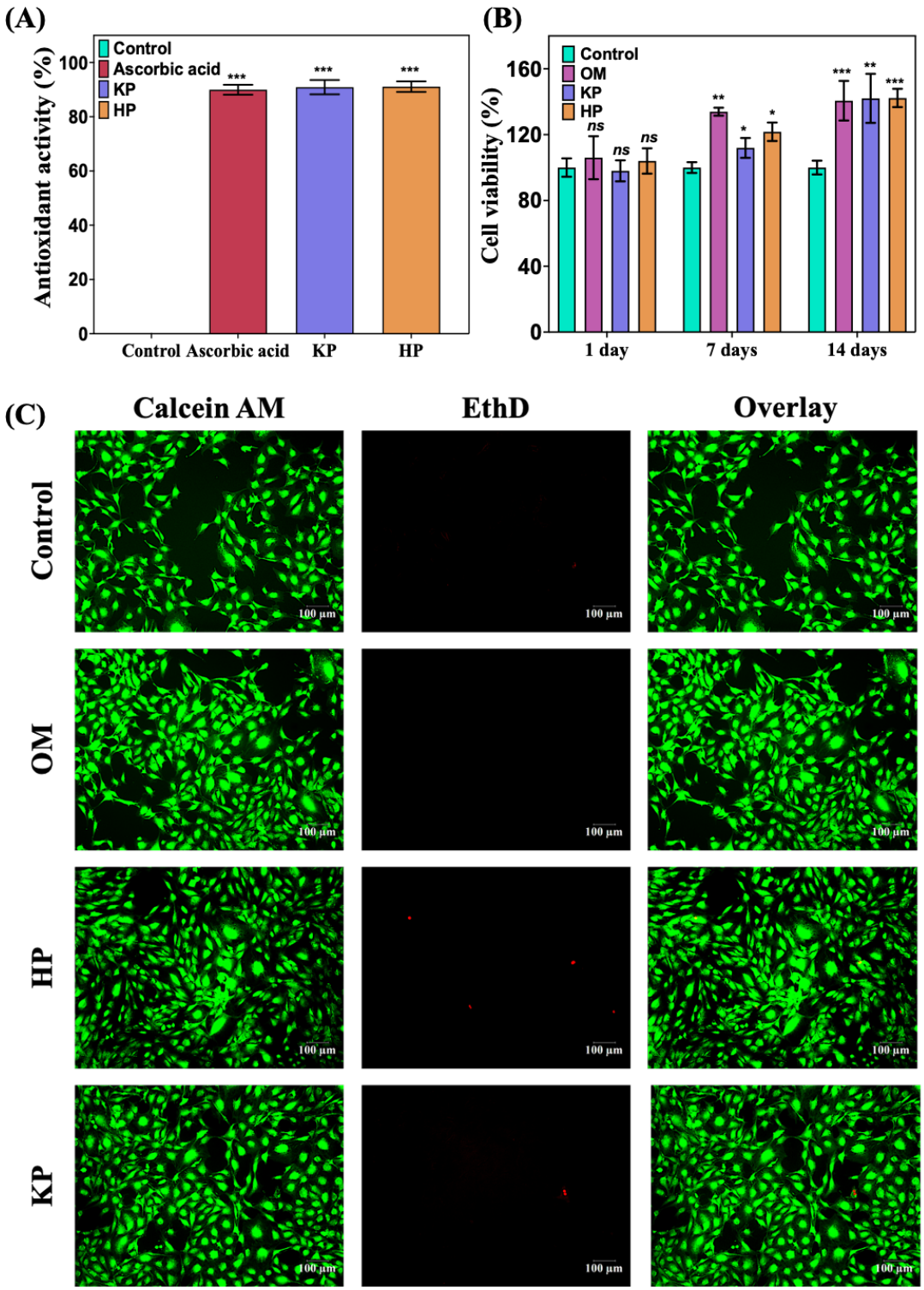

Figure 4.3. Antioxidant activity and cell viability analysis of CPNTs. (A) ABTS assay determining the antioxidant activity of HP and KP CPNTs, with ascorbic acid (1 mg/mL) taken as positive control and untreated cells taken as negative control. (B) MTT assay determining the cell viability of MC3T3-E1 cells on exposure to CPNTs for 1, 7, and 14 days. (C) Live/dead fluorescence assay of MC3T3-E1 cells on treatment with CPNTs for 24 h. Untreated cells were taken as control. Scale bar: 100 μm. The data are presented as mean ± standard deviation (n = 3), with *ns* denoting the insignificant difference and *P* values <0.05 (*), 0.01 (**), and 0.001 (***) denoting significant differences.

4.4.4. p-Nitro phenyl phosphate (pNPP) hydrolysis

The investigation into the ALP-mimicking activity of imidazole-presenting cyclic peptide nanotubes (HP-CPNTs) involved the assessment of their catalytic efficacy in the hydrolysis of p-nitrophenyl phosphate (pNPP) to p-nitrophenol (pNP). This conversion yields a yellow solution, with the progress measurable by an increase in absorbance at 405 nm. Absorbance readings were taken at 15-minute intervals over a duration of 150 minutes, and a time-dependent increase in absorbance provided confirmation of the catalytic capacity of HP-CPNTs to mimic alkaline phosphatase (ALP) activity. Comparatively, HP-CPNTs exhibited a more pronounced increase in absorbance over time at 405 nm when contrasted with free imidazole and KP-CPNTs, underscoring the catalytic influence of the multiple imidazole rings incorporated within HP-CPNTs. Notably, after 150 minutes, HP-CPNTs demonstrated 3.81 times greater absorbance than KP-CPNTs **(Figure A39, Appendix).** The catalytic activity is comparable to the earlier report by Gulseren *et al*.[34]

4.4.5. Cytocompatibility assessment

Cytocompatibility assessment is a fundamental step in the development and application of biomaterials to ensure their safety and effectiveness. Moreover, it determines the compatibility of the material with the host tissue to prevent any adverse inflammatory response. The cytocompatibility of nanotubes was evaluated by MTT assay, Live/dead fluorescence, cytoskeletal imaging, and immune reaction analysis. MTT assay was performed to investigate the cell viability, proliferation, and cytotoxicity analysis on treatment with nanotubes for 1, 7, and 14 days (**Figure 4.3B**). The study was performed using murine preosteoblast MC3T3-E1 cells. MTT assay quantitively assess the cellular viability based on the metabolic activity of the cell. It operates on the principle that metabolically active cells are capable of converting the yellow tetrazolium dye, MTT, into purple formazan crystals. This conversion is primarily facilitated by the action of the mitochondrial NAD(P)H-dependent oxidoreductase enzymes, signaling the presence of living, active cells. The formazan crystals were solubilized in DMSO and the absorbance was measured at 570 nm to allow for the quantification of cellular metabolic activity. The HP and KP nanotubes exhibited 104.14 ± 7.67 and 98.95 ± 6.38% cell viability on

24 h of treatment, while 7 and 14 days of treatment showed viability for HP to be around 121.75 ± 5.60 and 142.28 ± 5.54%, and for KP, 111.93 ± 6.03 and 142.06 ± 14.92% viability.

Live/dead fluorescence imaging was performed to further confirm the cell viability results (**Figure 4.3C**). This study involves the staining of cells with ethidium homodimer-1 and calcein AM following the treatment with nanotubes. Ethidium homodimer, due to its membrane-impermeable nature, selectively stains dead cells. In contrast, calcein AM can permeate live cell membranes and, intracellular esterases activity converts it into green fluorescent calcein. This characteristic allows for the distinction between living, proliferative cells and dead cells when observed under a fluorescence microscope. The observed predominance of green fluorescence indicates a majority of live and actively dividing cells. The observations from the live-Dead assay corroborate the results obtained from the MTT assay, reinforcing the conclusion that the cell population is predominantly viable and proliferative.

Cytoskeletal staining, further investigated the morphology of MSCs on 7-day treatment with the nanotubes (**Figure 4.4A**). The cells were stained with the Alexa Fluor 488 phalloidin and DAPI stains. Alexa Fluor 488 phalloidin stains the cytoskeleton by binding of phalloidin to filamentous actin (F-actin), while DAPI (4′,6-diamidino-2-phenylindole) is a blue-fluorescent nuclear stain that exhibits fluorescence upon binding to AT regions of dsDNA. We observed a mononucleated, fibroblast-like shape of MCT3T3-E1 cells with an extended cytoplasmic projection on treatment with nanotubes. This intact and healthy morphology of cells further ensures the cytocompatibility of nanotubes.

Immune response to the nanotubes was investigated by analyzing the gene expression profile of proinflammatory M1-macrophage markers, iNOS, TNF-α and anti-inflammatory M2-macrophage marker IL-10 prior to the 14-days of treatment (**Figure 4.4B).** We observed a significant reduction in the expression of proinflammatory genes iNOS and TNF-α in both HP and KP CPNTs. HP downregulates the expression of iNOS and TNF-α by 0.44- and 0.67-fold, while KP showed a 0.41- and 0.49-fold decrease. Furthermore, the expression of IL-10, M2 related gene upregulates significantly by 5.28 and 4.90-fold. This decrease in the pro-inflammatory activity can be attributed to the antioxidant and ROS-scavenging potential of the material.

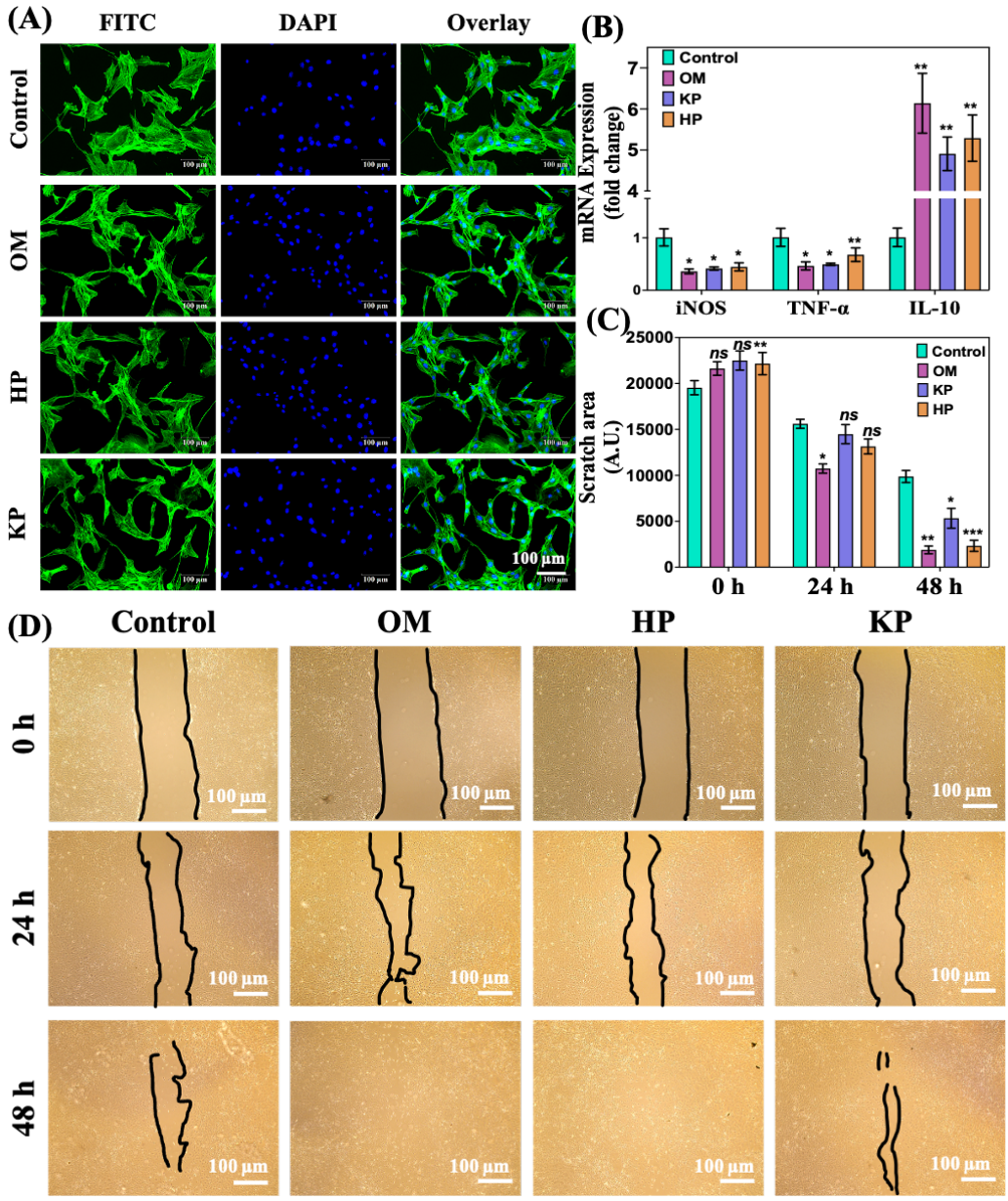

Figure 4.4. Cytocompatibility and cell migration analysis. (A) Cytoskeletal staining to determine the cellular morphology of MC3T3-E1 cells using Alexa Fluor phalloidin and DAPI after 7 days treatment with CPNTs. Untreated cells served as controls. Scale bar: 100 µm. (B) qRT-PCR analysis of M1 and M2 macrophage related genes iNOS, TNF-α, and IL-10 to determine the immunogenic response to the 7-day CPNTs treatment. (C, D) Scratch assay to analyze the cell migration on CPNTs treatment: (C) Semiquantitative analysis of the unhealed area of scratch at different time intervals. (D) Microscopic images of scratch healing taken at 0, 24, and 48 h. Untreated cells taken as negative control, while osteogenic media (OM) served as positive control. Scale bar: 100 µm. The data are presented as mean ± standard deviation (n = 3), with *ns* denoting the insignificant difference and *P* values <0.05 (*), 0.01 (**), and 0.001 (***) denoting significant differences.

4.4.6. *In vitro* cell migration

Migration of cells from the bone marrow and surrounding tissue to the site of injury is crucial for effective bone regeneration. Stem cells, once at the injury site, have the potential to differentiate into osteoblasts, which are the cells responsible for bone regeneration. Hence, the capacity to encourage cell migration is a critical factor to be considered in the development of biomaterials aimed at bone regeneration. We investigated the potential of nanotubes to promote cell migration by performing the scratch assay on murine MC3T3-E1 cells. Following an incision on the confluent monolayer of cells, the migration of cells into the scratch was observed by taking microscopic images after 24 and 48 h of treatment, where the untreated cells were considered control set (**Figure 4.4D**). The unhealed scratch area was estimated using ImageJ software, where we observed that HP nanotubes healed the scratch by around 90% in contrast to the KP and untreated cells, which showed 76 and 50% healing (**Figure 4.4C**). Thus, the HP-nanotubes were found to promote the cell migration and ensure the recruitment of essential cells at the injury site, thereby, supporting their functions and facilitating the overall healing process.

4.4.7. Oxidative stress inhibition

Reactive oxygen species (ROS) play a critical role in the bone remodeling process by facilitating the degradation of the mineralized matrix by osteoclasts (OCs).[61] However, the dysregulation of ROS can lead to oxidative stress, subsequently affecting the behavior of all cells implicated in bone remodeling, including precursor cells. Elevated ROS stress in damaged bones can affect the genetic integrity, potentially resulting in mutations or cell death in osteoblast precursors and mature osteoblasts, thereby hindering the process of osteogenic differentiation. Moreover, excessive ROS can also interfere with signaling pathways crucial for osteoblast function, such as Wnt/β-catenin, BMP/Smad, and MAPK pathways.[62] Therefore, developing the biomaterials that can regulate the elevated ROS-stress is crucial for effective bone regeneration and preventing disorders related to impaired osteogenesis. We investigated the potential of nanotubes to **scavenge excessive ROS-stress** using DCFDA assay, where the cells induced with oxidative stress were given treatment with nanotubes and observed. Cell permeable H_2DCFDA gets converted into 2′,7′-dichlorodihydrofluorescein (H_2DCF) by the intracellular esterases. Further, H_2DCFDA gets converted to 2′,7′-dichlorofluorescein (DCF) in the presence of ROS and gives green fluorescence. However, when observed under a fluorescence microscope, HP- and KP-treated cells exhibited a significant decrease in the green fluorescence as compared to the untreated cells (**Figure 4.5A**).

Moreover, the ROS-scavenging ability of materials was quantitatively evaluated by measuring the fluorescence intensity in a 96-well black plate. The fluorescence intensity on treatment with HP and KP nanotubes reduced by 6.18 times in comparison to H_2O_2 (0.5 mM) treated cells (**Figure 4.5B**). The results obtained are consistent with the ABTS assay for antioxidant activity. Also, the cell viability of the ROS-stressed MC3T3-E1 cells was analyzed by MTT assay after 24 h of treatment with CPNTs. We observed that on incubation with our ROS scavenging

CPNTs, even the H_2O_2-treated cells showed good viability. While the peroxide treated cells showed only 48.28% viability, on treatment with HP and KP CPNTs, around 101.32% and 94.52% cells were found viable (**Figure 4.5C**).

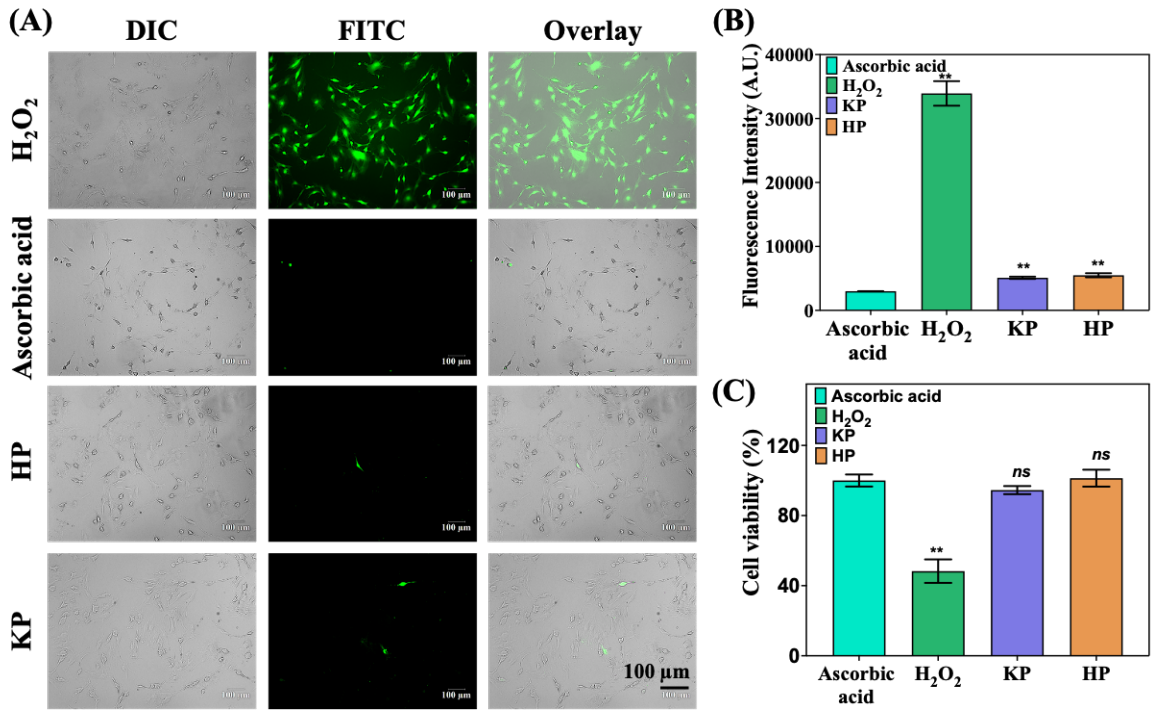

Figure 4.5. ROS-scavenging evaluation of HP and KP CPNTs. (A, B) DCFDA assay: (A) Fluorescence imaging of ROS-stressed MC3T3-E1 cells on 24 h treatment with CPNTs. Scale bar: 100 µm. (B) Fluorescence intensity of ROS-stressed MC3T3-E1 cells at excitation and emission wavelengths of 485 and 530 nm. Cells were treated with CPNTs for 24 h and stained with DCFDA dye. (C) Cell viability analysis of ROS-stressed MC3T3-E1 cells by MTT assay after incubation with CPNTs for 24 h. The H_2O_2-treated cells were used as negative control, while ascorbic acid was taken as positive control. The data was presented as mean ± standard deviation (n = 3), with *ns* denoting the insignificant difference and *P* values <0.05 (*), 0.01 (**), and 0.001 (***) denoting significant differences.

4.4.8. Osteogenic differentiation studies

To explore the potential of ALP-mimetic nanostructures in bone tissue engineering, their ability to induce osteogenic differentiation was studied on MC3T3-E1 preosteoblasts. These nanostructures have been found to facilitate the formation of bone-like structures by hydrolysing the organophosphate molecules. The evaluation focused on two key osteogenic markers, ALP activity and extracellular calcium deposition. Moreover, the expression profile of osteogenesis-related genes, *ALP*, *Runx2*, *OCN* and *OPN* were also studied. These markers are crucial in understanding the extent of osteogenic differentiation and the subsequent formation of bone tissues, thus, highlighting the potential of CPNTs in supporting bone regeneration.

4.4.8.1. Alkaline phosphatase activity

The assessment of early-stage osteogenic differentiation can be quantitatively analyzed through the measurement of Alkaline Phosphatase (ALP) activity. ALP serves as a crucial biomarker, indicative of bone metabolic efficacy, and its concentration is intimately associated with the differentiation of osteoblasts, significantly influencing the matrix mineralization phase.[63,64] Typically, osteoblastic cells undergo a proliferation phase for approximately 7 to 14 days. Post this proliferative phase, these cells commence the secretion of extracellular matrix (ECM) proteins and exhibit early differentiation markers like ALP, observable from the 7th day onwards.[65] We have observed that on 7 days treatment with HP CPNTs, there has been a significant if not remarkable increase in the alkaline phosphatase activity compared to the untreated and KP-treated cells. The cells on 7-day treatment with HP-CPNTs showed a 1.57 folds increase in the ALP activity, while KP-CPNTs showed only 1.26 times increase in contrast to untreated cells. On the contrary, cells cultured in HP CPNTs showed a dramatic increase by 4.33 times in the ALP-activity after 14-days of treatment, which is comparable to that of the osteogenic media (4.14 times). KP exhibited only 1.55 folds increase in 14 days (**Figure 4.6C**). This enhanced activity in HP CPNTs is attributed to the presence of imidazole ring presenting histidine residues, which catalyzes the hydrolysis of organic phosphates and mimic the native ALP enzyme.

4.4.8.2. Calcium deposition

The development of mineralized nodules is a crucial marker of late-stage osteogenic differentiation. To investigate this process, Alizarin Red S (ARS) staining was utilized due to its ability to assess the mineralization of the extracellular matrix (ECM) by detecting calcium deposits.[66] This mineralization is vital for the formation of hydroxyapatite crystals, which are instrumental in providing structural integrity and strength to bone tissue. Alizarin Red S achieves this by binding to calcium ions through chelation, thus, creating a stable orange-red complex that can be observed under a microscope.[67] Our studies revealed that ALP-inspired cyclic peptide nanotubes (HP) formed bone-like nodules after 7 and 14 days of incubation, indicative of enhanced mineralization. The effectiveness of ARS staining was confirmed through both microscopic observation and semi-quantitative assessment of calcium deposition. When observed under microscope, the HP CPNTs showed a significant improvement in bone mineralization when compared to KP CPNTs and untreated cells, thus, offering promising insights into the potential of these nanotubes in bone tissue regeneration (**Figure 4.6A**).

Further, the quantification was performed by calcium extraction using 10% cetylpyridinium chloride and absorbance measurement at 405 nm using a plate reader (**Figure 4.6B**). We have seen a significantly high absorbance on exposure to HP CPNTs compared to other groups in both 7- and 14-days of observation. HP CPNTs exhibited a 2.17 times upregulation compared to untreated cells, while KP showed only 1.38 folds in 7 days. After 14 days, the bone mineralization in the presence of HP CPNTs and osteogenic media markedly increased by 3.88

and 4.43 folds compared to untreated, while KP (1.32) did not show any significant upregulation. This confirms the significance of imidazole groups presented on the peptide nanotubes for CaP deposition.

4.4.8.3. Osteogenic gene expression analysis

To explore the underlying mechanism for the spontaneously promoted osteodifferentiation of murine preosteoblast MC3T3-E1 cells in the presence of HP CPNTs, the expression levels of osteogenesis-related genes *RUNX2*, *OCN* (osteocalcin), *OPN* (osteopontin), and *ALP* (alkaline phosphatase) were thoroughly examined using real-time qRT-PCR (**Figure 4.6E-H**). *OCN*, also known as bone gamma-carboxy glutamic acid-containing protein (*BGLAP*), is a calcium-binding protein that serves as a critical marker for bone formation due to its exclusive secretion by osteoblasts.[68] Our observations revealed an elevation in *OCN* mRNA levels in cells treated with histidine-presenting cyclic peptide nanotubes (HP) by displaying a significant increase, approximately 2.30 and 4.02-fold, in 7 and 14 days, respectively, compared to the control group. The transcription factor RUNX2 plays a crucial role in early osteoblast differentiation as the primary gene involved in bone formation although it is not necessary for the later stages of osteoblast differentiation.[69] We observed a substantial increase in *Runx2* expression in cells exposed to HP CPNTs, with levels rising by 3.80- and 4.71-fold compared to untreated cells after 7 and 14 days of treatment. The gene expression of *OPN*, bone sialoprotein I (*BSP-1*), is crucial as it is a negatively charged protein component of the extracellular matrix that enables robust binding to different forms of calcium-based biominerals in bones and teeth.[70] In the HP CPNT-treated cells after 7 and 14 days of treatment, there was a notable elevation of OPN expression by 3.61 and 4.28 folds when compared to the untreated control cells. Similarly, the expression of ALP was also enhanced by 2.35 and 3.96 folds. However, the KP-nanotubes did not demonstrate any significant change in the gene expression of osteogenic differentiation markers, confirming the potential of histidine presenting HP nanotubes to promote osteogenic differentiation.

We further investigated the effect of HP and KP CPNTs in a co-culture model of MC3T3-E1 and RAW 264.7 cells. Bone regeneration involves a fine balance between the bone resorption by osteoclasts and bone formation by osteoblasts. Receptor activator of nuclear factor kappa-B ligand (RANKL) and Tartrate-Resistant Acid Phosphatase (TRAP) are the key cytokines involved in the process. Osteocytes and osteoblasts secrete the RANKL that stimulates the osteoclastogenesis by interacting with the RANK-expressing osteoclast precursors and inducing their differentiation to mature osteoclasts. TRAP is an enzyme highly expressed in osteoclasts and serves as a biochemical marker for osteoclast activity and bone resorption. It degrades the bone matrix proteins and contributes to the acidic environment needed for bone resorption.[71] Therefore, we analyzed the effect of CPNTs on the gene expression levels of RANKL and TRAP in the co-culture system (**Figure 4.6D**). After 7 days of incubation with the

nanotubes, we observed a downregulation in the expression level of both the genes in HP CPNTs. However, KP CPNTs did not exhibit any significant effect on their expression levels. A reduction in the secretion of RANKL and TRAP in HP CPNTs provides a protective mechanism for preventing excessive osteoclast differentiation, pre-osteoclast maturation, and osteoclast resorption activity.

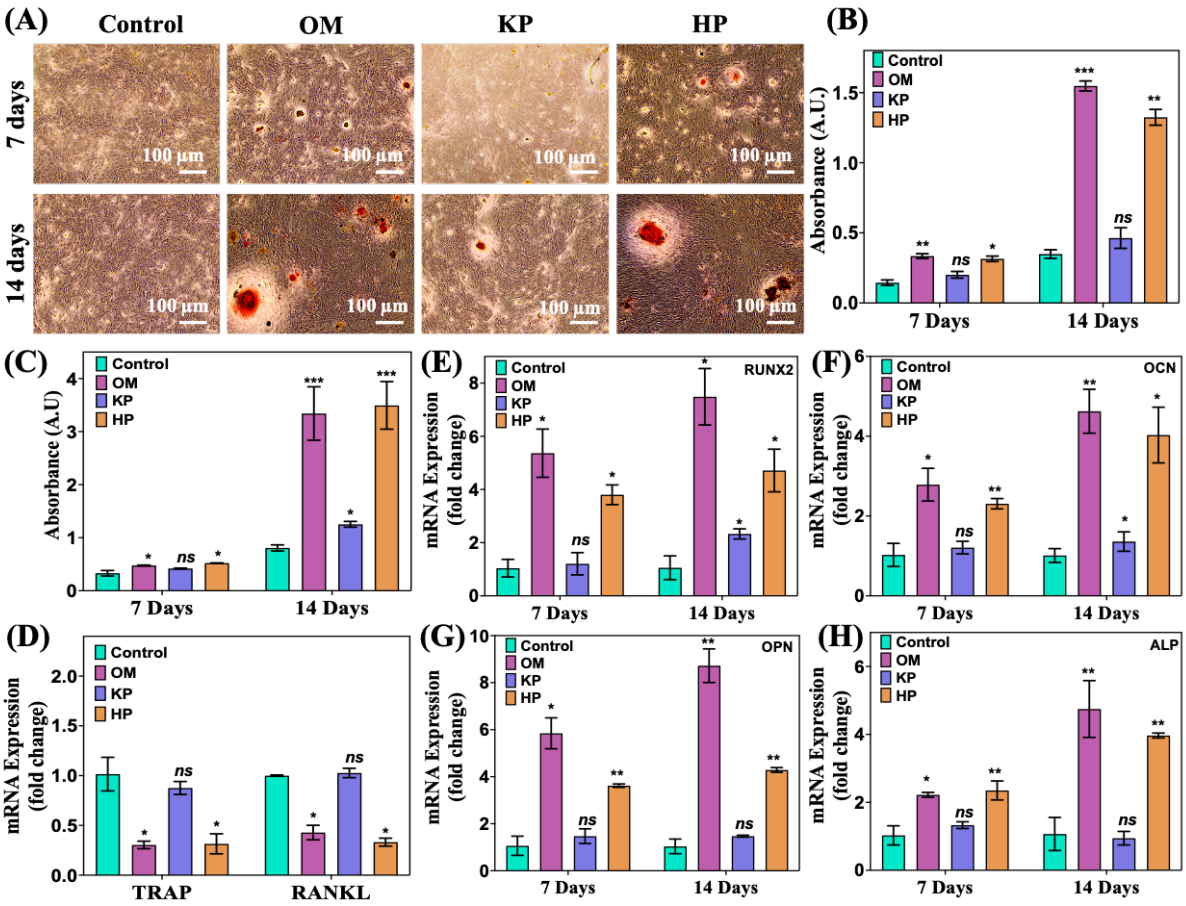

Figure 4.6. Osteogenic differentiation and bone mineralization analysis on murine preosteoblast MC3T3-E1 cells. (A, B) Bone mineralization studies: (A) Microscopic images of calcium deposition, captured using Alizarin Red S staining on CPNT-treated cells. Scale bar: 100 µm. (B) Quantitative analysis of calcium deposited on mineralized cells by measuring absorbance at 405 nm. Osteogenic media (OM) and untreated cells were taken as controls. (C) Quantitative analysis of alkaline phosphatase (ALP) activity in cells on treatment with CPNTs. OM and untreated cells served as controls for comparative analysis. (D) qRT-PCR of osteoclastic factors *TRAP* and *RANKL* for relative mRNA expression analysis in MC3T3-E1 and RAW 264.7 following a 7-day treatment in an indirect coculture procedure. (E-H) Gene expression analysis of osteogenic differentiation marker genes after culturing with OM and CPNTs: (E) *RUNX2*, (F) *OCN*, (G) *OPN*, and (H) *ALP*. The data are presented as mean ± standard deviation (n = 3),

with *ns* denoting the insignificant difference and *P* values <0.05 (*), 0.01 (**), and 0.001 (***) denoting significant differences.

4.5. Conclusions

This work led to the development of self-assembled peptide-based enzyme-mimetic nanotubes with the bioactive functional groups present on the surface of the material. The imidazole rings, present in the functionally active domain of alkaline phosphatase, have been strategically placed in close proximity to mimic the activity of enzyme to hydrolyze the organic phosphatase and induce the bone mineralization. Furthermore, it facilitates osteogenic differentiation to promote bone regeneration. The developed nanotubes were cytocompatible and did not induce any immunogenic response. Their reactive oxygen species (ROS) scavenging capability further underscores their potential in mitigating oxidative stress, which often hampers the regeneration process. These histidine-presenting nanotubes have demonstrated a potential to promote osteogenic differentiation *in vitro*, without any exogenous support, as evidenced by the upregulated activity of alkaline phosphatase, an early osteogenic differentiation marker and enhanced bone mineralization, a crucial marker for late osteogenesis. The upregulation of osteogenesis-related genes, coupled with a reduction in the expression of genes associated with osteoclastogenesis, suggest their ability to support the molecular pathways involved in bone regeneration. Moreover, their dimensions, ranging from 100 to 130 nm, are comparable to the diameter of collagen fibrils in bone (20-500 nm),[72] which may provide biophysical advantages for bone regeneration by offering biomimetic topographical cues to osteoprogenitor cells. The artificial enzyme-mimetic peptide nanotubes presented a promising approach to facilitate the maturation of preosteoblasts into osteoblasts and promote bone regeneration by potentially addressing the challenges associated with the use of bone grafts, native growth factors, and enzymes. However, further *in vivo* investigations are required to evaluate their effectiveness in more complex bone regeneration models. These nanotubes can be integrated into the existing regenerative matrices to enhance osteogenesis or used as an adjunct to provide osteoinductive cues within the microenvironment. Since, cyclic peptide has well reported stability, their controlled biodegradability will allow them to be absorbed naturally as new bone forms, aligning with the remodeling process and seamless integration into the host tissue. Chapters 2 and 3 emphasized on the development of peptide-based biomaterials with innate attributes for the treatment of chronic wounds. This chapter continued in a similar vein by establishing an approach for promoting bone tissue regeneration that does not rely on growth factors, enzymes or drugs. The developed biomaterial demonstrated intrinsic capabilities in augmenting bone mineralization and promoting osteogenic differentiation and, thus, adheres to the overarching theme of this thesis by circumventing the reliance on externally sourced biomolecules or drugs.

References

(1) Sheehy, E. J.; Kelly, D. J.; O'Brien, F. J. Biomaterial-Based Endochondral Bone Regeneration: A Shift from Traditional Tissue Engineering Paradigms to Developmentally Inspired Strategies. *Materials Today Bio* **2019**, *3*, 100009.

(2) Ma, H.; Feng, C.; Chang, J.; Wu, C. 3D-Printed Bioceramic Scaffolds: From Bone Tissue Engineering to Tumor Therapy. *Acta Biomaterialia* **2018**, *79*, 37–59.

(3) Qu, H.; Fu, H.; Han, Z.; Sun, Y. Biomaterials for Bone Tissue Engineering Scaffolds: A Review. *RSC Adv.* **2019**, *9* (45), 26252–26262.

(4) El-Rashidy, A. A.; Roether, J. A.; Harhaus, L.; Kneser, U.; Boccaccini, A. R. Regenerating Bone with Bioactive Glass Scaffolds: A Review of in Vivo Studies in Bone Defect Models. *Acta Biomaterialia* **2017**, *62*, 1–28.

(5) Dimitriou, R.; Jones, E.; McGonagle, D.; Giannoudis, P. V. Bone Regeneration: Current Concepts and Future Directions. *BMC Med* **2011**, *9* (1), 66.

(6) Ansari, M. Bone Tissue Regeneration: Biology, Strategies and Interface Studies. *Prog Biomater* **2019**, *8* (4), 223–237.

(7) Marsell, R.; Einhorn, T. A. The Biology of Fracture Healing. *Injury* **2011**, *42* (6), 551–555.

(8) Bigham-Sadegh, A.; Oryan, A. Basic Concepts Regarding Fracture Healing and the Current Options and Future Directions in Managing Bone Fractures. *International Wound Journal* **2015**, *12* (3), 238–247.

(9) Szwed-Georgiou, A.; Płociński, P.; Kupikowska-Stobba, B.; Urbaniak, M. M.; Rusek-Wala, P.; Szustakiewicz, K.; Piszko, P.; Krupa, A.; Biernat, M.; Gazińska, M.; Kasprzak, M.; Nawrotek, K.; Mira, N. P.; Rudnicka, K. Bioactive Materials for Bone Regeneration: Biomolecules and Delivery Systems. *ACS Biomater. Sci. Eng.* **2023**, *9* (9), 5222–5254.

(10) Raphel, J.; Holodniy, M.; Goodman, S. B.; Heilshorn, S. C. Multifunctional Coatings to Simultaneously Promote Osseointegration and Prevent Infection of Orthopaedic Implants. *Biomaterials* **2016**, *84*, 301–314.

(11) Sun, Y.; Li, L.; Wang, J.; Liu, H.; Wang, H. Emerging Landscape of Osteogenesis Imperfecta Pathogenesis and Therapeutic Approaches. *ACS Pharmacol. Transl. Sci.* **2024**, *7* (1), 72–96.

(12) Ajeganova, S.; Andersson, M.; Forslind, K.; Gjertsson, I.; Nyhäll-Wåhlin, B.-M.; Svensson, B.; Hafström, I. Long-Term Fracture Risk in Rheumatoid Arthritis: Impact of Early Sustained DAS28-Remission and Restored Function, Progressive Erosive Disease, Body Mass Index, Autoantibody Positivity and Glucocorticoids. A Cohort Study over 10 Years. *BMC Rheumatol* **2023**, *7* (1), 23.

(13) Zhang, X.; Cui, J.; Cheng, L.; Lin, K. Enhancement of Osteoporotic Bone Regeneration by Strontium-Substituted 45S5 Bioglass *via* Time-Dependent Modulation of Autophagy and the Akt/mTOR Signaling Pathway. *J. Mater. Chem. B* **2021**, *9* (16), 3489–3501.

(14) Liao, J.; Shi, K.; Jia, Y.; Wu, Y.; Qian, Z. Gold Nanorods and Nanohydroxyapatite Hybrid Hydrogel for Preventing Bone Tumor Recurrence via Postoperative Photothermal Therapy and Bone Regeneration Promotion. *Bioactive Materials* **2021**, *6* (8), 2221–2230.

(15) Soucacos, P. N.; Kokkalis, Z. T.; Piagkou, M.; Johnson, E. O. Vascularized Bone Grafts for the Management of Skeletal Defects in Orthopaedic Trauma and Reconstructive Surgery. *Injury* **2013**, *44*, S70–S75.

(16) Cui, Y.; Liu, H.; Tian, Y.; Fan, Y.; Li, S.; Wang, G.; Wang, Y.; Peng, C.; Wu, D. Dual-Functional Composite Scaffolds for Inhibiting Infection and Promoting Bone Regeneration. *Materials Today Bio* **2022**, *16*, 100409.

(17) Panetta, N. J.; Gupta, D. M.; Slater, B. J.; Kwan, M. D.; Liu, K. J.; Longaker, M. T. Tissue Engineering in Cleft Palate and Other Congenital Malformations. *Pediatr Res* **2008**, *63* (5), 545–551.

(18) Jiao, H.; Xiao, E.; Graves, D. T. Diabetes and Its Effect on Bone and Fracture Healing. *Curr Osteoporos Rep* **2015**, *13* (5), 327–335.

(19) Sheppard, A. J.; Barfield, A. M.; Barton, S.; Dong, Y. Understanding Reactive Oxygen Species in Bone Regeneration: A Glance at Potential Therapeutics and Bioengineering Applications. *Front. Bioeng. Biotechnol.* **2022**, *10*, 836764.

(20) Wu, A.-M.; Bisignano, C.; James, S. L.; Abady, G. G.; Abedi, A.; Abu-Gharbieh, E.; Alhassan, R. K.; Alipour, V.; Arabloo, J.; Asaad, M.; Asmare, W. N.; Awedew, A. F.; Banach, M.; Banerjee, S. K.; Bijani, A.; Birhanu, T. T. M.; Bolla, S. R.; Cámera, L. A.; Chang, J.-C.; Cho, D. Y.; Chung, M. T.; Couto, R. A. S.; Dai, X.; Dandona, L.; Dandona, R.; Farzadfar, F.; Filip, I.; Fischer, F.; Fomenkov, A. A.; Gill, T. K.; Gupta, B.; Haagsma, J. A.; Haj-Mirzaian, A.; Hamidi, S.; Hay, S. I.; Ilic, I. M.; Ilic, M. D.; Ivers, R. Q.; Jürisson, M.; Kalhor, R.; Kanchan, T.; Kavetskyy, T.; Khalilov, R.; Khan, E. A.; Khan, M.; Kneib, C. J.; Krishnamoorthy, V.; Kumar, G. A.; Kumar, N.; Lalloo, R.; Lasrado, S.; Lim, S. S.; Liu, Z.; Manafi, A.; Manafi, N.; Menezes, R. G.; Meretoja, T. J.; Miazgowski, B.; Miller, T. R.; Mohammad, Y.; Mohammadian-Hafshejani, A.; Mokdad, A. H.; Murray, C. J. L.; Naderi, M.; Naimzada, M. D.; Nayak, V. C.; Nguyen, C. T.; Nikbakhsh, R.; Olagunju, A. T.; Otstavnov, N.; Otstavnov, S. S.; Padubidri, J. R.; Pereira, J.; Pham, H. Q.; Pinheiro, M.; Polinder, S.; Pourchamani, H.; Rabiee, N.; Radfar, A.; Rahman, M. H. U.; Rawaf, D. L.; Rawaf, S.; Saeb, M. R.; Samy, A. M.; Sanchez Riera, L.; Schwebel, D. C.; Shahabi, S.; Shaikh, M. A.; Soheili, A.; Tabarés-Seisdedos, R.; Tovani-Palone, M. R.; Tran, B. X.; Travillian, R. S.; Valdez, P. R.; Vasankari, T. J.; Velazquez, D. Z.; Venketasubramanian, N.; Vu, G. T.; Zhang, Z.-J.; Vos, T. Global, Regional, and National Burden of Bone Fractures in 204 Countries and Territories, 1990–2019: A Systematic Analysis from the Global Burden of Disease Study 2019. *The Lancet Healthy Longevity* **2021**, *2* (9), e580–e592.

(21) The Lancet Diabetes & Endocrinology. Osteoporosis: Overlooked in Men for Too Long. *The Lancet Diabetes & Endocrinology* **2021**, *9* (1), 1.

(22) Ye, G.; Bao, F.; Zhang, X.; Song, Z.; Liao, Y.; Fei, Y.; Bunpetch, V.; Heng, B. C.; Shen, W.; Liu, H.; Zhou, J.; Ouyang, H. Nanomaterial-Based Scaffolds for Bone Tissue Engineering and Regeneration. *Nanomedicine (Lond.)* **2020**, *15* (20), 1995–2017.

(23) Qu, H.; Fu, H.; Han, Z.; Sun, Y. Biomaterials for Bone Tissue Engineering Scaffolds: A Review. *RSC Adv.* **2019**, *9* (45), 26252–26262.

(24) Jansen, J. A.; Vehof, J. W. M.; Ruhé, P. Q.; Kroeze-Deutman, H.; Kuboki, Y.; Takita, H.; Hedberg, E. L.; Mikos, A. G. Growth Factor-Loaded Scaffolds for Bone Engineering. *Journal of Controlled Release* **2005**, *101* (1–3), 127–136.

(25) Liu, J.; Ruan, J.; Chang, L.; Yang, H.; Ruan, W. Porous Nb-Ti-Ta Alloy Scaffolds for Bone Tissue Engineering: Fabrication, Mechanical Properties and in Vitro/Vivo Biocompatibility. *Materials Science and Engineering: C* **2017**, *78*, 503–512.

(26) Lee, J.; Kim, G. Three-Dimensional Hierarchical Nanofibrous Collagen Scaffold Fabricated Using Fibrillated Collagen and Pluronic F-127 for Regenerating Bone Tissue. *ACS Appl. Mater. Interfaces* **2018**, *10* (42), 35801–35811.

(27) Fielding, G.; Bose, S. SiO2 and ZnO Dopants in Three-Dimensionally Printed Tricalcium Phosphate Bone Tissue Engineering Scaffolds Enhance Osteogenesis and Angiogenesis in Vivo. *Acta Biomaterialia* **2013**, *9* (11), 9137–9148.

(28) Ozturk, B. Y.; Inci, I.; Egri, S.; Ozturk, A. M.; Yetkin, H.; Goktas, G.; Elmas, C.; Piskin, E.; Erdogan, D. The Treatment of Segmental Bone Defects in Rabbit Tibiae with Vascular Endothelial Growth Factor (VEGF)-Loaded Gelatin/Hydroxyapatite "Cryogel" Scaffold. *Eur J Orthop Surg Traumatol* **2013**, *23* (7), 767–774.

(29) Raja, N.; Yun, H. A Simultaneous 3D Printing Process for the Fabrication of Bioceramic and Cell-Laden Hydrogel Core/Shell Scaffolds with Potential Application in Bone Tissue Regeneration. *J. Mater. Chem. B* **2016**, *4* (27), 4707–4716.

(30) Qu, H.; Fu, H.; Han, Z.; Sun, Y. Biomaterials for Bone Tissue Engineering Scaffolds: A Review. *RSC Adv.* **2019**, *9* (45), 26252–26262.

(31) Dimitriou, R.; Jones, E.; McGonagle, D.; Giannoudis, P. V. Bone Regeneration: Current Concepts and Future Directions. *BMC Med* **2011**, *9* (1), 66.

(32) Xia, B.; Deng, Y.; Lv, Y.; Chen, G. Stem Cell Recruitment Based on Scaffold Features for Bone Tissue Engineering. *Biomater. Sci.* **2021**, *9* (4), 1189–1203.

(33) Osathanon, T.; Giachelli, C. M.; Somerman, M. J. Immobilization of Alkaline Phosphatase on Microporous Nanofibrous Fibrin Scaffolds for Bone Tissue Engineering. *Biomaterials* **2009**, *30* (27), 4513–4521.

(34) Gulseren, G.; Yasa, I. C.; Ustahuseyin, O.; Tekin, E. D.; Tekinay, A. B.; Guler, M. O. Alkaline Phosphatase-Mimicking Peptide Nanofibers for Osteogenic Differentiation. *Biomacromolecules* **2015**, *16* (7), 2198–2208.

(35) Fan, Y.; Ren, G.; Cui, Y.; Liu, H.; Li, S.; Tian, Y.; Wang, G.; Peng, C.; Wang, Y.; Wu, D. Peptide-Based Hydrogel for Enhanced Bone Repair. *Materials & Design* **2023**, *229*, 111862.

(36) Quan, C.; Zhang, Z.; Liang, P.; Zheng, J.; Wang, J.; Hou, Y.; Tang, Q. Bioactive Gel Self-Assembled from Phosphorylate Biomimetic Peptide: A Potential Scaffold for Enhanced Osteogenesis. *International Journal of Biological Macromolecules* **2019**, *121*, 1054–1060.

(37) Lee, S. S.; Hsu, E. L.; Mendoza, M.; Ghodasra, J.; Nickoli, M. S.; Ashtekar, A.; Polavarapu, M.; Babu, J.; Riaz, R. M.; Nicolas, J. D.; Nelson, D.; Hashmi, S. Z.; Kaltz, S. R.; Earhart, J. S.; Merk, B. R.; McKee, J. S.; Bairstow, S. F.; Shah, R. N.; Hsu, W. K.; Stupp, S. I. Gel Scaffolds of BMP-2-Binding Peptide Amphiphile Nanofibers for Spinal Arthrodesis. *Adv Healthcare Materials* **2015**, *4* (1), 131–141.

(38) Zhou, A.; Chen, S.; He, B.; Zhao, W.; Chen, X.; Jiang, D. Controlled Release of TGF-Beta 1 from RADA Self-Assembling Peptide Hydrogel Scaffolds. *DDDT* **2016**, *Volume 10*, 3043–3051.

(39) Segman-Magidovich, S.; Grisaru, H.; Gitli, T.; Levi-Kalisman, Y.; Rapaport, H. Matrices of Acidic β -Sheet Peptides as Templates for Calcium Phosphate Mineralization. *Advanced Materials* **2008**, *20* (11), 2156–2161.

(40) Sugino, A.; Miyazaki, T.; Ohtsuki, C. Apatite-Forming Ability of Polyglutamic Acid Hydrogels in a Body-Simulating Environment. *J Mater Sci: Mater Med* **2008**, *19* (6), 2269–2274.

(41) Hartgerink, J. D.; Beniash, E.; Stupp, S. I. Self-Assembly and Mineralization of Peptide-Amphiphile Nanofibers. *Science* **2001**, *294* (5547), 1684–1688.

(42) Spoerke, E. D.; Anthony, S. G.; Stupp, S. I. Enzyme Directed Templating of Artificial Bone Mineral. *Advanced Materials* **2009**, *21* (4), 425–430.

(43) Suh, J.; Oh, S. Remarkable Proteolytic Activity of Imidazoles Attached to Cross-Linked Polystyrene. *J. Org. Chem.* **2000**, *65* (22), 7534–7540.

(44) Parkin, G. Synthetic Analogues Relevant to the Structure and Function of Zinc Enzymes. *Chem. Rev.* **2004**, *104* (2), 699–768.

(45) Tolosa, L.; Donato, M. T.; Gómez-Lechón, M. J. General Cytotoxicity Assessment by Means of the MTT Assay. In *Protocols in In Vitro Hepatocyte Research*; Vinken, M., Rogiers, V., Eds.; Methods in Molecular Biology; Springer New York: New York, NY, 2015; Vol. 1250, pp 333–348.

(46) Zhang, Y.; Remy, M.; Leste-Lasserre, T.; Durrieu, M.-C. Manipulating Stem Cell Fate with Disordered Bioactive Cues on Surfaces: The Role of Bioactive Ligand Selection. *ACS Appl. Mater. Interfaces* **2024**, *16* (15), 18474–18489.

(47) Huang, Y.-F.; Li, L.-J.; Gao, S.-Q.; Chu, Y.; Niu, J.; Geng, F.-N.; Shen, Y.-M.; Peng, L.-H. Evidence Based Anti-Osteoporosis Effects of Periplaneta Americana L on

Osteoblasts, Osteoclasts, Vascular Endothelial Cells and Bone Marrow Derived Mesenchymal Stem Cells. *BMC Complement Altern Med* **2017**, *17* (1), 413.

(48) Cheng, X.; Gao, D.-X.; Song, J.-J.; Ren, F.-Z.; Mao, X.-Y. Casein Glycomacropeptide Hydrolysate Exerts Cytoprotection against H_2O_2-Induced Oxidative Stress in RAW 264.7 Macrophages via ROS-Dependent Heme Oxygenase-1 Expression. *RSC Adv.* **2015**, *5* (6), 4511–4523.

(49) Suh, J.; Oh, S. Remarkable Proteolytic Activity of Imidazoles Attached to Cross-Linked Polystyrene. *J. Org. Chem.* **2000**, *65* (22), 7534–7540.

(50) Byler, K. G.; Li, Y.; Houghten, R. A.; Martinez-Mayorga, K. The Role of Imidazole in Peptide Cyclization by Transesterification: Parallels to the Catalytic Triads of Serine Proteases. *Org. Biomol. Chem.* **2013**, *11* (18), 2979.

(51) Jencks, W. P.; Carriuolo, J. Imidazole Catalysis. *Journal of Biological Chemistry* **1959**, *234* (5), 1280–1285.

(52) Xu, N.; Chen, G.; Liu, H. Antioxidative Categorization of Twenty Amino Acids Based on Experimental Evaluation. *Molecules* **2017**, *22* (12), 2066.

(53) Ding, Y.; Lambden, E.; Peate, J.; Picken, L. J.; Rees, T. W.; Perez-Ortiz, G.; Newgas, S. A.; Spicer, L. A. R.; Hicks, T.; Hess, J.; Ulmschneider, M. B.; Müller, M. M.; Barry, S. M. Rapid Peptide Cyclization Inspired by the Modular Logic of Nonribosomal Peptide Synthetases. *J. Am. Chem. Soc.* **2024**, *146* (24), 16787–16801.

(54) Shivange, A. V.; Daugherty, P. S. De Novo Discovery of Bioactive Cyclic Peptides Using Bacterial Display and Flow Cytometry. In *Peptide Libraries*; Derda, R., Ed.; Methods in Molecular Biology; Springer New York: New York, NY, 2015; Vol. 1248, pp 139–153.

(55) Song, Q.; Cheng, Z.; Kariuki, M.; Hall, S. C. L.; Hill, S. K.; Rho, J. Y.; Perrier, S. Molecular Self-Assembly and Supramolecular Chemistry of Cyclic Peptides. *Chem. Rev.* **2021**, *121* (22), 13936–13995.

(56) Jang, B.-B.; Lee, K.-P.; Min, D.-H.; Suh, J. Immobile Artificial Metalloproteinase Containing Both Catalytic and Binding Groups. *J. Am. Chem. Soc.* **1998**, *120* (46), 12008–12016.

(57) Ghadiri, M. R.; Granja, J. R.; Milligan, R. A.; McRee, D. E.; Khazanovich, N. Self-Assembling Organic Nanotubes Based on a Cyclic Peptide Architecture. *Nature* **1993**, *366* (6453), 324–327.

(58) Wu, Y.; Li, X.; Sun, Y.; Tan, X.; Wang, C.; Wang, Z.; Ye, L. Multiscale Design of Stiffening and ROS Scavenging Hydrogels for the Augmentation of Mandibular Bone Regeneration. *Bioactive Materials* **2023**, *20*, 111–125.

(59) Liang, X.; Yang, X.; Liu, J.; Tu, L.; Wei, W.; Wang, H.; Wu, M.; Cai, L.; Zheng, Y.; Chen, Y. ROS-Scavenging Bioactive Scaffold Orchestrates Bone Regeneration for Osteoporotic Bone Defect Repair. *Composites Part B: Engineering* **2024**, *281*, 111528.

(60) Asghar, M. S.; Li, J.; Ahmed, I.; Ghazanfar, U.; Irshad, M. S.; Idrees, M.; Haq, Z.; Rizwan, M.; Sheikh, F.; Yasmeen, F. Antioxidant, and Enhanced Flexible Nano Porous Scaffolds for Bone Tissue Engineering Applications. *Nano Select* **2021**, *2* (7), 1356–1367.

(61) Cerqueni, G.; Scalzone, A.; Licini, C.; Gentile, P.; Mattioli-Belmonte, M. Insights into Oxidative Stress in Bone Tissue and Novel Challenges for Biomaterials. *Materials Science and Engineering: C* **2021**, *130*, 112433.

(62) Iantomasi, T.; Romagnoli, C.; Palmini, G.; Donati, S.; Falsetti, I.; Miglietta, F.; Aurilia, C.; Marini, F.; Giusti, F.; Brandi, M. L. Oxidative Stress and Inflammation in Osteoporosis: Molecular Mechanisms Involved and the Relationship with microRNAs. *IJMS* **2023**, *24* (4), 3772.

(63) Golub, E. E.; Boesze-Battaglia, K. The Role of Alkaline Phosphatase in Mineralization. *Current Opinion in Orthopaedics* **2007**, *18* (5), 444–448.

(64) Ansari, S.; Ito, K.; Hofmann, S. Alkaline Phosphatase Activity of Serum Affects Osteogenic Differentiation Cultures. *ACS Omega* **2022**, *7* (15), 12724–12733.

(65) Jeon, S.; Lee, J. H.; Jang, H. J.; Lee, Y. B.; Kim, B.; Kang, M. S.; Shin, Y. C.; Shin, D.-M.; Hong, S. W.; Han, D.-W. Spontaneously Promoted Osteogenic Differentiation of MC3T3-E1 Preosteoblasts on Ultrathin Layers of Black Phosphorus. *Materials Science and Engineering: C* **2021**, *128*, 112309.

(66) Shin, Y. C.; Lee, J. H.; Jin, O. S.; Kang, S. H.; Hong, S. W.; Kim, B.; Park, J.-C.; Han, D.-W. Synergistic Effects of Reduced Graphene Oxide and Hydroxyapatite on Osteogenic Differentiation of MC3T3-E1 Preosteoblasts. *Carbon* **2015**, *95*, 1051–1060.

(67) Puchtler, H.; Meloan, S. N.; Terry, M. S. On The History and Mechanism of Alizarin and Alizarin Red S Stains for Calcium. *J Histochem Cytochem.* **1969**, *17* (2), 110–124.

(68) Moser, S. C.; Van Der Eerden, B. C. J. Osteocalcin—A Versatile Bone-Derived Hormone. *Front. Endocrinol.* **2019**, *9*, 794.

(69) Liu, T. M.; Lee, E. H. Transcriptional Regulatory Cascades in Runx2-Dependent Bone Development. *Tissue Engineering Part B: Reviews* **2013**, *19* (3), 254–263.

(70) Iline-Vul, T.; Nanda, R.; Mateos, B.; Hazan, S.; Matlahov, I.; Perelshtein, I.; Keinan-Adamsky, K.; Althoff-Ospelt, G.; Konrat, R.; Goobes, G. Osteopontin Regulates Biomimetic Calcium Phosphate Crystallization from Disordered Mineral Layers Covering Apatite Crystallites. *Sci Rep* **2020**, *10* (1), 15722.

(71) Tu, M.-G.; Chen, Y.-W.; Shie, M.-Y. Macrophage-Mediated Osteogenesis Activation in Co-Culture with Osteoblast on Calcium Silicate Cement. *J Mater Sci: Mater Med* **2015**, *26* (12), 276.

(72) Siadat, S. M.; Silverman, A. A.; DiMarzio, C. A.; Ruberti, J. W. Measuring Collagen Fibril Diameter with Differential Interference Contrast Microscopy. *Journal of Structural Biology* **2021**, *213* (1), 107697.

CHAPTER - 5

Conclusions and perspectives

Chapter 5
Conclusion and perspectives

5.1. Thesis summary

This thesis has explored the innovative use of self-assembled peptide-based biomaterials for wound healing and bone regeneration by presenting a drug and growth-factor free approach in it. The strategic choice of self-assembled peptides over other materials was to leverage their unique advantages like natural biocompatibility and optimal degradation. Unlike synthetic polymers or metallic materials, peptides are composed of natural amino acids, making them inherently biocompatible, reducing the risk of adverse immune responses and eliminating the long-term complications. Moreover, they offer a remarkable versatility in functionalization of the backbone. By incorporating specific amino acid sequences, peptides can be designed to possess desired biological activities, such as antibacterial properties, reactive oxygen species (ROS) scavenging, angiogenesis promotion and osteogenic differentiation. Self-assembled peptides can be precisely engineered to form a variety of nanostructures, such as hydrogels, nanotubes, and nanofibers, tailored with functionalities to meet specific biomedical needs. Various peptide-based biomaterials have been developed and investigated globally by the researchers for their wound healing and bone regeneration potential. These scaffolds have been loaded with antibiotics, drugs, growth factors, and stem cells but the exogenous administration of these biomolecules elicit the immunogenic response and have other drawbacks like off-targeting, drug-resistance, instability, and tumorigenesis. Therefore, we decided to develop the peptide-based biomaterials with the rational incorporation of amino acids and functional groups to impart the wound healing and bone regenerative properties without the use of any drugs or growth factors.

The thesis is structured into five chapters, focusing mainly on the peptide self-assembly process in **Chapter 1**. This chapter discusses the diverse nanostructures resulting from peptide self-assembly, along with the strategies for their fabrication and the factors influencing the self-assembly. It further presents a comprehensive review of existing literature, particularly highlighting the biomedical applications of these nanostructures in areas such as wound healing and bone regeneration. The literature review is followed by the identification of current knowledge gaps and the specific objectives of the thesis to address these gaps.

Chapter 2 elaborates on the development of a novel multifunctional wound-healing nanofibrous peptide gel (NLG), synthesized from the peptide sequence, LA-^{L}Lys-^{D}Phe-^{L}Lys-NH_2 loaded with Y_2O_3 nanoparticles. This scaffold demonstrated a potential in bactericidal, reactive oxygen species (ROS)-scavenging, and proangiogenic activities crucial for enhancing chronic wound

healing. The analysis of the peptide gel revealed its nanofibrous morphology, excellent self-healing attributes, viscoelasticity, and mechanical strength. A strategic incorporation of D-phenylalanine in the peptide sequence imparts the peptide with significant proteolytic stability to counter the elevated protease activities typically observed in wound sites. The selection of this particular peptide sequence was methodically approached to include basic amino acids such as lysine, endowed with side chains containing amine groups. These groups engage in interactions with the positively charged membranes of bacteria, disrupting their integrity and functionality, thereby exhibiting potent antibacterial effects against strains such as *E. coli* and *S. aureus*. Moreover, these amine groups have lone pair of electrons that can play a crucial role in shielding cells from oxidative damage and endows the material with reactive oxygen species (ROS)-scavenging capabilities. This characteristic is significantly enhanced by the passive incorporation of Y_2O_3 nanoparticles within the scaffold, which not only augments the mechanical strength of the gel but also endows it with angiogenic properties. The Y_2O_3 nanoparticles elicit a transient hypoxic state, which results in the activation of a hypoxia-inducible cellular pathway that promotes cell proliferation and angiogenesis. This is primarily mediated through the activation of hypoxia-inducible factor-1 (HIF-1), which subsequently upregulates the expression of vital angiogenic factors such as VEGF, EGFR, and FGF-2. These factors play pivotal role in modulating cellular behaviour encouraging enhanced cell proliferation and migration. Overall, this NP-loaded peptide-based scaffold provides a comprehensive approach to target the multifaceted challenges of chronic wound healing.

Chapter 3 reports the development of heparan sulfate-mimicking cyclic peptide nanotubes promoting angiogenesis under diabetic wound conditions. We have synthesized cyclic-hexapeptides, ^{D}Pro-^{L}Trp-^{D}Leu-^{L}Ser-^{D}Glu-^{L}Lys: SEK, ^{D}Pro-^{L}Trp-^{D}Leu-^{L}Lys-^{D}Glu-^{L}Lys: KEK, and ^{D}Pro-^{L}Glu-^{D}Leu-^{L}Lys-^{D}Phe-^{L}Lys: KFK, functionalized them with the bioactive sulfonate group and fabricated their nanotubes. The presence of heparin-inspired functional groups like hydroxyl, carboxylate, and sulfonate in the SEK nanotubes aids them to promote the binding of growth factors like VEGF and FGF-2 to their cognate receptors and activates the angiogenic signalling pathways. The comparative analysis of the SEK nanotubes with KEK and KFK demonstrated the impact of the hydroxyl group on the angiogenic potential of these nanomaterials. The nanotubes demonstrated excellent biocompatibility against murine fibroblast (L929) and human umbilical vein endothelial (HUVEC) cell lines and did not elicit immunogenic response or ROS stress. These nanostructures were also found to be hemocompatible when analyzed using fresh human blood samples. Interestingly, under the hyperglycemic conditions, SEK nanotubes significantly upregulated the expression levels of various angiogenic genes like *Zeb1, ETV2, vWF, eNOS, Tie2, TGF-β, VE-Cad, VEGF, FGF2, VEGFR2*, and *FGFR1* in HUVECs. Moreover, the elevated expression of proangiogenic marker proteins such as *VE-Cad, VEGFR2, CD31, eNOS, Tie2, vWF, FGFR1,* and *Zeb1* was observed.

These nanotubes not only assisted in the growth factors-receptor binding but also prevented the degradation of growth factors under the proteolytic wound environment. Hence, it demonstrated an upregulated expression of proangiogenic genes compared to the hyperglycemic untreated endothelial cells. Furthermore, the nanotubes were found to restore the activity of dysfunctional hyperglycemic HUVECs and significantly improve their migration, invasion, and tube formation capabilities in a 3D Matrigel matrix. These results underline the therapeutic potential of SEK nanotubes in enhancing impaired vascularization, particularly under hyperglycemic conditions that mimic diabetic complications. Their ability to upregulate proangiogenic processes positions them as valuable tools in the development of advanced treatments for diabetic wound healing.

Chapter 4 delves into the innovative development of cyclic-octapeptide nanotubes, which are ingeniously designed to replicate the activity of the alkaline phosphatase (ALP) enzyme. This is achieved through the strategic incorporation of histidine into the peptide sequence, ^{L}His-^{D}Lys-^{L}His-^{D}Lys-^{L}Ala-^{D}Leu-^{L}Ala-^{D}Pro, thus, endowing these nanotubes with catalytically active imidazole rings that promote the bone mineralization and osteogenic differentiation, effectively emulating the natural activity of ALP. The imidazolyl group is prevalent in the functional domain of various proteinase enzymes, and its ability to ionize at nearly neutral pH endows it with the versatility to act in several catalytic roles, such as nucleophiles, general acids, and general bases. This ability is harnessed in designing these artificial enzyme-mimicking nanostructures, where two histidine residues are integrated into the peptide chain, which upon self-assembly, formed nanotubes with multiple imidazolyl groups in close proximity. This arrangement facilitates their effective cooperative interaction in the catalytic process. The cell culture studies showed that the nanotubes were biocompatible to the murine preosteoblast MC3T3-E1 cells, and promoted their proliferation and migration. Importantly, these nanotubes did not trigger any immunogenic response. However, there was a notable downregulation in the expression of proinflammatory markers like *iNOS* and *TNF-α*, alongside an upregulation of the M2-macrophage marker *IL-10*, which suggests the fabricated nanotubes may possess anti-inflammatory properties. Additionally, nanotubes showcased their ROS-scavenging potential on H_2O_2-treated MC3T3-E1 cells. The investigations further extended to evaluate their ability to induce ossification by analyzing early and late-stage osteogenic differentiation markers. Results demonstrated an elevated alkaline phosphatase activity along with their ability to facilitate bone mineralization through calcium deposition in preosteoblast cells over 7- and 14-day periods. The upregulated expression of osteogenic differentiation marker genes such as *OCN*, *ALP*, *OPN*, and *RUNX2* further attested to their osteogenic effectiveness. In the coculture studies involving preosteoblasts and macrophages, the nanotubes exhibited their potential to inhibit osteoclastogenesis by downregulating the expression of osteoclast differentiation markers. Overall, this study describes the rational design and fabrication of ALP-mimetic self-

assembled cyclic peptide nanotubes and their considerable potential as an artificial enzyme-mimicking framework, fostering bone regeneration through a cell-free, growth factor-free approach.

In **Chapter 5**, an overall summary, contribution to the current knowledge, and prospects for future development has been provided.

5.2. Contribution to existing knowledge

In this thesis, our aim was to develop self-assembled peptide-based nanoassemblies with an inherent ability to address the challenges associated with current therapeutic approaches for chronic wound healing and bone regeneration, without employing drug or growth factor.

Chronic wounds pose significant challenges in their management due to multiple impediments such as impaired angiogenesis, infections, prolonged inflammation, and comorbid conditions like diabetes. The intricate nature of these wounds necessitates a comprehensive approach to treatment. However, the current therapeutic strategies often target a singular aspect of wound pathology or utilize complex systems containing a combination of antibiotics, drugs, and growth factors. Such approaches may either fall short of effectiveness or present overwhelming complexity in predicting their biological outcomes. This situation highlights the critical need for innovative treatment modalities capable of addressing the multifaceted aspects of wound healing without incorporating undue complexity into the treatment regimen. The emergence of antibiotic-resistant bacteria presents a significant challenge, a problem compounded by the toxicity concerns associated with traditional antimicrobial materials such as metals, metal oxides, polymers, and ceramics towards healthy cells. We have addressed these challenges by developing self-assembled, antimicrobial peptide gel with inherent bactericidal properties and loaded them with proangiogenic Y_2O_3 nanoparticles. This combination not only provides material with inherent bactericidal and angiogenic properties but also effectively reduce the toxicity associated with nanoparticles. Furthermore, the peptide gel demonstrated considerable antioxidant and ROS-scavenging activities, underscoring its potential as a multifunctional scaffold designed to target infections, impaired angiogenesis and preventing ROS-induced inflammation to promote chronic wound healing.

Conventional proangiogenic strategies primarily focused on using natural biomolecules like angiogenesis-promoting growth factors (notably VEGF and FGF-2) as well as glycosaminoglycans (specifically heparan sulfate) to foster the angiogenic process. However, these biomolecules face several challenges in the chronic wound microenvironment, including poor stability, relatively short half-life, and issues related to delivery, dosage, and cost-effectiveness. Moreover, their exogenous administration can trigger an immunogenic response,

leading to inflammation or other adverse effects. Peptide-based nanomaterials tailored with desired functional groups offer a promising alternative by overcoming these limitations. We addressed these challenges by developing cyclic peptide nanotubes functionalized with key functional groups, such as sulfate, hydroxyl, and carboxylate present on heparan sulfate chains. These nanotubes were cytocompatible and exhibited an immune suppressive effect. Moreover, it upregulated the expression of proangiogenic marker genes and proteins along with restoring the activity of dysfunctional endothelial cells under hyperglycemic diabetic conditions. Thus, these nanotubes had the inherent ability to promote angiogenesis by avoiding the use of any exogenous growth factors or supplements like heparin. The developed peptide-based materials demonstrated proteolytic stability due to the incorporation of non-natural D-amino acids and cyclization, thus, addressing the challenge associated with peptide stability for use in chronic wound healing.

Current therapeutic modalities for bone damage primarily revolve around the use of auto/allo bone grafts. Recent years have witnessed a significant advancement in the research on bioactive scaffolds obtained from polymers, metals, ceramics, and composites. These scaffolds are often enhanced with additives such as drugs, enzymes, growth factors, and stem cells to facilitate bone repair and regeneration. Despite the promise, several notable challenges persist, such as secondary surgeries for graft removal, drugs off-targeting, growth factor stability, batch-to-batch variance in enzyme efficacy and potential tumorigenic and inflammatory responses to stem cells. Chapter 4 of the thesis contributed to address these gaps by developing artificial ALP enzyme-mimicking cyclic peptide nanotubes containing bioactive imidazole groups to promote osteogenic differentiation and bone mineralization. As imidazole groups are present in the functionally active domain of enzyme, they provide the material with an inherent ability to mimic the alkaline phosphatase activity. This inherent potential led nanotubes to promote the formation of bone-like nodules, upregulate the expression of osteogenic markers and inhibit osteoclastogenesis, thus, eliminating the need for external adjuvants. Moreover, the biomaterial demonstrated ROS-scavenging and anti-inflammatory properties, and it offers a comprehensive approach to bone regeneration.

5.3. Future perspectives

The thesis explores the advancement of peptide-based nanoassemblies by emphasizing their potential as versatile biomaterials with inherent capabilities for applications in chronic wound healing and bone regeneration. By focusing on multifunctional bioactivity, each project has been designed to meet specific therapeutic needs, from antibacterial action and ROS regulation to promoting angiogenesis and osteogenesis. Recognizing the interdependency of these biological processes, our approach has been to develop modular, adaptable peptide formulations that can target different regenerative environments. While each biomaterial targets a specific therapeutic

challenge, they are developed to support the body's natural healing processes by modulating the local biological environment. This integrative approach aligns well with the interconnectedness of oxidative stress, inflammation, and cellular differentiation seen in both wound healing and bone repair. Bringing these peptides closer to clinical use will require a strategy that balances efficacy with safety and reproducibility. To translate these peptides from laboratory to clinical application, preclinical and optimization studies will be essential. The *in vitro* results from each project provide a foundation to further explore these peptides through preclinical and animal studies to refine their bioactivity and therapeutic potential.

The self-assembled peptide gel loaded with Y_2O_3 nanoparticles offers a potential multifunctional strategy to simultaneously address bacterial infections, oxidative stress, and impaired angiogenesis, which are significant barriers to the healing process. Despite promising results in the *in vitro* studies on murine fibroblasts L929 and human umbilical vein endothelial cells cultured under standard conditions, evaluating the effectiveness of this gel in an *in vitro* chronic wound model stands as a critical next step prior to advancement to animal studies. Delving deeper into the molecular biology aspects of its application will shed light on the specific cellular mechanisms affected by the treatment. This multifunctional peptide gel has the potential to serve as a primary dressing. Further preclinical studies utilizing mouse wound models will provide valuable insights regarding wound closure rates, histological responses, inflammatory profiles, as well as their long-term biocompatibility and biodegradation characteristics within a complex cellular environment. Based on these insights, the biomaterial can be optimized for the dosage, concentration, and release profile of Y_2O_3 nanoparticles that balances proangiogenic activity without causing the toxicity. Moreover, it is imperative to assess the efficacy of the peptide gel against a diverse range of drug-resistant bacterial strains that are commonly associated with chronic wounds. If deemed necessary, further optimization of the lysine residues or other functionalization strategies can be pursued to augment the antibacterial and wound healing efficacy of the peptide gel for clinical translation.

The development of proangiogenic cyclic peptide nanotubes for diabetic wound healing addressed various challenges associated with the exogenously administered growth factors, drugs or glycosaminoglycans. We have extensively analyzed the efficacy of the nanotubes in promoting angiogenesis under hyperglycemic diabetic wound conditions and investigated the expressions of various proangiogenic marker proteins and genes. The developed nano assemblies have shown promising results in the *in vitro* studies and can be further taken up for *in vivo* analysis in a diabetic mice model. In preclinical studies involving diabetic murine models, the efficacy of peptide nanotubes in promoting angiogenesis and facilitating wound healing can be assessed through various measures, including wound closure rates, tissue morphology, collagen deposition, vascularization, and overall tissue regeneration. Additionally, tissue samples can be collected to evaluate the signs of inflammation, fibrosis, or other immune

responses that could indicate potential adverse effects. The degradation profile of the peptide nanotubes requires thorough *in vivo* examination to confirm that they degrade at a suitable rate. Given that peptide nanotubes address one of several barriers to chronic wound healing, it is vital to assess various concentrations and combinations of these nanotubes with other wound-healing biomaterials, such as antimicrobial and anti-inflammatory peptides and polymer matrices as well as different methods of administration, including hydrogels or injectable forms, prior to advancing to clinical trials. Thus, transitioning to animal studies will provide more profound insights into the ability of nanotubes to enhance vascularization within the complex diabetic wound microenvironment, thereby, potentially opening new avenues for improving the healing process in diabetic patients.

Lastly, the alkaline phosphatase-mimicking cyclic peptide nanotubes exhibited significant bone regeneration potential by promoting the osteogenic differentiation and bone mineralization in the *in vitro* studies on preosteoblast MC3T3-E1 and murine macrophage RAW264.7 cells for 7 and 14 days. These investigations may be carried out over an extended period of 4 to 8 weeks, which will provide a more in-depth understanding of the long-term cellular responses. Since the material has shown promising results in our studies, performing *in vivo* studies on an osteoporotic mice model will provide essential insights into its efficacy, biocompatibility, long-term safety and regenerative capabilities. To validate osteogenic differentiation, histological examination of tissue sections must be performed, focusing on the presence of a mineralized matrix and bone-specific markers, such as Runx2, Osteopontin, and Osteocalcin. Additionally, long-term toxicological assessments will be essential to establish the maximum safe dosage for *in vivo* applications while avoiding any adverse effects. Moreover, the potential synergistic/additive effect of combining these nanotubes with other osteoinductive scaffolds can be explored to enhance their overall effectiveness. Further, as we progress with preclinical validation, a key consideration should be given to refine the synthesis and scalability of these peptide-based biomaterials to ensure clinical-grade quality, reproducibility, and cost-efficiency.

These projects collectively have the potential address some major challenges in peptide-based therapies for wound healing and bone regeneration. Conducting animal studies is crucial in validating their safety and efficacy in more complex biological systems, which can further pave the way for clinical trials.

Appendix

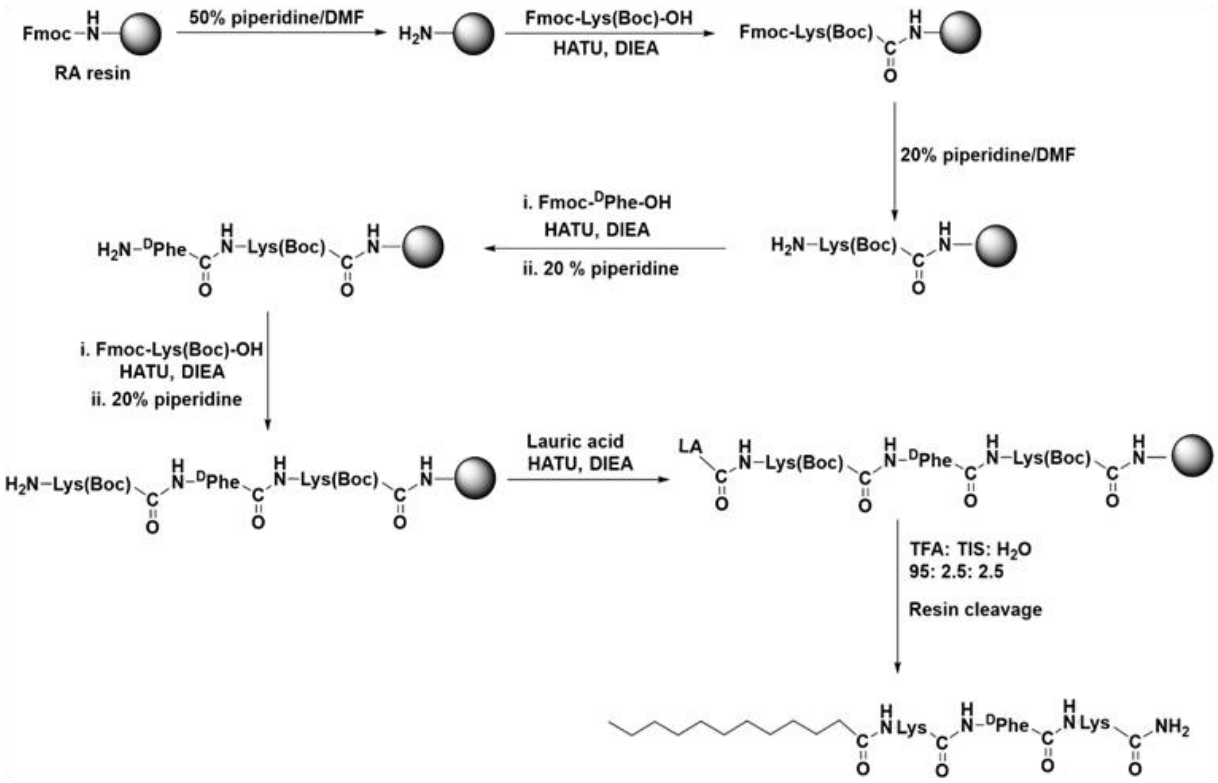

Figure A1. Synthesis of lauric acid-peptide conjugate (LPC) LA-^{L}Lys-^{D}Phe-^{L}Lys-NH_2 using solid-phase peptide synthesis (SPPS) on rink amide resin.

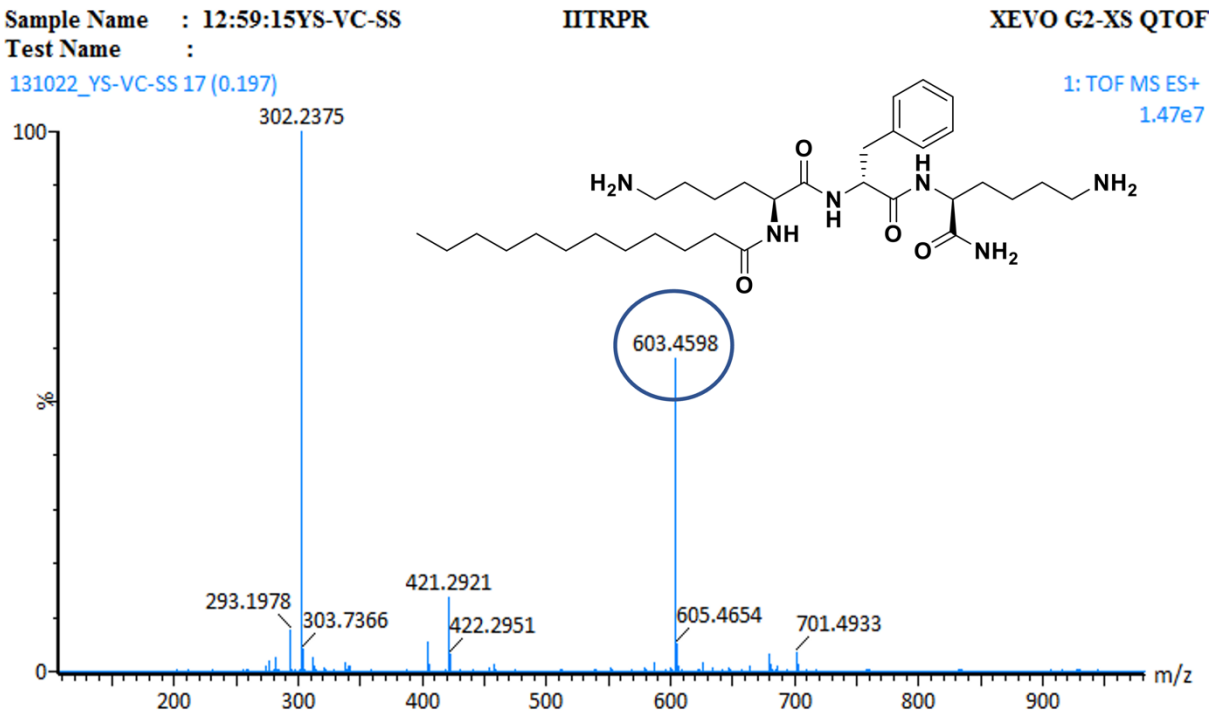

Figure A2. HR-MS data of LA-^{L}Lys-^{D}Phe-^{L}Lys-NH_2 with m/z: $[(M+H)^{+}]$ = 603.4598 Da, $[(M+2H)^{2+}]$ = 302.23 Da.

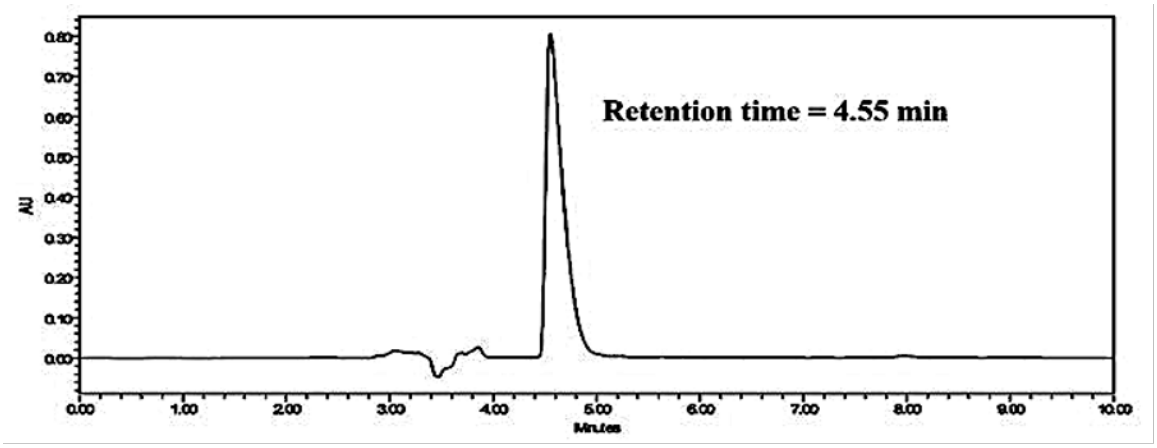

Figure A3. RP-HPLC profile of LA-^{L}Lys-^{D}Phe-^{L}Lys-NH_2. ACN:H_2O was used as the mobile phase in a 50:50 ratio with 0.1% TFA and 1 mL/min flow rate.

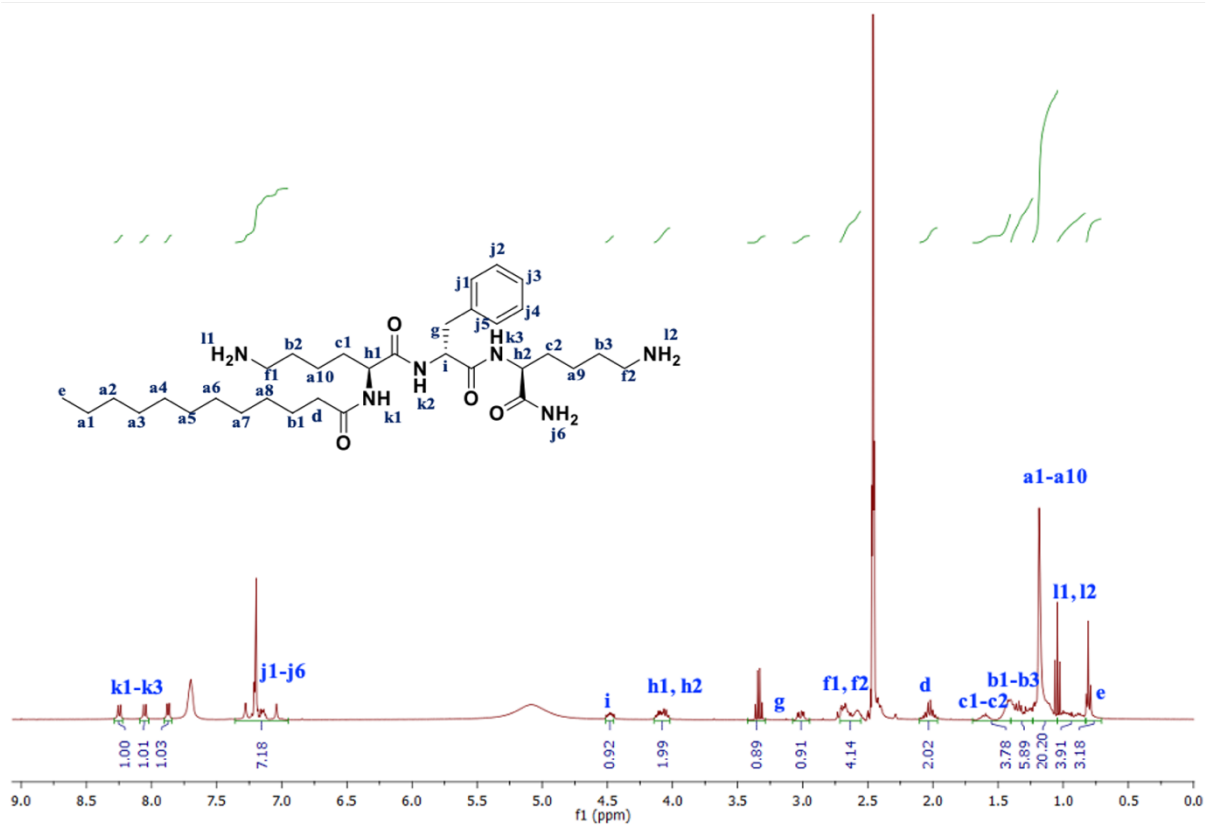

Figure A4. ^{1}H NMR (400 MHz, DMSO-D_6) spectrum of LA-^{L}Lys-^{D}Phe-^{L}Lys-NH_2.

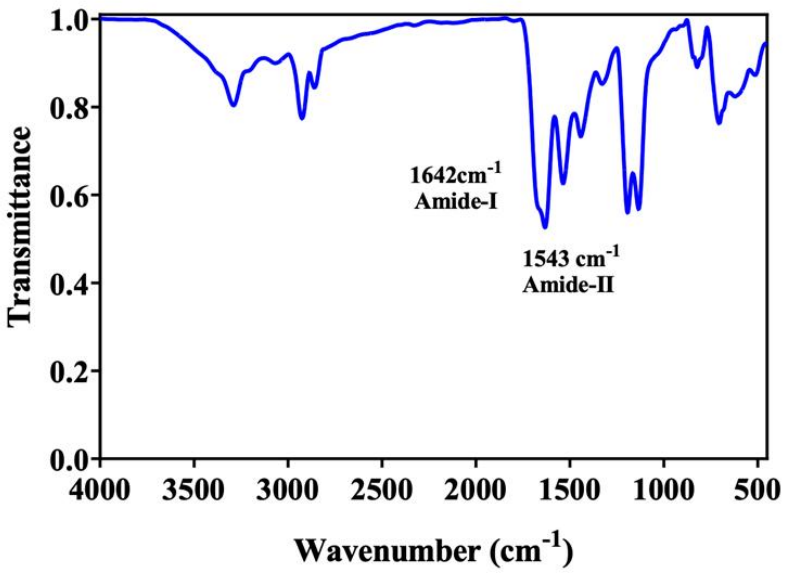

Figure A5. FT-IR spectrum of LA-^{L}Lys-^{D}Phe-^{L}Lys-NH_2.

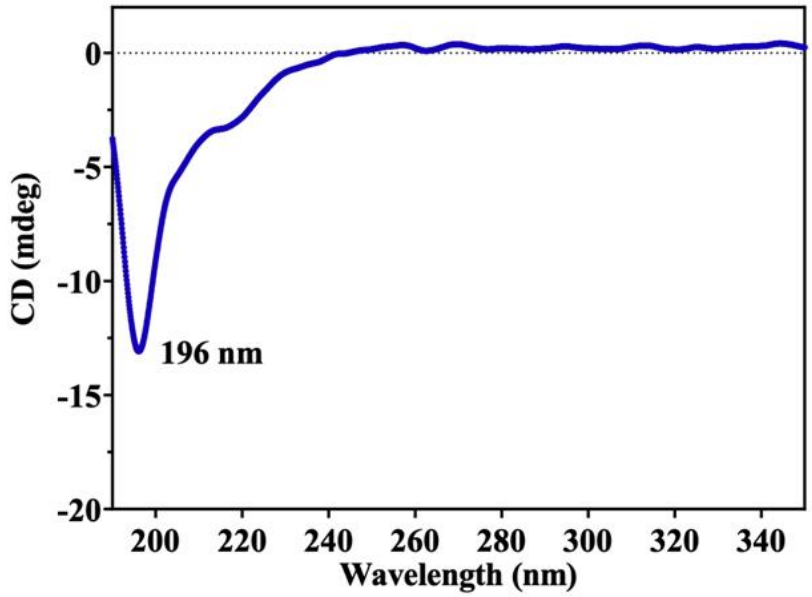

Figure A6. CD spectrum of LA-^{L}Lys-^{D}Phe-^{L}Lys-NH_2 showing minima at 196 nm, thus, confirming random coiled secondary structure.

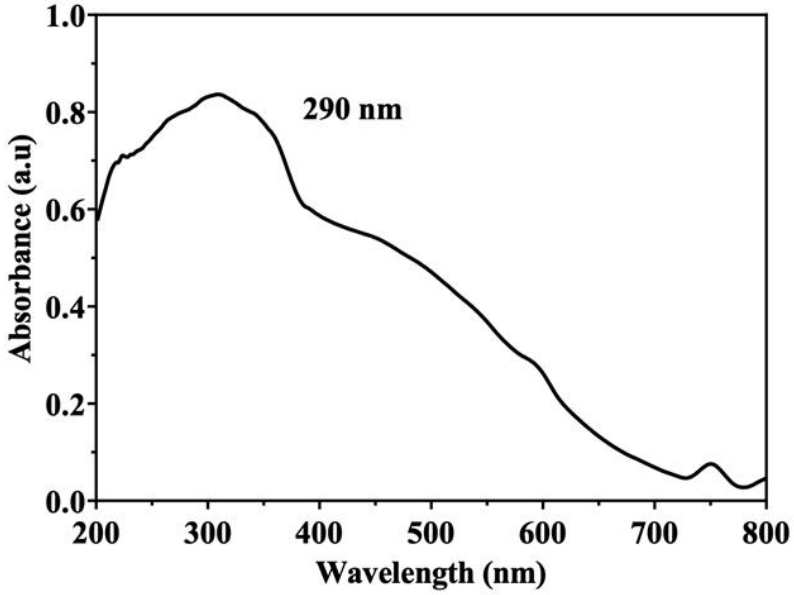

Figure A7. UV-Visible spectrum of yttrium oxide (Y_2O_3) nanoparticles.

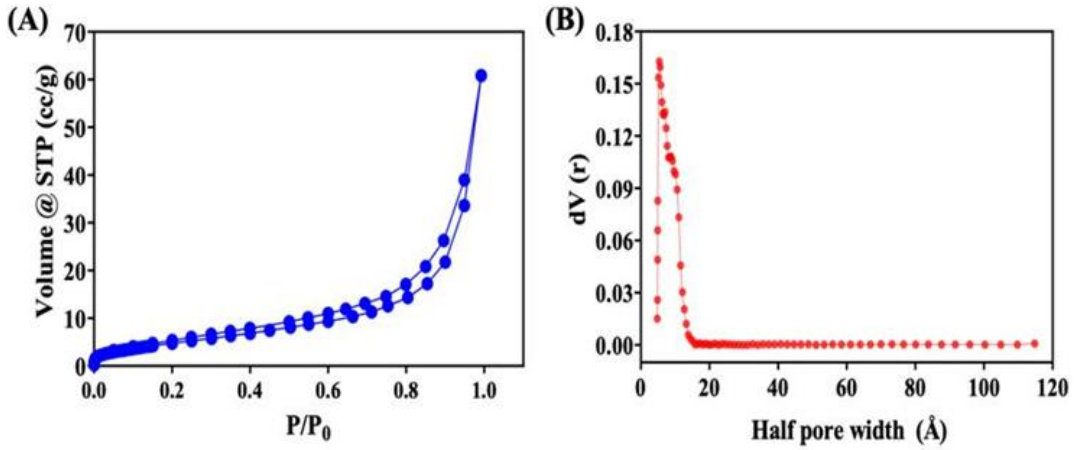

Figure A8. BET plots of Y_2O_3 nanoparticles. (A) N_2 adsorption-desorption isotherm carried out at 77 K. (B) Determination of half pore width by DFT-method.

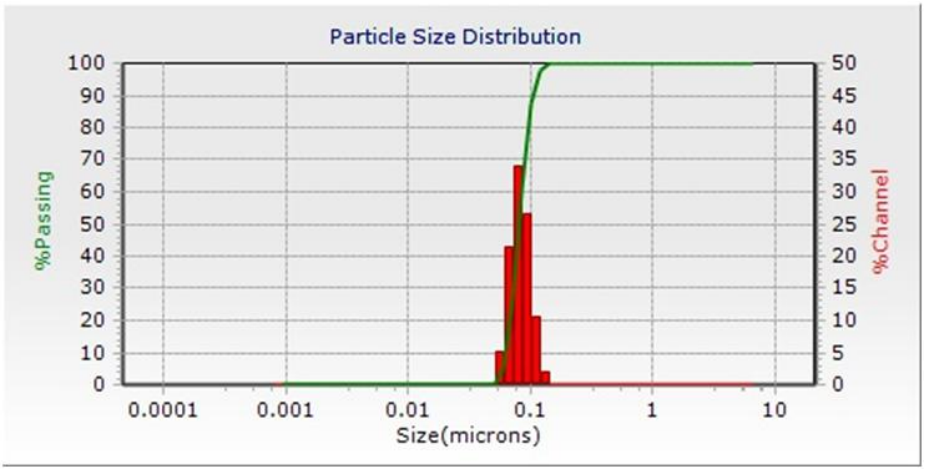

Figure A9. DLS data of Y_2O_3 nanoparticles. Mean particle size was observed to be 80.4 nm, with a polydispersity index of 0.0347.

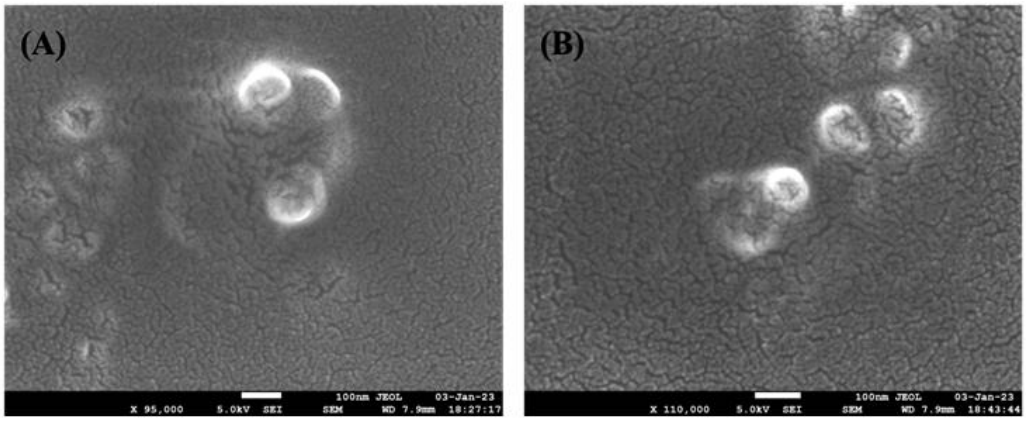

Figure A10. FE-SEM images of Y_2O_3 nanoparticles. Scale bar: 100 nm.

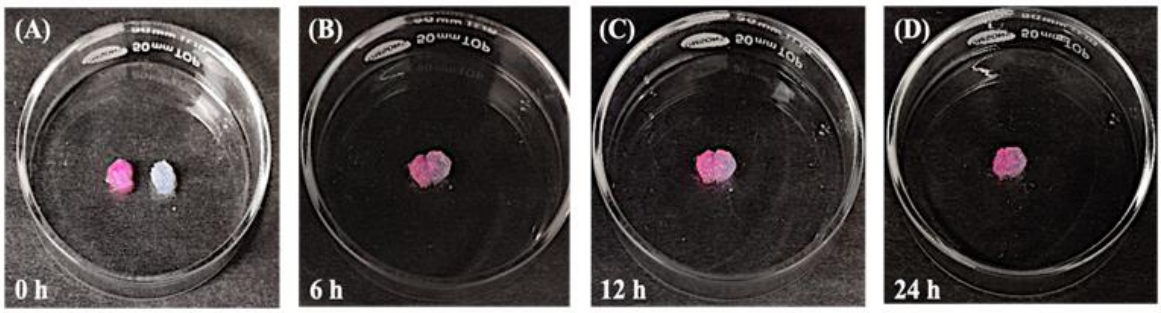

Figure A11. Self-healing of lauric acid-peptide conjugate gel (LPG) observed over different intervals. The gel was cut into half, with one half dyed with rhodamine B and the other left unstained. At various times, images of the dye diffusing from one part to the other were taken. (A) 0 h. (B) 6 h. (C) 12 h. (D) 24 h.

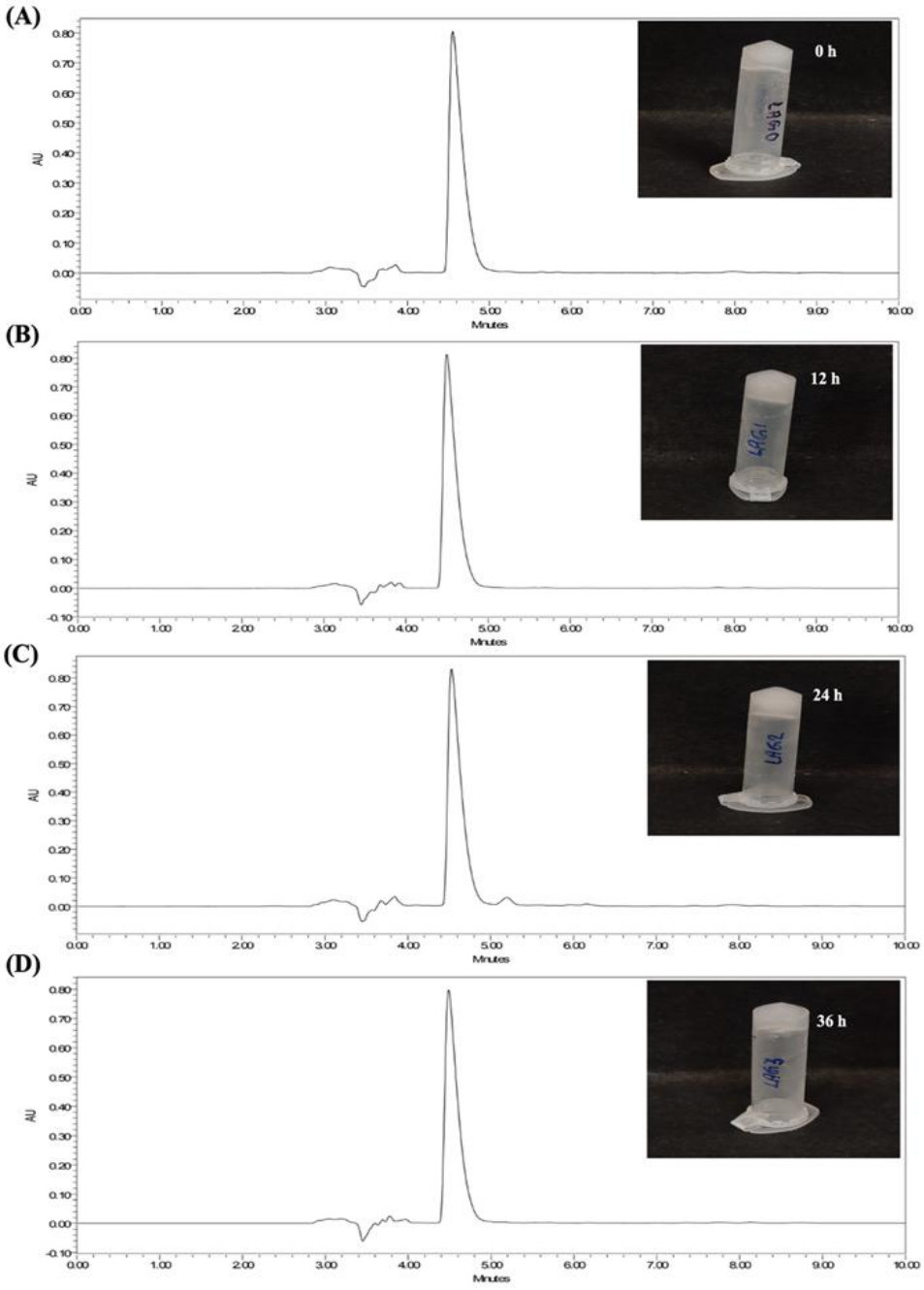

Figure A12. Proteolytic stability studies of peptide-conjugate gel (LPG, LA-^{L}Lys-^{D}Phe-^{L}Lys-NH_2). RP-HPLC profiles and images taken after incubation with a mocktail of proteolytic enzymes for 0, 12, 24, 36 h.

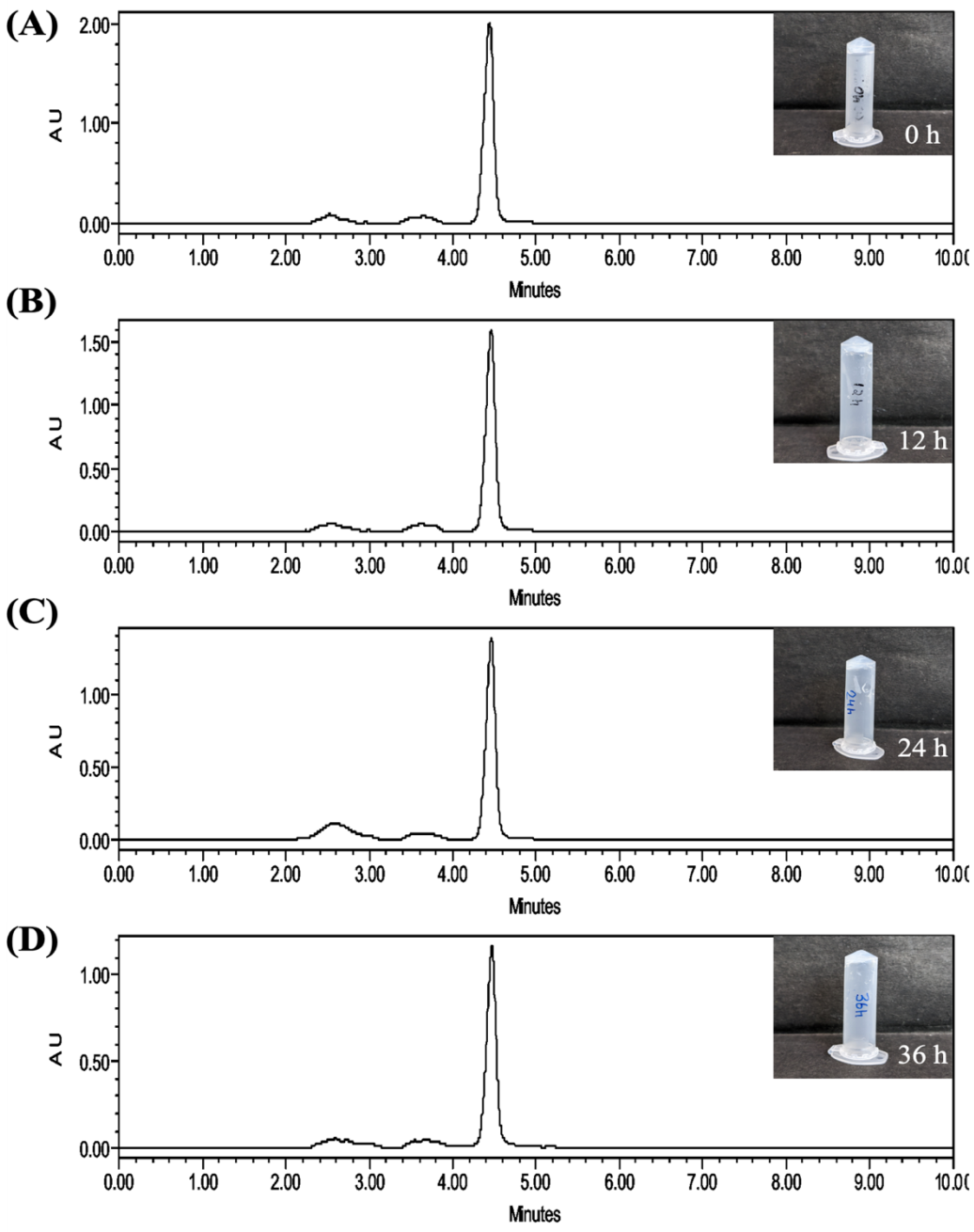

Figure A13. Proteolytic stability studies of peptide-conjugate gel (LA-^{L}Lys-^{L}Phe-^{L}Lys-NH_2). RP-HPLC profiles and images taken after incubation with a mocktail of proteolytic enzymes for 0, 12, 24, 36 h.

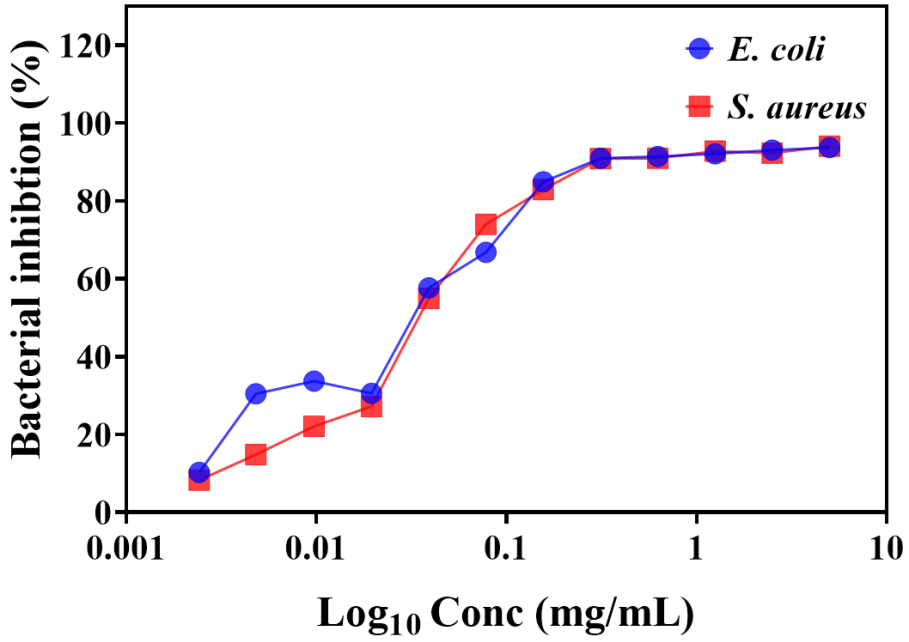

Figure A14. Minimum inhibitory concentrations (MIC) of lauric acid-peptide conjugate against both Gram-negative and Gram-positive bacterial strains, *E. coli* (312 µg/mL) and *S. aureus* (312 µg/mL).

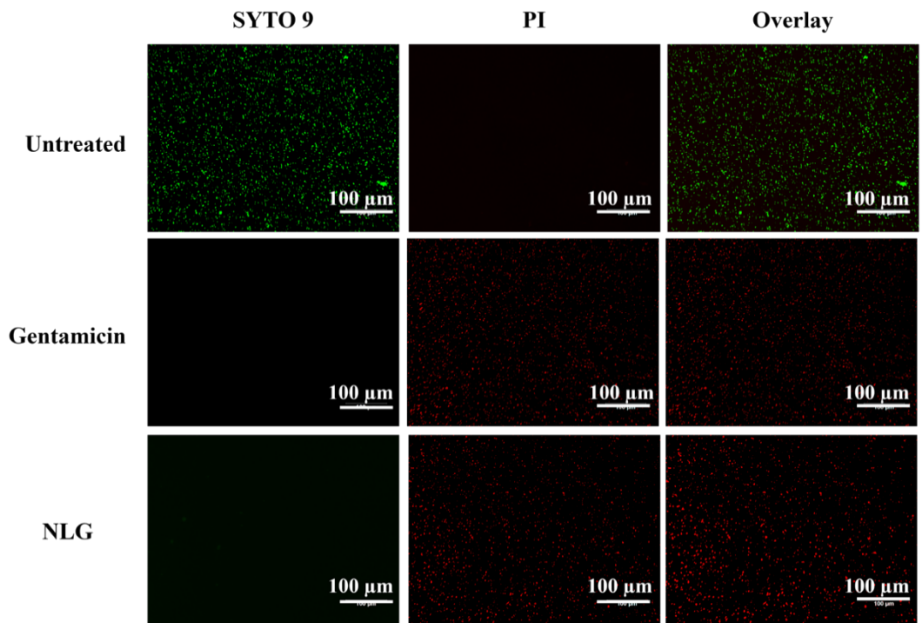

Figure A15. Live/dead fluorescence assay for analyzing antibacterial effect of NP-loaded lauric acid-peptide conjugate gel (NLG) against *E. coli.* Gentamicin sulfate (50 µg/mL) was used as a positive control and untreated bacterial cells served as a negative control. SYTO 9 stains live cells and emits green fluorescence, while PI stains dead cells and emits red fluorescence. The analysis was performed thrice with similar results. Scale bar: 100 µm.

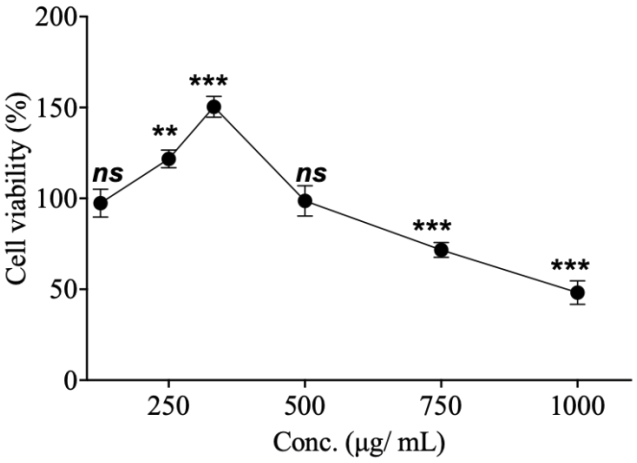

Figure A16. Dose-dependent cell viability of nanoparticle-loaded peptide gel (NLG) in murine fibroblast (L929) cell line. Data are presented as mean ± standard deviation (n = 3), where *P* values <0.05 (*), 0.01 (**), and 0.001 (***) were considered as significant difference, and *ns* represents the insignificant difference.

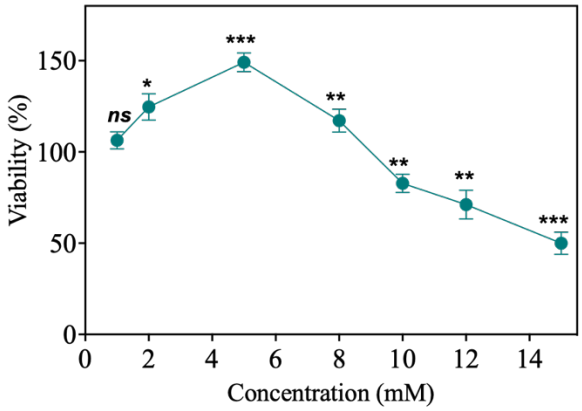

Figure A17. Cell viability analysis for the optimization of Y_2O_3 nanoparticle loading concentration in peptide gel on murine fibroblast (L929) cell line. Data are presented as mean ± standard deviation (n = 3), where *P* values <0.05 (*), 0.01 (**), and 0.001 (***) were considered as significant difference, and *ns* represents the insignificant difference.

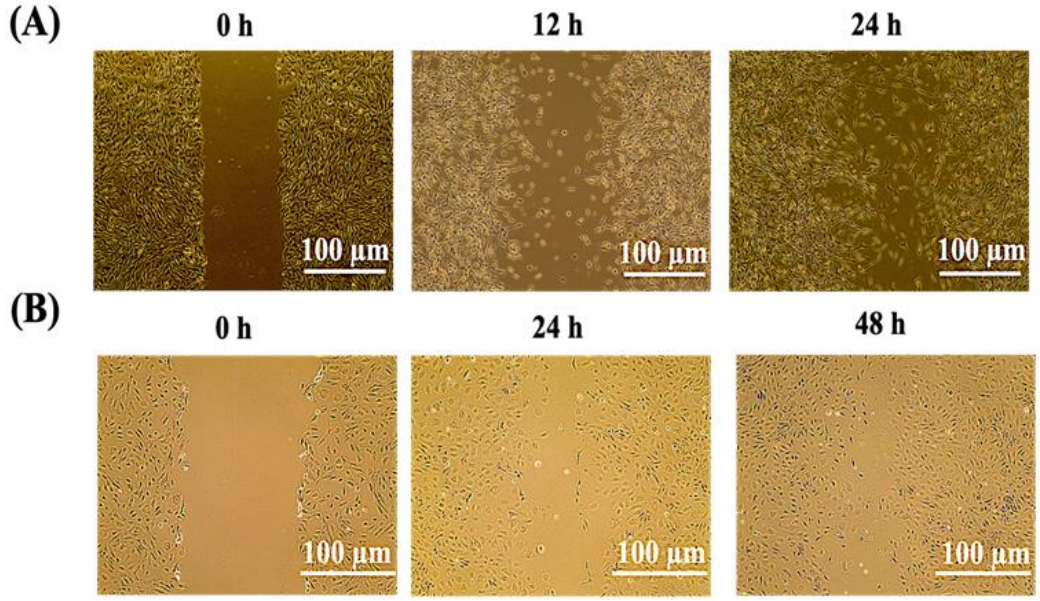

Figure A18. Scratch assay performed on cells treated with lauric acid-peptide conjugate gel (LPG). (A) Scratch healing of murine fibroblast (L929) cells at 0, 12, and 24 h. (B) Images of scratch assay on human umbilical vein endothelial cells (HUVECs) at 0, 24, and 48 h. Scale bar: 100 µm.

Table A1. Primer sequences used in qRT-PCR studies performed on HUVECs on treatment with NLG in Chapter 2.

Genes		Primer sequence (5'-3')
VEGF	Forward Reverse	5'-TACCTCCACCATGCCAAGTG-3' 5'-ATGATTCTGCCCTCCTCCTTC-3'
EGFR	Forward Reverse	5'-AGAAAGGCAGCCACCAAATTAGCC-3' 5'-TTCCTGGCTAGTCGGTGTAAACGT-3'
FGF-2	Forward Reverse	5'-AGCGGCTGTACTGCAAAAACGG-3' 5'-CCTTTGATAGACACAACTCCTCTC-3'
HIF-1	Forward Reverse	5'-TATGAGCCAGAAGAACTTTTAGGC-3' 5'-CACCTCTTTTGGCAAGCATCCTG-3'
Beta-actin	Forward Reverse	5'- AGCGAGCATCCCCCAAAGTT-3' 5'- GGGCACGAAGGCTCATCATT-3'

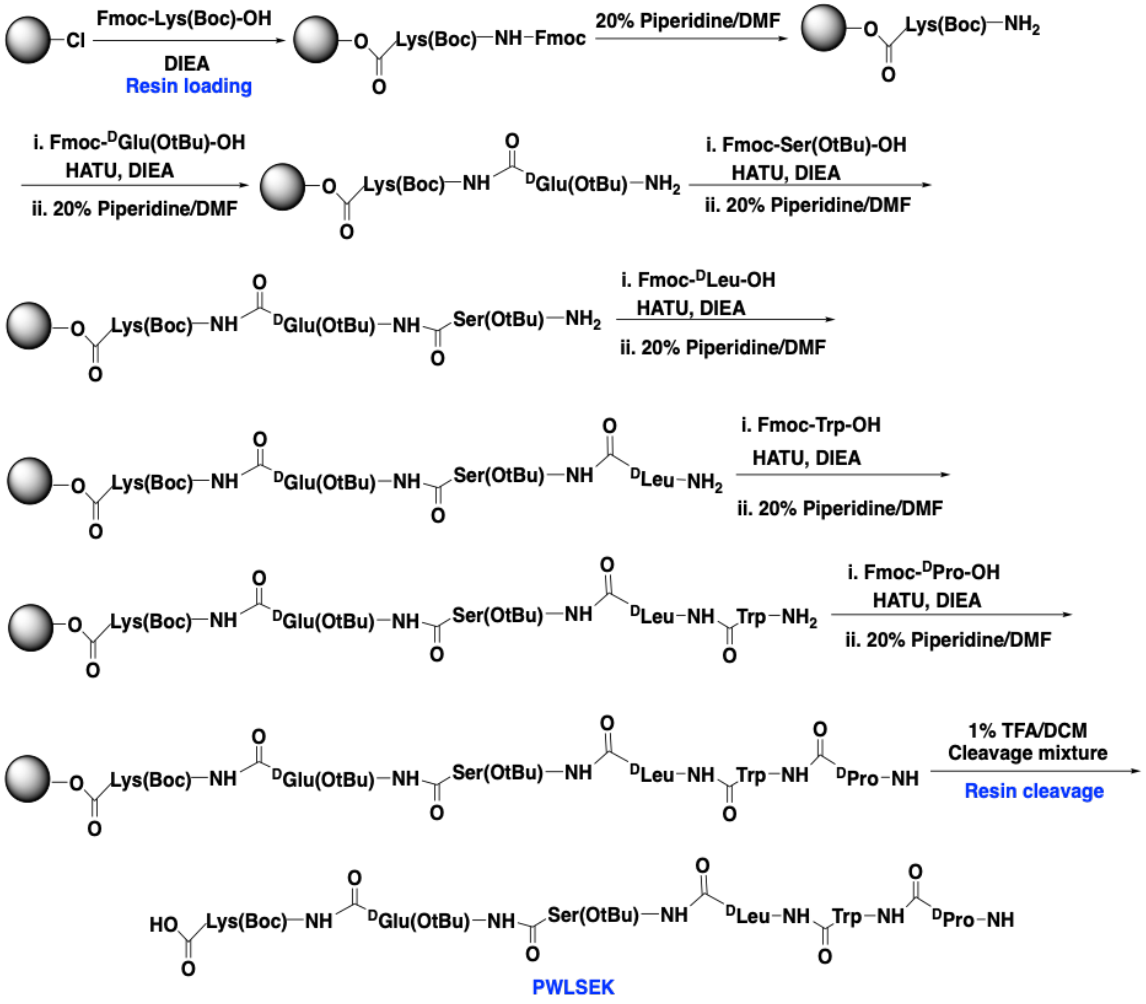

Figure A19. Synthesis of linear hexapeptide, PWLSEK, by solid-phase peptide synthesis (SPPS) using 2-CTC resin.

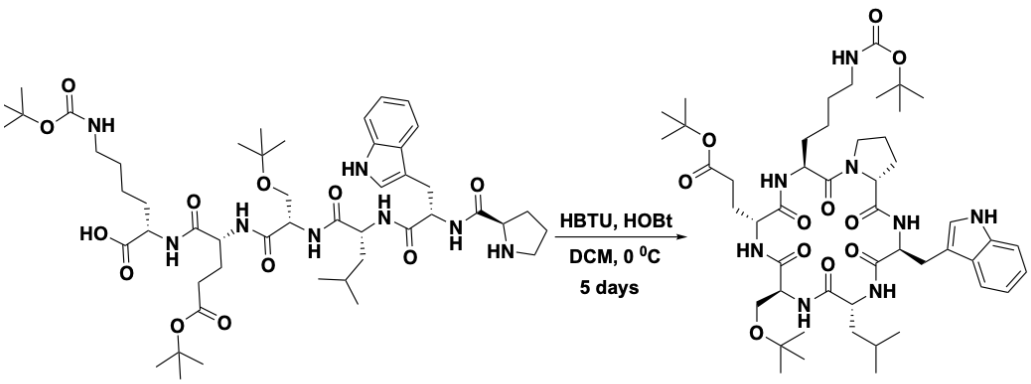

Figure A20. Scheme for the synthesis of cyclic peptide PWLSEK.

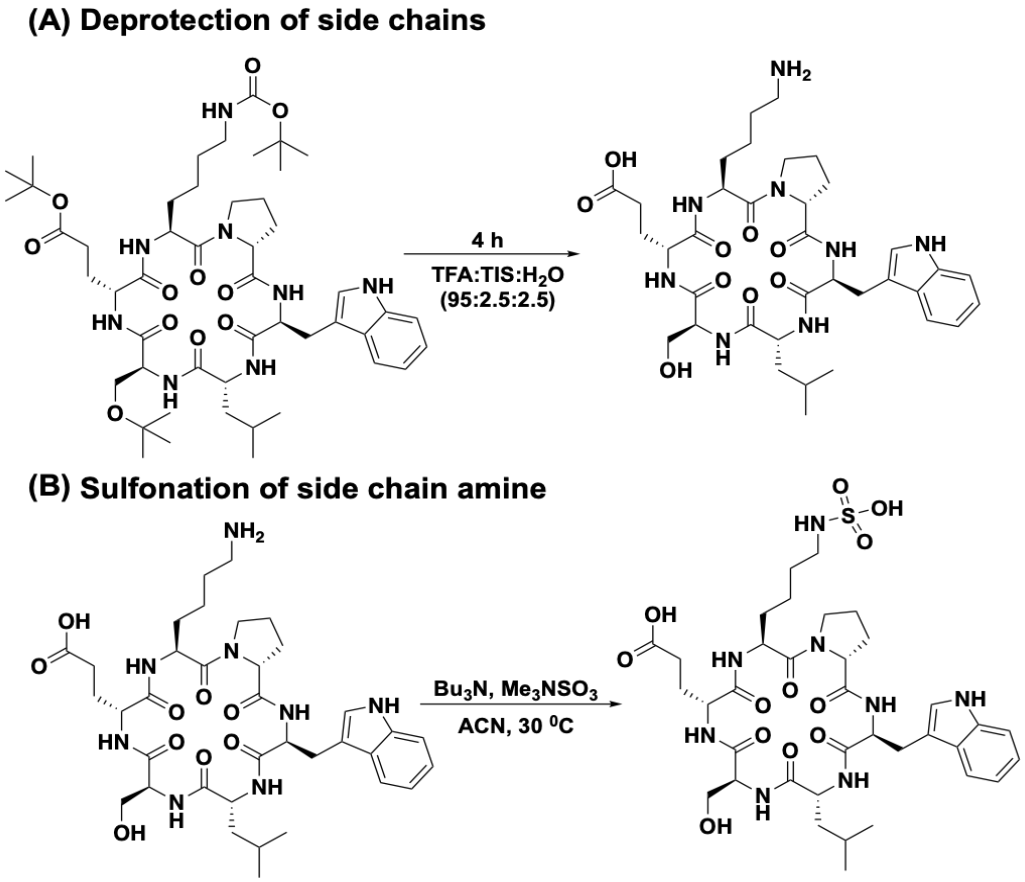

Figure A21. Synthesis of sulfonated cyclic peptide. (A) Deprotection of cyclic peptide side chains, and (B) Sulfonation of cyclic peptide (PWLSEK).

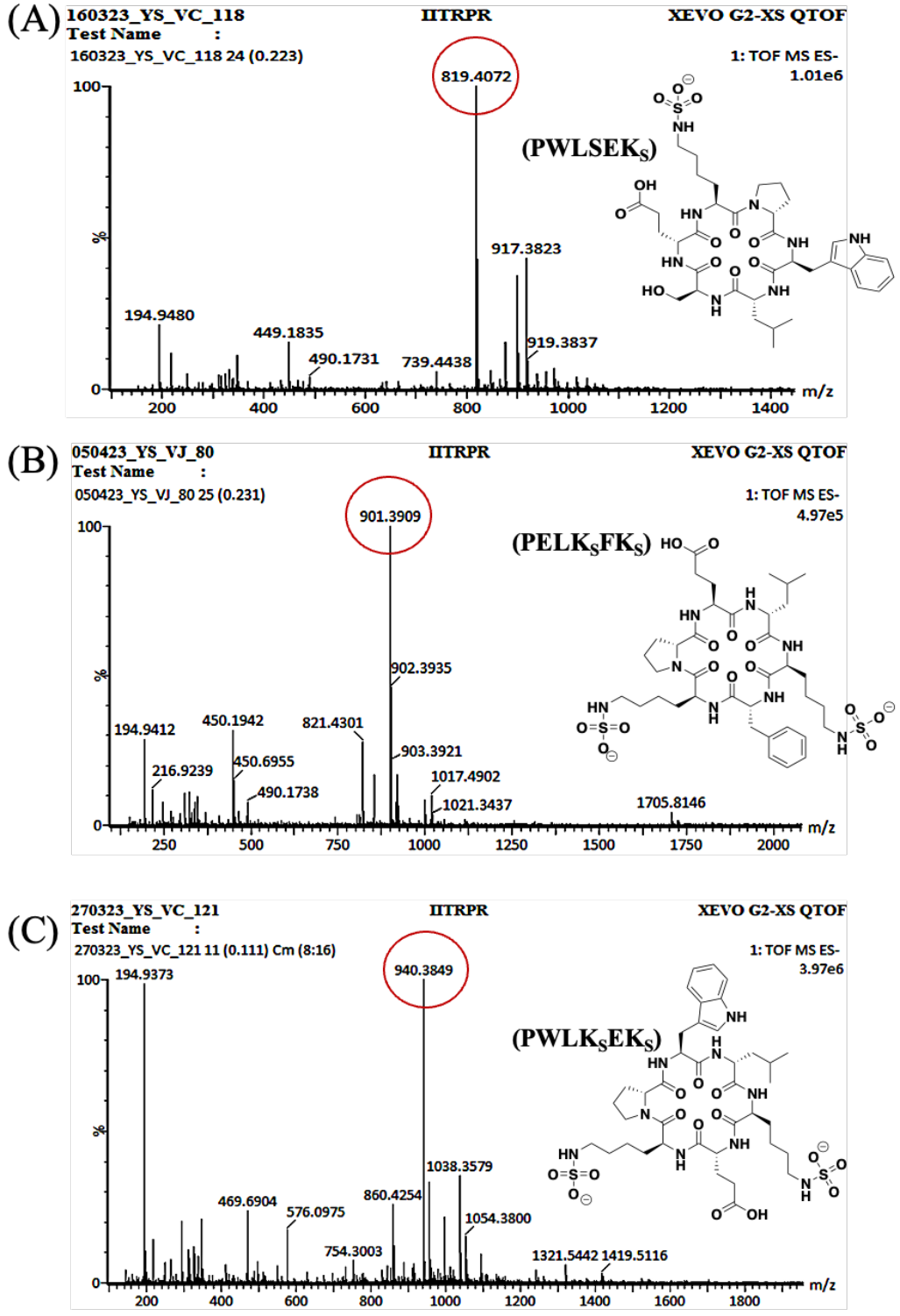

Figure A22. Mass spectra of sulfated cyclic peptides**,** SEK, KFK, and KEK.

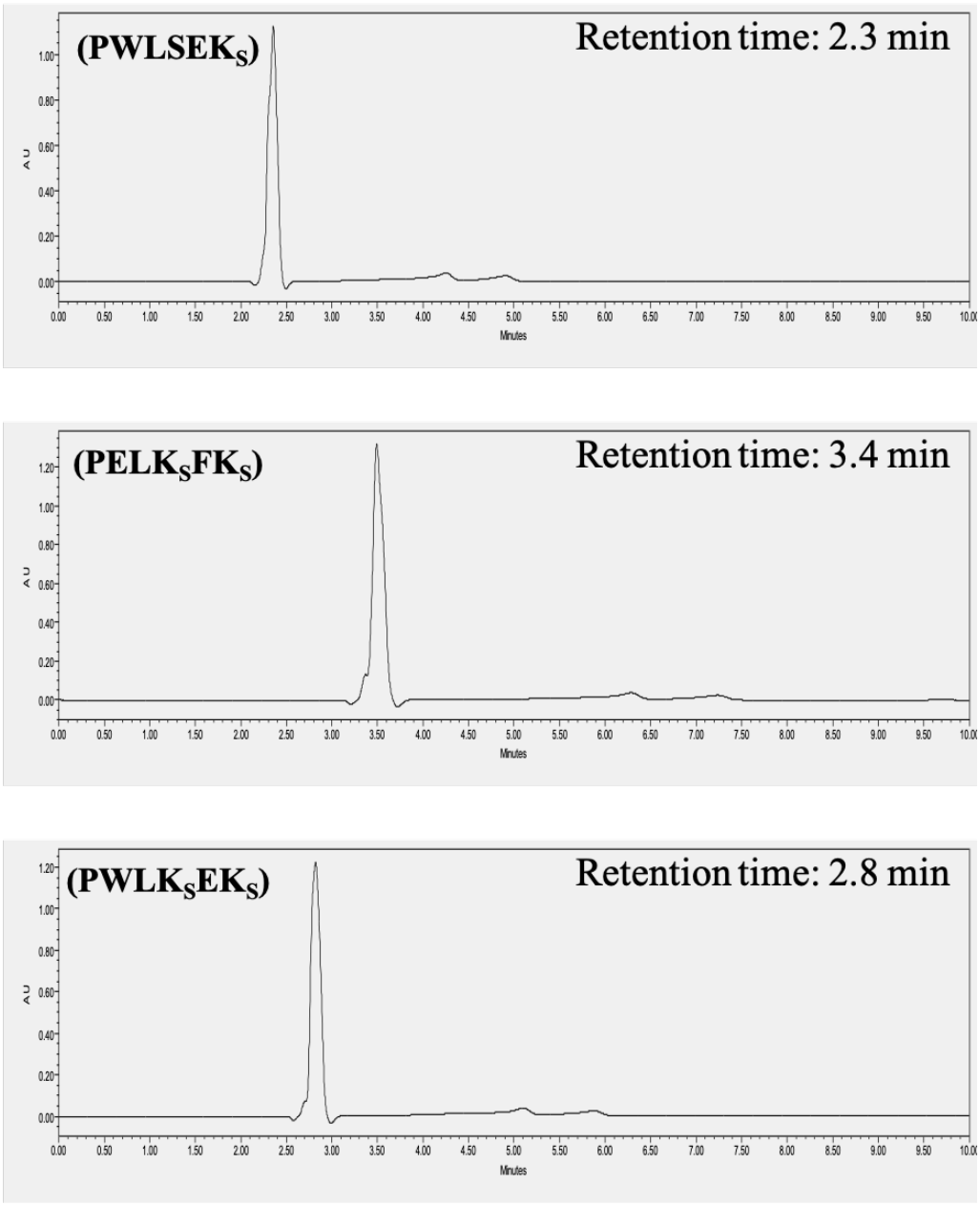

Figure A23. RP-HPLC profiles of sulfated cyclic peptide nanotubes (CPNTs), SEK, KFK, and KEK. ACN:H_2O (20:80) with 0.1% TFA was used as a mobile phase at a flow rate of 0.8 mL/min.

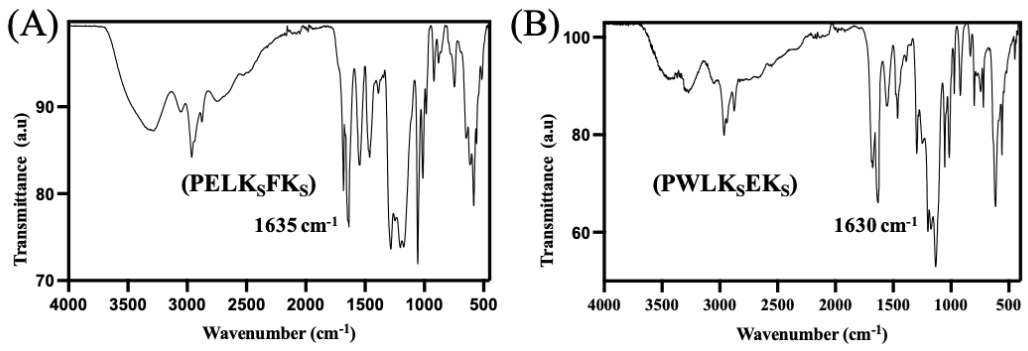

Figure A24. FTIR spectra of cyclic peptides, KFK and KEK.

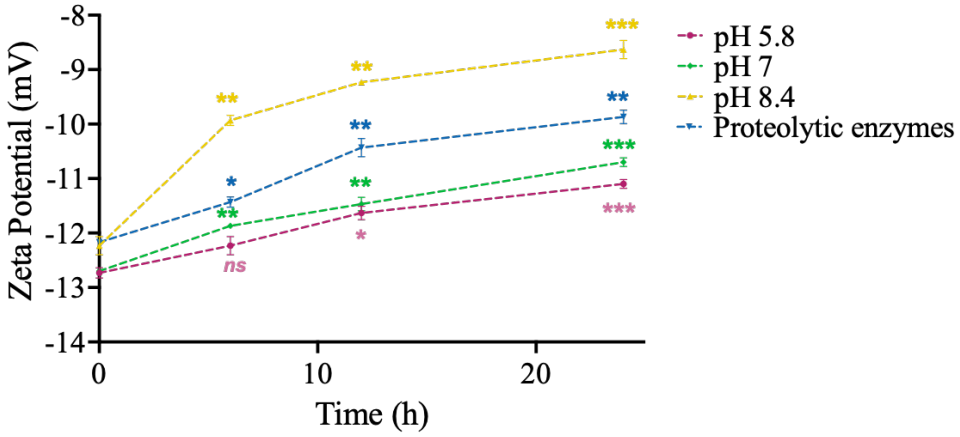

Figure A25. Stability of cyclic peptide nanotubes by estimating the zeta potential under different conditions of pH (5.8, 7, and 8.4) and proteolytic enzymes (chymotrypsin, pepsin, and proteinase K). Data are presented as mean ± standard deviation (n = 3), where *P* values <0.05 (*), 0.01 (**), and 0.001 (***) were considered as significant difference, and *ns* represents the insignificant difference.

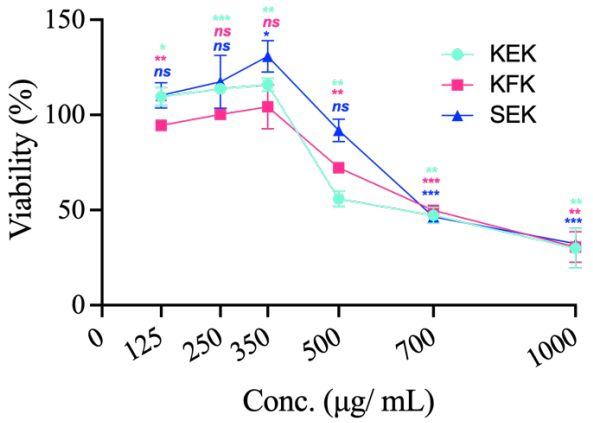

Figure A26. Dose-dependent cell viability analysis of cyclic peptide nanotubes by MTT assay in murine fibroblast (L929) cell line. Data are presented as mean ± standard deviation (n = 3), where *P* values <0.05 (*), 0.01 (**), and 0.001 (***) were considered as significant difference, and *ns* represents the insignificant difference.

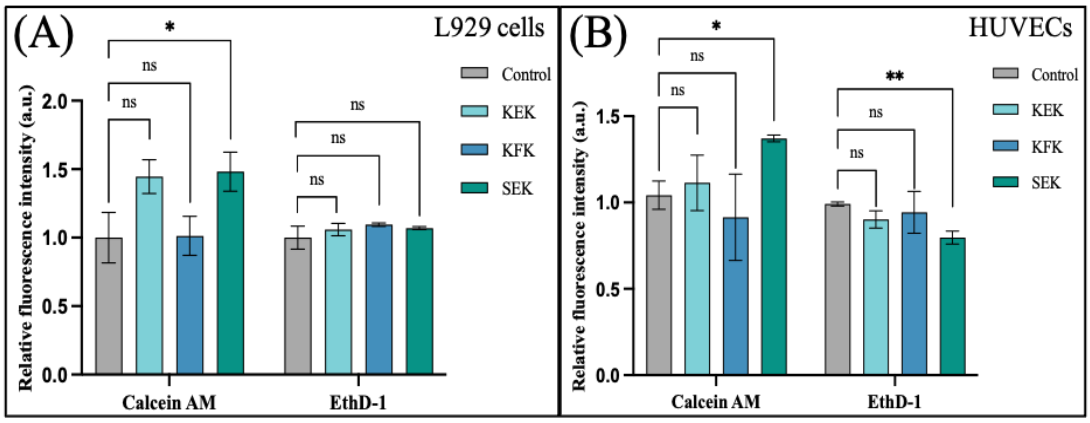

Figure A27. Semi-quantitative analysis of live/dead fluorescence intensity: (A) murine fibroblast (L929) cells, and (B) human umbilical vein endothelial cells (HUVECs). Untreated cells were used as controls. Data are presented as mean ± standard deviation (n = 3), where *P* values <0.05 (*), 0.01 (**), and 0.001 (***) were considered as significant differences, and *ns* represents the insignificant difference.

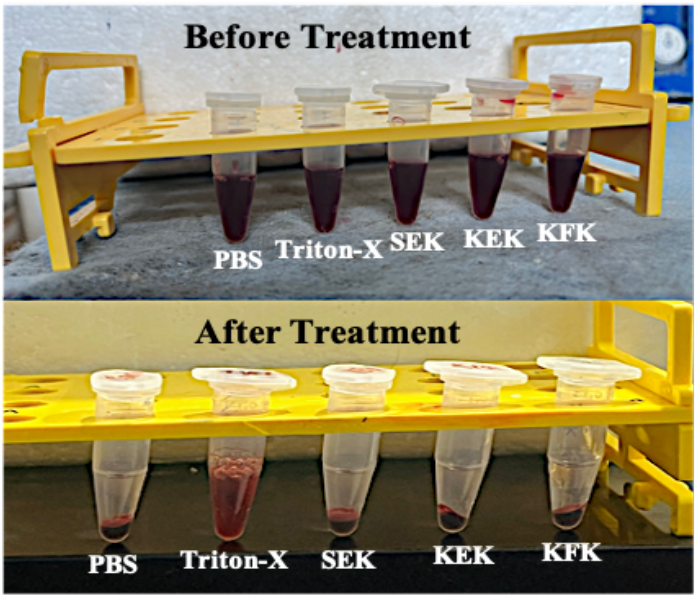

Figure A28. Hemocompatibility analysis of cyclic peptide nanotubes (CPNTs). Triton-X (0.1 % in PBS) was used as a positive control, while PBS alone was used a negative control.

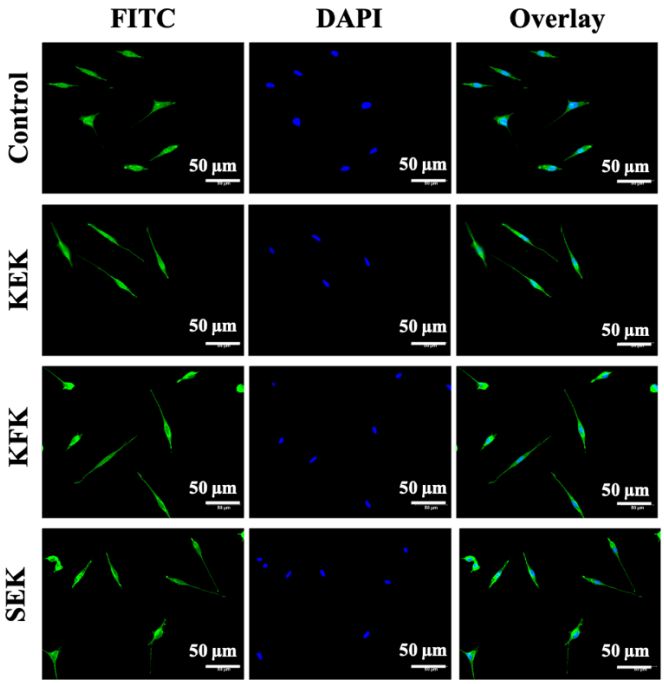

Figure A29. Morphological assessment by cytoskeletal staining of murine fibroblast L929 cells using Alexa Fluor phalloidin and DAPI after 24-h treatment with SEK CPNTs. Untreated cells served as controls. Scale bar: 50 µm.

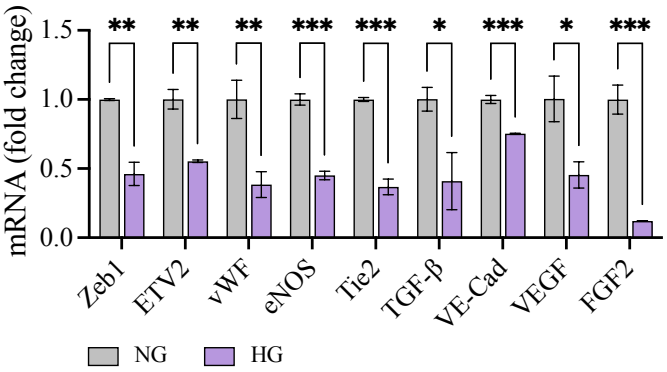

Figure A30. qPCR analysis of proangiogenic genes under hyperglycemic (HG) conditions. Data are presented as mean ± standard deviation (n = 3), where *P* values <0.05 (*), 0.01 (**), and 0.001 (***) were considered as significant difference, and *ns* represents the insignificant difference.

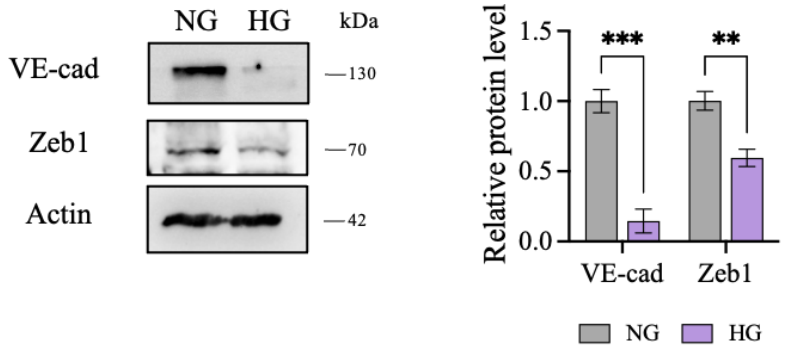

Figure A31. Immunoblotting analysis of VE-cad and Zeb1 expressions under hyperglycemic conditions in comparison to nonglycemic (NG) cells. Data are presented as mean ± standard deviation (n = 3), where *P* values <0.05 (*), 0.01 (**), and 0.001 (***) were considered as significant differences, and *ns* represents the insignificant difference.

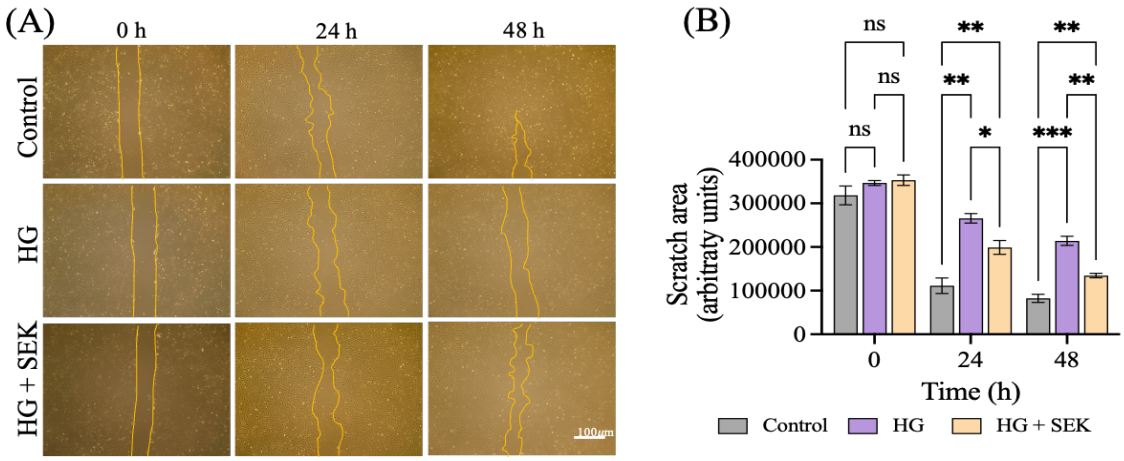

Figure A32. *In vitro* wound closure analysis under hyperglycemic (HG) conditions. (A) Scratch assay of NG, HG, and HG + SEK at 0, 24, and 48 h, and (B) Scratch area left unhealed at different time intervals. Data are presented as mean ± standard deviation (n = 3), where *P* values <0.05 (*), 0.01 (**), and 0.001 (***) were considered as significant differences, and *ns* represents the insignificant difference.

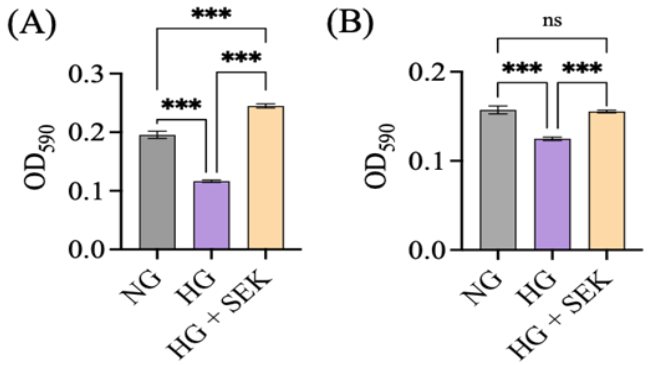

Figure A33. Absorbance value (OD_{590}) of SEK-treated hyperglycemic HUVECs on crystal violet staining. (A) Transwell cell invasion, and (B) Transwell cell migration. Non-glycemic (NG) cells were taken as controls. Data are presented as mean ± standard deviation (n = 3), where *P* values <0.05 (*), 0.01 (**), and 0.001 (***) were considered as significant differences, and *ns* represents the insignificant difference.

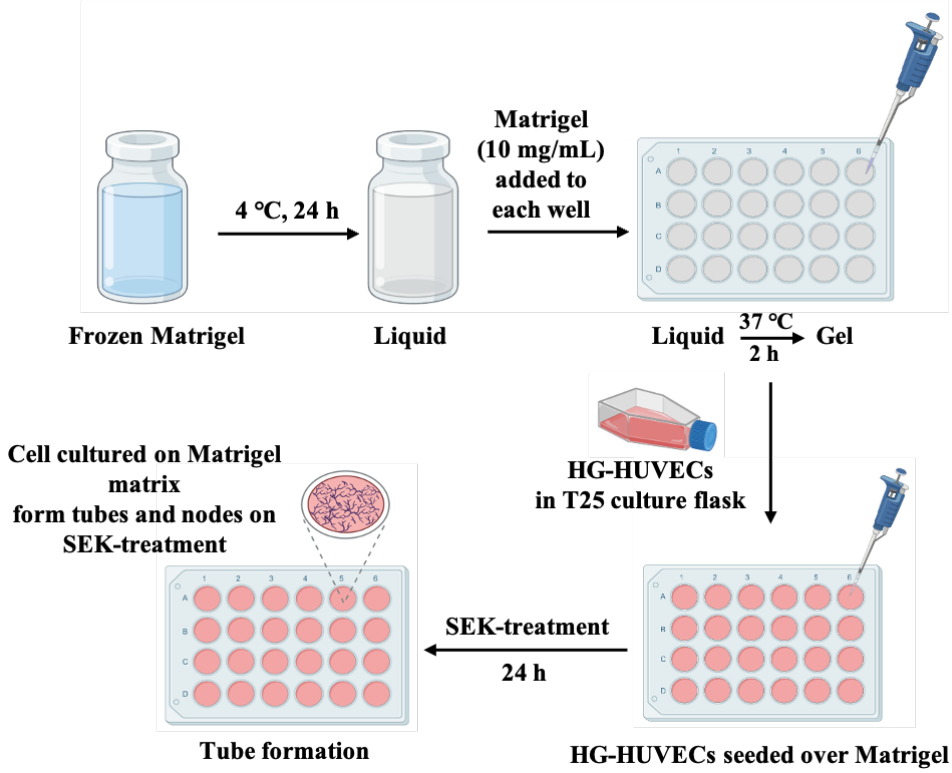

Figure A34. Schematic of in vitro endothelial tube formation assay on Matrigel after 24-h treatment with SEK cyclic peptide nanotubes.

Table A2. Primer sequences used in qPCR studies performed on HUVECs treated with proangiogenic CPNTs.

Genes	Forward primer (5'-3')	Reverse primer (5'-3')
Human primers		
VEGF	TACCTCCACCATGCCAAGTG	ATGATTCTGCCCTCCTCCTTC
FGF2	AGCGGCTGTACTGCAAAAACGG	CCTTTGATAGACACAACTCCTCTC
VEGFR2	GGAACCTCACTATCCGCAGAGT	CCAAGTTCGTCTTTTCCTGGGC
FGFR1	GCACATCCAGTGGCTAAAGCAC	AGCACCTCCATCTCTTTGTCGG
VE-Cadherin	GAAGCCTCTGATTGGCACAGTG	TTTTGTGACTCGGAAGAACTGGC
vWF	GTGTGTCCGAGTGAAGGAGG	CAGCACGCTGAGGTCTTACA
CD31	AAGTGGAGTCCAGCCGCATATC	ATGGAGCAGGACAGGTTCAGTC
Zeb1	TACCAGAGGATGACCTGCCA	TGCCCTTCCTTTCCTGTGTC
Tie2	TGCCACCCTGGTTTTTACGG	TTGGAAGCGATCACACATCTC
ETV2	ACGTCTCGGAAAATTCCCCC	ATGTCTCTGCTGTCGCTGTC
TGF-β	CAAGCAGAGTACACACAGCAT	TGCTCCACTTTTAACTTGAGCC
β-actin	AGCGAGCATCCCCCAAAGTT	GGGCACGAAGGCTCATCATT
Mouse primers		
β-actin	GTACTCTGTGTGGATCGGTGG	AGGGTGTAAAACGCAGCTCAG
CCL5	CTGCCTCCCCATATTCCTCG	TCGGGTGACAAAGACGACTG
CCL2	GATGCAGTTAACGCCCCACT	AGCTTCTTTGGGACACCTGC
TLR2	GCCACCATTTCCACGGACT	GGCTTCCTCTTGGCCTGG
IL-15	TTCTCTGCGCCCAAAAGACT	TTTCCTGACCTCTCTGAGCTG
MHCII	GAAGACGACATTGAGGCCGA	GGAACACAGTCGCTTGAGGA
IL-6	GGGACTGATGCTGGTGACAA	ACAGGTCTGTTGGGAGTGGT
IL-4	GCATGGCCCAGAAATCAAGG	GAGAAATCGATGACAGCGCC
Ym1	GTTTGGACCTGCCCCGTTC	CCTTGGAATGTCTTTCTCCACAG
NfkB	CCACAAGGGGACATGAAGCA	GATGGTACCCCCAGAGACCT
IL-1β	TGCCACCTTTTGACAGTGATG	GAAGGTCCACGGGAAAGACA
iNOS	CTTGGTGAAGGGACTGAGCTG	CGTTCTCCGTTCTCTTGCAGT

Table A3. List and details of antibodies used for protein expression analysis performed on HUVECs on treatment with proangiogenic CPNTs.

Antibody	Catalog no.	Dilution
iNOS	Cell Signaling Technology (#13120)	1:500 for ICC
CCL2	Santa Cruz Biotechnology (sc-32771)	1:250 for ICC
IL-1β	Invitrogen (P420B)	1:100 for ICC
vWF	Santa Cruz Biotechnology (sc-53466)	1:250 for ICC
Zeb1	Abcam (#ab181451)	1:1000 for ICC
Tie2	Abcam (#ab24859)	1:1000 for ICC
eNOS	Cell Signaling Technology (#32027)	1:250 for ICC
CD31	Cell Signaling Technology (#3528)	1:1500 for ICC
FGFR1	Novus Biologicals (NB600-1287)	1:1000 for WB 1:500 for ICC
VEGFR2	Novus Biologicals (NB600-530)	1:1000 for WB 1:500 for ICC
VE-Cad	Cell Signaling Technology (#2158)	1:1000 for WB
β-actin	Invitrogen (AM4302)	1:1000 for WB
Anti-Mouse IgG (Alexa Fluor 488-conjugated)	Invitrogen (A-11001)	1:1000 for ICC
Anti-Rabbit IgG (Alexa Fluor 568-conjugated)	Invitrogen (A-11012)	1:1000 for ICC
HRP-conjugated anti-mouse IgG antibody	Sigma-Aldrich (#A9044)	1:20000 for WB
HRP-conjugated anti-rabbit IgG antibody	Sigma-Aldrich (#A9169)	1:20000 for WB

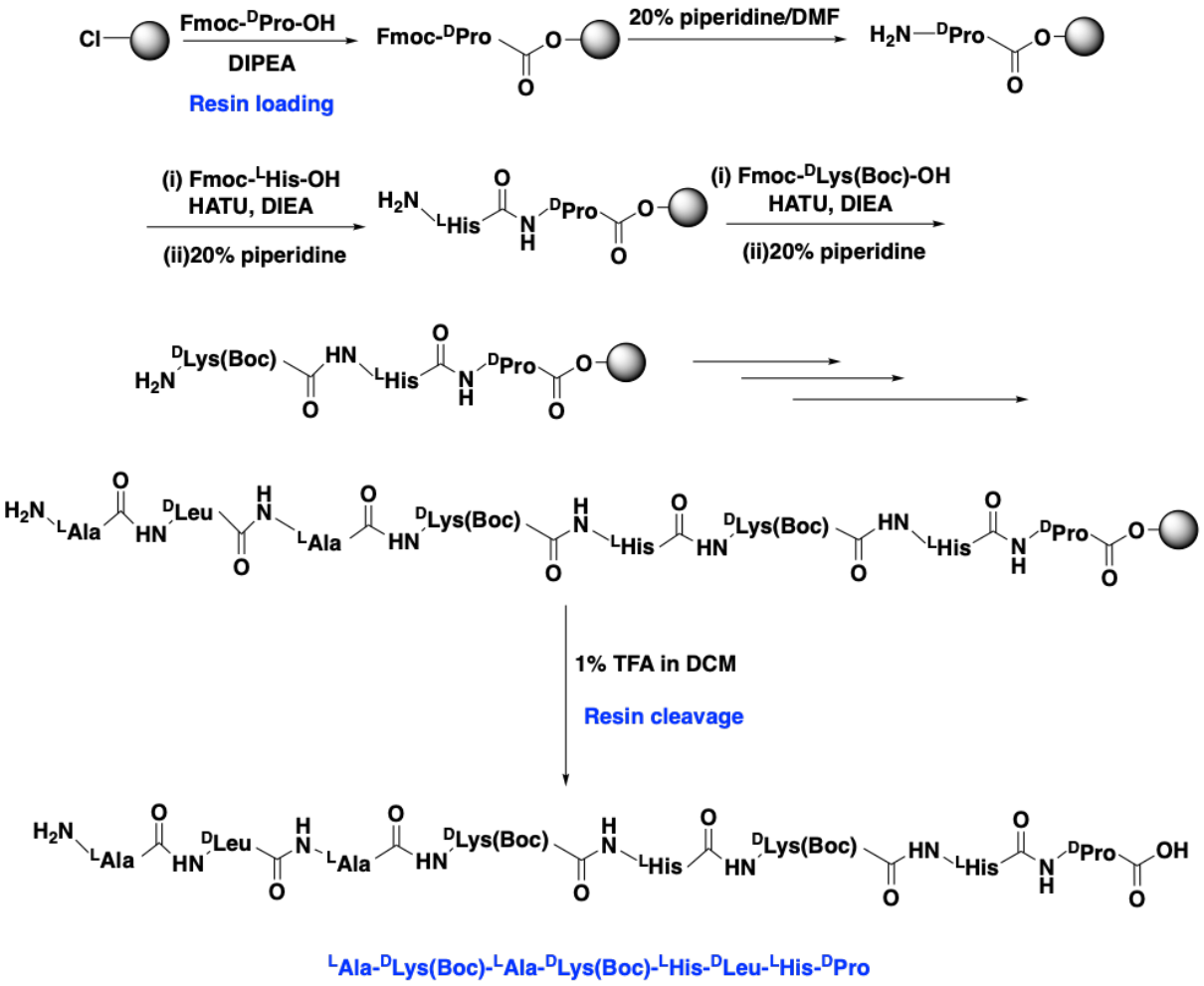

Figure A35. Synthesis of linear peptide ^{L}Ala-^{D}Leu-^{L}Ala-^{D}Lys(Boc)-^{L}His-^{D}Lys(Boc)-^{L}His-^{D}Pro by solid-phase peptide synthesis (SPPS) using 2-CTC resin.

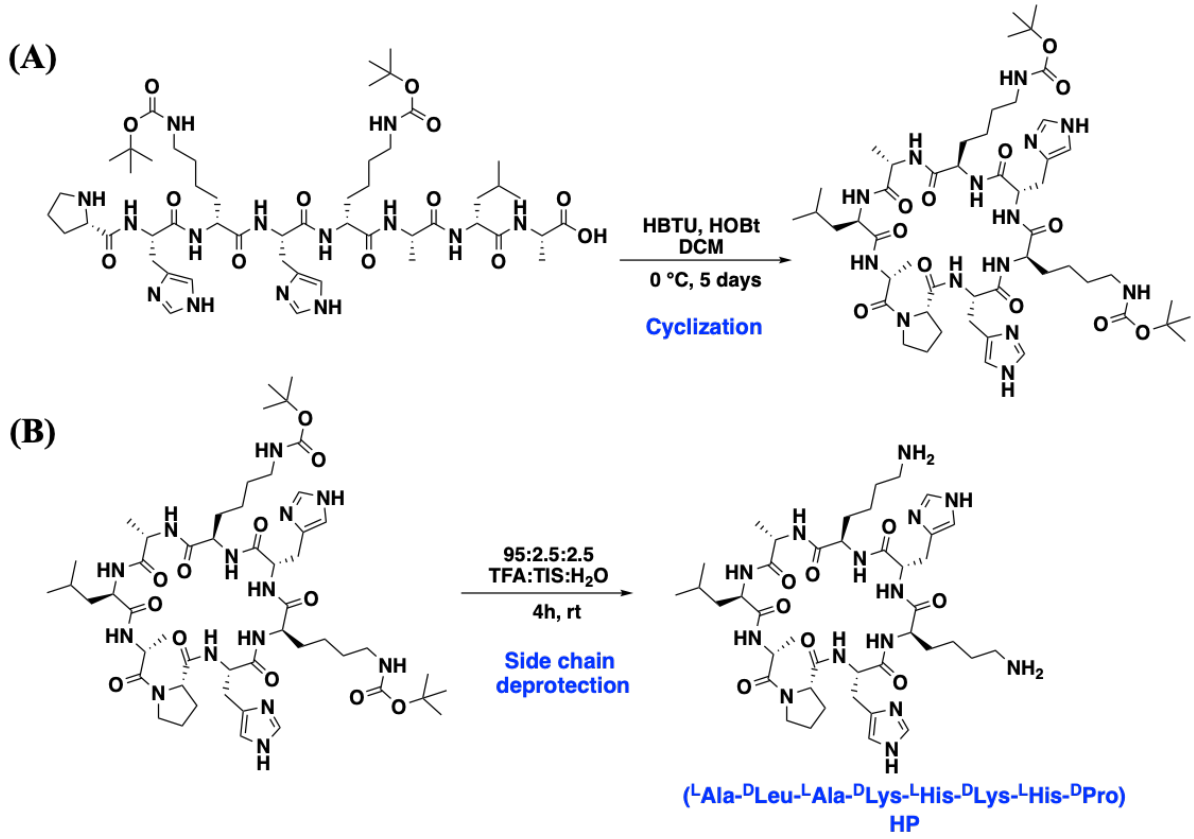

Figure A36. Synthesis of cyclic peptide, ^{L}Ala-^{D}Leu-^{L}Ala-^{D}Lys-^{L}His-^{D}Lys-^{L}His-^{D}Pro. (A) Cyclization of side-chain protected linear peptide ^{L}Ala-^{D}Leu-^{L}Ala-^{D}Lys(Boc)-^{L}His-^{D}Lys(Boc)-^{L}His-^{D}Pro. (B) Reaction scheme for the side-chain deprotection.

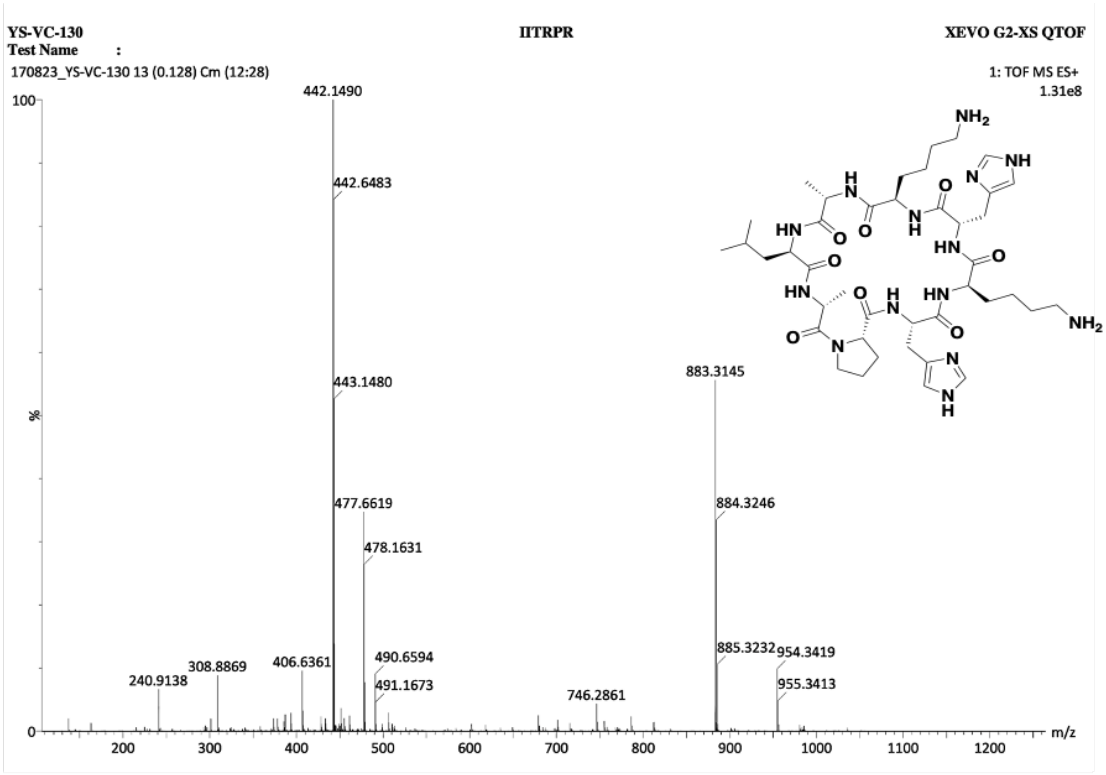

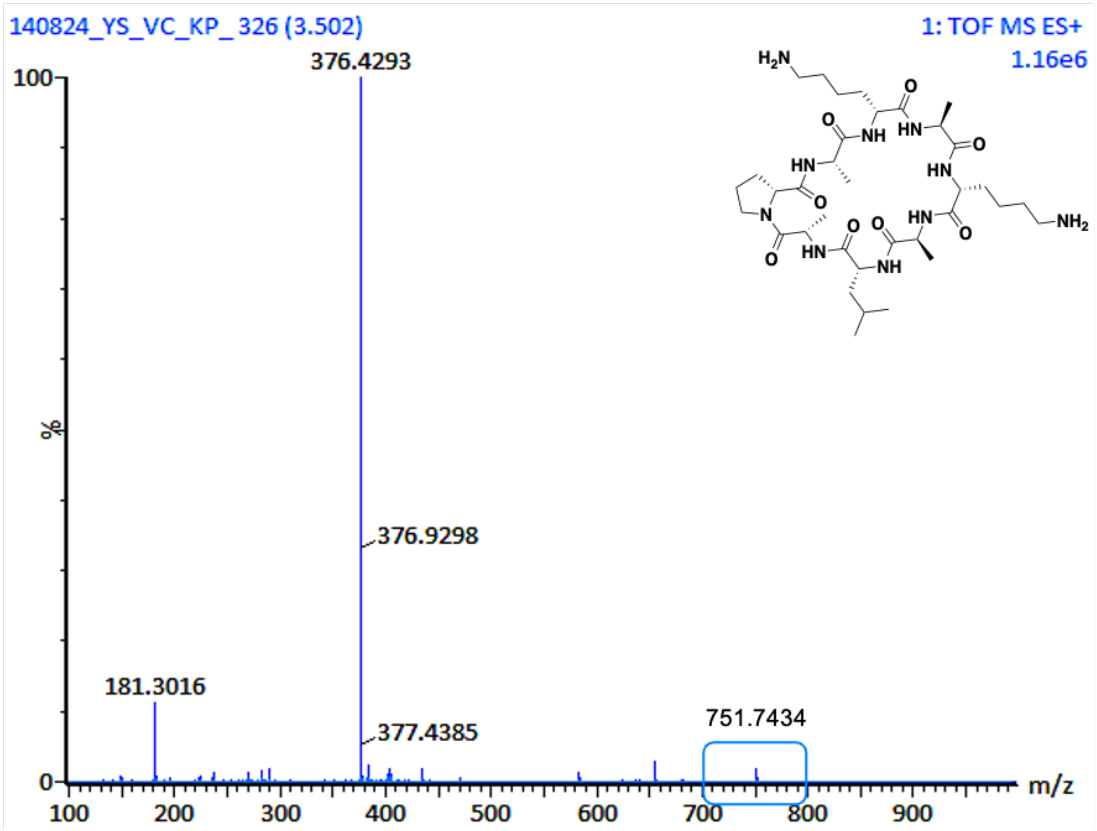

Figure A37. Mass spectra of HP and KP cyclic peptides. (A) ^{L}His-^{D}Lys-^{L}His-^{D}Lys-^{L}Ala-^{D}Leu-^{L}Ala-^{D}Pro, m/z: $[(M+H)^{+}]$ = 883.3145 Da, $[(M+2H)^{2+}]$ = 442.1490 Da. (B) ^{L}Ala-^{D}Lys-^{L}Ala-^{D}Lys-^{L}Ala-^{D}Leu-^{L}Ala-^{D}Pro, m/z: $[(M+H)^{+}]$ = 751.7434Da, $[(M+2H)^{2+}]$ = 376.4293 Da.

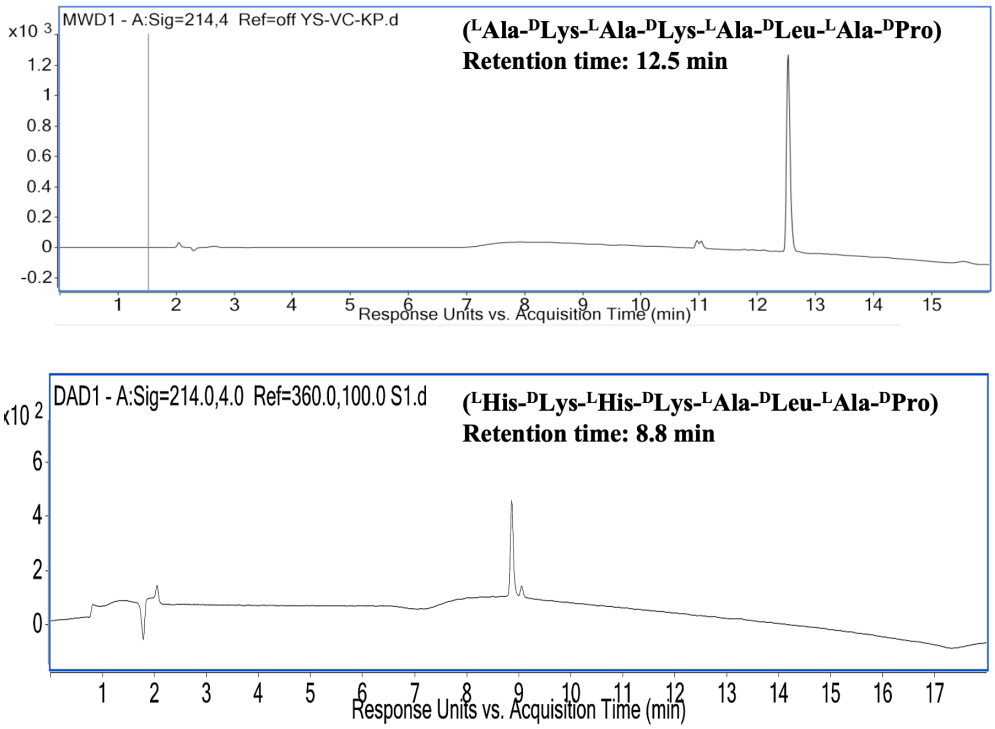

Figure A38. HPLC chromatograph of KP and HP. Chromotagraphs obtained under the conditions of linear gradient 10-100% of acetonitrile (0.08% TFA) over 10 min with 4 min equilibration, using Aglilent Zorbax SB-C3 LC coloumn at the 0.9 mL/min flow rate. UV-absorbance of eluent was monitored at 214 nm.

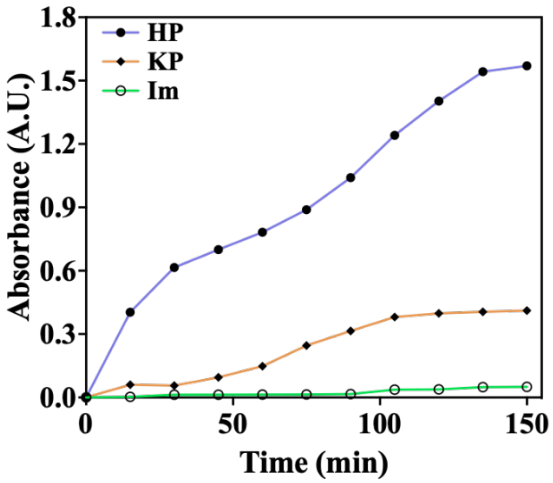

Figure A39. Time-dependent absorbance of p-nitro phenyl phosphate (pNPP) hydrolysis to determine the catalytic efficiency of HP-CPNTs. KP-CPNTs and free imidazole (Im) were used for the comparative analysis.

Table A4. Primer sequences used in qPCR studies on MC3T3 and RAW264.7 cells treated with ALP-mimetic CPNTs.

Genes	Forward primer (5'-3')	Reverse primer (5'-3')
β-actin	GTACTCTGTGTGGATCGGTGG	AGGGTGTAAAACGCAGCTCAG
iNOS	CTTGGTGAAGGGACTGAGCTG	CGTTCTCCGTTCTCTTGCAGT
TNF-α	CTGTCTTGCGTTGGGGGAG	TTAAGCTGCCTCACTCCCGT
IL-10	GCTCTTACTGACTGGCATGAG	CGCAGCTCTAGGAGCATGTG
RUNX2	TCCACCACGCCGCTGTCT	TCAGTGAGGGATGAAATGCT
ALP	CTGATCAGTGTGCCCCTGCAG	GGAGCTTGGAACGAATGTTCTG
OCN	CAAAGGTGCAGCCTTTGTGTC	TCACAGTCCGGATTGAGCTCA
OPN	CTTGCTTGGGTTTGCAGTCTT	GGTCGTAGAGTTAGTCCCTCAGA
RANKL	CTAAGAGACATGGCCCACGG	GTCCAGGGGTTAGACCCAGA
TRAP	AGCAGCCAAGGAGGACTACGTT	TCGTTGATGTCGCACAGAGG